New initiators for the polymerisation of bio-based monomers

Beament, James

Award date:
2019

Awarding institution:
University of Bath

New initiators for the polymerisation of renewable monomers

James Beament

A thesis submitted for the degree of Doctor of Philosophy

Department of Chemistry

University of Bath

March 2019

Abstract

Decades of reliance on petrochemical and non-degradable plastics has forced the world's habitats into a critical state. Recent exposure of the extent of marine plastic pollution has forced a fundamental rethink of our relationship with plastic. To this end poly(lactic acid) (PLA) has gained significant attention. Despite already being commercial, for PLA to reach its full potential, a redesign of its production and use is required. This thesis opens with discussion on how understanding the interplay between metal, ancillary ligand, and monomer can be used to progress the area of polymerisation catalysis, improving the production of new bio-based and bio-degradable plastics with enhanced properties.

Investigating the influence of the metal centre, chapter 2 focuses on how group 13 based complexes have become a central research focus in the synthesis of PLA. Exploring how atomic radii impacts reactivity, a series of novel tetradentate salan bipyrrolidine and ethylene diamine ligated complexes were synthesised. When applied to the ring-opening polymerisation (ROP) of *rac*-lactide (*rac*-LA) indium systems were shown to be highly selective, producing heterotactic PLA with the aluminium analogue being poorly active.

In a similar vein, chapter 3 explores the efficacy of lanthanide complexes for the ROP of LA, as well as the copolymerisation of epoxides and anhydrides. This chapter focuses on the how the use of modern spectroscopic methods can allude to the nature of the catalytically active species. Through such experiments the discovery of a co-operative mechanism between metal centres on a bimetallic initiator is proposed. This study also evaluates the influence of hydrolytic degradation on complex structure and reactivity, addressing the desire for robustness in industrial production. Chapter 4 evaluates the influence of the ancillary ligand on catalyst activity. Altering the sterics and electronics of a bidentate mono pyrrolidine ligand, a series of novel aluminium initiators which impart good rates and high isoselectivities are reported. Varying the ligand coordination number showed unpredictable behaviour with a more exposed coordination site giving improved activities and selectivities.

Chapter 5 describes research into how catalyst selection is integral in the development of novel and promising polymers. Focusing on the copolymerisation of LA and a cyclic phosphonate monomer, monomer selectivity achieved as a result of judicial initiator choice. Using *in-situ* spectroscopic methods the growth of the polymer and nature of the microstructure is monitored and controlled. The enhanced degradability of poly(phosphonates) and their biological compatibility makes these copolymers ideal for further exploration into biomedical and short life packaging applications.

Acknowledgements

Firstly, I would like to acknowledge the excellent supervision of Dr Matthew Jones and Dr Antoine Buchard. Matthew has shown utmost dedication and interest in my projects as well running all my solid-state structures with haste on weekdays or weekends. I would also like to thank Dr Mary Mahon for her assistance in solving my structures, most of which were not facile. I would like to thank Antoine for his patience, guidance and thoroughness. His desire for excellence has developed me into a confident researcher who is both analytical and critical. I have been very fortunate to have such encouraging supervisors, something I am very grateful for, without which my PhD would not have been as successful.

I would also like to acknowledge my collaborators at the Max Planck Institute for Polymer Research. Dr. Frederik Wurm, Jens Markwert and Dr. Thomas Wolf have supplied me with materials, analysis, and discussion in building what has become a highly successful collaboration. I am ever thankful to the assistance of the characterisation specialists at the University of Bath, namely Dr. Tim Woodman, Dr. John Lowe and Dr. Rémi Castaing. Notably, Tim, who has given much time to assist me with great enthusiasm. His passion and wealth of knowledge on all things lanthanide and DOSY has provided me with the expertise and confidence to discuss these topics with experts around the world.

No PhD is possible without the support and comradery of fellow colleagues. For this I have many people to acknowledge. I would firstly like to thank all the group members of the Jones and Buchard groups, past and present, with special mention to Dr. Paul McKeown for his relentless help on all things chemistry. In addition, the ever expanded 'suschem group' have provided interesting discussions in a range of topics surrounding sustainability. Most significantly, I would like to thank Michael Joyes and Jamie Courtenay who have been integral to an exceptional experience through the last four years.

I would like to thank the EPSRC for funding my PhD project, the University of Bath Alumni Fund for travel support and the Commonwealth Blue Charter Fellowship for funding my placement at Memorial University, Canada.

Finally I would like to thank my family, specifically my Mum for the love, support, and drive to push myself and achieve.

Table of contents

Table of abbreviations

bio-PE : bio-sourced poly(ethylene)

BnOH : benzyl alcohol

BTX : benzene, toluene, xylene

CHN : elemental microanalysis

CHO : cyclohexene oxide

CTA : chain transfer agent

D : diffusion constant of analyte

$Đ$: molecular weight dispersity

DBU : 1,8-diazabicyclo[5.4.0]undec-7-ene

DFT : density functional theory

DMF : dimethylformamide

DOSY : diffusion ordered spectroscopy

DSC : differential scanning calorimetry

D_{sol} : diffusion constant of solvent

ESI-MS : electrospray ionisation mass spectroscopy

FDA : US Food and Drug Administration

k_{init} : initiation rate constant

k_{obs} : observable rate constant

k_{prop} : propagation rate constant

LA : lactide

LCST : lower critical solution temperature

LDPE : Low density poly(ethylene)

LS : light scattering

MALDI-ToF : Matrix-assisted laser desorption and ionisation time-of-flight

MePPn : 2-methyl-1,3,2-dioxaphosphalone-2-oxide

M_n : number average molecular weight

M_n^{SEC} : number average molecular weight calculated by SEC

M_w : weight average molecular weight

NEt_3 : triethylamine

NMR : nuclear magnetic resonance

PA : phthalic anhydride

PBAT : poly(butylene adipate-co-terephthalate)

PBS : poly(butylenesuccinate)

PCL : poly(ε-caprolactone)

PE : poly(ethylene)

PEF : poly(ethylene furanoate)

PET : poly(ethyleneterephtalate)

pEtPPn : ethylene ethyl phosphonate

PHAs : poly(hydroxyalkanaotes)

PLA : poly(lactic acid)

PPE : poly(phosphoesters)

PPn : poly(phosphonates)

P_r : probability of racemic enchainment

PS : poly(styrene)

r_i : reactivity ratios

RI : refractive index

ROCOP : ring-opening copolymerisation

ROP : ring-opening polymerisation

SEC : size exclusion chromatography

TBD : triazabicyclodecene

T_c : crystallisation temperature

T_g : glass transition temperature

TGA : thermograviometric analysis

THF : tetrahydrofuran

T_{inf} : temperature of fastest mass loss

T_m : melting temperature

T_{ons} : Onset of degradation

TU : thiourea

UCST : upper critical solution temperature

δ_{con} : Fermi contact shift

ΔG_p : Gibbs free energy of polymerisation

δ_{obs} : isotropic shift

δ_{orb} : orbital shift

δ_{pc} : pseudo contact shift

ε-CL : ε-caprolactone

Chapter 1

Introduction

1. Introduction

1.1. Global plastic production

Commodity plastics have been one of the great technological leaps of the 20th century. Dominating all aspects of our lives, our reliance on plastics has been embedded. To meet humankinds growing demands, the annual global production of plastic surpassed 311 million tonnes in 2014, and is expected to double by 2034.[1] With over 90% of this derived from virgin crude oil, predictions show by 2050, that plastic production will represent 20% of global oil consumption.[1] Consumer packaging represents the largest application, where the need to deliver products safely, and at low cost, are the forefront of product design. To this end, hydrocarbon plastics show their prowess, being durable, lightweight and part of a well-established production system. However, recent exposure surrounding plastic persistence in the environment, recycling inefficiencies, and dwindling fossil fuel reserves has highlighted the dark side of the current approach.[2–4]

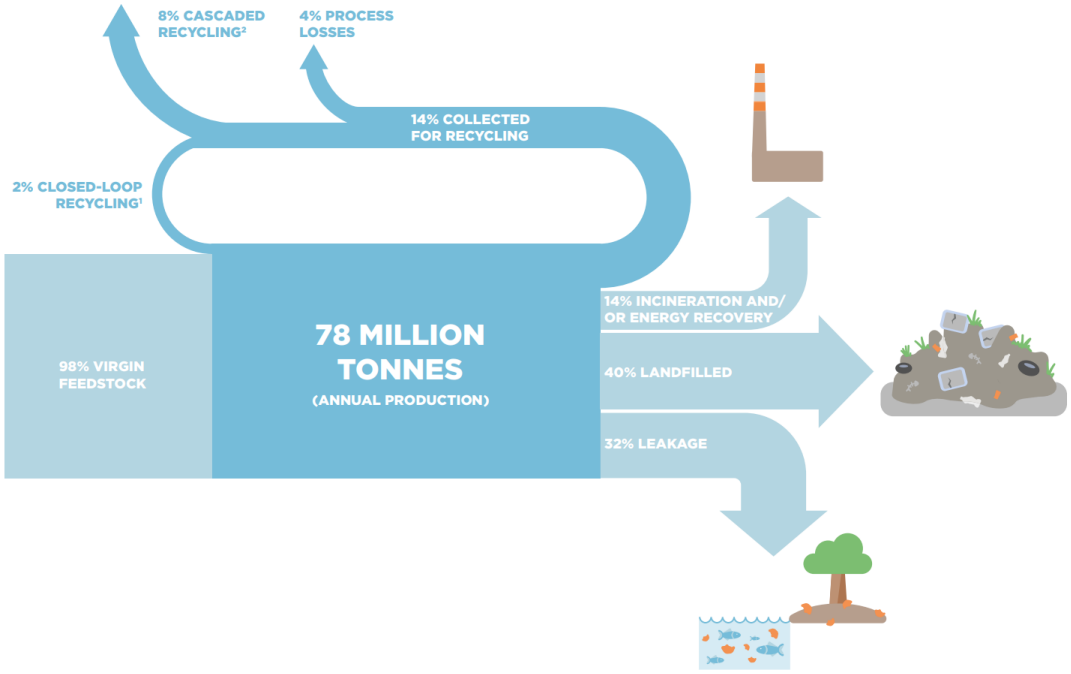

Figure 1.1. Global percentage flow of plastic packaging in 2013, as published from 'The New Plastics Economy'.[1]

Of the 78 million tonnes of plastic packaging produced annually, only 2% is recycled back into virgin feed (Figure 1.1).[1] With 40% ending up in landfill and 32% leaking out of the controlled collection system, a value loss of $120 billion is associated. Of that which is leaked, the majority finds its way into the world's oceans, where it persists, generating a risk to marine ecosystems.[5] Due to the lack of a closed-loop approach and derivation primarily from

petrochemical feeds, current estimates show plastic production will represent 15% of global carbon budget by 2050.[1] In order to agree with the terms of the Paris agreement to limit global carbon emissions to 18 Gt(CO_2)yr^{-1}, the current model for plastic production, usage and end-of-life is not fit for purpose.[6]

Generating consumer and governmental pressure to address this, notable schemes and projects have been established. For example, in the UK, the 'UK plastics pact roadmap' seeks to focus business efforts towards redesign and adoption of highly recyclable or compostable materials by 2025.[7] Signed by 68 businesses who are responsible for 80% of the UK plastic packaging market, this agreement represents a shift in business approach to tackling the issue. Other governmental supported projects such as the 'Commonwealth Blue Charter' seek to carry out more fundamental research in addressing marine plastic pollution.[8] These organisations and others worldwide address two main aspects of sustainability; Where do we source our plastics from in the future? What can we do to mitigate their end-of-life options?

Renewable alternatives to petrochemical plastics can come under two terms: bio-replacement or bio-advantaged.[9] Bio-replacement plastics are drop-in mimics to commercial systems. They can be adopted into the production line without modification often presenting a good economic argument with wide scalability. Historically however, bio-sourced replacements are equally reliant on fluxional market prices, which has since hindered, for example, the adoption of bio-sourced poly(ethylene) (bio-PE), sourced from sugar cane.

The adoption of bio-derived ethylene glycol in the production of 30% bio-based polyethylene terephthalate (PET) has been pioneered by CocaCola in the form of PlantBottle™. Their commitment to fully adopt this semi-renewable bottle by 2020, presents a large shift in the percentage of bio-renewable plastics in the global market. In addition, significant progress in accessing and commercialising terephthalic acid from biomass has made the prospect of 100% renewable PET a commercial possibility in the coming years. The leading technology for this process focuses around aqueous-phase reforming of highly oxygenic biomass to a BTX (benzene, toluene, xylene) mixture. Separation of *p*-xylene followed by oxidation yields the terephthalic diacid monomer (Scheme 1.1).[10] This approach raises questions regarding the overall sustainability of the approach, with many steps required to achieve the desired replacement. Whilst other methods have been realised for terephthalic acid production, including conversion from furfural and HMF, the BTX process has been shown to have the lowest environmental footprint.[10–13]

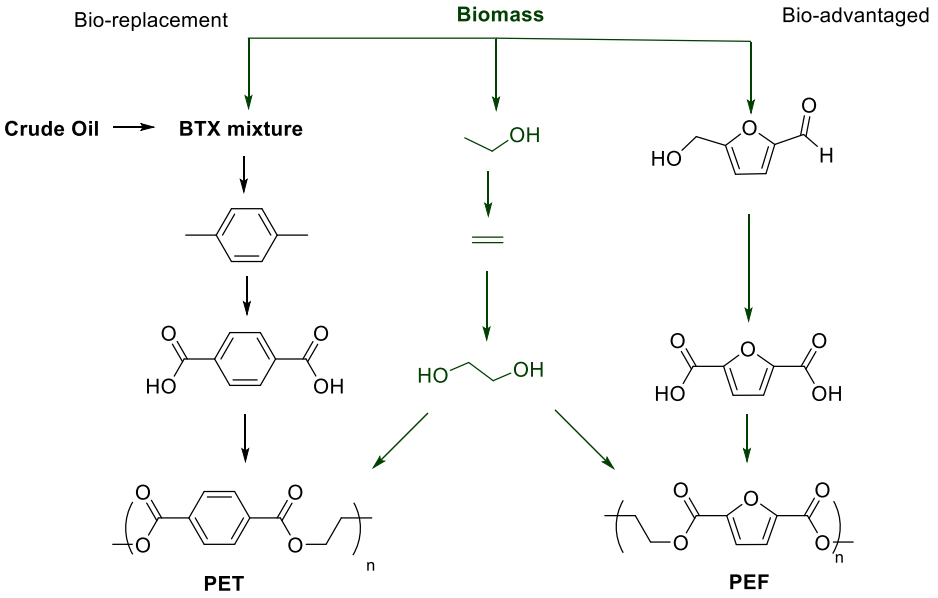

Scheme 1.1. Synthetic routes to access bio-PET and PEF.

Bio-advantaged plastics represent a different approach, by designing new plastics with superior properties which can outcompete the petrochemical alternative. To this effect, plastics with tuneable degradation timeframes, superior barrier and thermal properties can be developed, addressing modern concerns on how we use plastic. Aiming to replace PET is polyethylene furanoate (PEF), a copolymer of ethylene glycol and 2,5-furandicarboxylic acid (FDCA). FDCA can be obtained readily from biomass and is considered one of the major building blocks of the bio-based society.[14–16] Research in the last decade in developing the industrial applicability, has seen this polymer currently synthesised at pilot scale. A joint venture between Avantium and BASF hoping to be see this product commercial by 2023.[17] PEF boasts more favourable green credentials than PET, with lower total emissions during production.[18] In addition, the 19-fold reduction in CO_2 and 11-fold reduction in O_2 gas permeability means the processed plastic can be made thinner, whilst maintaining the shelf life of the contents.[19–21]

Research into the production of high-value polyesters from forestry and other agricultural lignocellulosic feeds shows great promise.[22,23] Driven by the desire to add value to biorefinery projects, terpene derived polymers,[24,25] hydrophobic polymers from suberised cell walls and other lignocellulosic derived polymers represent a class of polymers with huge production potential in the infancies of development.[26]

Within the development of bio-advantaged polymers, designing for degradation has been an important aspect. One of the more recent of this class to gain prominence is poly(hydroxyalkanaotes) (PHAs).[27] These polyesters represent a class of biodegradable polymers produced naturally *via* fermentation. Biological engineering has been an avenue which has successfully been employed for PHAs to deliver a variety of side-chain functionalities, yielding a range of accessible materials properties.[28–31] However, the high costs associated with the manufacturing of large quantitates of PHAs is reported as one of the major restrictions in PHA emergence.[32] Currently, the most widely produced biodegradable polyesters are poly(butylenesuccinate) (PBS), poly(butyleneadipate-co-terephthalate) (PBAT), poly(ε-caprolactone) (PCL), and poly(lactic acid) (PLA). Whilst PBS, PBAT and PCL are currently petrochemically derived, recent market data highlights significant developments into sourcing their analogous monomers from bio-renewable feedstocks.[33,34]

1.2. Poly(lactic acid)

PLA is the worlds most produced synthetic bio-derived and compostable polymer.[33] An aliphatic polyester, it is derived from the fermentation of sugar feedstocks (typically corn starch and sugarcane) to lactic acid. The wide variety of feedstocks suitable for the production of lactic acid, including 2nd and 3rd generation waste food streams mean it is not under geopolitical constraints or socio-economic 'food *vs* fuel' debates.[35] In addition, it is bio-compatible, fully bio-renewable and industrially compostable. Compared to polystyrene (PS), PET and polypropylene (PP), PLA has lower O_2 and H_2O permeability, as well as 30 – 50% lower emissions.[36] Natureworks LLC are the world's leading producer of PLA, with yields of 140 kt yr^{-1}.[36,37] This market has been set to reach a value of $851.5 million by 2019 following the expansion by Corbion-Total in opening a 75 kt yr^{-1} plant.[36,38]

Commercial PLA can be characterised as a colourless stiff thermoplastic with mechanical properties similar to that of PS.[39,40] However, compared to PS, the degradation of PLA in the environment is more facile occurring in the order of 6 to 24 months rather than 100 to 500 years.[41] This enhanced degradation allows it to be classed as industrially compostable, highlighting a more sustainable option as a 'cradle to cradle' alternative to non-biodegradable plastics.

1.2.1. Preparation and Properties

PLA was first synthesised by Carothers and co-workers in 1932, *via* the polycondensation reaction of lactic acid.[42] Due to the equilibrium nature of polycondensation, high molecular weight polymer can only be prepared at very high conversions, requiring the effective removal of water, which is formed as a by-product. In addition, water can potentially cause chain transfer and hinder propagation. As a result, only highly disperse, low molecular weight PLA (~5 kDa) is produced *via* this method.[40,43] To avoid this, Carothers showed the potential of the ring-opening polymerisation (ROP) of lactide (3,6-dimethyl-1,4-dioxan-2,5-dione) as a means to access higher molecular weight PLA.[42]

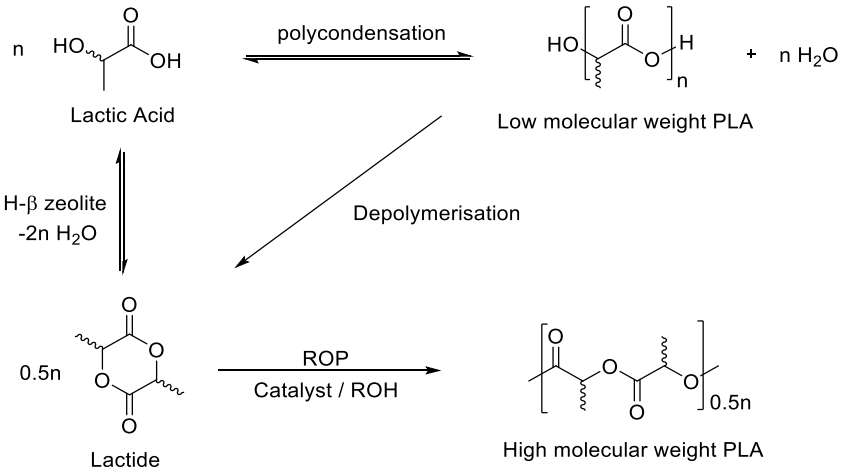

Scheme 1.2. Routes for the preparation of polylactic acid (PLA)

Lactide is the cyclic, di-lactone condensation product of two lactic acid units. Thermal depolymerisation of low-molecular weight PLA yields this monomer, which can be collected in high purity *via* sublimation from the crude mixture. Recently, approaches have been studied for the direct production of lactide from lactic acid alleviating some of the economic and synthetic burdens of the traditional route.[44,45] Most notably, a heterogeneous H-β zeolite has been able to catalyse the production of lactide from lactic acid under mild conditions without epimerisation.[46]

Subsequent ROP of the cyclic ester under solvent free conditions can lead to PLA with high molecular weights and narrow dispersities, avoiding the issue of unwanted protic by-products. Stannous bis(2-ethylhexanoate), commonly known as $Sn(Oct)_2$, is used industrially as the catalyst for this process by activating the carbonyl group of lactide for nucleophilic attack from a propagating alkoxide chain (Figure 1.2). Favoured for being highly active and robust, $Sn(Oct)_2$ is also considered as safe for the use in the production of food packaging being approved by the US Food and Drug Administration (FDA).

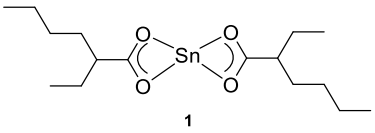

1

Figure 1.2. Stannous bis(2-ethylhexanoate), commonly known as tin(II) octanoate.

PLA produced *via* this method has relatively poor thermal properties, limiting its adoption for high temperature applications. Developing new catalysts which can deliver PLA with improved thermal properties has been a focus of much research in the preceding decades. To do this researchers have sought to control the chirality of the polymerisation process, aiming to produce microstructures with regular stereochemical orientations.

1.2.2. PLA stereochemistry

Lactic acid can exist in two optically isomeric forms, *R*-lactic acid and *S*-lactic acid. Cyclisation into lactide (LA) leads to two possible enantiomeric structures, *L*-LA and *D*-LA and a diastereoisomer, *meso*-LA (Figure 1.3). The current industrial production of lactide from low molecular weight PLA produces a racemic mixture of *D*- and *L*-LA, commonly known as *rac*-LA.

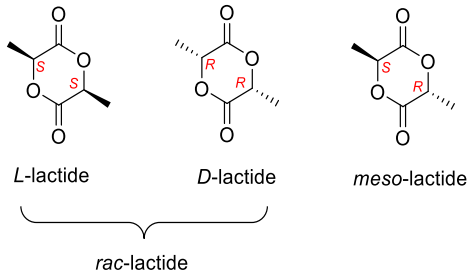

Figure 1.3. Stereoisomers of lactide.

From these isomers a variety of different polymer microstructures, with different thermal properties, can be produced (Scheme 1.3). From the racemic mixture of enantiomers (*rac*-LA), atactic PLA is the most common microstructure, and is the form which is commercially available. With an amorphous macrostructure the polymer displays no defined melting point and a relatively low glass transition temperature ($T_g \leq 45$ °C) (Figure 1.4).[47] It is this form which commonly leads to criticism, throwing into question the potential for the widespread adoption of this biopolymer. However if selectivity can be imparted during the polymerisation process it is possible to produce stereochemically arranged forms with improved glass transition and melting temperatures.

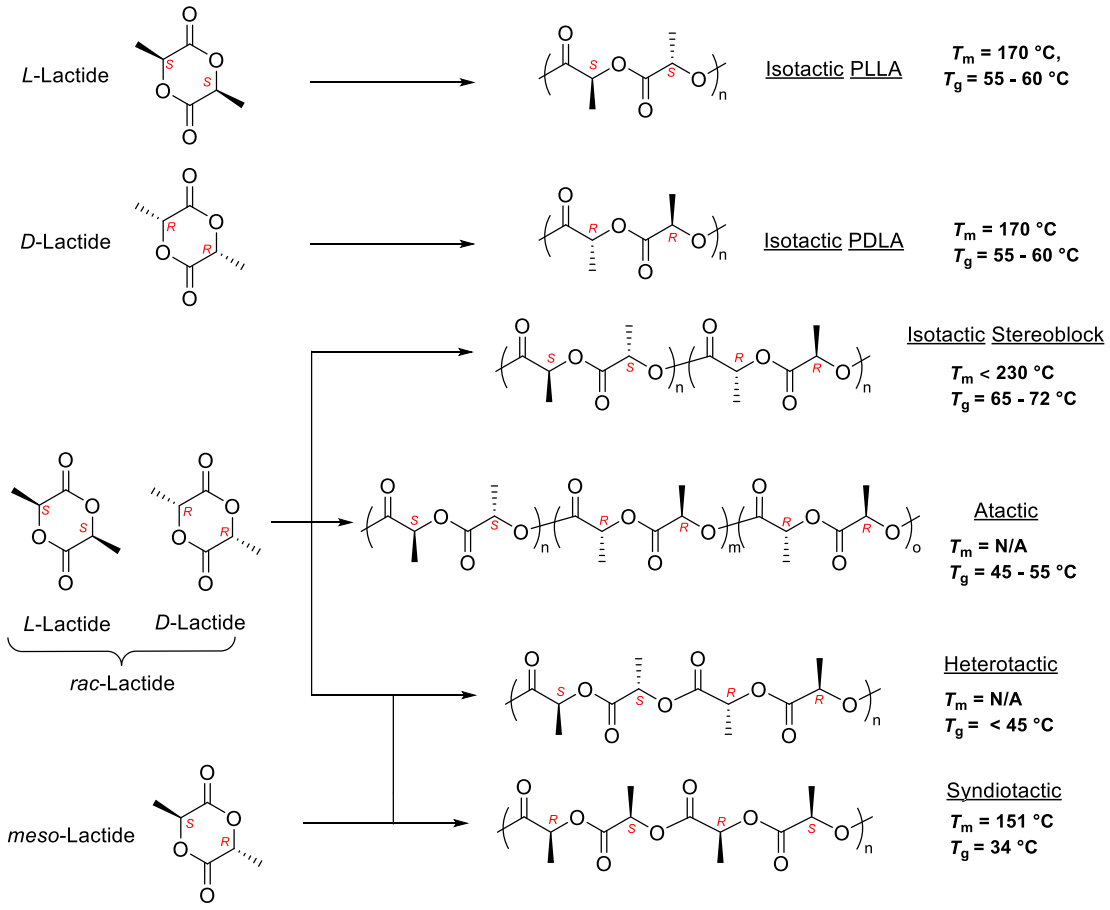

Scheme 1.3. Stereochemical outcomes and resultant thermal properties of different PLA microstructures.[39,47,48]

Isolation and ROP of either *L*-LA or *D*-LA yields the isotactic PLLA or PDLA respectively. The polymer has an enhanced glass transition and melting temperature (T_g = 55 – 60 °C, T_m = 170 °C), relative to other polymer conformations. The polymerisation of *meso*-lactide can furnish atactic, heterotactic or syndiotactic polymers. Whilst not commonly discussed, syndiotactic PLA is shown to be semi-crystalline with a defined melt temperature (T_m = 152 °C).[49]

Whilst heterotactic PLA yields no improvement in thermal properties, isotactically enriched PLA from the mixture of enantiomers can be, if sufficiently isotactic, stereocomplexed into PDLLA. This crystalline form has drastically enhanced thermal properties (T_g = 65 – 72 °C, T_m ≤ 230 °C), in comparison to the PLLA or PDLA produced from polymerisation of the individual enantiomers.[50,51] It is the desire to access this conformation from the stereoselective ROP of *rac*-LA which has driven a significant research effort in the last few decades.[52] Whilst sequential addition of enantiomers would yield the same architecture, the chiral resolution required prior to polymerisation, is costly and inefficient. The development of highly selective catalysts has instead been the primary target for researchers, following the commercial success of the Ziegler-Natta catalyst for isoselective olefin polymerisation.[53]

1.2.3. Degradation

It is widely known that the highly oxygenic character of PLA, as with many other polyesters, plays a large part in the bio-degradation process, acting as points for enzymatic cleavage of polymer links.[54] Subsequent mineralisation through assimilation into microorganisms ultimately leads to the production of carbon dioxide and water, completing the carbon cycle. However, this process is very slow, with recent studies showing that in marine environments the degradation of PLA is similar to 'non-biodegradable' polyethylene (PE).[55–57] This new understanding has since limited the green credentials of PLA which is now only considered 'industrially compostable' requiring elevated conditions in a specific microbial environment.[58]

Companies which look to bear the 'green' image are ever more looking for polymers which can offer degradative features to meet EU directives on 'Packaging and Packaging Waste' (94/62/EC). This directive and subsequent EN-13432 standard on compostability have put added pressure on the liberal use of terms such as 'bioplastics' and 'biodegradable'. Biodegradability is now defined as when >90% of material is converted into CO_2 and water by the action of microorganisms within 6 months.[59] Despite the inability to meet these requirement, the market for PLA has grown in the last decade with major market expansions in degradable food packaging and mulch films. In recent years the chemical recycling of PLA has provided a potential alternative to composting. Catalytic depolymerisation of PLLA into *L*-LA or lactate derivatives has been achieved with high yields and selectivity using a metal catalyst.[27,60,61] If commercial, this approach could prevent cascaded recycling, which is common in PET and PP recycling streams, representing a significant loss in value.[1]

1.2.4. Polymer characterisation

For PLA and other related polyesters typical analytical techniques can be applied to elucidate the structural properties of the material. For instance, size exclusion chromatography (SEC) is a technique used to calculate to the polymer molecular weight and dispersity. This technique involves the elution of polymeric material through porous particles with detection at the end of the column. According to the principles of SEC, faster elution applies to larger particles, which cannot travel within the porous column media and so typically take a shorter path through the column. Inversely, smaller molecules can diffuse through pores and generally take a longer path through the column media and elute later.

Refractive index (RI) is the most commonly used detection method and when referenced to an internal standard, typically polystyrene, size information can be deduced from the

refraction of light relative to a cell of pure solvent. The Mark-Houwink equation gives a relation between intrinsic viscosity [η] and molecular weight *M*, where *K* and α are constants related to the polymer-solvent system (Equation 1.1). By running a series of monodisperse standards, the relationship within the chosen solvent system is defined. Applying this to the response of the sample polymer can give the molecular weight. Due to differences in hydrodynamic volume between polyesters and polystyrene materials there is often an associated error with these measurements. It has been suggested by Kowalski *et al*., that a correction factor of 0.58 can be applied to the M_n value for PLA samples to obtain a more realistic image of polymer weight.[62]

Equation 1.1**.** The Mark-Houwink equation for detecting molecular weight by using measurements from a well-defined reference.

$$[\eta] = KM^a$$

$$K_1 M_1^{1+a_1} = K_2 M_2^{1+a_2}$$

Arguably, a more accurate measurement can be obtained from the use of triple detection methods. This involves the combination of RI, light scattering (LS), and viscometry measurements to calculated molecular weight. Light scattering involves the production of a collimated beam of monochromatic light that illuminates a region of the sample. The incident beam is generally plane polarised, perpendicular to plane of measurement. As the beam hits the sample, the intensity of the scattered light relates to the molecular weight of the sample. Viscometry relates the intrinsic viscosity of the sample to the molecular weight through the Mark-Houwink equation, by applying the principle that a higher molecular weight sample will be more viscous in solution. This is with the assumption that at the analysed concentrations no inter- or intra-molecular interactions are occurring.

When referring to polymeric size and uniformity, three main values are commonly reported (Equation 1.2). These are the number average molecular weight (M_n), weight average molecular weight (M_w) and the dispersity of chains (*Đ*). The number average molecular weight, M_n, is the statistical average weight of all chains in the sample, whereas the weight average molecular weight, M_w, takes into account the contribution of heavier chains to the distribution. *Đ* is a measure of how broad a distribution is, being a ratio between M_w and M_n.

Equation 1.2. Equations related to the polymer chain length and distribution.

$$M_w = \frac{\sum {M_i}^2 N_i}{\sum M_i N_i}; \quad M_n = \frac{\sum M_i N_i}{\sum N_i}; \quad Đ = \frac{M_w}{M_n}$$

Nuclear magnetic resonance spectroscopy (NMR) is an important characterisation technique for determining conversion from the integration of the monomer resonances against that of the analogous polymer resonances. Additionally, polymer chain composition, end groups and hence chain length can be ascertained from the polymer ^{1}H NMR spectra. One of the most important aspects when referring to control is the stereochemistry, which is deduced by ^{1}H{^{1}H} NMR spectra. In the analysis of PLA, due to an overlap of polymer resonances, decoupling the methine quartets reveal discrete tetrads described by stereochemical relationships of syndiotacticity, *s*, or isotacticity, *i* (Figure 1.4).

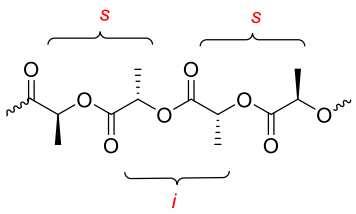

Figure 1.4. Example of a *sis* tetrad where *i* and *s* refer to an "iso" and "syndio" relationship.

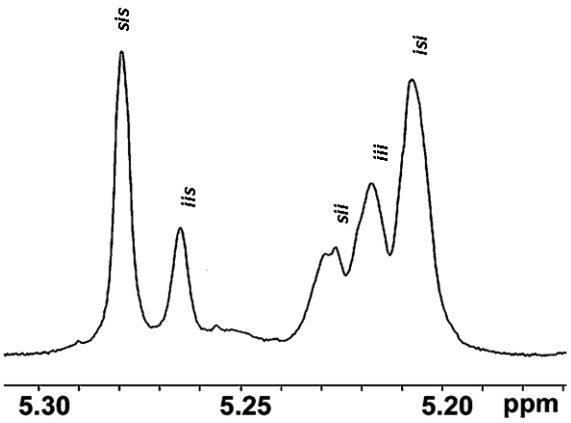

Tetrad	Probability
[*iii*]	$P_m^2 + P_rP_m/2$
[*iis*]	$P_rP_m/2$
[*sii*]	$P_rP_m/2$
[*sis*]	$P_r^2/2$
[*isi*]	$(P_r^2 + P_rP_m)/2$

Figure 1.5. Example of a ^{1}H{^{1}H} NMR spectra showing the five possible tetrad possibilities in PLA.[63] Tetrad probabilities based on Bernoullian statistics for *rac*-lactide.[64]

The relationships between tetrads gives rise to five distinct possibilities in the ^{1}H{^{1}H} NMR spectrum (Figure 1.5).[63] The relative intensities of the resonances is related to the overall tacticity of the sample based on Bernoullian statistics.[64,65] From this, the value of P_r, the probability of racemic enchainment, is conveniently found by calculating the normalised intensity of the [*sis*] tetrad. Hence, a polymer with heterotactic bias will have a P_r value greater than 0.5. Conversely, a P_r less than 0.5 shows the polymer has an isotactic bias. Perfect heterotacticity or isotacticity is denoted by a P_r value of 1 or 0 respectively.

Differential scanning calorimetry (DSC) is a technique used to provide information on a materials thermal properties. It is the principal method of distinguishing glass transition (T_g), melting (T_m), and crystallisation temperatures (T_c) of polymeric samples – such as stated in the stereochemical forms of PLA. By measuring the heat flux needed by a sample to maintain a given heating rate these phase changes can be identified. The difference in heat flux can be plotted against temperature and depending on if the phase change is exo- or endothermic this will be represented by a trough or a peak on the trace. Thermogravimetric analysis (TGA) is also commonly employed for polymers to elucidate degradation profiles. By measuring the mass change as a function of temperature, TGA is used to identify the temperature at which the polymer begins to thermally degrade (T_{ons}), as well as the temperature which the degradation process is fastest (T_{inf}). These parameters are especially important when considering industrial processing, which is often carried out at high temperatures, above the melting point.

1.3. Ring Opening Polymerisation

Ring-opening polymerisation (ROP) is a specific class of addition-elimination reactions that result in the ring opening and propagation of a cyclic monomer. In the case of cyclic esters this exists through the use of a nucleophilic initiator to cleave the acyl oxygen bond and form an aliphatic linear ester. This process can be thermodynamically driven by the relief of ring strain.[52,66–68] The Gibbs free energy of polymerisation (ΔG_p) for the ring opening of different sized cyclic esters is well studied within the literature, which detail favourable enthalpic and entropic precedent for the ROP of 4, 6 and 7 membered cyclic esters at 25 °C.[68,69] Five membered rings generally exhibit less ring strain and poor entropic drive and so generally hold a positive ΔG_p value.[68]

Various mechanisms exist for ROP including anionic, cationic, activated monomer, and coordination insertion, dictated by the nature of the catalytically active species.[52,67] Whilst the development of new bio-based cyclic esters represents a crucial aspect of research into realising the bio-based economy, understanding the ROP process through mechanistic work and catalyst development is equally vital. Testament to this is the misrepresentation of the term "catalyst". With initiation and propagation steps often leading to an irreversible change in the complex structure the catalytically active species can be significantly different to feed "catalyst". As a result the feed is more appropriately referred to as an initiator or pre-initiator, facilitating the production of the catalytically active species.

It is common in ROP catalysis to refer to the rate constants associated in the process, namely the initiation constant (k_{init}) and the propagation constant (k_{prop}). Polymerisations can be classed as "living" when the rate of initiation is much faster than that of propagation. This leads to linear growth of the polymer chains and is usually associated with a low distribution of molecular weights, predictable by the feed ratios of monomer and initiator. In this process there is no appreciable termination step so addition of further monomer units would facilitate the continued growth of the polymer chain. Deviation from this desired behaviour can occur if transesterification of chains becomes prevalent. This is often the case at low monomer concentrations and can lead to a broadening in distribution of molecular weights.

Whilst "living" polymerisations can be terminated by the addition of excess alcohol to the polymerisation mixture, "immortal" ROP can use the excess addition of alcohol as a chain transfer agent to control molecular weights. This process occurs through preferential alkoxide exchange at the catalyst centre, increasing the number of growing polymer chains. In this scenario molecular weights are predictable from the ratio of monomer to chain transfer agent.

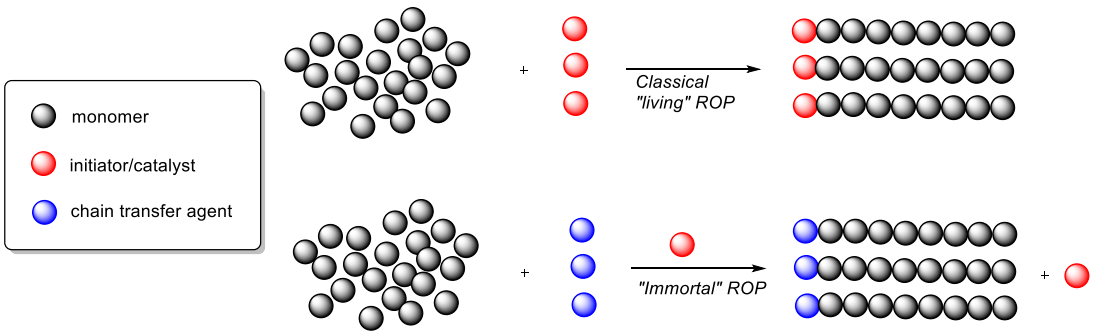

Figure 1.6. Adapted illustration on the mechanism of "living" and "immortal" ROP.[70,71]

Transesterification is a common side reaction during ROP and is often dictated by monomer concentration, temperature and the nature of the catalytically active species. This undesired effect occurs by two specific mechanisms regardless of the nature of the polymer, namely intermolecular and intramolecular transesterification. Intermolecular transesterification occurs through a nucleophilic addition-elimination of the active alkoxide on the polymer chain with a dormant ester functional group on another chain. This results in a scission of chains, altering distribution of the molecular weights. Intramolecular transesterification follows a similar mechanism, albeit on the internal growing chain. This "backbiting" is common when the chain can coil around and leads to cyclic species.[72]

Matrix-assisted laser desorption and ionisation time-of-flight (MALDI-ToF) is a mass spectrometry technique which is commonly used to identify the prevalence of transesterification in polymers as well as the repeat units and end groups. In MALDI-ToF, a soft ionisation potential is applied to a sample to prevent fragmentation of chains. To assist in this process the analyte is mixed in a solution with a suitable matrix and ionising source and is co-crystallised upon evaporation of the solvent. The matrix serves as a strong electron acceptor or a proton source during ionisation of the analyte. As a result matrices are either strong acids or molecules with strong conjugated π-interactions. As with more commonly used forms of mass spectrometry such as electrospray, the mass and distribution of the chain lengths can be determined by the time taken for the charged polymer ions to reach the detector plate.

For PLA, spacing of 144 g mol^{-1} between the peaks in the chromatogram, highlight the PLA repeating unit with no transesterification in the chain. Conversely a spacing of 72 g mol^{-1} highlights some degree of transesterification has occurred during the process. Taking the mass of any given peak, the number of repeating units can be established, detailing the degree of polymerisation in the process. Any residual mass can be used to identify the end groups, elucidating to the mechanism of initiation and termination. If cyclic species were present from intramolecular transesterification, the mass balance would show the lack of any clear end group. However, due to the nature of ionisation MALDI-ToF is limited to polymer samples with good ionisability, which are below 12 kg mol^{-1} and with reasonably low dispersities ($Đ$ = 1.2).[73,74]

1.3.5. Organocatalysis

Often centred around strongly basic organic compounds, organocatalysts represent a growing area of interest in ROP research.[75] Whilst many variations exist, utilising urea complexes as catalysts has presented the most active organocatalytic systems for the ROP of LA (Scheme 1.4).[76–80] Waymouth and co-workers recently reported how, in the presence of potassium methoxide as co-initiator, the urea system **2**, was extremely active, achieving 96% conversion in 6 seconds {[**2**]$_0$:[KOMe]$_0$:[*L*-LA]$_0$ = 3:1:100, THF, 25 °C}, with no epimerisation of the stereocentres.[78] Conversely, very high isoselectivity (P_r = 0.12) was recently reported by Dove and co-workers using a chiral urea catalyst (**3**).[79] With only a few stereoerrors, PLA with enhanced thermal properties (T_m = 156 °C) relative to the atactic form was produced from the racemic mixture of monomers. Despite these promising results, organocatalysts are currently hindered by the prominence of transesterification and inability to work under industrially relevant conditions such as temperatures as high as 180 °C.[81]

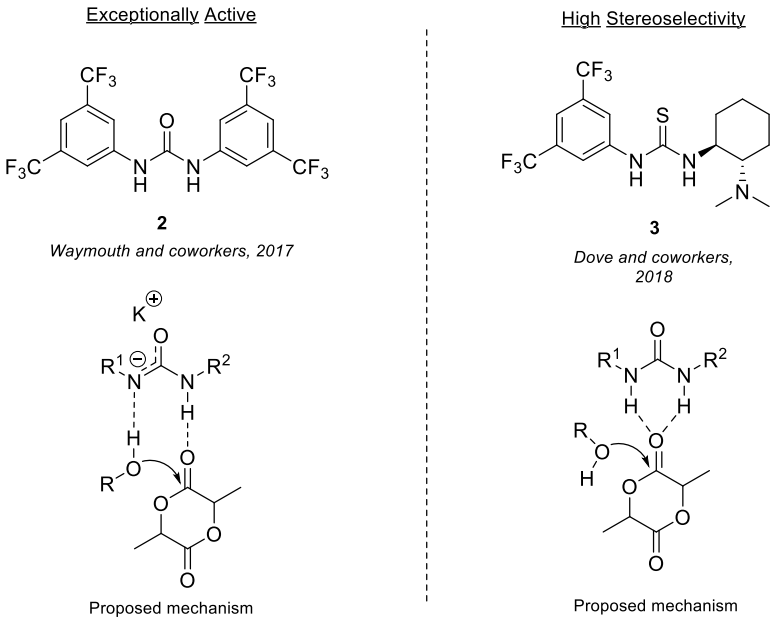

Scheme 1.4. Urea and thiourea initiators used to good effect for the ROP of LA.[78,79]

The mechanism of propagation shown for these urea and thiourea systems (Scheme 1.4) is an example of the activated-monomer mechanism. The role of the central Lewis acidic site is simply to activate the monomer, making the carbonyl ester labile to attack from an external nucleophile.[82] Whilst common for organocatalysts, this mechanism is also seen for metal based initiators.[82–84] This mechanism is often postulated when the Lewis acidic initiator is coordinatively saturated and has no labile ligands or contains reactively inert groups such as chloride ligands.[85]

1.3.6. Metal catalysis

Developing metal complexes which can act as active, selective and benign catalysts for the ROP of cyclic esters represents the main focus of scientific exploration in the development of polyesters.[27] The wide possibilities of the metal centres and ancillary ligands has allowed fundamental structural-activity relationships to be established, habilitating the design for future, more effective, ROP catalysts. The high thermal stability that many metal catalysts possess make them ideal candidates for industrial application. Whilst metal complexes can act by a variety of different mechanisms, the most commonly reported mechanism is the coordination-insertion mechanism.[52] In this mechanism coordination of a lactide carbonyl oxygen to a metal centre provides an activated site for nucleophilic attack; the attacking moiety may be a labile group on the complex or a reaction additive (Scheme 1.5). Propagation occurs through the oligomeric chain alkoxide activating the ring opening of another monomer.

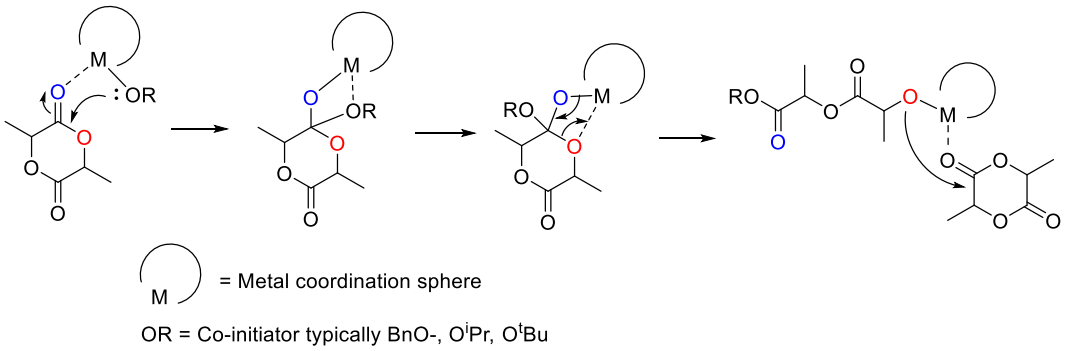

Scheme 1.5. General mechanism for coordination-insertion ROP using an metal alkoxide co-initiator.

It is within the coordination-insertion mechanism the donating capabilities and steric bulk of ligands, as well as size and Lewis acidity of the metal centre, play a big part in dictating the rate of growth and tacticity of the polymer chain. The tacticity is controlled by two distinct mechanisms; chain-end control and enantiomorphic site control. Chain-end control stipulates that the stereocentre currently attached to the metal dictates the configuration of the next monomer added; typically bulky achiral complexes progress through this regime. Conversely, enantiomorphic site control requires the metal and its coordination sphere to impart a chirality bias on the growing polymer by favouring one incoming isomer over another. Historically, metal catalysts have commonly suffered from being unable to combine stereocontrol, high rates of polymerisation and robustness simultaneously, presenting one of the last remaining challenges in PLA development.

1.4. Summary and project Aims

The urgent need to reduce reliance on persistent petrochemically sourced plastics, presents a great opportunity for the scientific community to present sustainable alternatives to industry with the aim of commercialisation. To this effect, PLA represents a well-established fully bio-based plastic which has seen global production grow steadily throughout the 21st century. However, the vast majority of commercial PLA and its blends have limited applications due to poor thermal and mechanical properties. The desire to produce the more widely applicable isotactic stereoblock PDLA, produced from selective polymerisation of *rac*-LA, has been a focus of much research effort.

Despite decades of research, combining selectivity, rate and robustness has proved difficult. One aim of this research is to continue catalyst development, focusing on structural-activity relationships to design systems which are effective for the ROP of *rac*-LA. Building on some of the most noteworthy initiators previously reported, this project focuses on the use of group 13 and lanthanide metals to build novel initiators. Furthermore, understanding the nature of the catalytically active species is arguably the most integral aspect in developing catalytic systems, yet is often overlooked. By carrying out mechanistic investigations, this study aims to explore possible spectroscopic methods to ascertain the form of the active species. From this understanding new catalytic systems can be intelligently designed.

Whilst commonly only discussed for the ROP of LA, many metal catalysts have excellent versatility for a range of cyclic monomers.[86–88] Developing and showcasing the versatility of catalysts is an important aspect when being able to develop new promising monomers. Maintaining molecular weight control and the activity which many complexes show for LA ROP are common challenges when polymerising poorly developed and highly functional monomers. To this end, this research also aims to test the best performing catalytic systems for a variety of functional monomers including epoxides, anhydrides and cyclic carbonates. With the ultimate aim to develop more hydrolytically degradable PLA, copolymers of poly(phosphonates) and PLA are investigated using the best performing catalytic systems.

1.5. References

1 World Economic Forum. and Ellen MacArthur Foundation., *The New Plastics Economy: Rethinking the future of plastics*, 2016.

2 E. Royte, *Natl. Geogr. Mag.*, 2018.

3 D. Carrington, Microplastic pollution in oceans is far worse than feared, say scientists, https://www.theguardian.com/environment/2018/mar/12/microplastic-pollution-in-oceans-is-far-greater-than-thought-say-scientists, (accessed 5 February 2019).

4 S. Laville, UK plastics recycling industry under investigation for fraud and corruption, https://www.theguardian.com/environment/2018/oct/18/uk-recycling-industry-under-investigation-for-and-corruption, (accessed 5 February 2019).

5 J. R. Jambeck, R. Geyer, C. Wilcox, T. R. Siegler, M. Perryman, A. Andrady, R. Narayan and K. L. Law, *Science*, 2015, **347**, 768–771.

6 R. Chris, *The Paris Agreement - Implications for greenhouse gas removal and zero emissions energy production*, Academic Press, 2019.

7 A Roadmap to 2025 - The UK Plastics Pact, http://www.wrap.org.uk/content/the-uk-plastics-pact-roadmap-2025, (accessed 5 January 2019).

8 The Commonwealth Blue Charter, https://bluecharter.thecommonwealth.org/, (accessed 5 January 2019).

9 N. Hernández, R. C. Williams and E. W. Cochran, *Org. Biomol. Chem.*, 2014, **12**, 2834–49.

10 J. Pang, M. Zheng, R. Sun, A. Wang, X. Wang and T. Zhang, *Green Chem.*, 2016, **18**, 342–359.

11 F. Cavani, S. Albonetti, F. Basile and A. Gandini, *Chemicals and Fuels from Bio-Based Building Blocks*, Wiley, 2016.

12 M. Rabnawaz, I. Wyman, R. Auras and S. Cheng, *Green Chem.*, 2017, **19**, 4737–4753.

13 Y. Akanuma, S. E. M. Selke and R. Auras, *Int. J. Life Cycle Assess.*, 2014, **19**, 1238–1246.

14 E. de Jong, M. A. Dam, L. Sipos and G.-J. M. Gruter, in *Biobased Monomers, Polymers, and Materials*, American Chemical Society, 2012, vol. 1105, p. 1.

15 G.-J. M. Gruter, L. Sipos and M. A. Dam, *Comb. Chem. High Throughput Screen.*, 2012, **15**, 180–188.

16 C. Vilela, A. F. Sousa, A. C. Fonseca, A. C. Serra, J. F. J. Coelho, C. S. R. Freire and A. J. D. Silvestre, *Polym. Chem.*, 2014, **5**, 3119–3141.

17 Avantium Press Release, https://www.avantium.com/press-releases/pef-pilot-phase-set-extended/.

18 A. J. J. E. Eerhart, A. P. C. Faaij and M. K. Patel, *Energy Environ. Sci.*, 2012, **5**, 6407–6422.

19 M. Konstantopoulou, Z. Terzopoulou, M. Nerantzaki, J. Tsagkalias, D. S. Achilias, D. N. Bikiaris, S. Exarhopoulos, D. G. Papageorgiou and G. Z. Papageorgiou, *Eur. Polym. J.*, 2017, **89**, 349–366.

20 S. K. Burgess, R. M. Kriegel and W. J. Koros, *Macromolecules*, 2015, **48**, 2184–2193.

21 S. K. Burgess, O. Karvan, J. R. Johnson, R. M. Kriegel and W. J. Koros, *Polymer* , 2014, **55**, 4748–4756.

22 S. A. Miller, *ACS Macro Lett.*, 2013, **2**, 550–554.

23 F. H. M. Graichen, W. J. Grigsby, S. J. Hill, L. G. Raymond, M. Sanglard, D. A. Smith, G. J. Thorlby, K. M. Torr and J. M. Warnes, *Ind. Crops Prod.*, 2017, **106**, 74–85.

24 N. J. Van Zee and G. W. Coates, *Angew. Chem Int. Ed.*, 2015, **54**, 2665–2668.

25 P. A. Wilbon, F. Chu and C. Tang, *Macromol. Rapid Commun.*, 2013, 8–37.

26 J. Graça, *Front. Chem.*, 2015, **3**, 1–11.

27 X. Zhang, M. Fevre, G. O. Jones and R. M. Waymouth, *Chem. Rev.*, 2018, **118**, 839–885.

28 Cambridge Consultants, *Polyhydroxyalkanoates: plastic the way nature intended?*, 2018.

29 Z. A. Raza, S. Abid and I. M. Banat, *Int. Biodeterior. Biodegrad.*, 2018, **126**, 45–56.

30 Z. Li, J. Yang and X. J. Loh, *NPG Asia Mater.*, 2016, **8**, e265-20.

31 M. Koller, L. Marsalek, M. M. de Sousa Dias and G. Braunegg, *N Biotechnol*, 2017, **37**, 24–38.

32 C. Kourmentza, J. Pl, N. Venetsaneas, A. Burniol-figols, C. Varrone, H. N. Gavala and M. A. M. Reis, *Bioengineering*, 2017, **4**, 1–43.

33 European Bioplastics and Institute for Bioplastics and Biocomposites, *Bioplastics market data*, 2017.

34 F. Aeschelmann and M. Carus, *Bio-based Building Blocks and Polymers in the World Capacities, Production and Applications: Status Quo and Trends towards 2020*, Michael Carus, Hürth, 2015.

35 F. Rosillo-Calle, *ISRN Renew. Energy*, 2012, 1–15.

36 V. H. Sangeetha, H. Deka, T. O. Varghese and S. K. Nayak, *Polym. Compos.*, 2018, **39**, 81–101.

37 E. Castro-Aguirre, F. Iñiguez-Franco, H. Samsudin, X. Fang and R. Auras, *Adv. Drug Deliv. Rev.*, 2016, **107**, 333–366.

38 Total Corbion PLA starts-up its 75,000 tons per year bioplastics plant, https://www.total-corbion.com/news, (accessed 22 January 2019).

39 R. Auras, B. Harte and S. Selke, *Macromol. Biosci.*, 2004, **4**, 835–864.

40 D. Garlotta, *J. Polym. Environ.*, 2001, **9**, 63–84.

41 R. G. Sinclair, *J. Macromol. Sci. Part A*, 1996, **33**, 585–597.

42 W. H. Carothers, G. L. Borough, F. J. van Natta, G. L. Dorough and F. J. van Natta, *J. Am. Chem. Soc.*, 1932, **54**, 761–772.

43 M. Jamshidian, E. A. Tehrany, M. Imran, M. Jacquot and S. Desobry, *Compr. Rev. Food Sci. Food Saf.*, 2010, **9**, 552–571.

44 P. Van Wouwe, M. Dusselier, E. Vanleeuw and B. Sels, *ChemSusChem*, 2016, **9**, 907–921.

45 M. Gozan, F. Kamilah, Y. Whulanza and Rahmayetty, *IOP Conf. Ser.: Mater. Sci. Eng.,* 2018, **334**, 1–8.

46 M. Dusselier, P. Van Wouwe, A. Dewaele, P. A. Jacobs and B. F. Sels, *Science*, 2015, **349**, 78–80.

47 K. M. Benabdillah, M. Boustta, J. Coudane and M. Vert, in *Polymers from Renewable Resources*, American Chemical Society, 2001, vol. 764, pp. 14–200.

48 T. M. Ovitt and G. W. Coates, *J. Am. Chem. Soc.*, 2002, **124**, 1316–1326.

49 T. M. Ovitt and G. W. Coates, *J. Am. Chem. Soc.*, 1999, **121**, 4072–4073.

50 H. Tsuji, *Macromol. Biosci.*, 2005, **5**, 569–597.

51 K. Fukushima and Y. Kimura, *Polym. Int.*, 2006, **55**, 626–642.

52 M. J. Stanford and A. P. Dove, *Chem. Soc. Rev.*, 2010, **39**, 486–494.

53 J. J. Eisch, *Organometallics*, 2012, **31**, 4917–4932.

54 P. Stloukal, S. Pekařová, A. Kalendova, H. Mattausch, S. Laske, C. Holzer, L. Chitu, S. Bodner, G. Maier, M. Slouf and M. Koutny, *Waste Manag.*, 2015, **42**, 31–40.

55 T. Haider, C. Völker, J. Kramm, K. Landfester and F. R. Wurm, *Angew. Chem Int. Ed.*, 2018, **58**, 50–62.

56 Y. Rudeekit, J. Numnoi, M. Tajan, P. Chaiwutthinan and T. Leejarkpai, *J. Met. Mater. Miner.*, 2008, **18**, 83–87.

57 D. Adhikari, M. Mukai, K. Kubota, T. Kai, N. Kaneko, K. S. Araki and M. Kubo, *J. Agric. Chem. Environ.*, 2016, **5**, 23–34.

58 C. K. Williams and M. A. Hillmyer, *Polym. Rev.*, 2008, **48**, 1–10.

59 M. Breulmann, A. Künkel, S. Philipp, V. Reimer, K. O. Siegenthaler, G. Skupin and M. Yamamoto, in *Ullmann's Encyclopedia of Industrial Chemistry*, Wiley-VCH Verlag GmbH & Co. KGaA, 2000.

60 P. Mckeown, M. D. Jones, J. Wood and L. A. Roma, *ACS Catal.*, 2019, **9**, 409–416.

61 M. Omura, T. Tsukegi, Y. Shirai, H. Nishida and T. Endo, *Ind. Eng. Chem. Res.*, 2006, **45**, 2949–2953.

62 A. Kowalski, A. Duda and S. Penczek, *Macromolecules*, 1998, **31**, 2114–2122.

63 B. Gao, Q. Duan, Y. Li, D. Li, L. Zhang, Y. Cui, N. Hu and X. Pang, *RSC Adv.*, 2015, **5**, 13437–13442.

64 B. M. Chamberlain, M. Cheng, D. R. Moore, T. M. Ovitt, E. B. Lobkovsky and G. W. Coates, *J. Am. Chem. Soc.*, 2001, **123**, 3229–3238.

65 L. S. Baugh and J. A. M. Canich, *Stereoselective Polymerization with Single-Site Catalysts*, CRC Press, 2007.

66 A. Duda and S. Penczek, in *Polymers from Renewable Resources*, American Chemical Society, 2001, vol. 764, pp. 13–160.

67 O. Dechy-Cabaret, B. Martin-Vaca and D. Bourissou, *Chem. Rev.*, 2004, **104**, 6147–6176.

68 P. Olsén, K. Odelius and A.-C. Albertsson, *Biomacromolecules*, 2016, **17**, 699–709.

69 M. Save, M. Schappacher and A. Soum, *Macromol. Chem. Phys.*, 2002, **203**, 889–899.

70 N. Ajellal, J.-F. Carpentier, C. Guillaume, S. M. Guillaume, M. Helou, V. Poirier, Y. Sarazin and A. Trifonov, *Dalton Trans.*, 2010, **39**, 8363–8376.

71 T. Steinbach, S. Ritz and F. R. Wurm, *ACS Macro Lett.*, 2014, **3**, 244–248.

72 P. Dubois, C. Jacobs, R. Jérôme and P. Teyssté, *Macromolecules*, 1991, **24**, 2266–2270.

73 J. Blais, A. Caminade, J. Majoral and M. Curie, *Anal. Chem.*, 2000, **72**, 5097–5105.

74 R. X. E. Willemse, B. B. P. Staal, E. H. D. Donkers and A. M. Van Herk, *Macromolecules* , 2004, 5717–5723.

75 M. K. Kiesewetter, E. J. Shin, J. L. Hedrick and R. M. Waymouth, *Macromolecules*, 2010, **43**, 2093–2107.

76 N. Zhu, Y. Liu, J. Liu, J. Ling, X. Hu, W. Huang, W. Feng and K. Guo, *Sci. Rep.*, 2018, **8**, 4–11.

77 J. U. Pothupitiya, N. U. Dharmaratne, T. M. M. Jouaneh, K. V. Fastnacht, D. N. Coderre and M. K. Kiesewetter, *Macromolecules*, 2017, **50**, 8948–8954.

78 B. Lin and R. M. Waymouth, *J. Am. Chem. Soc.*, 2017, **139**, 1645–1652.

79 B. Orhan, M. J.-L. Tschan, A.-L. Wirotius, A. P. Dove, O. Coulembier and D. Taton, *ACS Macro Lett.*, 2018, **7**, 1413–1419.

80 A. Dove, H. Sardon and S. Naumann, *Organic Catalysis for Polymerisation*, Royal Society of Chemistry, 2018.

81 L. Mezzasalma, A. P. Dove and O. Coulembier, *Eur. Polym. J.*, 2017, **95**, 628–634.

82 P. Kubisa, *Makromol. Chemie. Macromol. Symp.*, 1988, **13**–**14**, 203–210.

83 N. Maudoux, T. Roisnel, V. Dorcet, J. F. Carpentier and Y. Sarazin, *Chem. - A Eur. J.*, 2014, **20**, 6131–6147.

84 M. Normand, V. Dorcet, E. Kirillov and J. F. Carpentier, *Organometallics*, 2013, **32**, 1694–1709.

85 T. Rosen, I. Goldberg, V. Venditto and M. Kol, *J. Am. Chem. Soc.*, 2016, **138**, 12041–12044.

86 C. Romain, Y. Zhu, P. Dingwall, S. Paul, H. S. Rzepa, A. Buchard and C. K. Williams, *J. Am. Chem. Soc.*, 2016, **138**, 4120–4131.

87 A. Buonerba, A. De Nisi, A. Grassi, S. Milione, C. Capacchione, S. Vagin and B. Rieger, *Catal. Sci. Technol.*, 2015, **5**, 118–123.

88 R. Jianming, X. Anguo, W. Hongwei and Y. Hailin, *Des. Monomers Polym.*, 2014, **17**, 345–355.

Chapter 2

Group 13 Tetradentate Pyrrolidine Complexes and their Application in the ROP of *rac*-Lactide

Relating Publication

NJC

PAPER

View Article Online
View Journal | View Issue

Cite this: *New J. Chem.*, 2017, **41**, 2198

Salan group 13 complexes – structural study and lactide polymerisation†

James Beament, Mary F. Mahon, Antoine Buchard* and Matthew D. Jones*

Received 8th December 2016,
Accepted 6th February 2017

DOI: 10.1039/c6nj03844a

rsc.li/njc

Herein the preparation and characterisation of a series of group 13 salan complexes, with a bipyrrolidine or *N*,*N*′-ethylenediamine backbone are disclosed. For the bipyrrolidine derived-salan ligand **1**H_2, the Al(III) and Ga(III) complexes are pseudo trigonal bipyramidal in the solid-state, whereas the In(III) complexes are best described as square based pyramidal structures. However, for the ethylenediamine derived-salan ligand **2**H_2, all complexes are effectively square based pyramidal in their structure. The complexes' solution behaviour is also investigated by NMR spectroscopic methods and it is observed that the solid-state structure is maintained in solution. The complexes have all been trialled for the ring opening polymerisation of *rac*-lactide. With In(**1**)Cl controlled polymerisation and narrow molecular weight distributions (1.01–1.08) are observed with heterotactic polylactide being prepared. Under the conditions tested the Ga(III) and Al(III) complexes were shown to be inactive.

Introduction

In recent years there has been an explosion of research concerning new initiators for the controlled ring opening polymerisation (ROP) of lactide (LA) affording polylactide (PLA).[1] The resultant PLA is compostable and annually renewable from starch-rich plant based materials. This material has the potential to replace traditional petrochemical derived plastics for numerous applications, from high value biomedical areas to commodity uses.[2] While organocatalysts and initiators commonly yield atactic PLA from *rac*-LA,[3] there are many metal centres that are active for the stereoselective polymerisation of *rac*-LA to afford either heterotactic or isotactic stereoblock PLA. Examples of such metal centres include groups 1–4,[4] lanthanides, Zn(II)[4f,5] and pertinent to this study group 13 metals.[6] There are many ligands that have found utility in this area such as salan,[4a,b,6b,c] salen,[6e–h,7] salalen[8] and variations thereof, including phosphasalen.[9] In the case of indium the area is dominated by salen ligands.[10] However, other ligand systems are known.[11] $InCl_3$ alone was first shown to be an active catalyst by Tolman and Hillmyer in 2009, with high heterotacticity being favoured in THF solution, when used in combination with triethylamine and benzylalcohol.[12] Recently, extensive studies have been conducted by Mehrkhodavandi and co-workers who have elegantly illustrated the advantages of In(III) complexes for the controlled ROP of *rac*-LA.[7,13] These have typically utilised salen ligands with chirality in the backbone. For example, when indium is complexed with Jacobsen's ligand the resultant complex was seen to be faster than the corresponding Al(III) system, with isotactic (P_m = 0.77) PLA being realised.[13a] In these studies aggregation of the indium complexes, due to the large ionic radii of In(III),[13i] has be shown to be troublesome, and was controlled by the use of bulky ligands. Ga(III) initiated ROP of lactide is rare with only a handful of examples reported in the literature.[10,14] Further, complexes of In-"salan-like" ligands characterised in the solid-state are extremely rare.[15] Thus, it is pertinent to study the coordination chemistry of simple salan related ligands with In(III) (to compare with Al/Ga) and screen for the ROP of *rac*-LA.

New catalyst research in the area is driven by the need to develop structure–activity-relationships and understand the complex interplay between the ligand and the metal centre, such relationships are lacking in the area. It has been shown that very subtle changes to the ligand or switching the metal centre can have dramatic consequences to the polymerisation. For example, we have shown with a bipyrrolidine derived salan ligand there is a switch in selectivity from highly isotactic PLA Zr(IV)/Hf(IV) to highly heterotactic PLA for Al(III).[4a] Williams and co-workers have observed similar switches with phosphasalen complexes of different lanthanides.[16] Further switching in control are noted by comparing Al-(SalBinap) (isotactic) to Y(SalBinap) (heterotactic) complexes of Coates and Pappalardo respectively.[17] Kol first introduced the bipyrrolidine ligand in 2009 to pre-determine the chirality at a group 4 metal centre.[18] We have previously illustrated that ligands based on the bipyrrolidine backbone are highly effective for the ROP of lactide.[4a,b] More recently, Kol has also utilised this backbone with Mg(II) and to

Department of Chemistry, University of Bath, Claverton Down, Bath BA2 7AY, UK. E-mail: mj205@bath.ac.uk, a.buchard@bath.ac.uk; Fax: +44 (0)1225 386231; Tel: +44 (0)1225 384908

† Electronic supplementary information (ESI) available: Full experimental and the crystal data in the .cif format. CCDC 1510494–1510501. For ESI and crystallographic data in CIF or other electronic format see DOI: 10.1039/c6nj03844a

2. Group 13 Tetradentate Pyrrolidine Complexes and their Application in the ROP of *rac*-Lactide

2.1. Introduction

New catalytic systems applied to the ROP of cyclic esters must meet the criteria of robustness, activity, selectivity, molecular control, and low cost to compete with current industrial standards. With many initiators often falling short of meeting these criteria, academic research has continued to develop understanding on the subtle interplay of the ligand-metal coordination sphere in order to design systems which are industrially viable. For the polymerisation of *rac*-LA, aluminium has received much attention, often yielding some of the most selective and controlled initiators to date.[1–4] Despite this Al based catalysts are often described as lacking the activity required to make a commercially viable alternative.[1–4] With many exceptions to these findings it is this absence of a consistent trend around aluminium which has retained a high level of academic interest at present.[5,6]

Another group 13 based element, indium, has recently taken prominence in the field of catalytic ROP.[7] Unlike aluminium, indium initiators are generally considered as fast systems, with notable examples showing strong isotactic selectivity in the ROP of *rac*-LA.[7] Withstanding challenges on elemental scarcity and hydrolytic sensitivity,[8] research into indium offers a possible solution to the rate *vs* selectivity trade-off commonly seen for aluminium species. Despite the stark reactivity differences, to date only a few investigations exist concerning the metal influence in group 13 complexes, making this a poorly understood area of applied inorganic chemistry.[9–11]

Whilst many examples of triel metal complexes exist and are applied to ROP this work focuses primarily on tetradentate ligands. Tetradentate 'ONNO' ligands are commonly employed for coordination to M^{3+} centres with ability to provide good donation from the nitrogen lone pairs whilst simultaneously allowing the coordination to have an ancillary functional group which can act the initiating molecule or as a sacrificial group during initiation.[2,12] Herein, we discuss the state of the literature with regard to group 13 tetradentate bis(phenolate) complexes and their efficacy for the ROP of *rac*-LA.

2.1.1. Aluminium initiators

The inherent ability of aluminium complexes to act as an initiator for ROP is apparent with the commonly used complex precursor, $Al(O^iPr)_3$, being reported in the literature as a highly active initiator for LA and ε-caprolactone (ε-CL) polymerisation.[13,14] However, a large degree of transesterification is noted, leading to poor molecular weight control and broad molecular weight dispersities. In addition, when *rac*-LA is used as the monomer no stereo control is seen with atactic PLA being produced. To achieve control of the tacticity and molecular weights, a greater coordination sphere and larger steric bulk given from a ligand is often required, with many comprehensive reviews in the area.[1,2,15–19]

One of the most famous early generation of initiators was an aluminium binaphthyl 'salen' system (**4**) demonstrated by Spassky and co-workers. (Figure 2.1).[20] Using this achiral complex, a preference for the ROP of *D*-LA was observed at low conversions from the racemic mixture (*rac*-LA), with a switch to the polymerisation of *L*-LA at higher conversions. This iso-selective enchainment arises from an enantiomorphic site control mechanism, with tacticity sufficient enough to produce stereocomplexation of the chains yielding an increase in melting temperature of the PLA (T_m = 185 – 187 °C). Using this system important advances surrounding PLA production were realised by other research groups, notably the preparation of syndiotactic PLA from *meso*-LA and an improvement in polymer melt temperature due to the use of a racemic version of the initiator.[21,22]

Another early example of an aluminium salen complex being used to produce isotactic PLA was revealed by Feijen and coworkers.[23,24] Using the well-known chiral Jacobsen's ligand, the resultant initiator (**5**), highlighted the effectiveness of developing catalysts capable of enantiomorphic site control.[23–25] The *R,R* form shown (Figure 2.1), is noted to have a preference for the polymerisation of *L*-LA imposing an a overall isotacticity on the ROP of *rac*-LA. Best results were achieved under melt conditions of 130 °C at 200:1 $\{[LA]_0:[I]_0\}$ delivering a high isotactic preference (P_r = 0.12). Complete conversion was achieved after a reaction time of 2 days. Despite such mild activity under such intensive conditions molecular weight control is maintained.

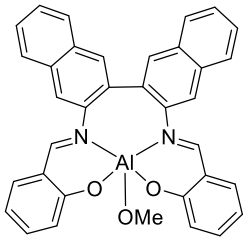

4

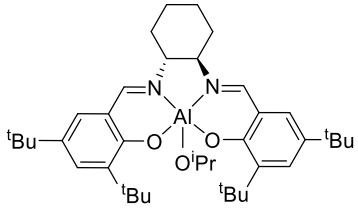

5

Figure 2.1. Early isoselective initiators reported by Spassky (**4**) and Feijen (**5**).[20,23,24]

The adoption of the Jacobsen's pro-ligand in inorganic synthesis shares significant overlap for Al and group 4 central metals, yet the divergence in structure and activity sets Al apart. When Zr and Hf are employed binuclear analogues are isolated, ultimately producing vastly improved rates whilst reducing selectivity compared to **5**, yielding atactic PLA.

The emergence of 'salen' pro-ligands to produce initiators for ROP of cyclic esters is largely due to the directionality of the orbitals, giving significant donation into the central metal ion. The simplicity in ligand synthesis from the condensation of the phenolic aldehyde and amine base allows the production of numerous variants. Investigations into modifying the steric bulk of phenyl substituents and the nitrogen backbone, as well as altering the flexibility of the coordination sphere by changing the size of the backbone, are common approaches to tuning the rate and selectivity for analogues of **6** (Figure 2.2). In its simplest form, Spassky demonstrated how an ethylenediamine salen system, **6a**, produced PLA with a isotactic bias via a chain-end controlled mechanism. Shaver and co-workers published an *ortho* bound adamantyl variant, which could produce PLA with a strong *iso*-tactic preference (P_r = 0.12), even under immortal conditions. More recently, the Spassky complex has been used for the initiation of macrolactones to produce "polyethylene like" polyesters. In addition, this system has been studied using density functional theory to describe the mechanism and activation energies for the ROP of a variety of cyclic esters.[26,27]

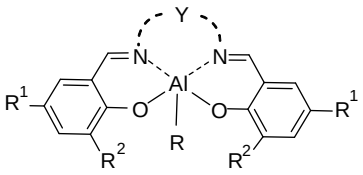

6

Y	R^1	R^2	Reference
$-H_2-H_2-$ C C	H	H	Spassky *et al*
$-H_2-H_2-$ C C	H	Ph	Nomura *et al*
	H	^{t}Bu	
	^{t}Bu	^{t}Bu	
	H	^{t}BuMe$_2$Si	
	Cumyl	Cumyl	Lin *et al*

Figure 2.2. Achiral salen Al complexes employed by Spassky *et al*.,[20] Nomura *et al*.,[25,28] and Lin *et al*.[29]

Nomura and co-workers have focused 'salen' studies on ascertaining the relationship between the bulk of the backbone and phenyl substituents on selectivity.[25,28] Whilst, a degree of selectivity is seen for all initiators, best results were achieved when bulky phenyl substituents were used in the *ortho*-position and an increased length of the backbone was employed. When a neopentyl linker was adopted with ^{t}BuMe$_2$Si– in the –*ortho* position an exceptionally high degree of isotacticty (P_r = 0.02) was seen in toluene at 70 °C ($[LA]_0$:$[I]_0$ = 100:1, 14 hours, T_m = 209 °C). Whilst only a slight reduction in selectivity was seen under melt conditions this proved enough to reduce the polymer thermal properties significantly (130 °C; P_r = 0.08, T_m = 189 °C, 180 °C; P_r = 0.16 and T_m = 176 °C). Like the eminent investigations led by Nomura,[30] Lin *et al.,* also investigated the impact of steric bulk, concluding with a system bearing Me$_2$PhC– (cumyl) substituents in the *ortho* and *para* positions which could balance high isoselectivity and moderate rates in solution, (70 °C, P_r = 0.03 – 0.06, 12 h, T_m = 203 – 205 °C).[29]

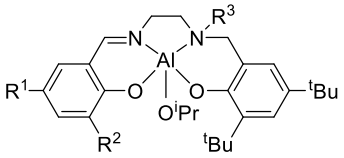

Jones, 2011

7	R^1	R^2	R^3	P_r
a	Me	H	Ph	0.41
b	H	H	Me	0.74
c	Cl	Cl	Me	0.63
d	Cl	Cl	Ph	0.4

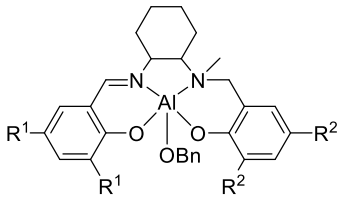

Jones, 2013

8	R^1	R^2	P_r
a	^{t}Bu	^{t}Bu	0.58
b	Cl	^{t}Bu	0.63
c	Cl	Cl	0.73

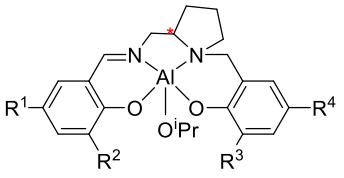

Kol, 2014

9	R^1	R^2	R^3	R^4	*	P_r
a	Cl	Cl	Ad	Me	*(S)*	0.24
b	Me	Ad	Cl	Cl	*(S)*	0.82
c	^{t}Bu	^{t}Bu	Cl	Cl	*(S)*	0.82
d	^{t}Bu	^{t}Bu	I	I	*(R)*	0.59

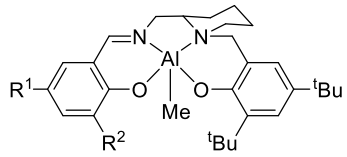

Jones, 2016

10	R^1	R^2	P_r
a	^{t}Bu	^{t}Bu	0.62
b	Me	Me	0.56
c	Ad	Me	0.68

Figure 2.3. Aluminium 'salalen' complexes with varying phenolic and backbone substituents reported by Jones and Kol.[3,31–34]

A series of a novel chiral aluminium 'salalens' or asymmetric 'ONNO' complexes bearing both imine and amine backbone have also been explored, looking to more precisely probe the effect of the ligand backbone on optimising ROP activity. Within this, the adaptation of the Feijen and Spassky systems has seen extensive examples of 'salalen' complexes from the Jones and Kol research groups (Figure 2.3).[3,31,32,34] Whilst many examples are reported, no significant increase in rate is observed for the 'salalen' variants. Interest is instead focused on how a selectivity switch is dependent on the serendipitous choice of aryl substituents for a given backbone. Jones and co-workers first showed this by the adoption of either a –methyl or more electron withdrawing –phenyl substituent on the amine nitrogen, leading to a switch from isoselectivity to heteroselectivity respectively.[31] Further investigation utilising DFT confirmed this proceeds via a chain-end mechanism and is not directly affected by the chirality on the backbone.[35] In a near mimic to the isoselective salen **7a**, Jones and co-workers showed that the salalen analogue (**8a**), was mildly heterotactic (P_r = 0.58). Substitution of the bulky –^{t}Bu substituent with the mildly electron withdrawing –Cl group

further embedded that a heteroselective bias was in place (P_r = 0.73).[32] Arguably the most pronounced switch in selectivity was seen by aminomethylpyrrolidine based 'salalen' initiators **9a** – **d**, revealed by Kol and co-workers.[3] Switching steric bulk between the amine and imine side yielded either highly isotactic (**9a**, P_r = 0.24) or highly heterotactic (**9b**, P_r = 0.82) PLA. Further work varying the size and type of cyclic amine backbone (**10a** – **c**) has not been able reproduce such a switch, indicating the potential importance of the chiral pyrrolidine in the ligand framework.[34,36]

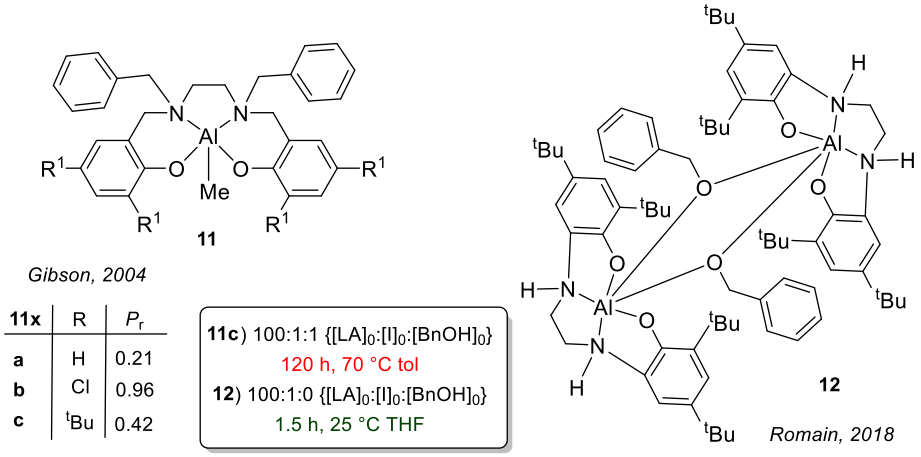

Figure 2.4. Aluminium 'salan' complexes reported by Gibson and Romain.[6,37]

Gibson and co-workers, showed that by varying the aryl substituents on an aluminium 'salan' system they were able to radically alter the tacticity of the PLA produced (**11a** – **c**, Figure 2.4).[37] 'Salan' refers to a diamine backbone on the ancillary ligand and is associated with greater flexibility. These ligands could be seen as a more versatile system, with facile synthesis via the Mannich reaction.[38–40] This method provides a cheaper alternative to salicylaldehyde reactants with greater variability arising from the wide variety of phenolates that could be used.

Moderately isotactic PLA (P_r = 0.21) was obtained with unsubstituted *ortho* and *para* groups on the phenols (**11a**) whilst highly heterotactic PLA (P_r = 0.96) was produced with chloro-substituted phenols (**11b**). An example of chain end control, this system shows the importance of the metal coordination sphere and the encompassing electronic and steric effects in the ROP mechanism. This system was one of the first examples within the literature that does not embody a classical alkoxide initiator bound to the metal centre. In this system, the highly labile methyl group is '*in situ*' replaced by a benzyl alcohol co-initiator, which is then activated for ROP. The addition of a co-additive or co-initiator to initiators without a bound alkoxide complex is a requirement to achieve high conversions and rates. Despite this,

the addition of co-initiators are associated with a longer initiation periods at the start of reactions. This was recently realised by Romain and co-workers on a dinuclear aluminium 'catam' type complex with bridging benzyl alkoxide groups between the metal centres (**12**, Figure 2.4).[6] A substantial rate improvement is seen under mild conditions in comparison to the early work of Gibson and coworkers.[37] Representing one of the most active Al systems to date, **12** highlights the potential of using pre-synthesised alkoxide complexes for polymerisation.

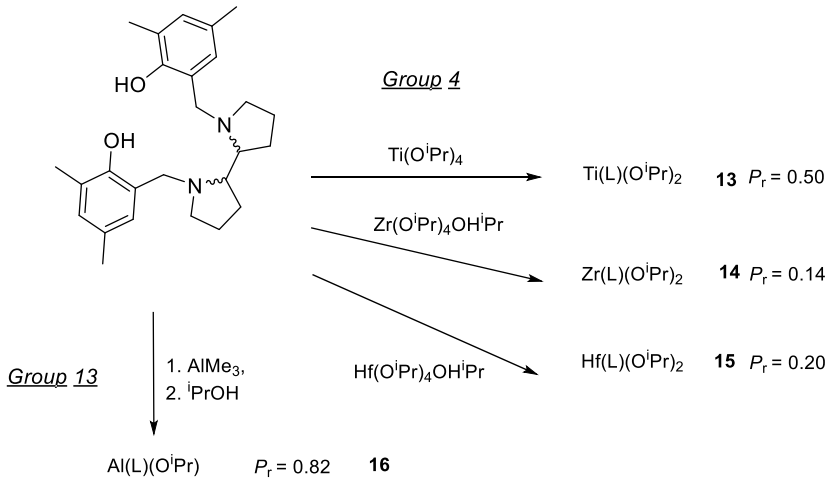

Scheme 2.1. Synthesis of initiators utilising bipyrrolidine ligands reported by Jones and co-workers.[41,42]

This approach has been extensively manipulated by Jones and co-workers surrounding the production of bipyrrolidine salan complexes (Scheme 2.1).[41,42] These systems were shown to have significant variation in ROP activity from the choice of metal. Whilst group 4 metals Hf and Zr were shown to produce isotactic PLA (**14** and **15**), Ti (**13**) yielded only atactic PLA. Most surprisingly the Al analogue (**16**) produced PLA with a highly heterotactic bias, a rarity in the field of aluminium initiators. The ligand chirality was shown to have a pronounced effect on the stereochemical outcome. Kol and co-workers have also investigated the virtue of bipyrrolidine based complexes with Mg.[43,44] Whilst no selectivity was seen for the ROP of *rac-LA*, the 'living' nature of the catalyst was studied producing octa-block copolymers from the sequential addition of *D*- LA and *L*-LA, whilst maintaining low dispersities and high rates (CH_2Cl_2, 25 °C, 60 minutes, M_n^{SEC} = 51.0 kg mol^{-1}, $Đ$ = 1.12). Whilst stereoblock copolymers from sequential addition presents a synthetically more intensive route, the efficacy of this system to keep low dispersities throughout multiple monomer additions is noteworthy.

Whilst significantly less studied, the development of group 13 complexes based on Ga and In could address concerns over the activity of Al. The larger ionic radii could alter the coordination sphere and hence activity of the initiator. Specifically focusing on the

polymerisation of *rac*-LA this review herein discusses how catalyst development within group 13 has been a focus of research efforts in recent years, expanding knowledge of metal-ligand-monomer interactions and providing important mechanistic insight for future development.

2.1.2. Gallium initiators

Unlike other group 13 metals, gallium has received comparably less attention in the literature with only a few studies reported on its use in ROP.[11,45–50] This is mostly due to the high sensitivity of gallium complexes to hydrolytic degradation and their poor performance for ROP.[46] Looking into the trends in Lewis acidity of group 13 complexes Kremer *et al.*, carried out a number of experimental and computational studies to explore this phenomenon.[10] Whilst it is shown to vary on solvation structure and aggregation of molecules in solution, the Lewis acidity trend of {Al > Ga ~ In} is generally supported in the comparable 'salen' architectures studied.[51] One noteworthy example by Williams and co-workers showed how moderately isotactic polymer (P_r = 0.31) could be produced from a quinolinolato gallium complex bearing a labile isopropoxide group **17** (Figure 2.5).[46] However the complex presented only mild activity, with 90% conversion of *rac*-LA in toluene at 80 °C after 50 hours at ratio of 100.1 {$[LA]_0$:$[I]_0$}, a value comparatively low compared to the In analogue.

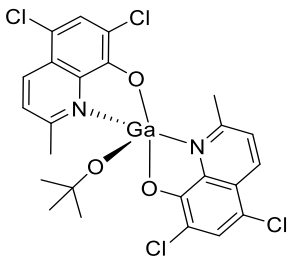

17

Figure 2.5. 2,4-di-chloro quinolinlato gallium complex shown by Williams and co-workers.[46]

In contrast, Chakraborty and co-workers showed how a mono-ligated gallium species, **18**, (Figure 2.6) could provide excellent activity with a strong isotactic bias (P_r = 0.16).[45] At a ratio of 800:1 {$[LA]_0$:$[I]_0$}, complete conversion was shown after 60 minutes under solvent free conditions, giving excellent molecular weight control. The corresponding indium analogue, **19**, exhibited slightly lower rates with retention of stereocontrol. Increasing the steric bulk and ancillary donating groups on the bonding phenolate had little impact on the stereocontrol with only a slight variation in rates observed. These findings reinforce that the chain-end control mechanism was present under this metal coordination structure. This reactive comparison between the group 13 metals for this system highlights the importance of metal optimisation for future design of catalysts and structural activity relationships.

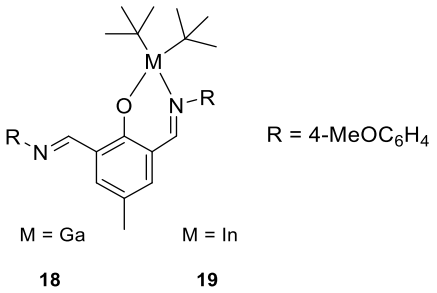

Figure 2.6. Mono ligated alkyl gallium and indium complexes employed by Chakraborty and co-workers.[52]

2.1.3. Indium initiators

Whilst aluminium catalysts have been prevalent in the literature, a few more recent studies have shown that indium complexes have the potential to be more reactive and functional group tolerant than their aluminium analogues.[48,53–58] However, the high propensity for aggregation of species often makes isolation difficult and the nature of the active species difficult to predict. Studies by Tolman and co-workers showed how indium(III) trichloride could be used *in-situ* with equimolar equivalents of triethylamine (NEt_3) and benzyl alcohol (BnOH) to produce highly heterotactic PLA (P_r = 0.97) within 2 hours (CH_2Cl_2, 25 °C $[LA]_0$:$[InCl_3]_0$:$[BnOH]_0$;$[NEt_3]_0$ = 200:1:1:2).[59,60] This is quite remarkable as it is one of a few examples of stereo-selectivity where the incumbent catalyst does not possess any ancillary 'directing' ligand. Under the same conditions $AlCl_3$ and $GaCl_3$ show no activity for *rac*-LA polymerisation.[49]

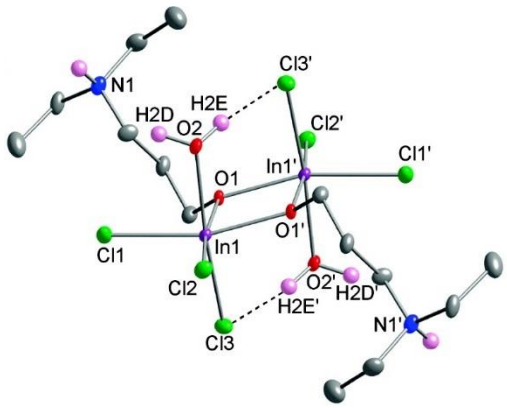

Figure 2.7. Replicated X-ray crystal structure of $[InCl_3(deapH)(H_2O)]_2$ reported by Tolman and co-workers.[60]

Further kinetic studies by Tolman and co-workers showed that the use of triethylamine as a base in activating the initiator is the key in unlocking the high activities shown.[60] In an attempt to isolate the possible initiation complex, crystals suitable for X-ray diffraction were grown using 3-diethylamino-1-propanol (deapH) in lieu of BnOH and NEt_3 (Figure 2.7). This was done to exploit the propensity of the ammonium salt to crystallise. The crystal structure shows that in the presence of adventitious water a bridged dimeric complex is formed with activation of the indium chloride from the release of HCl, which is trapped within the salt structure. Whilst providing a robust and cheap catalyst, this system relies on the *in situ* synthesis of the coordination complex between $InCl_3$, BnOH and NEt_3 before lactide initiation can occur. This methodology has been known to produce high dispersities of molecular weights.[60]

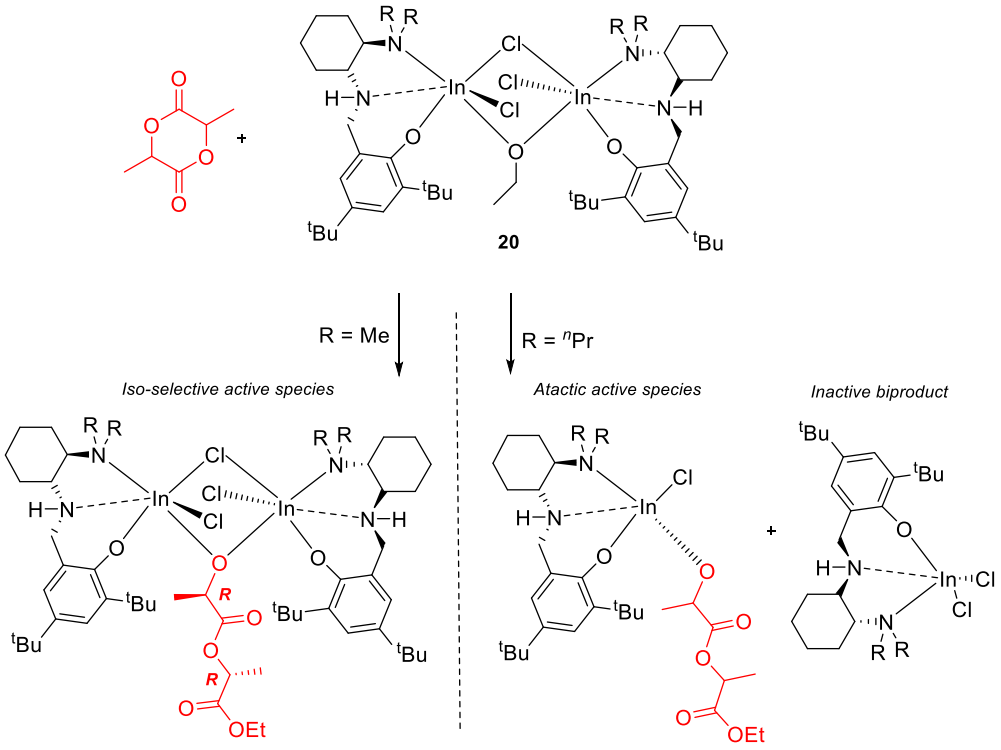

Scheme 2.2. Dimeric indium salan chloride complex reported by Mehrkhodavandi and co-workers.[54]

Mehrkhodavandi and co-workers showed enhanced activity from indium chloride initiators by producing a chiral dimeric indium monophenolate complex (**20**, Scheme 2.2) capable of producing mildly isotactic polymer (P_r = 0.53 – 0.62), within 30 minutes (25 °C, CH_2Cl_2) at a 200:1 {$[LA]_0$:$[I]_0$} feed ratio.[61] Mechanistic investigations showed a significant rate difference towards the ROP between complex enantiomers.[62] Identifying the nature of catalytically active species in solution is important, especially when using metal centres with larger ionic radii where aggregation into intractable multinuclear species is common. In addition, the

catalytically active species are often different to the feed complex. Despite using many equivalents of sodium ethoxide, it was shown that only the single bridging ethoxide complex (**20**) could be isolated, highlighting the stability around the bridging chloro group. In the presence of trace H_2O the alkoxide bridge was replaced by a hydroxide group, providing a stable, albeit less active, dimeric complex.

Further mechanistic investigation into the nature of catalytically active species found that the dimeric structure was retained in solution when less bulky methyl groups are used on the amine linker. Hypothesising a 'co-operative' interaction between metal centres, these systems ultimately display high rates and good isoselectivity. Conversely, when ^{n}propyl groups are used, the species is shown to break up upon lactide coordination, yielding an active species propagating at a slower rate with no selectivity (Scheme 2.2). Recent advances, using this system have shown that the nature of the bridging alkoxide initiator is integral to achieving appreciable activity and selectivity. Increasing the steric clash of the initiating group was found to not only increase the length of the initiation period but also alter the observable rate of reaction.[63]

Further research by Mehrkhodavandi and co-workers showed that it was possible to create a di-alkoxide bridging indium 'ONNO' species through utilisation of a sal-BINAP ligand system (**21**, Figure 2.8).[54] Bridging of the ligand between the metal centres and formation of an octahedral coordination geometry was seen as the major product with other coordination modes existing as minor products. Whilst this particular complex showed very little activity for lactide polymerisation, the effect of steric bulk on the formation of a bridging di-alkoxide and its role on limiting the destructive aggregation effect is noteworthy.

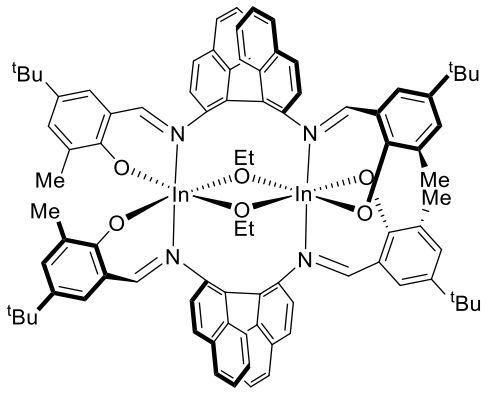

21

Figure 2.8. Indium sal-BINAP complex with di-alkoxide bridge reported by Mehrkhodavandi and co-workers.[61]

Previous work by Coates and co-workers showed how a bulkier alkoxide could be used to produce a monomeric aluminium sal-BINAP complex, avoiding aggregation of complexes.[22,64] However, with indium the same phenomenon was not seen with only bridging ligand, alkoxide/chloride or chloride/hydroxyl complexes being able to be formed. In recent years, it has been shown possible to overcome aggregation in dimeric indium alkoxides. An extension of previous studies, Mehrkhodavandi and co-workers utilised a sterically hindered Jacobsen's ligand to produce an indium di-ethoxide species (Figure 2.9).[53,64–66] A keynote complex, **22** showed moderate activity (99%, 1 hour, $[LA]_0:[I]_0 = 200:1$, $Đ = 1.39$, toluene, 80 °C), as well as a strong isotactic bias ($P_r = 0.15$) for the ROP of *rac*-LA. Kinetic studies complemented earlier work showing that the dimeric complex experienced an extended initiation period in comparison to the monomeric form (**23**), ultimately leading to a lower activity. Quan *et al.,* have since shown a monomeric indium alkoxide with ferrocyl bridged imine backbone to be proficient for the ROP of other cyclic esters and cyclic carbonates, detailing high rates and low dispersities.[67]

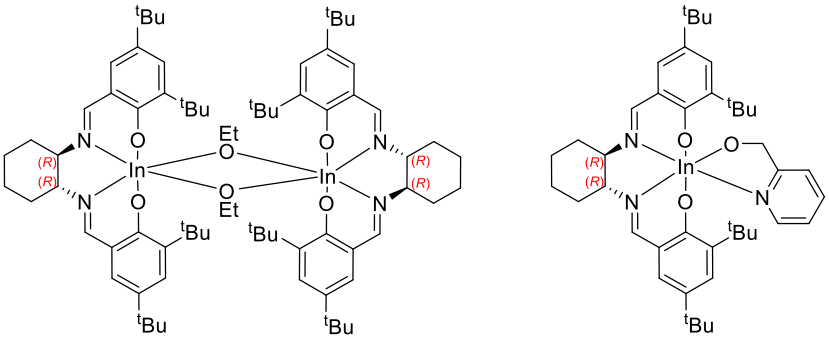

Figure 2.9. Salen indium ethoxide complexes using Jacobsen ligand reported by Mehrkhodavandi and co-workers.[66]

In the same vein as studies with aluminium catalysts, a comparison between 'salen' and 'salan' structures has been applied to indium by Ebrahimi *et al*.[68] Utilising a reduced chiral Jacobsen's ligand the resultant complex was isolated as a bridged –chloro mono ethoxide system (**24**) similar to monophenolate work previously established with the group.[61] Whilst the synthesis of the indium 'salan' version does not represent a high degree of innovation, upon exposure to water the complex produced a mono-hydroxide bimetallic system which was air-stable and acted in reversible fashion to yield the catalytically active ethoxide system upon addition of ethanol. No report of further degradation products allows this system to be used with 'technical' or wet LA, removing the need for any solvent intensive purification. Whilst not involved in the ROP mechanism, the importance of the –chloro group in providing

further moisture stability is highlighted. This reversible system was tested under immortal polymerisation conditions achieving high molecular weights >90 kg mol^{-1} in 2 hours (120 °C, $[LA]_0$:[**24**]$_0$:$[I]_0$ = 10000:1:10, $Đ$ =1.34) using 1,3,5-tris(hydroxymethyl)benzene as chain transfer agent.

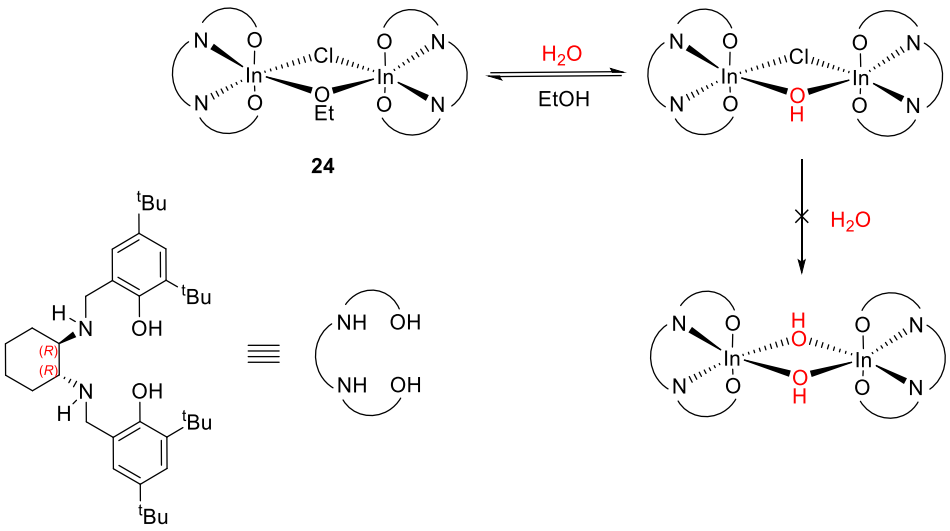

Scheme 2.3. Reversible dimeric indium salan complex published by Ebrahimi *et al.*[68]

The high rate often associated with indium was recently married with the isoselectivity which has often eluded this metal centre, with an indium phosphasalen complex reported by Williams and co-workers (**25**, Figure 2.10).[69] Using a bulky, sterically constrained ligand, at feed ratios of 500:1 {$[LA]_0$:[**25**]$_0$} complete conversions were achieved within 60 minutes yielding polymer with low dispersity ($Đ$ = 1.15) and a high isotactic bias (P_r = 0.13) in THF at 20 °C.

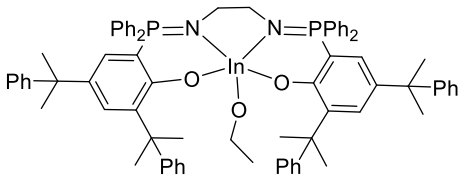

Figure 2.10. Indium phosphasalen complex presented by Williams and co-workers.[69]

2.1.4. Chapter aims

Notable improvements in the rate of indium species can lead to loose activity trends of In > Ga > Al, yet with many exceptions to the rule and no fully evaluated trends in stereoselectivity, the understanding of group 13 metals for ROP is not complete. Common issues of aggregation have limited the synthetic variability in indium systems, which are often employed with sterically hindered substituents. Throughout group 13, the impact of Lewis acidity, metal size, the bite angle of the ligand and the ligand donation effects clearly have a profound effect on ROP activity, with examples not limited to the polymerisation of LA. Herein, this work aims to bridge the work in synthesis surrounding group 13 initiators for ROP. An initial focus is further investigating the serendipitous activity previously seen the bipyrrolidine based systems (Scheme 2.1) with the coordination to gallium and indium. By looking into structural-activity relationships this works aims to provide knowledge to facilitate the design of future initiators. Whilst LA polymerisation is a crowded academic space, utilisation of the extensive knowledge to provide comparisons between catalytic system is invaluable in catalyst design for the application in the polymerisation of novel bio-based monomers.

2.2. Complexation of bipyrrolidine ligands with group 13 metals

2.2.1. Synthesis of *meso*-bipyrrolidine ligands

Previously reported *meso*-bipyrrolidine ligands were prepared by a modified Mannich reaction, using two equivalents of the 2,4-disubtituted phenol and *p*-formaldehyde (Scheme 2.4).[41,70] Upon cooling white crystals were collected, washed with methanol and confirmed pure by ^{1}H NMR spectroscopy.[41,71] Both –methyl (**1**H_2) and –^{t}butyl (**2**H_2) di-substituted ligands were prepared in similar yields to literature reports, with **3** – **5**H_2 representing new additions to the series. The effect of withdrawing groups in **3**H_2 and largely sterically hindering **4**H_2 is proposed to tune the properties of the complex as seen in literature.[2,72]

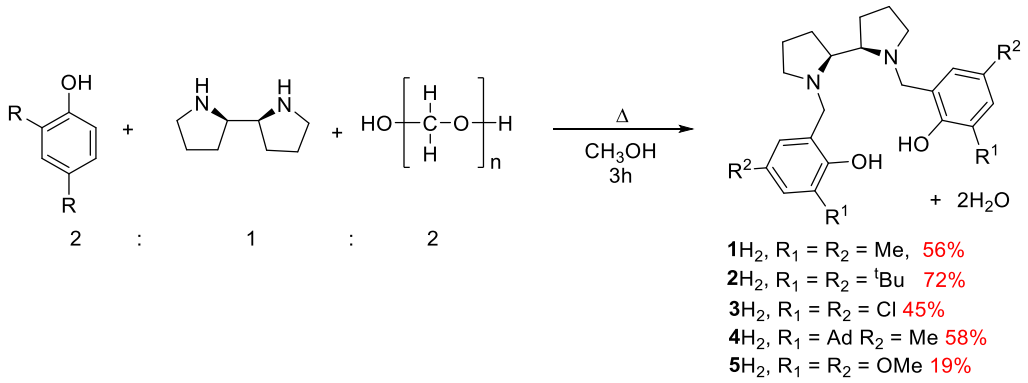

Scheme 2.4. Synthesis of bipyrrolidine ligands from a modified Mannich reaction.

2.2.2. Complexation of *meso*-bipyrrolidine ligands with indium halides

Whilst Zr, Hf, Ti and Al bipyrrolidine analogues are commonly synthesised from the M(O^{i}Pr)$_x$ precursors, this method proved unsuitable when applied to indium, with no conversion seen upon reaction with **1** – **5**H_2 under a range of conditions. In the synthesis of indium complexes, transmetallation of $InCl_3$ with a reactive intermediate is often employed to produce the corresponding metal chloride complex. This species can be further modified to yield the desired metal alkoxide complex as the initiator. For this method **1**H_2 and **2**H_2 were initially reacted with 2 equivalents of potassium hydride at 195 K to yield the corresponding di-potassium-ligand salt (Scheme 2.5). Subsequent transmetallation with $InCl_3$ yielded the metal chloride complex and KCl as a side product.[53] The –methyl substituted ligand **1**H_2 was initially targeted due to previously reported increases in activity in polymerisation between Me group and bulkier –^{t}Bu groups. Isolation at each step, allowed confirmation of reaction progress through ^{1}H NMR spectroscopy. Due to the low solubility of the isolated potassium salt, the sample was solubilised in tetrahydrofuran-d_8. Fluxionality of the sample was

confirmed at 298 K by broad resonances in the ^{1}H NMR spectrum. Carrying out NMR analysis at 238 K reduced molecular motion to improve signal definition allowing quantification of all expected ligand salt signals (Figure 2.11). A set of doublets with coupling constants of 10.5 Hz for the CH_2 benzylic protons suggests the potassium ion causes rigidity at the given temperature forcing the protons into magnetically inequivalent environments.

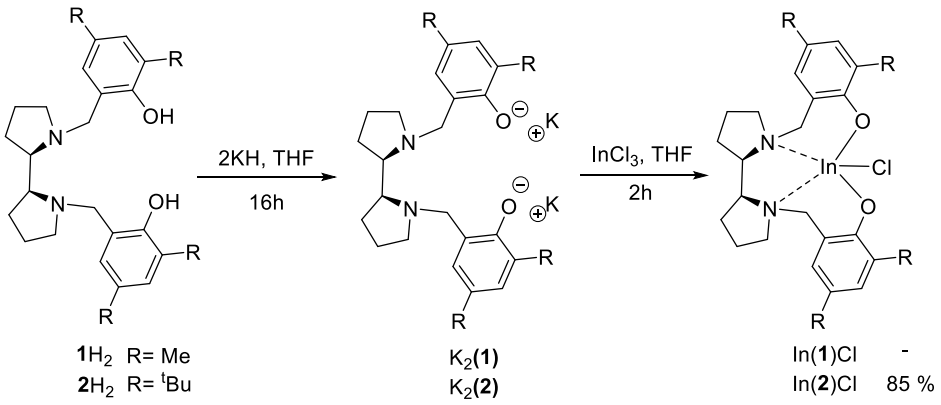

Scheme 2.5. Synthetic route to indium chloride complexes via transmetallation.

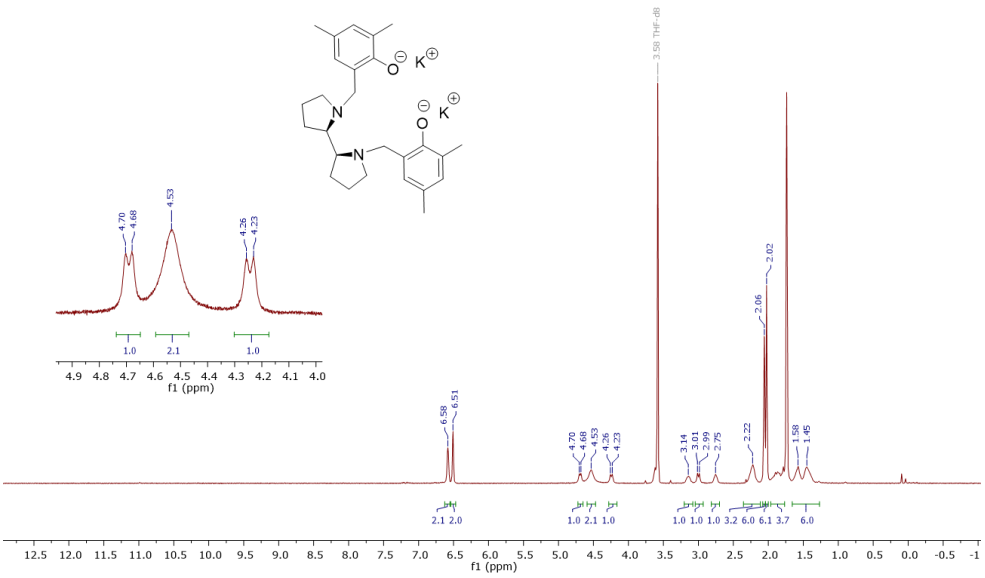

Figure 2.11. ^{1}H NMR spectra of K_2(**1**) (500 MHz, THF-d_8, 238 K).

Transmetallation of K_2(**1**) with $InCl_3$ yielded an insoluble precipitate in the reaction solvent. Solubility studies with a range of polar and non-polar solvents failed to solubilise the material, suggesting aggregation of complexes. This follows a similar phenomenon shown by Mehrkhodavandi and co-workers that indium complexes commonly aggregate producing poorly soluble large macromolecular clusters.[53,54] Variation of reaction solvent, temperature of complexation and use of sodium hydride as a metalation source was attempted. Despite this, it was shown that complex aggregation still occurred, suggesting the ligand system or reaction methodology was not suitable under the given conditions.

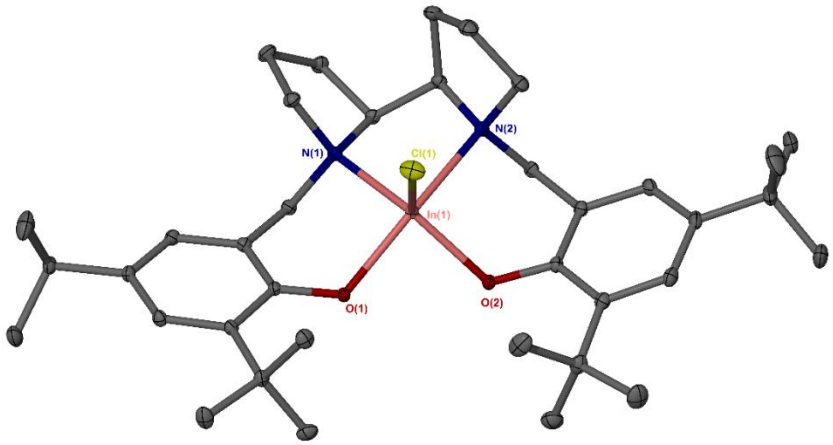

Figure 2.12. Solid-state structure for In(**2**)Cl Ellipsoids are shown at the 30% probability level. All hydrogen atoms have been removed for clarity.

When the –^{t}Bu substituted ligand was adopted the increase in steric bulk yielded a suspension upon *in-situ* addition of $InCl_3$ to the potassium salt K_2(**2**). The small amount of precipitate was hypothesised to be the formation of potassium chloride as an insoluble by-product, which was isolated by centrifugation of the mixture. *In-vacuo* removal of the solvent yielded a solid which upon recrystallisation in a hexane/toluene mixture precipitated as white crystals in high yield (85%). Single crystal X-ray diffraction (XRD) confirmed the solid state structure of In(**2**)Cl (Figure 2.12). ^{1}H and ^{13}C{^{1}H} NMR spectroscopy corroborated the structure was retained in solution with CHN analysis confirming the complex was pure of inorganic residues. The compound was confirmed to be stable in air by identical ^{1}H NMR spectra recorded after 3 days exposure of the solid to atmospheric conditions (Figure 2.13). Whilst air/moisture sensitivity are common in indium complexes, it is hypothesised the In-Cl bond is sufficiently strong to prevent hydrolysis reactions.[54,61] Synthesis with **3** – **5**H_2 did not yield an isolatable product with **3**H_2 and **5**H_2 producing an insoluble suspension upon formation of the potassium salt, whilst **4**H_2 yielded only pro-ligand upon recrystallisation.

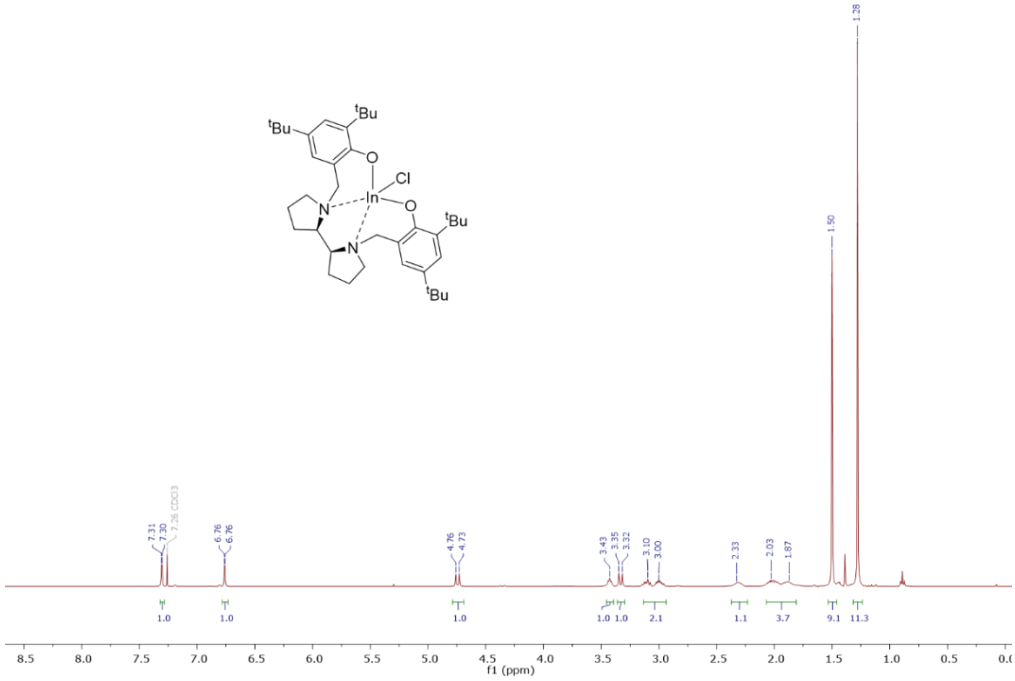

Figure 2.13. ^{1}H NMR spectra of In(**2**)Cl (400 MHz, $CDCl_3$, 298 K) after 3 days exposed to air.

For the *in-situ* activation of metal halides with an alcohol, it is thought the indium halide bond would have to be sufficiently weak to extend and allow the approach of the incumbent lactide monomer. It was postulated that using a bulkier halide with poorer π-acceptor abilities would potentially increase the initial rate of polymerisation.[73] Following the methodology for the synthesis of In(**2**)Cl (Scheme 2.5), an indium iodide complex In(**2**)I was synthesised from indium(III)triiodide and K_2**2**. The solid-state structure obtained confirmed the formation of In(**2**)I (Figure 2.14).

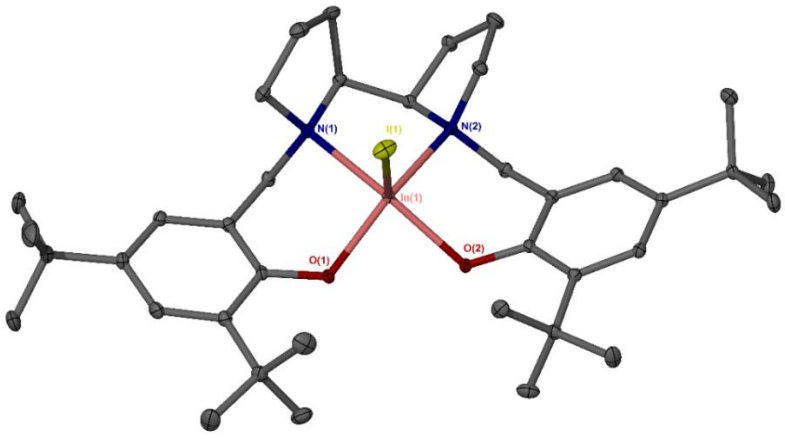

Figure 2.14. Solid state structure of In(**2**)I. Ellipsoids are shown at the 30% probability level. All hydrogen atoms have been removed for clarity.

^{1}H NMR spectroscopy ($CDCl_3$, 258 K), $^{13}C\{^{1}H\}$ NMR spectroscopy and elemental analysis confirmed the solid-state structure was synthesised cleanly, albeit in a lower yield (42%) to the InCl analogue. At time of publication In(**2**)Cl/I represented the first examples of indium 'salan' complexes fully characterised, offering comparison with salen systems on In–N bond lengths and their significance towards ROP activity.[74] The geometric classification of these five coordinate complexes holding tetradentate ligands can be calculated from the triognality (τ) values (Equation 2.1).[75] τ values range from 0 to 1, zero being perfectly square pyramidal and one being perfectly trigonal bipyramidal. Using data obtained from the solid state structures it can be said that both the metal centres are seen to be in a pseudo square based pyramidal geometry, which is exemplified by τ = 0.32 for In(**2**)Cl and 0.28 for In(**2**)I (Table 2.1). This system puts the chloride perpendicular to the tetradentate ligand system, exposing the opposite face of the molecule to activation to a greater degree than in a trigonal bipyramidal system. These findings are analogous to those shown for rigid indium 'salen' species within the literature.[66]

Equation 2.1. Definitions of angles and equation for calculating the degree of trigonality "τ" value.[76]

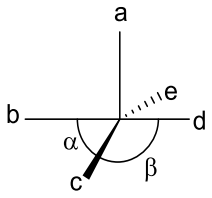

$$\tau = \frac{(\beta - \alpha)}{60}$$

Table 2.1.Comparative information on the bond lengths, bond angles and τ values of In(**2**)Cl and In(**2**)I obtained from single crystal X-ray diffraction.

	In(**2**)Cl	In(**2**)I
In(1)–X(1)	2.3683 (4)	2.7529
In(1)–O(1)	2.0768(9)	1.9550
In(1)–O(2)	1.9749 (3)	1.9887
In(1)–N(1)	2.3138	2.4879
In(1)–N(2)	2.4051	2.2772
O(1)–In(1)–X(1)	105.47	120.11
O(2)–In(1)–X(1)	112.72	104.63
O(1)–In(1)–O(2)	93.91	90.50
N(2)–In(1)–N(1)	76.31	75.03
N(2)–In(1)–X(1)	95.41	111.80
τ	0.34	0.29

Metric data shows a consistent trend between the species with larger angles seen for all O–In–I and N–In–I angle than the chloride counterpart, likely a result of the greater size and electronic density of the iodide atom causing a repulsion of neighbouring atoms away from the plane. Comparison of the bond lengths clearly shows the extension of the In–X bond when iodide is used. The lower electronegativity of the iodide suggests the electron density of the In–I bond is centred more closely on the indium ion than in the chloride analogue.

2.2.3. Synthesis of aluminium and gallium chloride complexes.

Whilst the aluminium alkoxide analogue (Al(**2**)O^{i}Pr) has already been realised by Jones and co-workers, analogous Ga(**2**)Cl and Al(**2**)Cl complexes were synthesised in order to build a basis for structural and activity comparison between the group 13 metals complexes.[41] Utilising the same methodology for the synthesis of In(**2**)Cl, solid state structures were achieved for Ga(**2**)Cl and Al(**2**)Cl (Figure 2.15). Purification and characterisation by ^{1}H, ^{13}C{^{1}H} NMR spectroscopy and CHN analysis demonstrated Ga(**2**)Cl to be pure, isolated with moderate yields (52%).

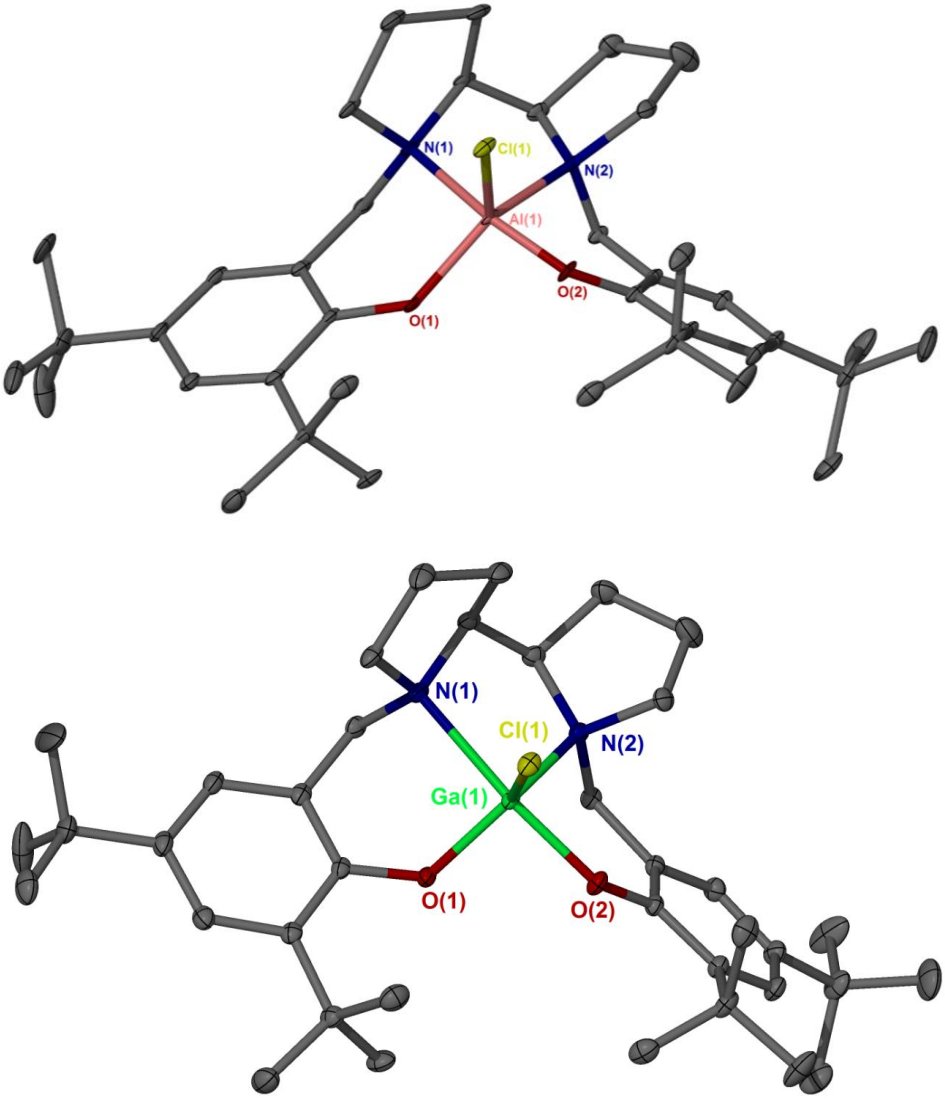

Figure 2.15. Solid-state structures of Al(**2**)Cl and Ga(**2**)Cl. Ellipsoids are shown at the 30% probability level . All hydrogen atoms have been removed for clarity.

In comparison to the indium analogue, Ga(**2**)Cl and Al(**2**)Cl were shown to be unstable in air. Difficulty in removing expected inorganic impurities from Al(**2**)Cl led to the redesign of the synthetic methodology (Scheme 2.6). Direct reaction of the pro-ligand **2**H_2 with an equivalent of Et_2AlCl in toluene avoided the formation of inorganic by-products allowing the clean synthesis of Al(**2**)Cl in moderate yields (55%) (Figure 2.16). The direct reaction of an alkyl metal halide with the chosen ligand could be argued to be an effective one step strategy with evolution of the gaseous alkane generating a strong entropic driving force.

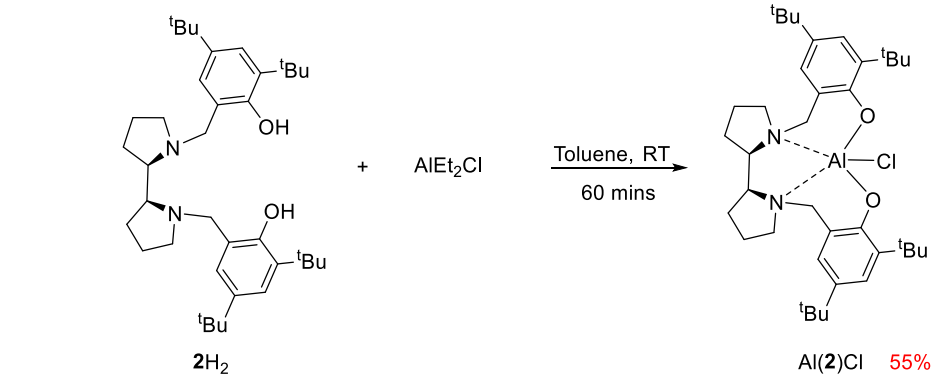

Scheme 2.6. Synthetic route to Al(**2**)Cl via diethylaluminium chloride.

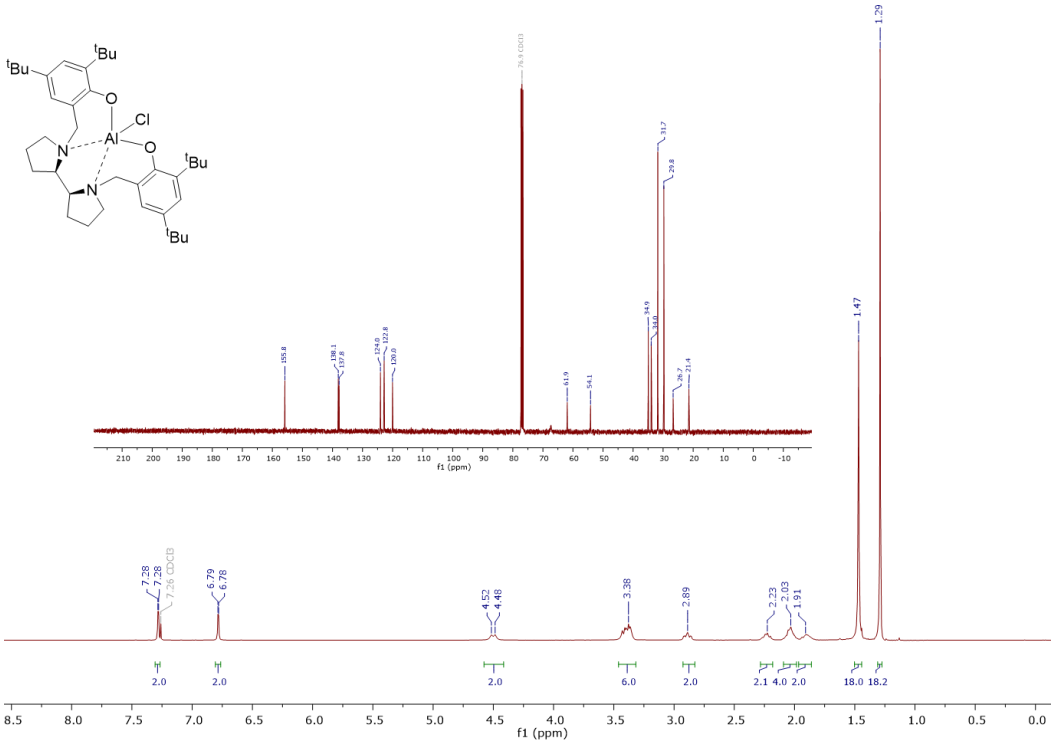

Figure 2.16. Stacked ^1H (400 MHz) and $^{13}C\{^1H\}$ (100 MHz) NMR spectra of Al(**2**)Cl in $CDCl_3$ at 298 K.

2.2.4. Structural comparison of group 13 meso-bipyrrolidine complexes

Metric data obtained from solid-state structures shows a linear increase in the metal-halide bond length as the metal size increases (Table 2.2). This finding could be rationalised to be the result of increasing ionic radii as well as a lower charge density of the metal centre in latter group 13 metals. This supports the expected decrease in Lewis acidity of the metals shown by shifts in the M–X bond lengths from 2.1802 Å (Al–Cl) to 2.3683 Å (In–Cl).[10] The larger ionic radius is also shown to have an effect on bond lengths by a consistent trend between the metals in the extension of the M–O(1), M–O(2) and M–N(1) bond lengths down the group. However, this effect is less apparent and within the error range for Ga–N(1) and In–N(1). Calculation of the τ values (Equation 2.1) using bond angles obtained from the solid state structures (Table 2.2) shows a clear difference between Al and Ga complexes compared to the indium counterpart (τ = 0.32). For Ga(**2**)Cl a τ value of 0.76 is indicative of a distorted trigonal bipyramidal geometry at the metal centre, this is also the case for Al(**2**)Cl with τ = 0.68. Previously published Al(**2**)O^{i}Pr also affords this same degree of trigonality showing that the size of the metal centre is more influential than the nature of the ancillary mono dentate ligand in controlling complex geometry. In all cases the solid-state structure is maintained in solution and the ligand is “locked" once coordinated as evidenced by the formation of discrete diastereotopic doublets in the ^{1}H NMR spectrum for the benzylic protons.

Table 2.2. Comparative information on the bond angles, bond lengths and τ values of group-13 metal meso-bipyrrolidine complexes obtained from the solid state structures.

	Al(2)Cl	**Ga(2)Cl**	**In(2)Cl**
N(1)–M–O(2)	126.79(6)	122.74(5)	134.92(4)
O(1)–M–N(2)	167.65(5)	168.58(4)	154.02(4)
N(1)–M–X	114.99(4)	94.37(3)	111.62(3)
M–X	2.1802(6)	2.2043(4)	2.3683(4)
M–O(1)	1.7820(11)	1.8436(10)	2.0768(9)
M–O(2)	1.7540(11)	1.8828(10)	1.9749 (3)
M–N(1)	2.0285(13)	2.2527(11)	2.2684(11)
M–N(2)	2.2147(13)	2.0513(12)	2.3539(11)
τ	0.68	0.76	0.32

2.3. Complexation of ethylene diamine ligands with group 13 complexes

Attempts to increase the flexibility around the backbone of the complex have previously been reported by Bakewell *et al*., to produce contrasting results in the selectivity of the complex for the polymerisation of *rac*-LA.[77] For structural comparison as well as to identify if a –methyl substituted tetradentate indium chloride complex could be synthesised, a variety of known 'salan' ligands based around the N,N'-disubstituted ethylene diamine backbone were synthesised prior to complexation with $InCl_3$ (Figure 2.17).

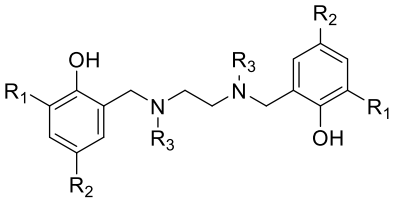

6H_2, R_1 = H, R_2 = R_3 Me
7H_2, R_1 = R_2 = R_3 =Me
8H_2, R_1 = H, R_2 = ^{t}Bu, R_3 =Me
9H_2, R_1 = Me, R_2 = ^{t}Bu, R_3 = Me
10H_2, R_1 = R_2 = ^{t}Bu, R_3 = Me
11H_2, R_1 = R_2 = ^{t}Bu, R_3 = Ph

Figure 2.17. Structure of a variety of ortho- and para- substituted phenol ligands synthesised.

Upon complexation with $InCl_3$ it was shown that all variants of ortho unsubstituted or –methyl substituted ligands produced an intractable mixture of products, analogous to the reactions of **2**H_2. 2,4-Di-tertbutyl substituted **10**H_2 produced a solvent soluble complex from which a crystalline precipitate could be obtained in moderate yields of 42%. Al(**10**)Cl and Ga(**10**)Cl analogues were also successfully prepared via the same procedure used for the bipyrrolidine variants, achieving similar yields (61% and 48% respectively). Crystals of sufficient quality were obtained to confirm the solid-state structures of all M(**10**)Cl complexes where M = Al, Ga, In (Figure 2.18).

Calculation of the trigonality of In(**10**)Cl shows good agreement with the bipyrrolidine analogue (In(**2**)Cl) (τ = 0.38 and 0.32 respectively), suggesting the structure exists in a distorted trigonal bipyramidal geometry (Table 2.3). A marked geometric shift is seen for Al and Ga analogues. A switch from the distorted trigonal bipyramidal Al/Ga(**2**)Cl, to a square based pyramidal structure was observed with the ethylene diamine complex Al/Ga(**10**)Cl (τ = 0.26 / 0.29). Solid state structures highlight a disparity in the geometric isomerism of the complex with the N–Me groups in In(**10**)Cl effectively *cis* to each other whereas in Al/Ga(**10**)Cl these groups are *trans* in geometry. The expected greater flexibility around the nitrogen between M(**10**)Cl and ring strained bipyrrolidine complex M(**2**)Cl, can be evidenced by a divergence in the N–In–Cl bond angles between N(1) and N(2).

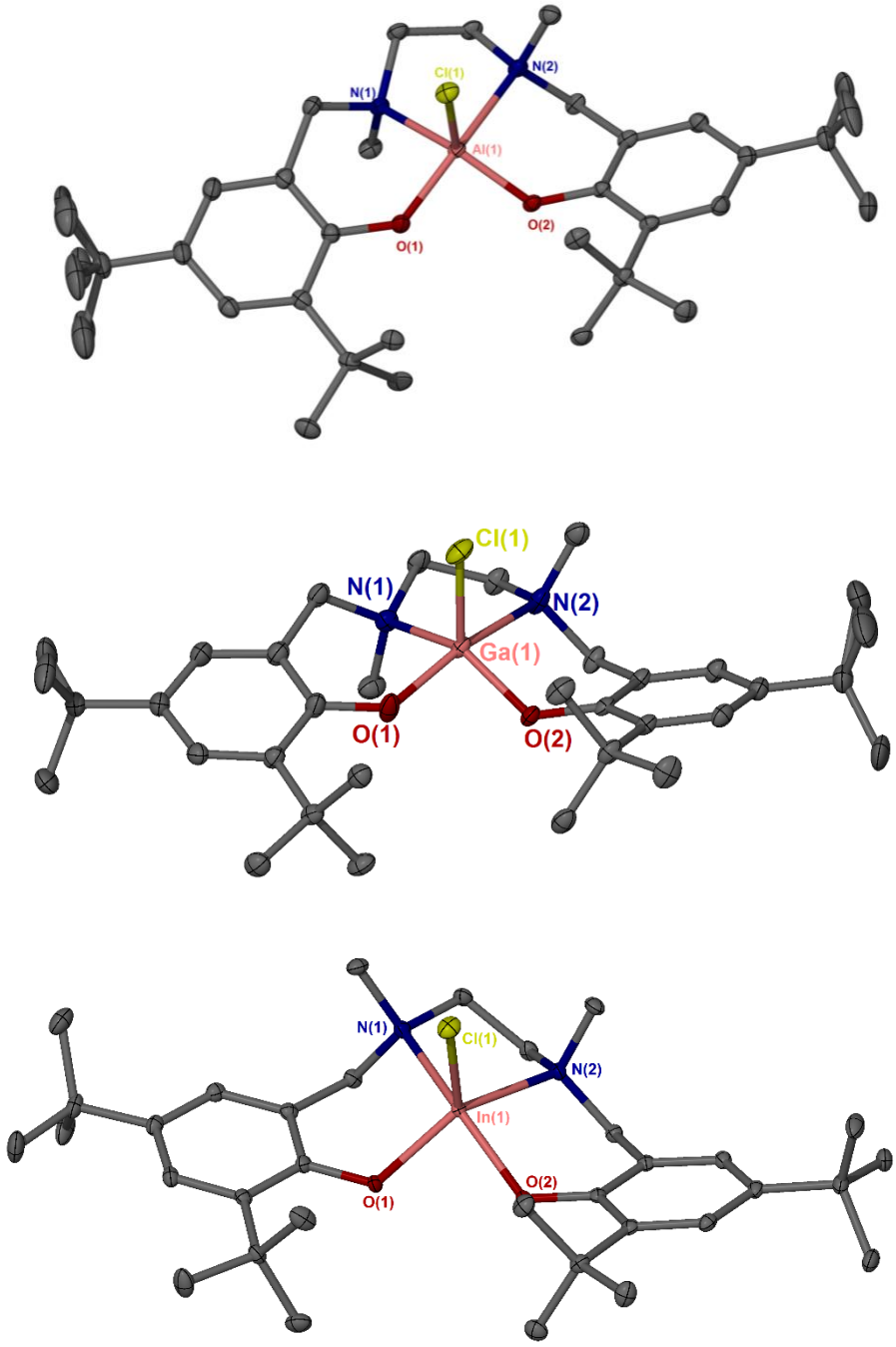

Figure 2.18. Solid-state structures for M(**10**)Cl where M = Al, Ga, In. Ellipsoids are shown at the 30% probability level. All hydrogen atoms have been removed for clarity. *Trans*- conformations of the N–CH_3 functional groups are seen with Al and Ga, with the *cis*- conformation isolated when In is the central metal ion.

Table 2.3. Comparative information on the bond angles and length of In(**10**)Cl obtained from the solid-state structures.

Bond Angles (°)	Al(**10**)Cl	Ga(**10**)Cl	In(**10**)Cl
O(1)–M–N(2)	159.19(9)	169.98(9)	132.71(6)
N(1)–M–O(2)	143.66(9)	142.42(7)	155.56(6)
N(1)–M–Cl	103.78(6)	104.74(5)	97.55(4)
M–Cl	2.172(1)	2.207(1)	2.370(1)
M–O(1)	1.779(2)	1.860(2)	2.031(1)
M–N(1)	2.052(2)	2.087(2)	2.354(2)
τ	0.26	0.29	0.38

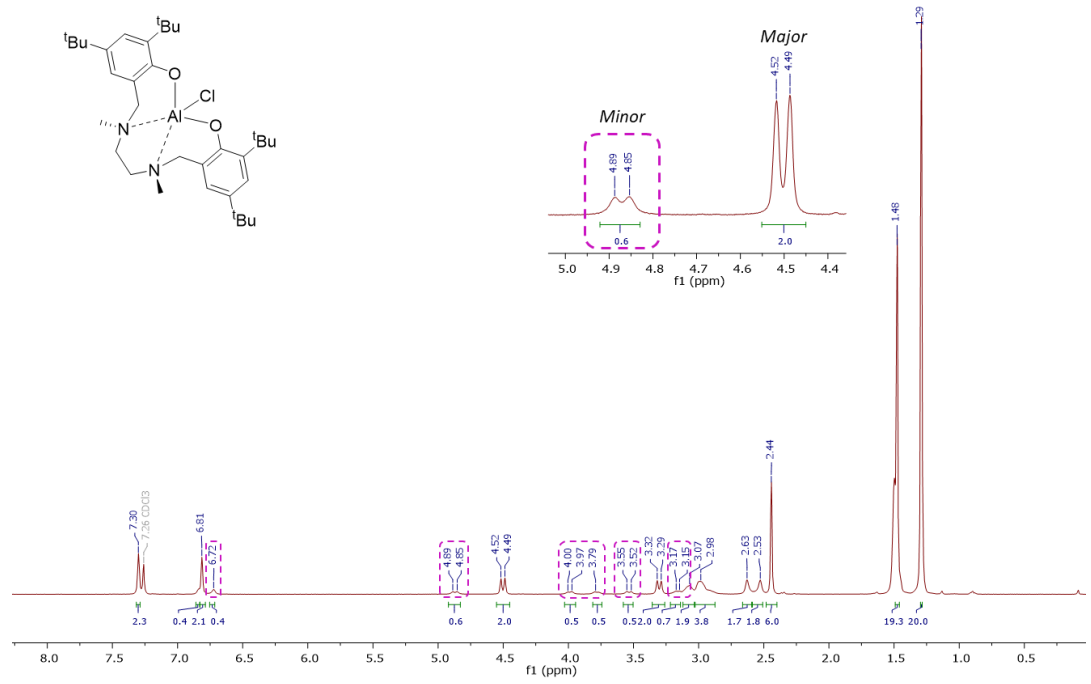

Figure 2.19. ^{1}H NMR (400 MHz, 298 K) spectra of Al(**10**)Cl in $CDCl_3$.

Solution state analysis through ^{1}H and ^{13}C{^{1}H} NMR spectroscopy was facile for In(**10**)Cl yet Al(**10**)Cl and Ga(**10**)Cl are believed to exist as diastereomers. This is evidenced by a minor species present at ~23% intensity of the major species with coupling constants in the same range as those of the major product (Figure 2.19). The major series has an analogous ^{1}H NMR spectrum to that of the In(**10**)Cl with only one resonance for the N–CH_3 group, implying in solution the major species is most likely the *cis*-isomer. The minor series has two distinct singlets identified through DEPT-135 and HSQC NMR spectroscopy as the corresponding N–CH_3 groups of the *trans*-isomer. Ga(**7**)Cl also produced this same diastereotopic pattern of major and minor signals albeit at a lower intensity (~5%). ^{1}H DOSY indicated that the two

species in solution have analogous diffusion constants, $D = 6.3 \times 10^{-10}\ m^2\ s^{-1}$, which would be expected for stereoisomers.

2.4. Synthesis of indium alkoxide complexes

Despite work carried out by Tolman and Merhkhodavandi, highlighting how chloride complexes could be turned into efficient initiators through the addition of extraneous alcohol to the monomer-initiator mixture,[59,68] the possibility to form indium alkoxide species is highly desired. The success of transmetallation to access metal-ligand chloride complexes suggests that further reaction of the chloride complex with basic metal alkoxides (M'OR) could cleave the M–Cl bond, Forming a M–OR functional and a molecule of M'Cl. The M-OR functionality could then act as an initiating group without any induction during polymerisation. Reaction of In(**2**)Cl with 6 equivalents of sodium ethoxide produced an orange suspension. Filtration and recrystallisation lead to the formation of a crystalline precipitate in low yields (15%), which was analysed by single crystal X-ray diffraction (Figure 2.20).

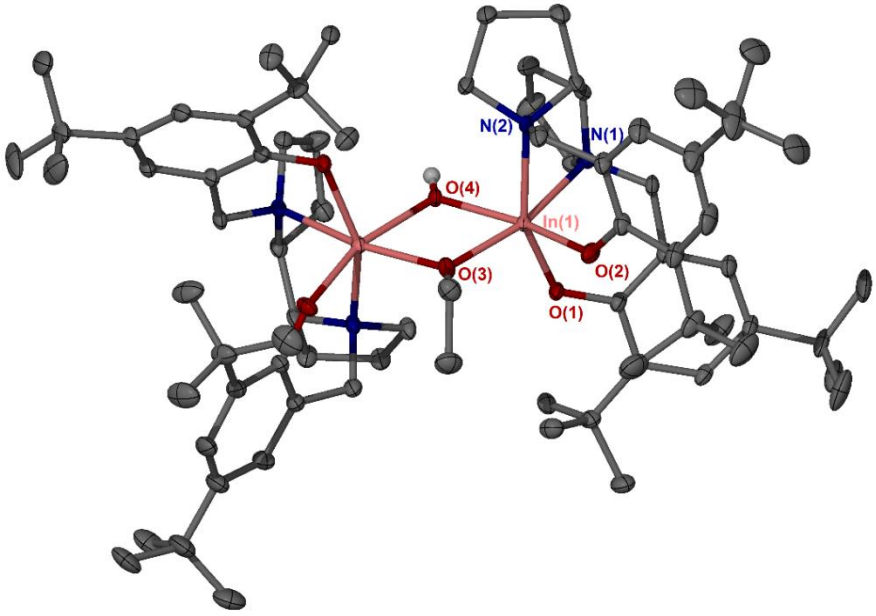

Figure 2.20. Solid-state structure of In_2(**2**)$_2$OEtOH. One ^{t}Bu– is disordered over two positions in a 50:50 ratio only one is shown. There are two and a half molecules of hexane in the unit cell, which (together with all H-atoms) have been removed for clarity.

The solid-state structure is dimeric in nature showing the presence of a bridging hydroxyl group and a bridging ethoxide between the two metal centres, In_2(**2**)$_2$OEtOH. The coordination motif of the ligand in this octahedral complex is analogous to that observed for similar *meso*-ligated group 4 complexes.[42] Following reports by Mehrkhodavandi it is likely

this complex breaks up upon initiation and retains a 6-coordinate geometry during propagation (ligand, lactide and polymer) illustrating the likely coordination of ligand in the catalytically active species.[62]

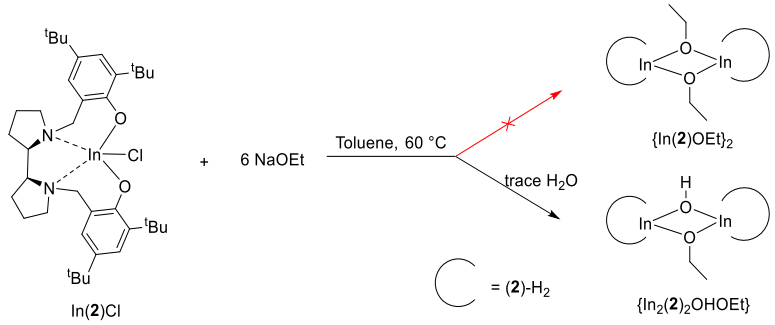

Scheme 2.7. Synthetic route for the reaction of In(**2**)Cl with NaOEt.

The presence of a hydrolysis product complements previous reports by Merhkhodavandi and co-workers of the high moisture sensitivity of In–OR bonds to adventitious water.[54,61] More stringent attention to drying of the of the reaction solvents as well as varying the reaction conditions had little effect with hydrolytic degradation still visible in the coordination sphere. The low yields produced for In_2(**2**)$_2$OEtOH is likely due to the formation of aggregate species as an intractable mix of products. Whilst a few cases exist where water assists activation of the complex for ROP, hydroxyl groups are prone to cause transesterification, leading to a loss in control as evidenced by a wider distribution of molecular weights.[54,59]

The ^{1}H NMR spectra of In_2(**2**)$_2$OEtOH (toluene-d_8, 298K) yielded broad resonances indicative of a fluxional structure at room temperature. Low temperature ^{1}H NMR spectroscopy in the range of 213 – 273 K failed to provide sufficient structural clarity to allow full assignment of the proton environments. Whereas air/moisture stability for hydroxyl bridged In^{3+} systems is reported by Merhkhodavandi and co-workers, exposure of In_2(**2**)$_2$OEtOH to air yielded an intractable mixture of products, evidence of further degradation. With the same methodology applied, but using the dimethyl-ethylenediamine based In(**10**)Cl, only a dihydroxide species could be isolated, {In(**10**)OH}$_2$ (Figure 2.21). Whilst it seems unlikely that only di-hydroxide species are produced through the reaction, the poor solubility of the other products meant further analysis was not possible.

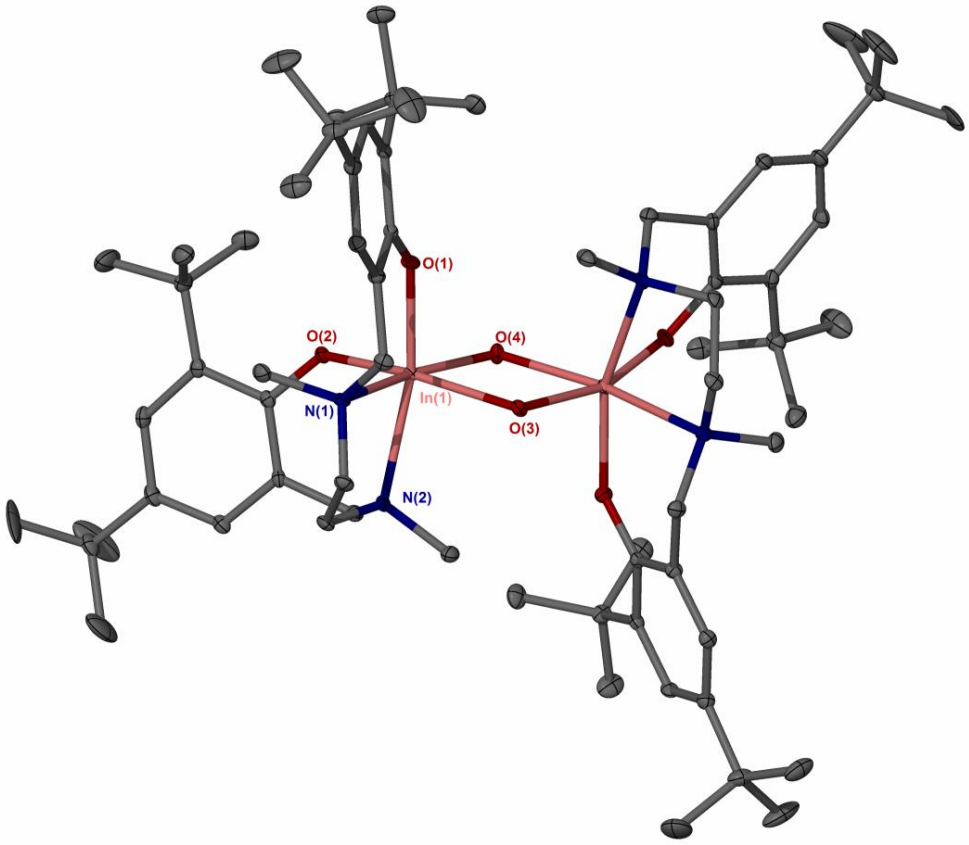

Figure 2.21. Solid-state structure of {In(**10**)OH}$_2$. Ellipsoids are shown at the 30% probability level. All hydrogen atoms have been removed for clarity including that of the bridging hydroxyl groups.

As discussed in the literature, bulkier alkoxides can lead the formation of monomeric complexes preventing aggregate formation.[53,67] Whilst rare in the field, the formation of monomeric indium alkoxide species has previously been achieved through reaction of the chloride complex with a bulky alkoxide.[53] To investigate if the increase in size of the coordination sphere upon formation of the dimeric species influences the susceptibility to hydrolytic degradation, In(**2**)Cl was reacted with 1 equivalent of potassium *tert*-butoxide (KO ^{t}Bu). ^{1}H NMR spectra of the crude material showed notable shift of the resonances from In(**2**)Cl (Figure 2.22). Integration of the new resonance at 7.66 ppm over that of known ArH resonance of reagent In(**2**)Cl suggests an 80% conversion. Due to broadness of signals and roofing effects in the alkyl region from 1.5 – 1.3 ppm it was difficult to ascertain the presence of ^{t}Bu peaks from the alkoxide. The ^{1}H NMR spectra showed no characteristic bridging –OH peaks suggesting no hydroxy groups were formed. Recrystallisation of the crude product produced a small yield of aggregated crystals, which were not suitable for analysis by single crystal X-Ray diffraction.

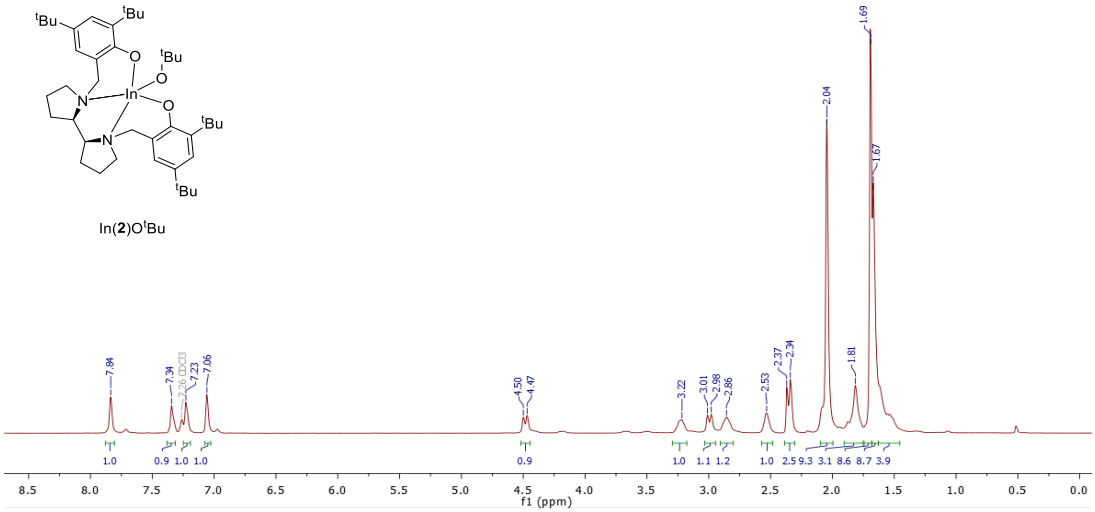

Figure 2.22. ^{1}H NMR (400 MHz, 298 K) spectra in $CDCl_3$ of product from reaction of In(**2**)Cl with KO^{t}Bu.

2.5. Indium salalen complexes

Initiators bearing the 'salalen' backbone, have previously been reported in the literature to produce serendipitous results for the selectivity imposed during polymerisation depending on the coordinating groups, with some examples showing very high isotacticity.[3] By synthesising a variety of indium salalen complexes a good structural as well as practical comparison can be made between the 'salalen' and 'salan' analogues. Additionally, synthetic methods to access salalen ligands allow the formation of highly tuneable systems. Using previously reported asymmetric salalen ligands **12**H_2 and **13**H_2, indium salalen complexes were synthesised to further draw structural comparisons between group 13 complexes.

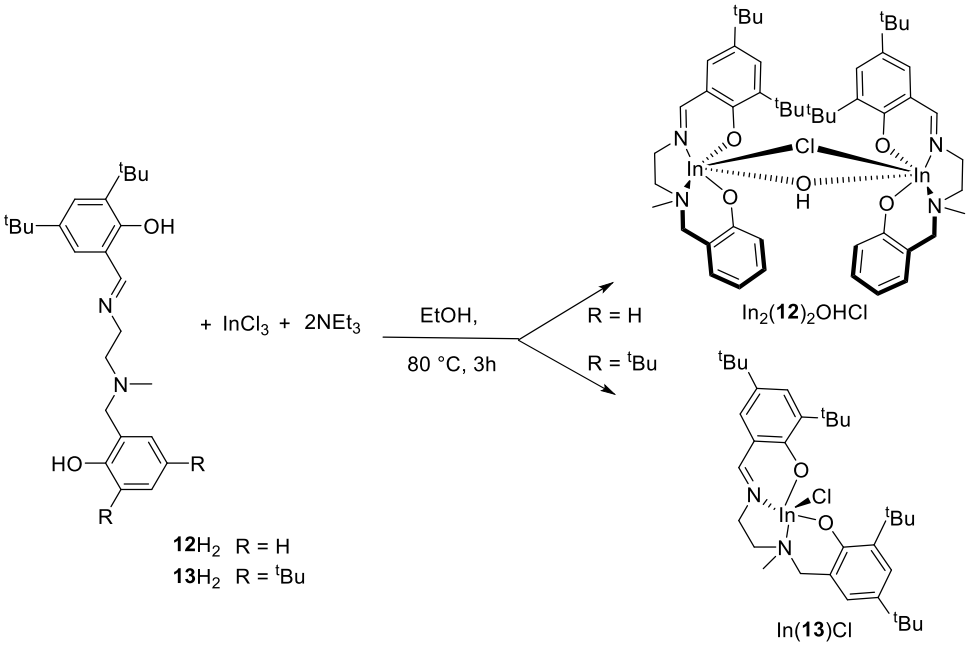

Scheme 2.8. Scheme for the production of indium salalen complexes, In_2(**12**)$_2$OHCl and In(**13**)Cl.

To avoid the two-step synthesis of the transmetallation of the analogous potassium salt, a new scheme was devised for the synthesis of indium chloride catalysts (Scheme 2.8). **12**H_2 was reacted with an equivalent of $InCl_3$ and 2 equivalents of triethylamine in air. Aqueous removal of the ammonium salts and excess starting materials followed by recrystallisation in a hexane/toluene mixture afforded a solid precipitate with suitable crystallinity to allow single-crystal XRD analysis. The solid-state structure shows a dimeric indium species with bridging chloride and hydroxide groups between the indium centres (Figure 2.23). The bridging chloride is in the same plane as the unsubstituted phenol, with a C_2 rotational axis of symmetry through the chloride atom. ^{1}H NMR spectroscopy of the sample reinforced the presence of a bridging –OH with a singlet present at 3.42 ppm. Using more air sensitive conditions via KH/$InCl_3$ (Scheme 2.5) yielded the same species. This shows the sensitivity of a less substituted complex to react with adventitious water. Synonymous to In Cl/OH species reported by Ebrahimi *et al.*,[68] this complex was confirmed as air-stable over the course of 2 weeks with exposure of air to the complex in toluene causing no observable shift in the NMR signals.

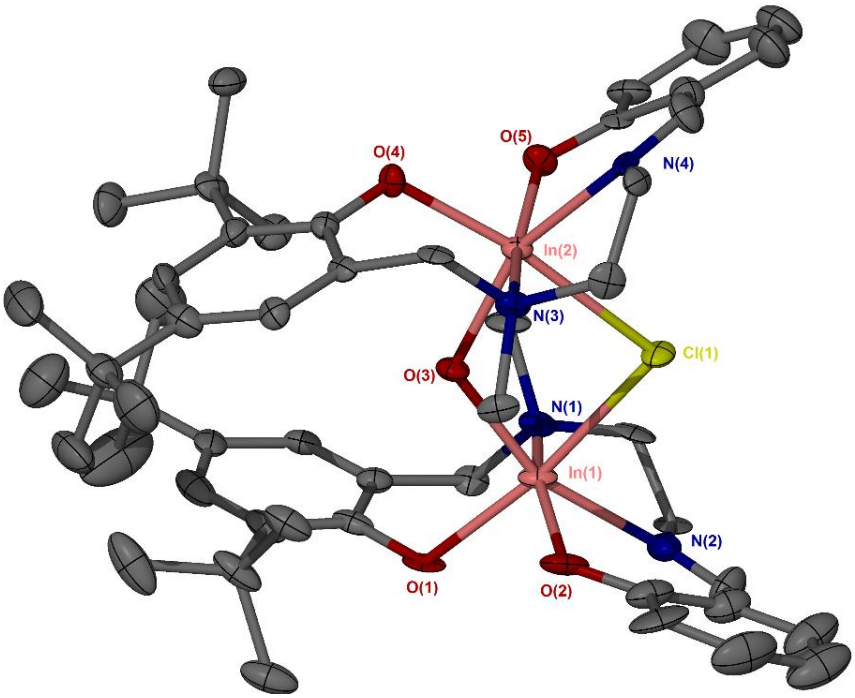

Figure 2.23. Solid-state structure for In_2(**12**)$_2$OHCl. Ellipsoids are shown at the 30% probability level. Two molecules of toluene and one of THF have been removed for clarity. The crystal is twinned and coupled with the weak diffraction it precludes a better solution than that presented.

Recrystallisation of the reaction mixture when **13**H_2 was the ligand yielded crystals unsuitable for single crystal X-ray diffraction. ^{1}H and $^{13}C\{^{1}H\}$ NMR spectroscopy alluded that the sample contained no –OH groups, with shifting in the aryl resonances and the formation of a doublet indicative of the geometrically fixed benzylic bridge. There is no indication this species exists as a dimer in solution and the lack of hydroxyl bound groups highlights a greater resistance to hydrolytic degradation (Figure 2.24). CHN analysis confirmed the bulk to exist as In(**13**)Cl, agreeing with solution state data. This compound was confirmed as air-stable over a 2 weeks period with no observable change in the ^{1}H NMR spectra when the sample was flushed with air.

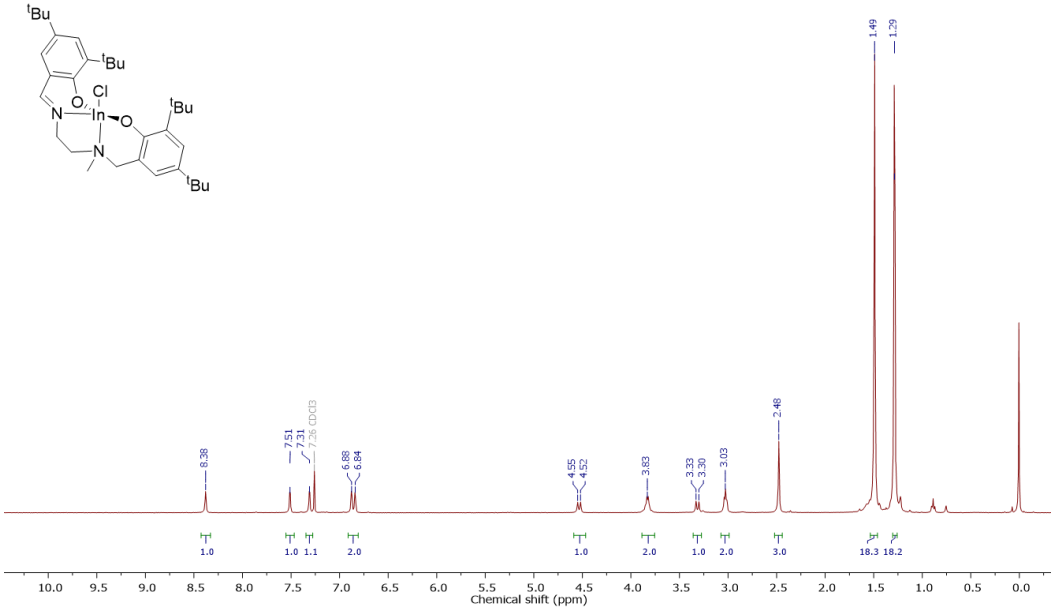

Figure 2.24. ^{1}H NMR spectra (400 MHz, 298 K) in $CDCl_3$ for In(**13**)Cl.

2.6. Polymerisation of *rac*-lactide with group 13 tetradentate complexes

To draw comparison in the activity of the synthesised novel group 13 complexes their applicability as initiators for the polymerisation of *rac*-lactide was tested. Due to the nature of chloride complexes, solution polymerisations consisted of the addition of triethylamine (NEt_3) alongside equivalent ratios of benzyl alcohol (BnOH) as a co-initiator. The addition of the NEt_3 is typical for In-Cl initiated polymerisations with notable mechanistic investigations unable to truly identify the exact role of the co-initiator.[60] All solution polymerisations were performed over a 24 hour period with variation of catalyst ratio as a means of exploring the relative activites.

2.6.1. Polymerisation with aluminium and gallium complexes

It was found that for Al/Ga complexes, both *meso*-bipyrrolidine or ethylenediamine ligands, showed no activity for *rac*-LA polymerisation under both solution conditions ($[LA]_0:[I]_0:[NEt_3]_0:[BnOH]_0$ = 100:1:1:1, $[LA]_0$ = 0.69 M, toluene, 80 °C, 120 h) as well as melt conditions ($[LA]_0:[I]_0:[NEt_3]_0:[BnOH]_0$ = 300:1:1:1, 130 °C, 24 h). Increasing the molar equivalents of co-initiators had little impact. Due to the sensitivity of gallium, a test reaction was carried out at a ratio of 25:1:1:1 over a period of 5 days to see if a small impurity in the recrystallised lactide was hindering initiation. This study showed no significant conversion. This lack of activity is not unexpected, it was shown that the –methyl substituted aluminium isopropoxide analogue of the bipyrrolidine ligand Al(**1**)O^{i}Pr, (Scheme 2.1) was poorly active, requiring 2 days under melt conditions to achieve moderate conversions (82%).[41] Whilst Al(**2**)Cl and the previously reported structure have analogous coordination spheres, the influence of the chloride group over the alkoxide can be shown to be significant. As evidenced from the solid-state analysis, the M–X bond length is notably small when M = Al and Ga, possibly crowding the coordination site of an incumbent lactide molecule. This could be enhanced by the trigonal bipyramidal structure shown in these complexes 'shielding' a possible point of coordination to the metal centre. This agrees with work by Carpentier and co-workers highlighting how a Al–Li 'BINAP' complex was inactive for ROP of LA compared to the indium and yttrium analogue.[78]

2.6.2. Polymerisation with indium salan complexes

Polymerisation studies using In(**2**)Cl and In(**10**)Cl showed moderate activity with a strong heterotactic bias (Entry 1 and 8, Table 2.4). The bipyrrolidine analogue proved more selective than the dimethylethylene diamine complex reaching P_r values as high as 0.82 (Figure 2.25). This selectivity bias is the same as is reported for Al^{3+} isopropoxide complexes previously reported but opposite of Zr^{4+} and Hf^{4+} analogues, increasing the serendipity in the work surrounding bipyrrolidine complexes.[41,42] With comparable activity to the group 4 catalysts, it is suggested that whilst there is a longer initiation period, the polymerisation rate is similar. The reactivity difference in comparison to other M(**2**)Cl complexes could be due to the difference in geometry with the square based pyramidal indium structures potentially providing a more 'open' coordination sphere for catalysis. In addition the larger In^{3+} nucleus is likely to better accommodate an incumbent LA molecule. A similar trend was seen by Carpentier and co-workers, with a higher reactivity and lower selectivity seen for fluorinated indium 'salen' complexes in comparison to the aluminium analogue.[57,79]

Table 2.4. Polymerisation data for indium salan complexes.

Entry	Initiator	Feed Ratio $[LA]_0:[I]_0:[BnOH]_0:[NEt_3]_0$	Conv. (%)[a]	M_n^{theo} (kg mol^{-1})[b]	M_n^{SEC} (kg mol^{-1})[c]	$Đ$ [c]	P_r[d]
1	In(**2**)Cl	100:1:1:1	95	13.8	17.6	1.01	0.82
2	In(**2**)Cl	100:1:1:0	60	9.9	9.6	1.08	0.79
3	In(**2**)Cl	300:1:1:1	95	41.1	34.3	1.07	0.80
4	In(**2**)Cl	300:1:1:0	30	13.1	13.9	1.02	0.84
5	In(**2**)Cl	900:1:1:1	86	111.6	77.9	1.07	0.80
6	In(**2**)Cl	900:1:1:0	42	54.6	10.2	1.08	0.82
7	In(**2**)I	300:1:1:1	48	20.8	21.7	1.08	0.67
8	In(**10**)Cl	100:1:1:1	95	13.8	10.4	1.10	0.73
9	In(**10**)Cl	100:1:1:0	34	5.0	9.6	1.13	0.72
10	In(**10**)Cl	300:1:1:1	95	41.1	45.9	1.16	0.71
11	In(**10**)Cl	900:1:1:1	76	98.7	79.1	1.13	0.70

Toluene, 80 °C, 24 h $[LA]_0$ = 0.69 M. [a] Conversion calculated from ^{1}H NMR spectra of the crude material by integration of the methane proton of the polymer and monomer, [b] {(Conv. × ($[LA]_0/[I]_0$) × 144.13) + Mw of end groups},[c] Determined from SEC in THF using triple detection methods, [d] Calculated from homo-nuclear decoupled ^{1}H NMR spectra of the purified polymer.

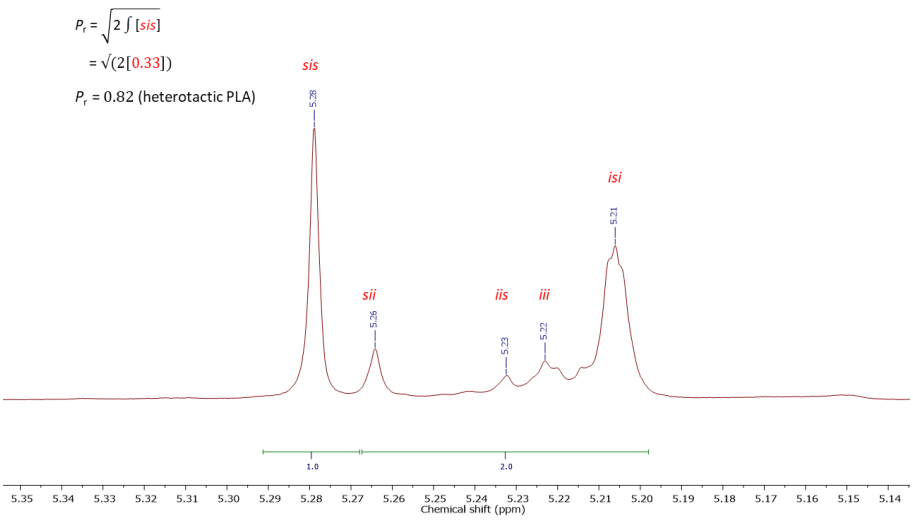

Figure 2.25. $^{1}H\{^{1}H\}$ NMR spectrum of the methine region of PLA formed using In(**2**)Cl at a feed ratio of 100:1:1:1 $\{[LA]_0:[I]_0:[BnOH]_0:[NEt_3]_0\}$ (Entry 1, Table 2.4).

This heterotactic behaviour is highly unusual in the field of indium catalysts, where only in the work of Tolman and co-workers using $InCl_3$ has heteroselective behaviour been seen.[59] In that study, the addition of NEt_3 was required to give enhanced rates, although no improvement in tacticity or molecular weight control was seen. This is in good agreement to experimental findings with In(**2**)Cl (Entry 3 – 6, Table 2.4). Good conversion seen after 24 h for both In(**2**)Cl and In(**10**)Cl at feeds ratios as low as 900:1:1:1 $\{[LA]_0:[I]_0:[NEt_3]_0:[BnOH]_0\}$. High molecular weight polymer was yielded with very little impact on the dispersity, molecular weight or tacticity of the polymer (Entry 5 and 11, Table 2.4). Due to the low boiling point of triethylamine (90 °C) melt ROP studies were not controllable with this additive, yielding lower conversions under these conditions.

In(**2**)I appeared significantly less active and selective than the analogous chloride complex (Entry 6 and 7, Table 2.4). The lower activity could be due to the larger size of the iodide blocking the coordination site of the incoming alcohol therefore hindering initiation. The lower selectivity suggests the catalytically active species might still interact with the halide group in some form, affecting the nature of propagation and supporting that an activated monomer mechanism is in effect. This is in agreement to studies by Mehrkhodavandi and co-workers, where the halide was shown to influence propagation by remaining coordinated to the 6-coordinate catalytically active species.[62] In this study the In–I bond was shown to increase reactivity in comparison to In–Cl analogue, the reverse to what is seen for In(**2**)Cl/I. All indium complexes tested were shown to given linear polymers (evidenced by a unimodal SEC traces) with a good fit of molecular weights to theoretically calculated values.

2.6.3. Polymerisation using other synthesised indium initiators

Preliminary studies using salalen indium chloride complexes In_2(**12**)$_2$OHCl and In(**13**)Cl showed a slower rate of polymerisation compared to In(**2**)Cl and In(**10**)Cl with 78% conversion achieved after 48 hours at a ratio of 600:1:1 {[LA]$_0$:[I]$_0$:[BnOH]$_0$:[NEt_3]$_0$} in toluene at 80 °C. Mild heteroselective behaviour (P_r = 0.69) was seen, closely comparable to the other tested salan initiators under these conditions. Due to low complexation yields and relatively slow rates this system was not taken for further investigation.

It has previously been shown that hydroxyl bound complexes generally lead to poor molecular weight control and broad dispersities. Melt polymerisations (130 °C, no solvent) with In_2(**2**)$_2$OEtOH, reached 66% after 4 hours at a ratio of 300:1 {[LA]$_0$:[I]$_0$}. SEC analysis showed a poor agreement between experimental and calculated molecular weights with a dispersity indicative of a poorly controlled polymerisation (M_n^{theo} = 28.6 kg mol^{-1}, M_n^{SEC} = 14.1 kg mol^{-1}, $Đ$ = 1.35). $^1H\{^1H\}$ NMR spectroscopy showed the polymer to be only mildly heterotactic (P_r = 0.55). {In(**10**)OH}$_2$ showed no activity for ROP with or without the addition of alcohol.

2.6.4. Further polymer analysis

MALDI-ToF (Matrix assisted laser desorption ionisation-time of flight) mass spectra were acquired to investigate the repeating unit, the end group as well as the level of transesterification present in the polymer samples. An experiment using In(**2**)Cl and two equivalents of benzyl alcohol with no triethylamine at feed ratios of 100:1:2 {[LA]$_0$:[I]$_0$:[BnOH]$_0$} in toluene at 80 °C produced a polymeric sample confirmed by SEC to be of the suitable mass range for analysis by MALDI-ToF (M_n^{SEC} = 5.3 kg mol^{-1}) (Figure 2.26).

The main series of peaks shows a good gaussian distribution of molecular weights with no substantial trailing of peaks, indicating a low dispersity of molecular weights in the sample. Using the m/z of each series obtained from MALDI-ToF the number of whole integer lactide units can be obtained by substituting the molecular mass of Na^+ as well as the expected benzyl alcohol (BnO–) and hydrogen end groups. Calculation indicates that a polymer with repeating units of 144 g mol^{-1} with both BnO– and MeO– end groups are present, in 98% abundance. A small degree of transesterification is present <1% abundance evidenced by peak spacing of 72 g mol^{-1}. Due to the very low quantity of transesterification in the sample

the polymerisation can be claimed to be very controlled with no evidence of major side reactions, an important point considering the potential alleviation of HCl from catalyst initiation.

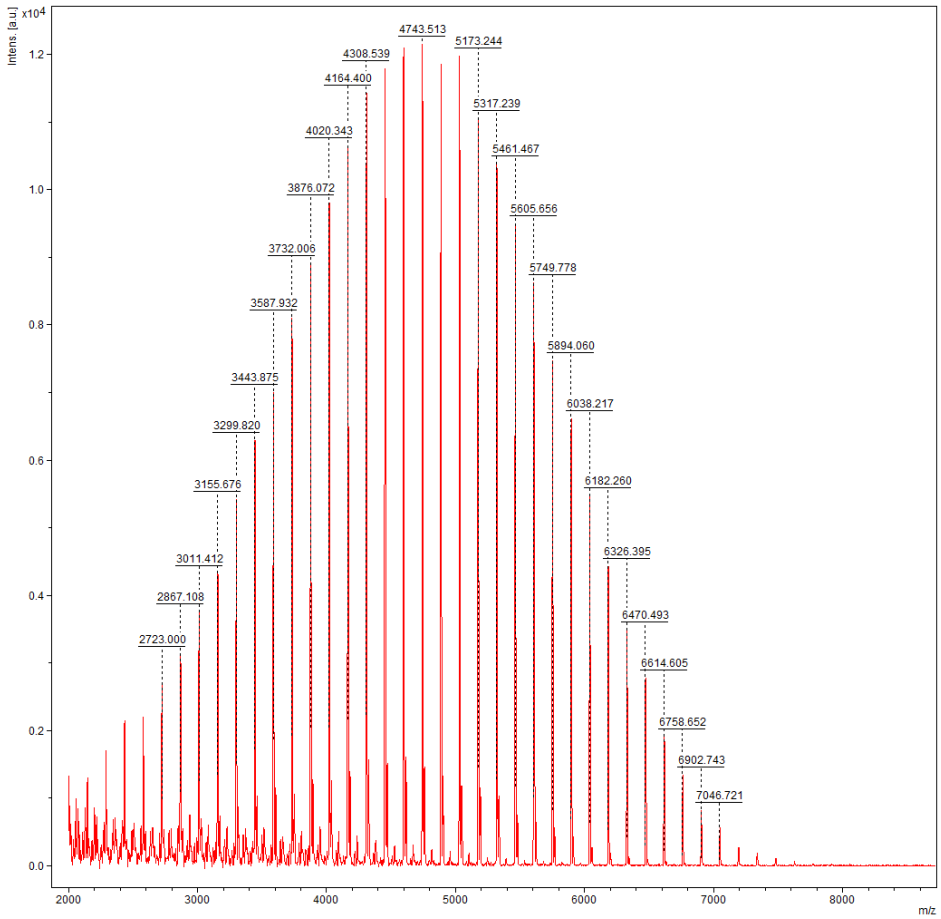

Figure 2.26. MALDI-ToF mass spectra of PLA formed at a 100:1:2 ratio {$[LA]_0$:$[I]_0$:$[BnOH]_0$} using In(**2**)Cl. Conversion = 70%, M_n^{theo} = 5.3 kg mol^{-1}, M_n^{SEC} = 5.1 kg mol^{-1}, $Đ$ = 1.10. Linear polymer is seen with repeating units of 144 g mol^{-1}.

2.7. Conclusions and future work

A range of novel group 13 complexes have been developed around a previously reported *meso*-bipyrrolidine ligand backbone, encompassing the first reported structures of indium and gallium salan complexes.[80] The choice of metal centre presented interesting structural deviations, with variations in Lewis acidity and ionic radii having a distinct effect on bond lengths and angles. Furthering this, an indium iodide complex showed how a halide with a more diffuse charge density, could alter the coordination sphere around the complex. Extending this structural comparison, dimethylethylene diamine analogues were synthesised with Al^{3+}, Ga^{3+} and In^{3+} providing structural insight into the impact of the pyrrolidine ring.

All observable group 13 complexes using the 'salan' microstructure thus far have contained the disubstituted $-^{t}$Bu functional group on the ligand. Attempts to alter the steric bulk on the side chains proved difficult with the production of an intractable mixture of products upon complexation, a result consistent with literature findings.[49,54,61] In contrast a 'salalen' architecture with low steric bulk yielded an isolatable compound, albeit with evidence of hydrolytic degradation. In a similar vein, attempts to isolate alkoxide complexes yielded structures bearing hydroxy bridging groups, further adding to literature reports on the difficulty in isolating indium alkoxide species.[68]

Indium halide complexes were active for the solution polymerisation of *rac*-LA in the presence of benzyl alcohol, producing highly heterotactic polymer. It was shown that upon addition of triethylamine the rates of polymerisation were significantly enhanced. Due to the addition of two different co-initiators, it is expected an induction period for catalyst activation occurs limiting rate, a regime which could be investigated further by kinetic experimentation. It was shown through SEC and MALDI-ToF analysis that polymerisations proceeded with excellent molecular weight control and negligible transesterification. No polymerisation activity was seen for aluminium or gallium complexes, possibly due to structural variations, with the adoption of a trigonal bipyramidal geometry. This inactivity could also be the result electronic effects with the increase in Lewis acidity, shortening the M–X bond and thus reducing the lability of this bond to activation.[10]

It has previously been demonstrated it is possible to isolate a structure for a coordinated benzyl alcohol-$InCl_3$-(deap)H microstructure, a possible intermediate in the production of an active catalyst for lactide polymerisation. To ascertain the mechanism of the catalytically

active species the isolation of a coordinated complex of BnOH–In(**2**)Cl–NEt_3 could be attempted. A study published by Tolman and co-workers, the production of an encapsulated amine salt could assist in the crystallisation of the complex.[60] Potential variation of the amine bases could provide structural information regarding the potential role of the base during polymerisation.

Through the testing of a variety of conditions for the production of dimeric alkoxides, promising results were obtained as evidenced by ^{1}H NMR spectra, for the synthesis of a monomeric indium *tert*-butoxide complex. The large steric bulk of the *tert*-butoxide is thought to provide a more stable coordination sphere, providing a degree of protection from adventitious water.[53] Optimisation of this process could provide the complex in greater yields to facilitate an extension of studies into this area. The reaction of indium complexes with a silver tetrafluoroborate via a salt metathesis reaction could be used to produce an active ionic salt which could be used for polymerisation (Scheme 2.9). The use of a non-coordinating counter ion that could produce a highly active indium species *in situ,* would avoid issues with the production of dimeric indium hydroxyl compounds.

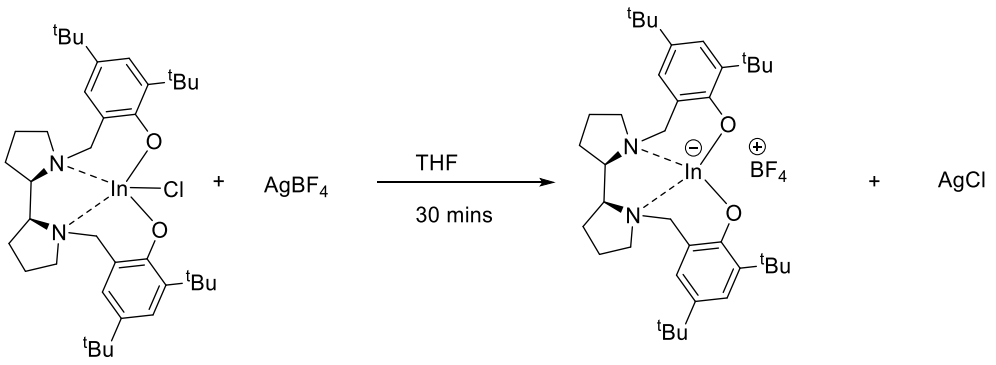

Scheme 2.9. Proposed scheme for the production of an indium-borate salt from In(**2**)Cl

Initial work on the production of these species has shown clear production of silver(I) chloride as a precipitate in addition to notable shifts in proton resonances. Whilst this preliminary work was met with difficulty in isolation and purification, optimisation of the work-up procedure could afford a system active for ROP which has been overlooked by many in the field. Depending on the reactivity and potential issue of transesterification from cationic species in solution, an increase in the steric bulk around the counter ion could produce a more labile system with little interference in the catalyst propagation. The use of BPh_4^+ as a weaker albeit bulkier borate counter ion could prove a solution if this is the case,

whilst also reinforcing work carried out in this study on the influence of coordinating groups on structure and reactivity.

Whilst this work has focused on the developing catalysts for the ROP of *rac*-LA, exploiting these systems for other catalytic reactions should be a priority for future studies. One such exploit could be the use of indium chloride complexes in cyclic carbonate/polycarbonate formation from the stoichiometric reaction of CO_2 with an epoxide (Scheme 2.10). Whilst aluminium chloride initiators have been extensively investigated for this process, little work has been done using indium complexes.[81,82] Initial investigation with propylene oxide using In(**2**)Cl in the presence of tetrabutylammonium bromide (TBAB), yielded propylene carbonate in high conversions (85%) under ambient conditions with catalyst loadings as low as 0.1 mol % after 24 hours. This finding surpasses many industrially optimised complexes known in the literature which are efficient only under elevated conditions of temperature and pressure.[83,84] Using an indium phosphasalen system (**25**), previously tested for the ROP of *rac*-LA, Williams and co-workers showed ring-opening copolymerisation (ROCOP) behaviour with CO_2 and epoxides.[82] This reverse in cyclic carbonate/polycarbonate selectivity between the two indium systems urges further investigation. The ability to carry out highly productive cyclic carbonate formation under ambient conditions presents an interesting industrial prospect, reducing energy costs associated with CCU as well as increasing throughput of this potentially 100% renewable chemical.

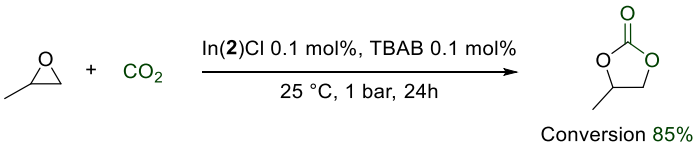

Scheme 2.10. Production of propylene carbonate from propylene oxide using In(**2**)Cl and tetrabutyl ammonium bromide (TBAB) at a loading of 0.1 mol%.

2.8. References

1 A. Routaray, N. Nath, T. Maharana and A. K. Sutar, *Catal. Sci. Technol.*, 2015, 1–68.

2 M. J. Stanford and A. P. Dove, *Chem. Soc. Rev.*, 2010, **39**, 486–494.

3 A. Pilone, K. Press, I. Goldberg, M. Kol, M. Mazzeo and M. Lamberti, *J. Am. Chem. Soc.*, 2014, **136**, 2940–2943.

4 X. Zhang, M. Fevre, G. O. Jones and R. M. Waymouth, *Chem. Rev.*, 2018, **118**, 839–885.

5 M. Anker, C. Balasanthiran, V. Balasanthiran, M. H. Chisholm, S. Jayaraj, K. Mathieu, P. Piromjitpong, S. Praban, B. Raya, W. J. Simonsick, J. L. Hedrick and E. J. Shin, *Dalton. Trans.*, 2017, **192**, 2051–2057.

6 S. Gesslbauer, H. Cheek, A. J. P. White and C. Romain, *Dalton. Trans.*, 2018, **47**, 10410–10414.

7 K. M. Osten and P. Mehrkhodavandi, *Acc. Chem. Res.*, 2017, **50**, 2861–2869.

8 T. E. Graedel, E. M. Harper, N. T. Nassar, P. Nuss and B. K. Reck, *Proc. Natl. Acad. Sci.*, 2015, **119**, 4257–4262.

9 G. Schnee, A. Bolley, F. Hild, D. Specklin and S. Dagorne, *Catal. Today*, 2017, **289**, 204–210.

10 A. B. Kremer, R. J. Andrews, M. J. Milner, X. R. Zhang, T. Ebrahimi, B. O. Patrick, P. L. Diaconescu and P. Mehrkhodavandi, *Inorg. Chem.*, 2017, **56**, 1375–1385.

11 N. Maudoux, E. Tan, Y. Hu, T. Roisnel, V. Dorcet, J. F. Carpentier and Y. Sarazin, *Main Gr. Met. Chem.*, 2016, **39**, 131–143.

12 H. E. Dyer, S. Huijser, N. Susperregui, F. Bonnet, A. D. Schwarz, R. Duchateau, L. Maron and P. Mountford, *Organometallics*, 2010, **29**, 3602–3621.

13 P. Dubois, C. Jacobs, R. Jérôme and P. Teyssté, *Macromolecules*, 1991, **24**, 2266–2270.

14 A. Kowalski, A. Duda and S. Penczek, *Macromolecules*, 1998, **31**, 2114–2122.

15 R. Jianming, X. Anguo, W. Hongwei and Y. Hailin, *Des. Monomers Polym.*, 2014, **17**, 345–355.

16 R. H. Platel, L. M. Hodgson and C. K. Williams, *Polym. Rev.*, 2008, **48**, 11–63.

17 A. Tiwari and S. Titinchi, *Advanced Catalytic Materials*, Wiley, 2015.

18 D. Atwood and M. J. Harvey, *Chem. Rev.*, 2001, **101**, 37–52.

19 Y. Wei, S. Wang and S. Zhou, *Dalton. Trans.*, 2016, **45**, 4471–4485.

20 M. Wisniewski, A. Le Borgne and N. Spassky, *Macromol. Chem. Phys.*, 1997, **198**, 1227–1238.

21 T. M. Ovitt and G. W. Coates, *J. Am. Chem. Soc.*, 1999, **121**, 4072–4073.

22 T. M. Ovitt and G. W. Coates, *J. Polym. Sci. Part A Polym. Chem.*, 2000, **38**, 4686–4692.

23 Z. Zhong, P. J. Dijkstra and J. Feijen, *Communications*, 2002, **98**, 4510–4513.

24 Z. Zhong, P. J. Dijkstra and J. Feijen, *J. Am. Chem. Soc.*, 2003, **125**, 11291–11298.

25 N. Nomura, R. Ishii, M. Akakura and K. Aoi, *J. Am. Chem. Soc.*, 2002, **124**, 5938–5939.

26 D. Chandanabodhi and T. Nanok, *Mol. Catal.*, 2017, **436**, 145–156.

27 I. Van Der Meulen, E. Gubbels, S. Huijser, R. Sablong, C. E. Koning, A. Heise and R. Duchateau, *Macromolecules*, 2011, **44**, 4301–4305.

28 N. Nomura, R. Ishii, Y. Yamamoto and T. Kondo, *Chem. - A Eur. J.*, 2007, **13**, 4433–4451.

29 H. L. Chen, S. Dutta, P. Y. Huang and C. C. Lin, *Organometallics*, 2012, **31**, 2016–2025.

30 P. Hormnirun, E. L. Marshall, V. C. Gibson, R. I. Pugh and A. J. P. White, *Proc. Natl. Acad. Sci. U. S. A.*, 2006, **103**, 15343–15348.

31 E. L. Whitelaw, G. Loraine, M. F. Mahon and M. D. Jones, *Dalton. Trans.*, 2011, **40**, 11469–11473.

32 S. L. Hancock, M. D. Jones and M. F. Mahon, *Dalton. Trans.*, 2013, **42**, 9279.

33 A. Pilone, N. De Maio, K. Press, V. Venditto, D. Pappalardo, M. Mazzeo, C. Pellecchia, M. Kol and M. Lamberti, *Dalton. Trans.*, 2015, **44**, 2157–2165.

34 P. McKeown, M. G. Davidson, J. P. Lowe, M. F. Mahon, L. H. Thomas, T. J. Woodman and M. D. Jones, *Dalton. Trans.*, 2016, **45**, 5374–5387.

35 I. D. S. Vieira, E. L. Whitelaw, M. D. Jones and S. Herres-Pawlis, *Chem. - A Eur. J.*, 2013, **19**, 4712–4716.

36 P. McKeown, J. Brown-Humes, M. G. Davidson, M. F. Mahon, T. J. Woodman and M. D. Jones, *Dalton. Trans.*, 2017, **46**, 5048–5057.

37 P. Hormnirun, E. L. Marshall, V. C. Gibson, a. J. P. White and D. J. Williams, *J. Am. Chem. Soc.*, 2004, **126**, 2688–2689.

38 M. Mandal, D. Chakraborty and V. Ramkumar, *RSC Adv.*, 2015, **5**, 28536–28553.

39 S. Segal, A. Yeori, M. Shuster, Y. Rosenberg and M. Kol, *Macromolecules*, 2008, **41**, 1612–1617.

40 H. Du, A. H. Velders, P. J. Dijkstra, J. Sun, Z. Zhong, X. Chen and J. Feijen, *Chem. - A Eur. J.*, 2009, **15**, 9836–9845.

41 M. D. Jones, L. Brady, P. McKeown, A. Buchard, P. M. Schäfer, L. H. Thomas, M. F. Mahon, T. J. Woodman and J. P. Lowe, *Chem. Sci.*, 2015, **6**, 5034–5039.

42 M. D. Jones, S. L. Hancock, P. McKeown, P. M. Schafer, A. Buchard, L. H. Thomas, M. F. Mahon and J. P. Lowe, *Chem. Commun.*, 2014, **50**, 15967–15970.

43 T. Rosen, I. Goldberg, W. Navarra, V. Venditto and M. Kol, *Chem. Sci.*, 2017, **8**, 5476–5481.

44 T. Rosen, I. Goldberg, V. Venditto and M. Kol, *J. Am. Chem. Soc.*, 2016, **138**, 12041–12044.

45 S. Ghosh, R. R. Gowda, R. Jagan and D. Chakraborty, *Dalton Trans.*, 2015, **44**, 10410–22.

46 C. Bakewell, A. J. P. White, N. J. Long and C. K. Williams, *Inorg. Chem.*, 2013, **52**, 12561–12567.

47 M. Van Aelstyn, T. S. Keizer, D. L. Klopotek, S. Liu, P. Wei and D. Atwood, 2000, 1796–1801.

48 A. Aprile, D. D. J. Wilson and A. F. Richards, *Dalton. Trans.*, 2012, **41**, 8550.

49 S. Dagorne, M. Normand, E. Kirillov and J. F. Carpentier, *Coord. Chem. Rev.*, 2013, **257**, 1869–1886.

50 P. Horeglad, M. Cybularczyk, B. Trzaskowski, G. Z. Zukowska, M. Dranka and J. Zachara, *Organometallics*, 2015, **34**, 3480–3496.

51 A. Elschenbroich, C.; Salzer, *Organometallics: A concise introduction, 2nd ed.*, VCH Publishers, Weinheim, Germany, second., 1989.

52 A. Hazari, L. Kanta Das, R. M. Kadam, A. Bauzá, A. Frontera and A. Ghosh, *Dalton. Trans.*, 2015, **44**, 3862–3876.

53 D. C. Aluthge, J. M. Ahn and P. Mehrkhodavandi, *Chem. Sci.*, 2015, **6**, 5284–5292.

54 D. C. Aluthge, E. X. Yan, J. M. Ahn and P. Mehrkhodavandi, *Inorg. Chem.*, 2014, **53**, 6828–6836.

55 S. M. Guillaume and J.-F. Carpentier, *Catal. Sci. Technol.*, 2012, **2**, 898.

56 M. Normand, V. Dorcet and E. Kirillov, *Organometallics*, 2013, **32**, 1694–1709.

57 M. Normand, E. Kirillov, T. Roisnel and J. F. Carpentier, *Organometallics*, 2012, **31**, 1448–1457.

58 N. Maudoux, T. Roisnel, V. Dorcet, J. F. Carpentier and Y. Sarazin, *Chem. - A Eur. J.*, 2014, **20**, 6131–6147.

59 A. Pietrangelo, M. A. Hillmyer and W. B. Tolman, *Chem. Commun.*, 2009, 2736–7.

60 A. Pietrangelo, S. C. Knight, A. K. Gupta, L. J. Yao, M. A. Hillmyer and W. B. Tolman, *J. Am. Chem. Soc.*, 2010, **132**, 11649–11657.

61 A. F. Douglas, B. O. Patrick and P. Mehrkhodavandi, *Angew. Chemie - Int. Ed.*, 2008, **47**, 2290–2293.

62 I. Yu, A. Acosta-Ramírez and P. Mehrkhodavandi, *J. Am. Chem. Soc.*, 2012, **134**, 12758–12773.

63 L.-E. Chile, T. Ebrahimi, A. Wong, D. C. Aluthge, S. G. Hatzikiriakos and P. Mehrkhodavandi, *Dalton. Trans.*, 2017, **46**, 6723–6733.

64 T. M. Ovitt and G. W. Coates, *J. Am. Chem. Soc.*, 2002, **124**, 1316–1326.

65 M. H. Chisholm, J. C. Gallucci, K. T. Quisenberry and Z. Zhou, *Inorg. Chem.*, 2008, **47**, 2613–2624.

66 D. C. Aluthge, B. O. Patrick and P. Mehrkhodavandi, *Chem. Commun.*, 2013, 4295–4297.

67 S. M. Quan and P. L. Diaconescu, *Chem. Commun.*, 2015, **51**, 9643–9646.

68 T. Ebrahimi, D. C. Aluthge, B. O. Patrick, S. G. Hatzikiriakos and P. Mehrkhodavandi,

ACS Catal., 2017, **7**, 6413–6418.

69 D. Myers, A. J. P. White, C. M. Forsyth, M. Bown and C. K. Williams, *Angew. Chemie - Int. Ed.*, 2017, **56**, 5277–5282.

70 R. Mayilmurugan, P. Traar, J. a. Schachner, M. Volpe and N. C. Mösch-Zanetti, *Eur. J. Inorg. Chem.*, 2013, **2**, 3664–3670.

71 E. Sergeeva, J. Kopilov, I. Goldberg and M. Kol, *Chem. Commun.*, 2009, 3053–3055.

72 H.-C. Tseng, M. Y. Chiang, W.-Y. Lu, Y.-J. Chen, C.-J. Lian, Y.-H. Chen, H.-Y. Tsai, Y.-C. Lai and H.-Y. Chen, *Dalton Trans.*, 2015, **44**, 11763–73.

73 K. Fagnou and M. Lautens, *Angew. Chemie Int. Ed. English*, 2002, **41**, 26–47.

74 J. Beament, M. F. Mahon, A. Buchard and M. D. Jones, *New J. Chem.*, 2017, **41**, 2198–2203.

75 D. A. Atwood, A. R. Hutchison and Y. Zhang, in *Structure and Bonding*, Springer Berlin Heidelberg, 105th edn., 2003, vol. 105, pp. 168–201.

76 M. a. Munoz-Hernandez, T. S. Keizer, P. Wei, S. Parkin and D. a. Atwood, *Inorg. Chem.*, 2001, **40**, 6782–6787.

77 C. Bakewell, T. Cao, X. F. Le Goff, N. J. Long, A. Auffrant and C. K. Williams, *Organometallics*, 2013, **2**, 1–15.

78 N. Maudoux, T. Roisnel, J. F. Carpentier and Y. Sarazin, *Organometallics*, 2014, **33**, 5740–5748.

79 M. Bouyahyi, E. Grunova, N. Marquet, E. Kirillov, C. M. Thomas, T. Roisnel and J. F. Carpentier, *Organometallics*, 2008, **27**, 5815–5825.

80 J. Beament, M. F. Mahon, A. Buchard and M. D. Jones, *New J. Chem.*, 2017, **41**, 2198–2203.

81 J. Cornil, L. Gonnard, A. Guérinot, S. Reymond and J. Cossy, *European J. Org. Chem.*, 2014, **2014**, 4958–4962.

82 A. Thevenon, A. Cyriac, D. Myers, A. J. P. White, C. B. Durr and C. K. Williams, *J. Am. Chem. Soc.*, 2018, **140**, 6893–6903.

83 I. S. Metcalfe, M. North and P. Villuendas, *J. CO2 Util.*, 2013, **2**, 24–28.

84 M. North and C. Young, *ChemSusChem*, 2011, **4**, 1685–1693.

Chapter 3

Lanthanide Bipyrrolidine Complexes for Ring Opening Polymerisation

Relating Publication

Dalton Transactions

PAPER

View Article Online
View Journal | View Issue

Cite this: *Dalton Trans.*, 2018, **47**, 9164

Bipyrrolidine salan alkoxide complexes of lanthanides: synthesis, characterisation, activity in the polymerisation of lactide and mechanistic investigation by DOSY NMR†

James Beament,[a] Gabriele Kociok-Köhn,[b] Matthew D. Jones *[a] and Antoine Buchard *[a]

Received 23rd May 2018,
Accepted 18th June 2018

DOI: 10.1039/c8dt02108b

rsc.li/dalton

Four dimeric lanthanide alkoxide complexes bearing ONNO bipyrrolidine salan ligands ($L^{Me}H_2$/$L^{tBu}H_2$) have been prepared with Nd, Sm and Yb. Depending on the metal and substituents, these complexes adopt varying coordination geometries. While investigating the hydrolytic degradation of these complexes, three dimeric mixed alkoxide/hydroxide and bis-hydroxide products were also prepared, isolated and characterised. Despite paramagnetism, ^{1}H NMR and diffusion ordered spectroscopy (DOSY) allowed additional characterisation alongside elemental and single-crystal X-ray diffraction analyses. These systems were very active for the controlled ring-opening polymerisation (ROP) of *rac*-lactide (LA), under industrially relevant melt conditions and in solution, yielding complete conversion within 5 minutes at [Ln] : [LA] ratios of up to 3000 : 1 in toluene, and at 80 °C, whilst retaining low dispersities ($Đ$ = 1.1). ^{1}H DOSY NMR spectroscopy was employed to monitor polymer growth from the metal centres *in situ*, and revealed a dinuclear catalytically active species.

Introduction

With the dependence on fossil fuel resources and the environmental persistence of most commodity polymers, our societal reliance on plastics is now unanimously viewed as unsustainable.[1] Supported by public opinion, this has triggered a concerted research effort between academia and industry towards the development of sustainable alternatives from renewable resources.[2–5] Polylactide (PLA), a thermoplastic aliphatic polyester derived from lactic acid, is arguably one of the most widely studied degradable and renewable polymers. PLA is commercially available for packaging and fibre applications,[6] and prepared through a solvent-free ring-opening polymerisation (ROP) of lactide (LA). LA can be utilised as either the enantiomerically pure L-LA, or as a racemic mixture of D and L monomers (*rac*-LA), the latter allowing atactic, heterotactic or isotactic microstructures. This is important as the physical properties of the polymer are intrinsically linked to the polymer microstructure, with atactic and heterotactic PLA being amorphous, and heterotactic PLA having a slightly lower T_g (~50 *vs.* 45 °C).[7,8] Isotactic PLA is the most sought after structure as it can form a crystalline stereocomplex with a melting temperature (T_m = 230 °C) enhanced compared to individual crystalline PLLA or PDLA (T_m = 180 °C).[8] Over the past decades, the drive to achieve isotactic PLA from *rac*-LA, for applications requiring enhanced thermal and mechanical properties, prompted the development of a wide range of organocatalysts and metal complexes for the controlled and stereoselective ROP of lactide.[2,7,9–11] Indeed, many studies have shown that the PLA microstructure can be controlled by the judicious choice of metal centre and ligand(s). However, despite much effort, including some computational studies,[12–15] challenges still remain to fully understand the interplay between metal, ligand, monomer and the growing polymer chain. There remains a high degree of serendipity in the stereochemical outcome of the polymerisation, with unpredictable tacticities achieved from metal–ligand combinations.

It is noteworthy that while subtle changes in ligands have been extensively shown to induce a change in stereoselectivity,[16–20] systematic studies across a range of metals (period or series) are less common. Several examples have however shown that the metal can significantly influence

[a]*Department of Chemistry, University of Bath, Claverton Down, Bath BA2 7AY, UK. E-mail: a.buchard@bath.ac.uk, mj205@bath.ac.uk; Tel: +44 (0)1225 386122*
[b]*Chemical Characterisation and Analysis Facility (CCAF), University of Bath, UK*

†Electronic supplementary information (ESI) available: ^{1}H and ^{13}C{^{1}H} NMR spectra of [L^{Me}Sm(OiPr)$_2$] and [L^{Me}Sm(OH)$_2$]; single-crystal X-ray diffraction data of all complexes; polymerisation kinetic data; DOSY NMR data; plots of M_n and $Đ$ *vs.* conversion; SEC traces and MALDI-ToF mass spectra of polymers. CCDC 1844088–1844094. For ESI and crystallographic data in CIF or other electronic format see DOI: 10.1039/c8dt02108b

3. Lanthanide Bipyrrolidine Complexes for Ring Opening Polymerisation

3.1. Introduction

The influence of the metal centre on the coordination and selectivity of Group 4 and Group 13 complexes bearing the bipyrrolidine backbone has shown to be imperative, imparting contrasting stereo-selective bias.[1–3] In order to fully investigate this trend and understand the nature of the catalytically active species bearing this promising ligand, a systematic study of lanthanide metal centres was performed. Using the well reported ROP of *rac*-LA as a model system, a comparison into the activity of complexes can be carried out. Extending the best candidates towards the polymerisation of other bio-sourced monomers can provide a route to delivering alternative renewable polymers.

The lanthanide (Ln) series possess some of the most active and selective catalysts for ROP in the literature and have attracted substantial attention, highlighted in a number of extensive reviews.[4–7] From a catalyst design perspective, some of the most consistent trends have been shown with the Ln^{3+} series, with work highlighting the impact of ionic radii on the rates and selectivities for lactide polymerisation.[7,8] The lanthanide contraction is a phenomenon leading to a larger than expected reduction in ionic radii along the periodic series to the point where the radii of Lu^{3+} is smaller than that of Y^{3+}.[9–11] This has been shown to increase charge density and Lewis acidity leading to increased polymerisation rates.[8,12] Group 3 metals yttrium and scandium are sometimes discussed alongside lanthanides due to similarities in electronic characteristics and behaviour.[5] Herein this work summarises some of the key scientific findings in lanthanide chemistry applied to the polymerisation of LA. With noteworthy exceptions, this work focuses on the adoption of tetradentate ligand structures, posing a comparison to the bis(phenolate) bipyrrolidine ligand, discussed previously.

3.1.1. Tripodal bis(phenolate) Ln^{3+} complexes

Early work in evaluating the impact of Ln^{3+} size and ancillary ligand effect was carried out in a high throughput screening study by Kerton *et al.,* using a tripodal bisphenolate ligand system.[12] This work observed three basic trends:

1) The steric demand of the ligand has a significant impact on the rate and stereo-control of the polymerisation process.
2) The nature of the donor ligand and initiating nucleophile proved crucial.

3) Yttrium and other mid-sized rare-earth complexes showed the highest rates in comparison to the larger atomic radii of lanthanum and praseodymium.

In the last decade, these conclusions have most notably been investigated by Carpentier and co-workers, who have carried out extensive work on tripodal tetradentate or 'heteroscorpinate' lanthanide systems.[7,13–18] This work encompasses a large variation of ligand substituents, metal centres, weakly coordinating nucleophiles and solvents (Figure 3.1). In agreement with the high-throughput screening work carried out Kerton *et al.,* it was shown that the bulkier the substituents on the -*ortho* position the more selective and reactive the complex was for ROP.[12] The use of –trityl (–CPh_3) groups was shown to give exceptionally high heteroselectivities (P_r = 0.96) and very high rates, with complete conversion within a minute at ratios of 400:1:40 ($[LA]_0$:$[I]_0$:$[^iPrOH]_0$) at room temperature. In contrast to group 13 work, decreasing the steric bulk was associated with slower rates.[15] This is explained due to the likelihood for dimerisation and aggregation of species.

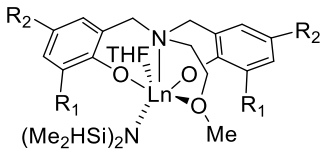

26 Ln = Y R_2 = ^{t}Bu R_1 = CPh_3

27 Ln = Y R_2 = ^{t}Bu R_1 = Me

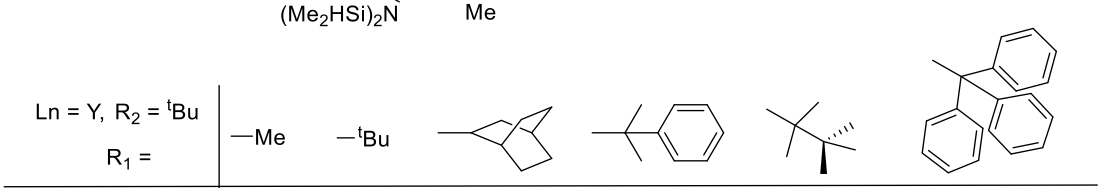

Ln = Y, R_2 = ^{t}Bu; R_1 =	—Me	—^{t}Bu				
P_r	0.56	0.80	0.82	0.91	0.95	0.96

R_1 = R_2 = ^{t}Bu; Ln =	La (1.15 Å)	Nd (1.12 Å)	Y (1.04 Å)
P_r	0.60	0.65	0.91

Figure 3.1 Tripodal 'ONOO' bis(phenolate) lanthanide(III) complexes presented by Carpentier and co-workers.[15,16]

Changing the metal centre, hence ionic radii, played an important role in improving stereo-selectivity, with smaller lanthanides leading to an increased hetero-selective preference. These catalysts were also shown to be very active for the ROP of other lactones and carbonates including ε-caprolactone (ε-CL), β-malolactonates and the challenging five membered cyclohexene carbonate.[19] Significantly, in recent ROP chemistry, the polymerisation of the 5 membered γ-butyrolactone was realised using Y^{3+}-tripodal complexes.[20] Famed by Carothers for its inactivity towards ROP,[21] this lanthanide system

represents one of only a small handful of complexes proven capable of delivering high molecular polymer from this difficult monomer.[20,22]

Lanthanide alkoxide complexes are not common.[7,23,24] This issue stems from the tendency of highly oxophilic rare-earth elements to generate oxo species which aggregate or collapse as multinuclear clusters.[7,17,23,25,26] It is for this reason that the majority of Ln^{3+} complexes in the literature employed for ROP are supported by labile coordinating ligands such as amido, borohydride or solvent molecules.[16,27–29] Work by the Mountford, Carpentier and Vissueaux groups have shown the activity of borohydride Ln complexes for the polymerisation of a variety of different monomers. Without the need for exogenous alcohol these systems have been versatile, polymerising isoprene, methylmethacrylate and ε-caprolactone.[30–32] It was reported by Bonnet *et al.,* that these borohydride or amido complexes were highly active for the ROP of LA (Figure 3.2).[33] However, poor molecular control is reported and explained as a result of poor initiation and transesterification caused by the unusual $–BH_4$ initiating groups. *In-situ* addition of large excesses of alcohol co-initiator alleviate this concern, breaking up aggregated clusters as well as moving the equilibrium position for monomer initiation towards the activated alkoxide complex leading to 'immortal' polymerisation behaviour.[16,18,23]

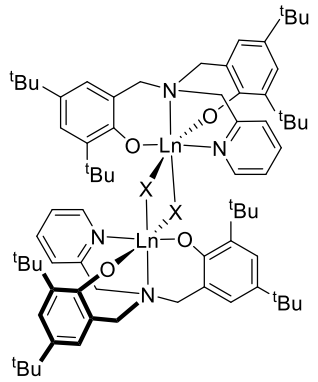

28 Ln = La **a)** X = BH_4
29 Ln = Y **b)** X = Cl
30 Ln = Sm

Figure 3.27. Dinuclear rare-earth(III) tripodal bisphenolate complexes bearing $–BH_4$ or –Cl bridging ligands employed for the ROP of LA.[34]

Zhao *et al.,* showed how altering the nature of exogenous alcohol could be used to make gradient block star-copolymers of LA when initiated with a lutetium tripodal (bis)phenolate complex (**31**) (Figure 3.3).[35,36] Due to the fast transfer between the primary alcohol and the lutetium alkoxide this living chain transfer polymerisation achieved turnover frequencies up to 10 000 h^{-1}.[35] Exceptionally high heterotactic PLA (P_r = 0.99) with excellent molecular weight control were also achieved at ratios of 500:1:5 {$[LA]_0$:$[I]_0$:$[CTA]_0$}, with 92% conversion seen after 60 minutes (THF, 25 °C).

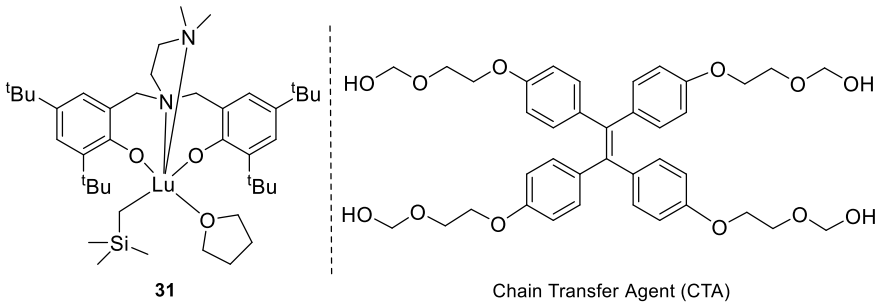

Figure 3.3. A silyl coordinated lutetium complex reported by Zhao et al.[36] Addition of a mono-, di- or tetra substituted alkoxy group lead to well controlled star polymers.[35]

When the reaction mixture was sequentially coupled with addition of an isotactic directing aluminium 'salen' complex a sequential heterotactic-isotactic block copolymer was synthesised.[36] Additionally, polymers designed with acetal groups have shown to improve the degradative properties, an important consideration for biomedical applications. **31** was also shown to be highly versatile; showing good control for the ROP of ε-caprolactone (ε-CL) and functionalised β-butyrolactones, providing an opportunity for post polymerisation modification.

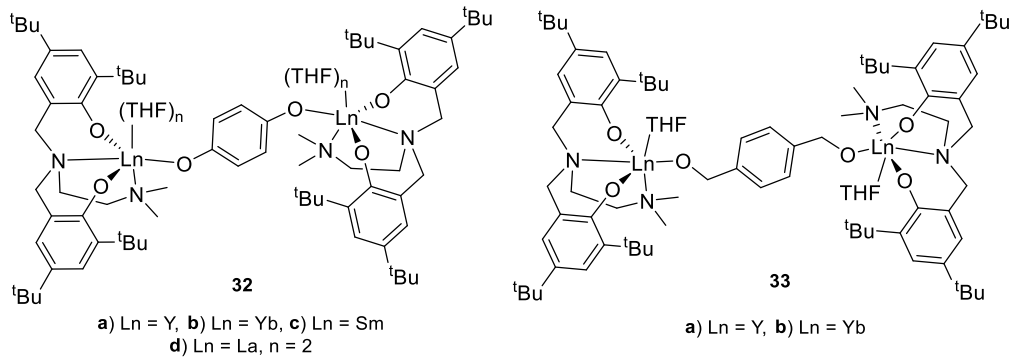

Figure 3.4. Dinuclear aryloxide Ln^{3+} complexes reported by Shen and co-workers.[37]

In a similar fashion, Shen and co-workers isolated aryloxide dinuclear complexes by reaction of the THF coordinated bisphenolate complex with bi-functional aryl-alcohols (Figure 3.4).[37] When applied to the ROP of *rac*-LA exceptionally high heterotactic polymer was prepared (P_r = 0.99) when using **32a-b** and **33a-b** as initiator. A mild drop in selectivity (P_r = 0.81 – 0.93) was observed when the larger metal ions of **32c-d** were tested. This drop in selectivity is compensated by an increase in rate, with **32d** capable of yielding complete conversion of *rac*-LA in 30 minutes at feed ratios of 2000:1 $\{[LA]_0[I]_0\}$ in THF at 25 °C. The different aryloxide groups were shown to have no effect on the activity of the complex with good agreement between calculated and observed molecular weights suggesting a linear growth on both sides of the alcohol initiator.

3.1.2. Salen, Salalen and Salan Ln^{3+} complexes

Like tripodal ligands bearing larger Ln^{3+} metals, linear salen, salalen and salan Ln^{3+} structures are isolated as multinuclear clusters making the catalytically active species difficult to study and control.[38–42] In order to yield di- or mononuclear complexes of these species Y^{3+} is often used as the central metal ion. Whilst arguably not a true lanthanide ion due to unoccupied 4*f*-orbitals, the comparable size of yttrium to the much heavier Lu^{3+} means it is often reported alongside other Ln^{3+} complexes. This small size leads to a reduced coordination sphere, reducing the prevalence of dimerisation (Figure 3.5).[43–47] In comparison to analogous dinuclear species it is reported that these mononuclear structures are faster ROP initiators due to a reduced initiation period.[42,47]

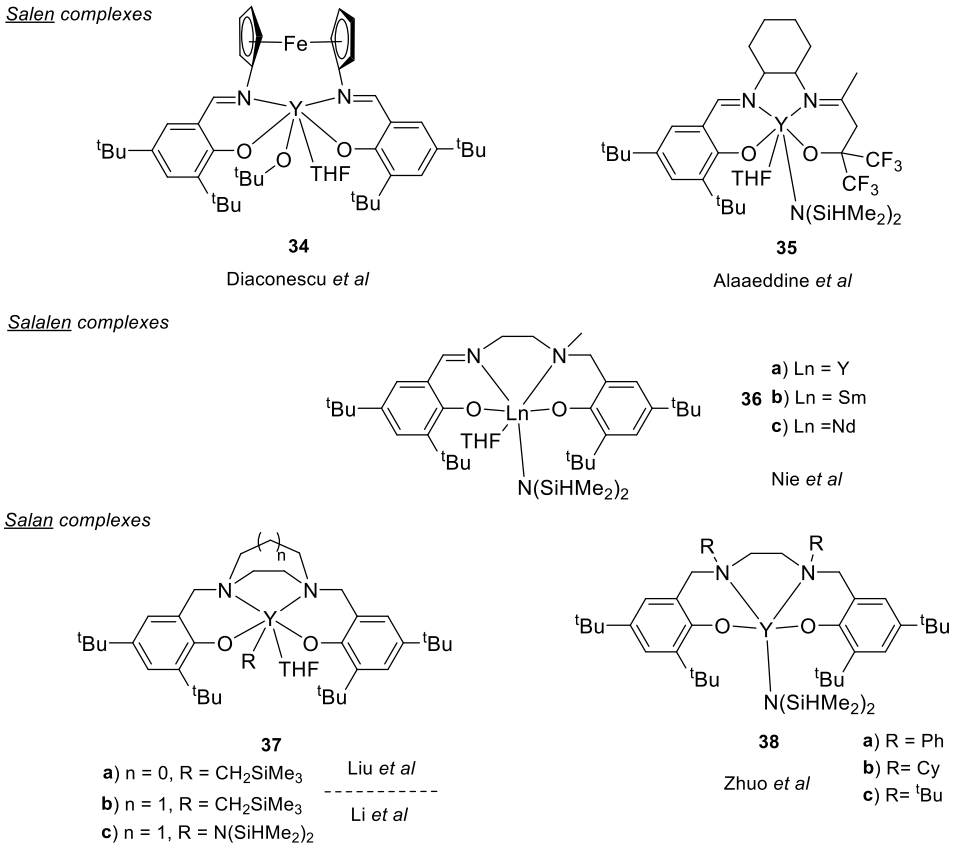

Figure 3.5. Example mononuclear bis(phenolate) lanthanide complexes bearing 'salen', 'salalen' or 'salan' ligand backbones employed for ROP.[42–48]

Unlike tripodal Ln systems, the same degree of monomer selectivity has not been realised for these linear 'ONNO' bisphenolate complexes applied to LA ROP. The most pronounced heterotacticites (P_r = 0.85) were achieved from the 'salalen' complex, **36a**.[42] The balance of selectivity and activity commonly discussed from the adoption of Ln^{3+} *vs* Group 13 metal complexes, is highlighted in **35** and the reported Al complex.[45] Whilst being significantly more

active, **35** only yielded atactic PLA whereas the Al analogue produced isotactically enriched polymer. For 'salan' Ln^{3+} complexes, changing from the flexible dimethylethylene diamine backbone **37a,** to the 6 membered piperazine ring **37b**, did not produce a significant increase in activity with completion being achieved in 1 hour (300:1 {$[LA]_0$:[**37b**]$_0$}, THF, 30 °C).[29,49] Changing the initiating group to a pendant $N(SiHMe_2)_2$ amide (**37c**) produced a significant increase in the activity under elevated conditions (toluene, 60 °C).[29] Complete conversion in 10 minutes at feed ratios of 3000:1 {$[LA]_0$:[**37c**]$_0$} was achieved, in comparison to 30 minutes required for **37b**, when at ratios of 300:1 {$[LA]_0$:[**37b**]$_0$}. Comparing with the 5 membered imidazolidine Ln complex (**39**) reported by Zhang *et al.*, the activity dependence on backbone is highlighted, as the rate increase is not sustained (Figure 3.6).[50] Whilst not directly comparable, further investigations showed how the bimetallic carbene variant of the imidazolinium ring (**40**) was significantly more active.[51]

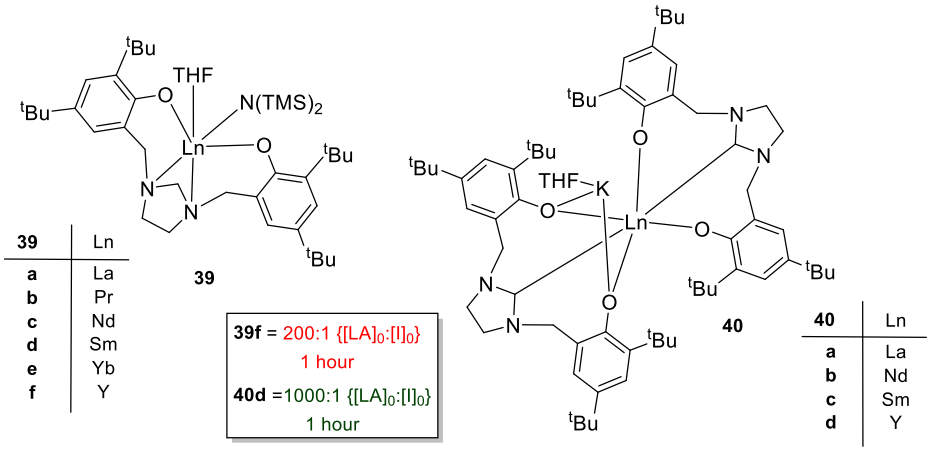

Figure 3.6. imidazolidine and carbene bis(phenolate) Ln complexes reported by Zhang *et al*.[50,51]

3.1.3. Phosphasalen Ln^{3+} complexes

Williams and co-workers showed the effectiveness of iminophosphorane aka 'phosphasalen' ligands by developing a series of highly active yttrium complexes (Figure 3.7).[52–54] These systems show a significant improvement in rate from analogous salen or salan complexes.[44] Computational calculation suggests the difference is a result of an increased charge difference (IΔqI) across the P=N bond (P=N IΔqI = 2.29, C=N IΔqI = 0.51).[52] This large variance in charge shows the iminophosphorane bond is dipolar with no π system and more accurately exists as P^+–N^- instead of P=N. Judicial choice over the bulk on the alkoxide yielded a variety of different coordination complexes.

The bulkier ^{t}BuO– complex(**41**) forces a terminal alkoxide environment with bridging phenolates, whereas the EtO– analogue (**42**) was seen to yield the more common bridging

alkoxide motif. This variance in coordination was shown to have a distinct impact in rate of polymerisation, with **42** having an observable rate constant 80 times faster than **41**. Increasing the bulk of substituents on the phenolate groups yielded a mononuclear complex (**43**), analogous to In^{3+} analogues recently developed.[55] Despite the added bulk, which has previously been shown to reduce rates, **43** was able to polymerise *rac*-LA within 5 seconds yielding highly heterotactic PLA (P_r = 0.81) at a ratio of 200:1 {$[LA]_0$:$[I]_0$}, in THF at 20 °C.

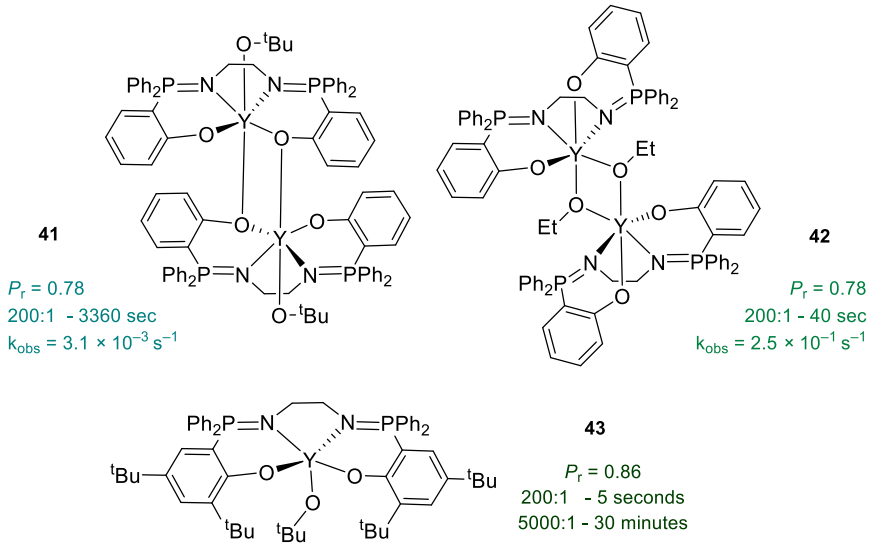

Figure 3.7. Yttrium phosphasalen complexes reported by Williams and co-workers.[52]

Pentadentate phosphasalen complex (**44**) was shown to yield the reverse selectivity, producing isotactic PLA (P_r = 0.24) with slightly lower activity in comparison to the tetradentate analogue. It is postulated that this dramatic switch is, in part due to the changes in coordination geometry, with **43** displaying a trigonal bipyramidal geometry and **44** occupying an octahedral geometry. This alters the approach of the monomer to the metal, highlighting that chain-end mechanism is in operation. In a follow up study, Bakewell *et al.,* showed how metal size could radically alter the stereoselectivity of the initiator (Figure 3.8).[8] Using the same phosphasalen ligand, a switch in stereocontrol was seen between the smaller Lu^{3+} centre (**46**) giving isotactic PLA (P_r = 0.25), and the larger La^{3+} centre (**45**) giving moderately heterotactic PLA (P_r = 0.73). These results reinforce the early reports of Kerton *et al.*, detailing the importance of ionic size when using lanthanide complexes.[12] Polymerisation rates were also shown to vary considerably, with **45** proving an exceptionally active catalyst for the ROP of *rac*-LA at a ratio of 1000:1:1 ($[LA]_0$:$[I]_0$:$[^iPrOH]_0$). At these ratios complete conversion was seen in a matter of seconds, whilst maintaining a narrow molecular weight distribution. In agreement with other studies it was shown that the rates experienced were proportional to metal size (Y ≈ Lu < La).

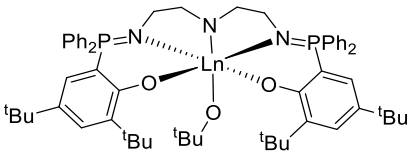

44 Ln = Y P_r = 0.24
45 Ln = La P_r = 0.73
46 Ln = Lu P_r = 0.25

Figure 3.8. Pentadentate Ln^{3+} phosphoaalen complexes reported by Bakewell *et al*.[8]

3.1.4. Chapter aims

Within lanthanide initiators the impact of complex chirality is poorly researched. As previously discussed, variation of the metal centre with a bipyrrolidine ligand system produced different behaviour with some complexes yielding highly isotactic PLA (P_r = 0.20),[2] and others producing heterotactic PLA (P_r = 0.84).[3] Herein, this chapter focuses on the further utilisation of this ligand system to evaluate the influence of metal size on reactivity and selectivity within the lanthanide series. Through this effort the identification of structural-activity relationships which can be adopted for further investigations is a focus.

One common feature described in the literature is the versatility of lanthanide complexes for the ROP of cyclic esters, including the ROCOP of epoxides and anhydrides.[7,56] From the perspective of catalyst design, this highlights functional group tolerance of the initiator. Using the ROP of LA as the model system for screening initiator efficacy this work looks into the potential of lanthanide-based complexes to polymerise less well-studied and potentially bio-renewable monomers.

3.2. Synthesis of lanthanide initiators

3.2.1. Synthesis of Nd^{3+}, Sm^{3+} and Yb^{3+} dialkoxide initiators

The synthesis of all reported lanthanide complexes are based on the reaction of the bisphenol *meso*-bipyrrolidine ligand **1**H_2 and **2**H_2, with the corresponding lanthanide(III) trisisopropoxide (Scheme 3.1). Neodymium, samarium and ytterbium were the focus due to considerable variance in the ionic radii. The proposed synthesis follows the same approach as that of the synthesis of indium alkoxide complexes (Chapter 2.2.2), using toluene as the solvent at 50 °C under an argon atmosphere. The release of isopropanol was expected to drive complex formation due a proposed positive reaction entropy. Recrystallisation of the crude mixture in a hexane/toluene co-solvent system was utilised as the method of purification, generating crystals suitable for analysis by single-crystal XRD.

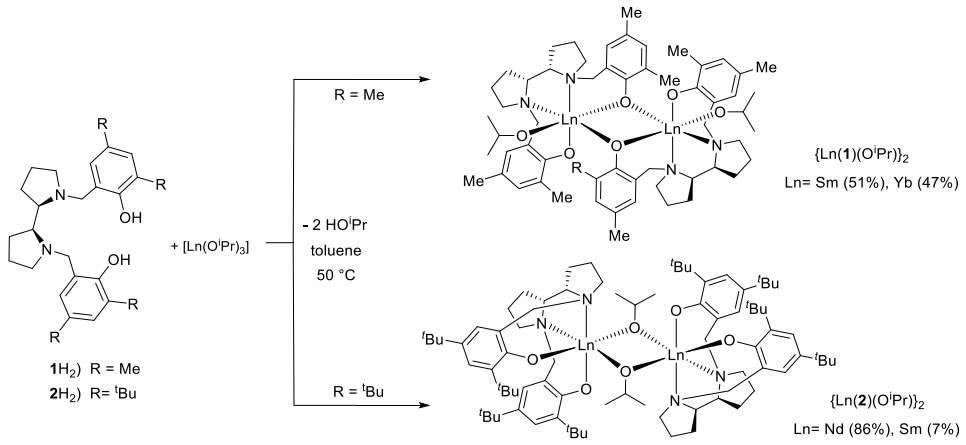

Scheme 3.11. Synthetic routes to access lanthanide bipyrrolidine alkoxide complexes.

When **1**H_2 was chosen as the pro-ligand, crystalline material could be obtained for Sm^{3+} and Yb^{3+} with moderate yields of 51% and 47% respectively. Despite variation of the feed ratios and reaction conditions, no crystalline product could be obtained when Nd^{3+} was the metal centre, with a very high solubility of the products observed in all tested solvents. Solid-state structures of both {Yb(**1**)O^{i}Pr}$_2$ and {Sm(**1**)O^{i}Pr}$_2$ show a phenolate group from the ligand bridging between the metal centres with terminal alkoxides and on opposite sides giving the complexes a centrosymmetric structure (Figure 3.9). This bridging phenolate motif has previously been reported for Ln complexes, notably by Sun *et al.*,[41] and more recently by Hao *et al.*[57] The complexes are all binuclear 6-coordinate with a distorted octahedral geometry. {Yb(**1**)O^{i}Pr}$_2$ bond angles are closer to ideal octahedral angles compared to {Sm(**1**)O^{i}Pr}$_2$ (Table 3.1). Bond lengths around the central metal are smaller in the case of Yb than for Sm, in agreement with a smaller ionic radii and higher charge density for the latter lanthanides.

Table 3.1.Selected bond lengths (Å) and angles (°) for {Sm(**1**)O^{i}Pr}$_2$ and of {Yb(**1**)O^{i}Pr}$_2$.

	{Yb(**1**)O^{i}Pr}$_2$	{Sm(**1**)O^{i}Pr}$_2$
Ln(1)–Ln(2)	3.696(4)	3.860(2)
Ln(1)–O(3)	2.112(3)	2.190(15)
Ln(1)–O$_{bridging}$	2.254(3)	2.399(14)
O(1)–Ln(1)–N(1)	80.73(12)	78.81(5)
O(1)–Ln(1)–N(2)	146.76(12)	141.50(6)
N(1)–Ln(1)–O(2)	171.02(11)	168.89(5)

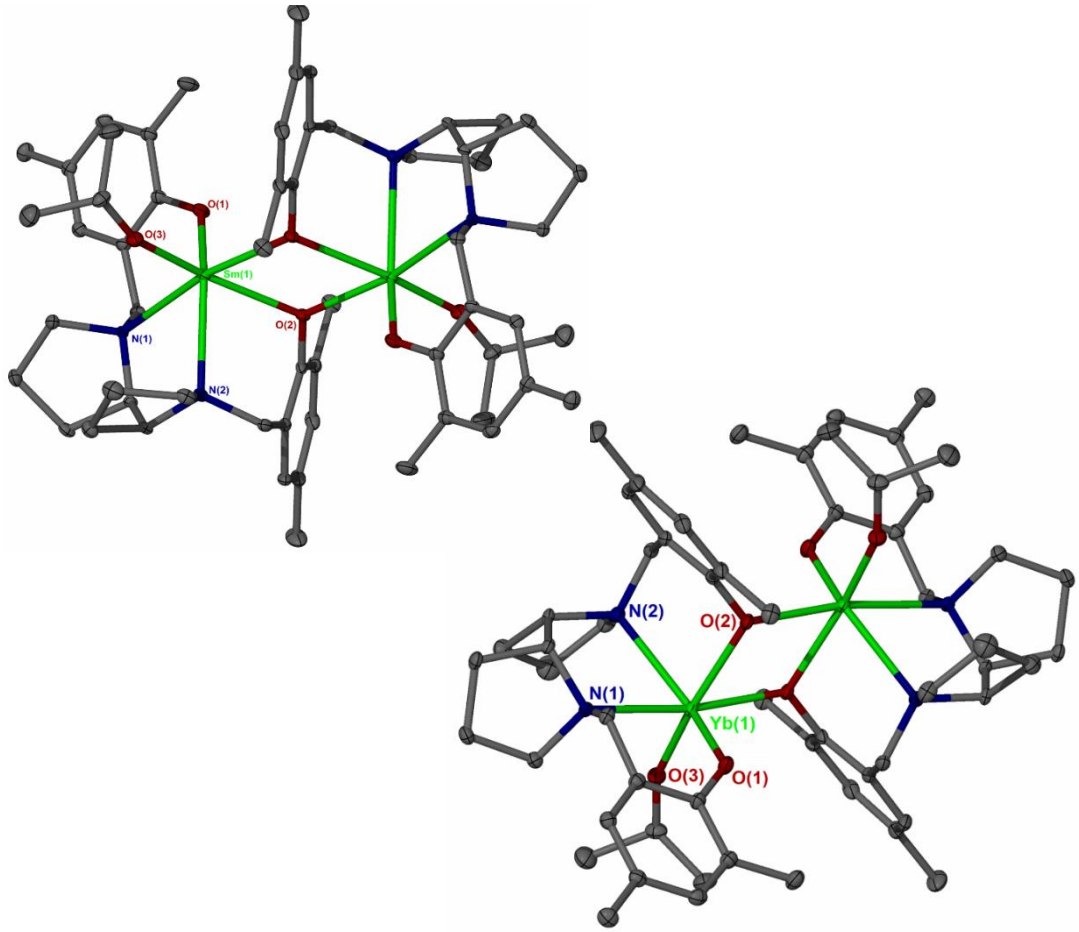

Figure 3.9. Solid state structures of {Sm(**1**)O^{i}Pr}$_2$ and of {Yb(**1**)O^{i}Pr}$_2$. Ellipsoids are shown at the 30% probability level. All hydrogen atoms are removed for clarity.

In contrast, complexation with **2**H_2 yielded bridging alkoxides across the Ln centres in a six coordinate structure as indicated by solid state structures of {Nd(**2**)O^{i}Pr}$_2$ and {Sm(**2**)O^{i}Pr}$_2$ (Figure 3.10). In contrast to **1**H_2, suitable crystals were obtained for {Nd(**2**)O^{i}Pr}$_2$ in very high yields (86%) and confirmed pure by CHN analysis. {Sm(**2**)O^{i}Pr}$_2$ proved synthetically more challenging, achieving yields of only 7%. Conversely, no dialkoxide structure could be obtained of {Yb(**2**)O^{i}Pr}$_2$. Isolated crystalline material instead showed evidence of hydrolytic degradation with a hydroxy bridge between the metal centres, [Yb_2(**2**)$_2$(μ-O^{i}Pr)OH] . Reaction of Y(O^{i}Pr)$_3$ with **1**H_2 and **2**H_2 showed minimal conversion by ^{1}H NMR spectroscopy (~10%) after 5 days of stirring in toluene at 80 °C. Poor solubility of La(O^{i}Pr)$_3$ in toluene and THF prevented using these reagents via this method.

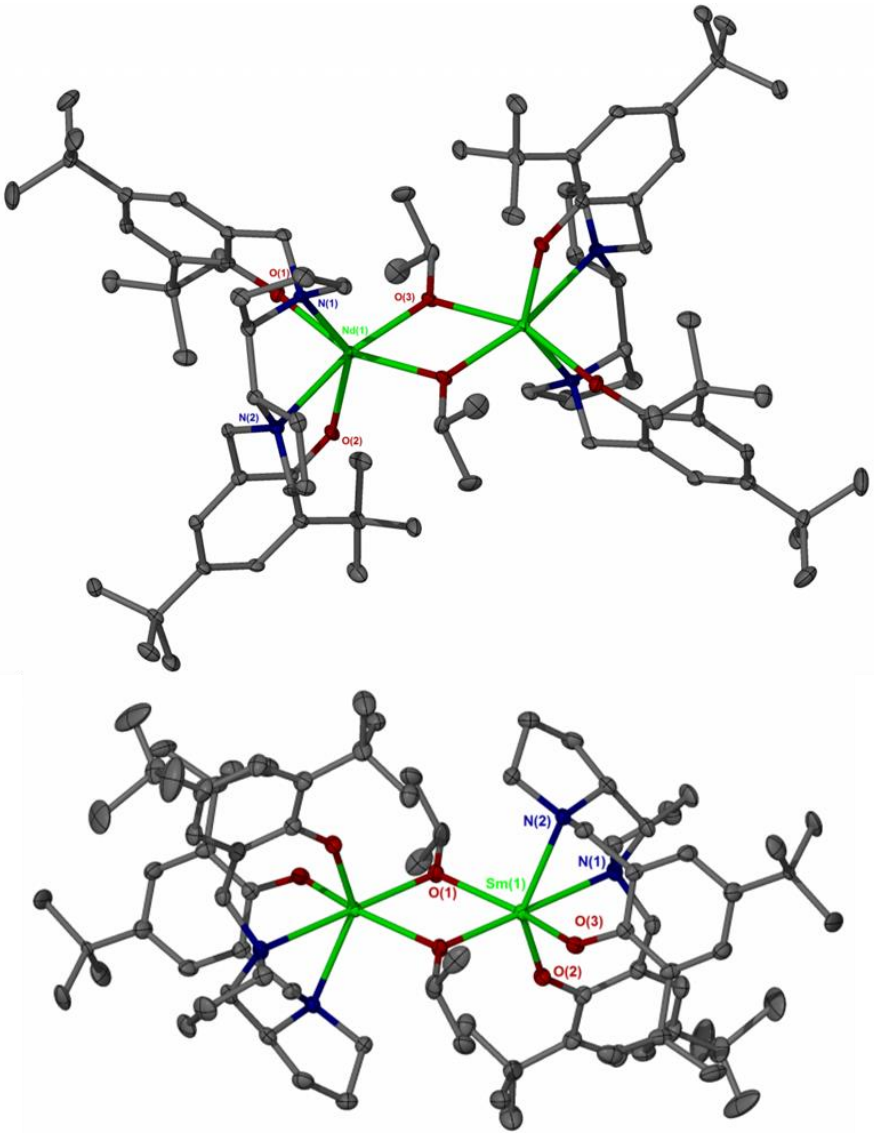

Figure 3.10. Solid state structures of {Nd(**2**)O^{i}Pr}$_2$ and of {Sm(**2**)O^{i}Pr}$_2$. Ellipsoids are shown at the 30% probability level. All hydrogen atoms are removed for clarity.

Despite the greater hydrodynamic radii of the ^{t}Bu– (**2**) complexes, bond lengths around the central metal are similar in comparison to the Me– (**1**) substituted complexes, suggesting polymerisation activity could be controlled by geometric and steric constraints (Table 3.2). The bond angles obtained from the solid-state structure of {Sm(**2**)O^{i}Pr}$_2$ show a larger distortion from the octahedral geometry as seen in {Sm(**1**)O^{i}Pr}$_2$, possibly due to the steric bulk of the ^{t}Bu– groups causing a steric clash from the bridging groups (Table 3.2). This effect is more pronounced when Nd^{3+} is the central metal ion, likely due to the larger nuclei forcing the ancillary ligand into a tighter binding angle. A comparison of the bond lengths between the metal complexes shows a shortening along the lanthanide series. This is highlighted for Ln-O(1) bond lengths in {Ln(**2**)O^{i}Pr}$_2$, evidencing the lanthanide contraction in action (Figure 3.11). This is likely to effect the bond energies and activity when the complexes are employed as initiators for polymerisation.

Table 3.2. Bond lengths (Å) and angles (°) for the {Sm(**1**)OiPr}$_2$ and {Sm(**2**)OiPr}$_2$.

	{Sm(**1**)O^{i}Pr}$_2$	{Sm(**2**)O^{i}Pr}$_2$
Ln(1)–Ln(2)	3.860(2)	3.856(3)
Ln(1)–N(1)	2.609(16)	2.674(3)
Ln(1) –$O_{bridging}$–Ln(2)	109.38(5)	110.85(10)
O(1)–Sm–N(2)	141.50(6)	139.70(7)
O(2)–Sm–N(1)	168.89(5)	141.27(9)
O(1)–Sm–N(1)	78.81(5)	74.52(6)
N(1)–Sm–N(2)	77.21(4)	68.58(6)

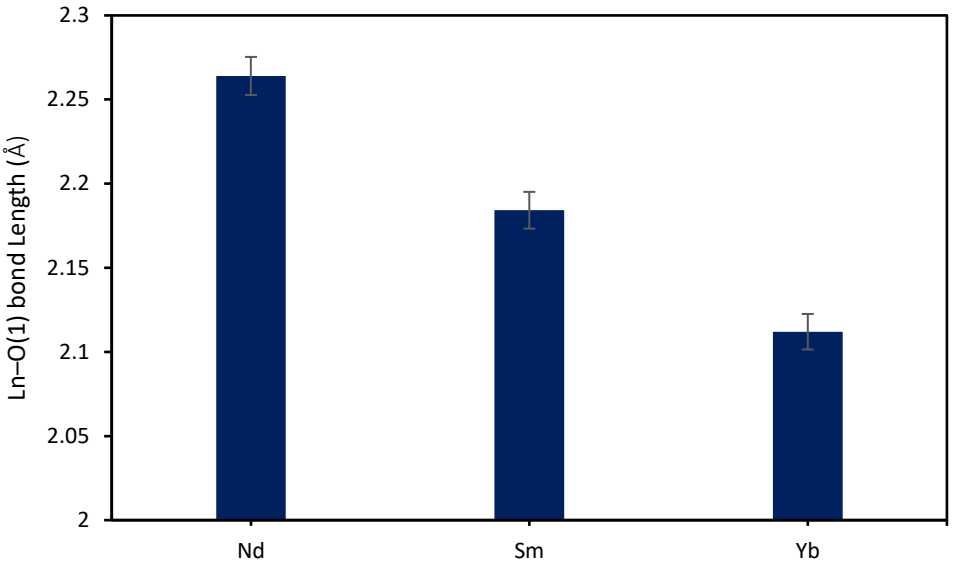

Figure 3.11. Bond lengths (Å) between Ln–O(1) bonds in {Nd(**2**)O^{i}Pr}$_2$, {Sm(**2**)O^{i}Pr}$_2$ and {Yb$_2$(**2**)$_2$(O^{i}Pr)(OH)}.

In order to probe the nature of these complexes in solution, the potential for alkoxide transfer was investigated. A switch to a bulkier alkoxide might produce a structure, which could potentially be isolated as a monomeric species, similar to reports by Shen and coworkers.[47] To this effect {Nd(**2**)O^{i}Pr}$_2$ was reacted with varying equivalents of 4-methylbenzylalcohol. The reaction was performed at high temperatures to push the removal of iso-propanol from the system and drive any equilibria towards the formation of the metal aryloxide.

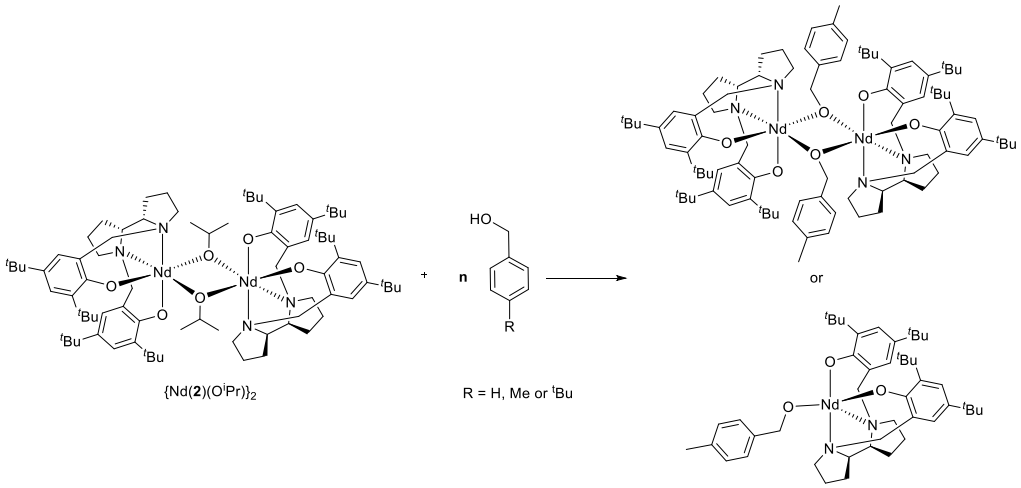

Scheme 3.2. Proposed route for the alkoxide transfer using 4-methylbenzylalcohol and {Nd(**2**)O^{i}Pr}$_2$.

Despite multiple attempts with 1, 2 and 10 equivalents of 4-methylbenzylalcohol to the solution no crystalline solid was yielded. The product appeared significantly more soluble than the di-nuclear reactant, suggesting the formation of a different coordination motif.

3.2.2. Solution state characterisation of lanthanide dialkoxide complexes

Due to the paramagnetism associated with Ln^{3+} complexes NMR spectroscopic analysis is not facile, limiting characterisation in the solution state. This ambiguity of the solution structure has restricted mechanistic investigation to solid state isolation of potential polymerisation intermediates. The theory of paramagnetism and the isotropic shift it generates on NMR spectra, has been well studied in recent decades with a focus on relevant d-electron shell structures.[58–61] Isotropic shift (δ_{obs}) is defined as the difference in chemical shift of paramagnetic compounds and the diamagnetic analogue. This shift results from three magnetic effects known as orbital shift (δ_{orb}), the Fermi contact shift (δ_{con}) and the pseudocontact shift (δ_{pc}) which are related by Equation 3.1.[62]

Equation 3.2. Calculation of isotropic shift for paramagnetic system.[62]

$$\delta_{obs} = \delta_{orb} + \delta_{hf} \cong \delta_{orb} + \delta_{con} + \delta_{pc}$$

Orbital shift (δ_{orb}) – vanishes in the absence of spin-orbit coupling and is the main term in defining the chemical shift of diamagnetic compounds.[58]

Fermi contact shift (δ_{con}) – generated by the coupling of the unpaired electrons with the atomic nuclei and is transmitted through chemical bonds. It is proportional to residual spin density and is often the most significant term in the observed isotropic shift.[62]

Pseudo contact shifts (δ_{pc}) – arise from anisotropic hyperfine interactions at the nucleus.[63] It depends strongly on the distance of the paramagnetic centre and the examined nucleus.[62]

The result of a large Fermi contact shift associated with f-orbitals and increasingly significant impact of pseudo contact shifts means Ln^{3+} complexes are expected to have increased line broadening and a significant isotropic shift of potential diagnostic environments. This effect is often mapped using lanthanide shift reagents to measure a shift in signal of a simple molecule in the presence of a lanthanide compound (Figure 3.12).[64–66]

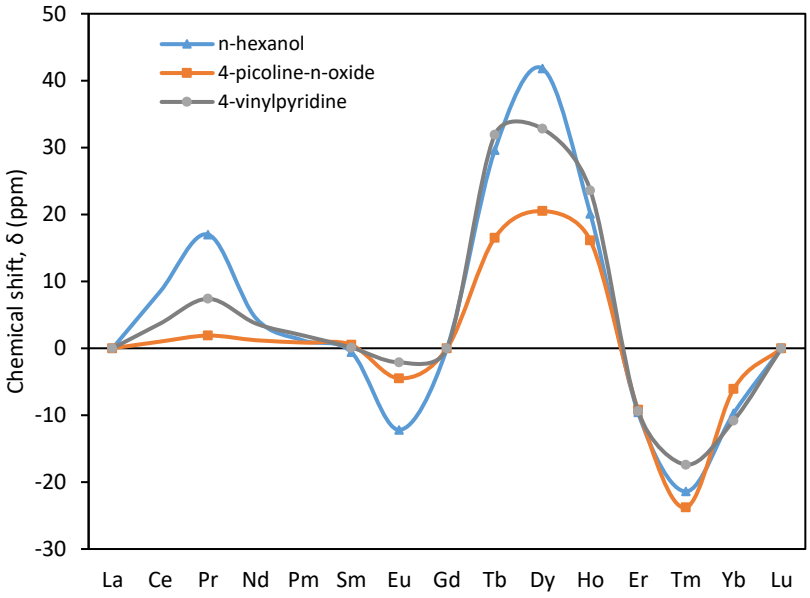

Figure 3.12. Observed isotropic shifts reported for n-hexanol, 4-picoline-N-oxide and 4-vinylpyridine in the presence of $Ln(dpm)_3$ adapted from work by Sipe and coworkers.[64]

To improve characterisation of Ln^{3+} complexes in the solution state, ^1H NMR spectroscopy of synthesised Ln^{3+} complexes was tested, identifying, where possible, diagnostic groups in order to build a database for future studies. An interpretable ^1H NMR spectrum was produced with the centrosymmetric $\{Sm(\mathbf{1})O^iPr\}_2$ by increasing the spectral width to ±200 ppm and the T_1 delay to 5 seconds (Figure 3.13).

Despite a small shift, four aromatic signals (doublets at 7.92, 6.89, 6.01 and 4.80 ppm) and the evidence of two isopropoxide groups (doublets at 2.83 ppm and broad signal at 2.20 ppm) suggest the solid-state structure is maintained in solution (Figure 3.13). Backbone signals were also assigned with the acquisition of ^1H-^1H COSY spectra, however they are significantly more shifted (1 – -5 ppm). This is likely the pronounced effect of the pseudo contact shift, indicating close proximity to the Sm^{3+} centre. The complete assignment of proton environments between the range of 8 – -5ppm highlights a low shift in agreement with $Sm(dpm)_3$ shift reagent studies by Sipe and coworkers.[64]

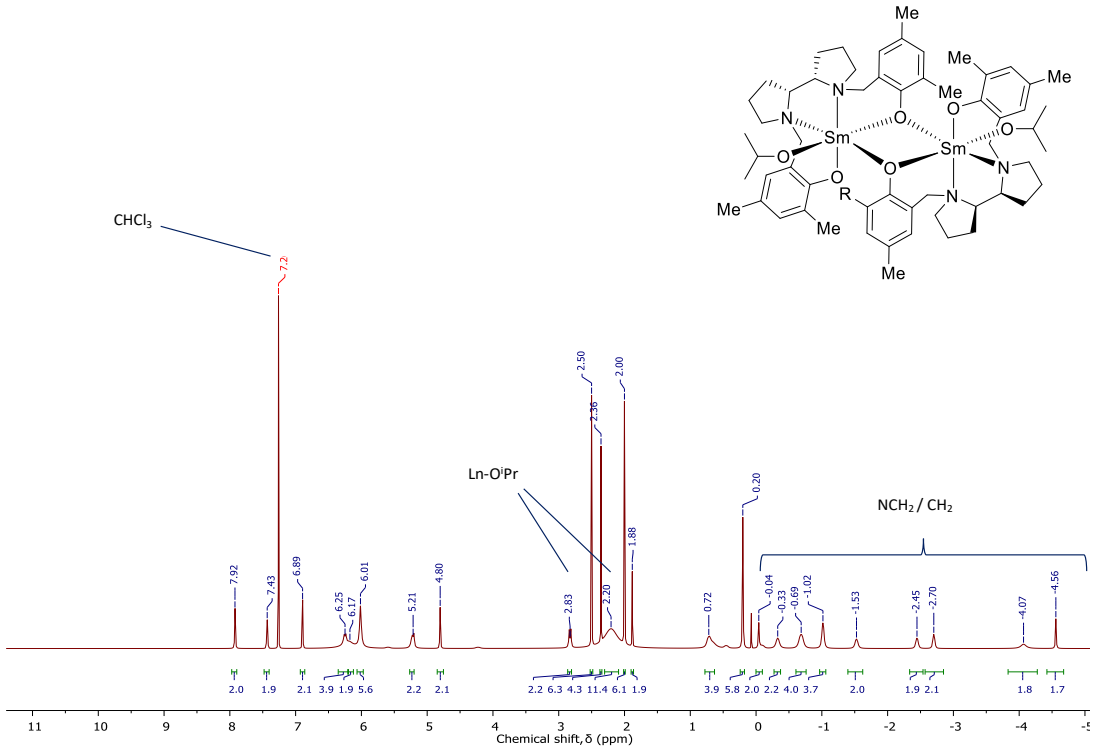

Figure 3.13. ^{1}H NMR (298 K, 500 MHz) spectra of {Sm(**1**)O^{i}Pr}$_2$ in $CDCl_3$.

In order to confirm the dimeric structure, ^{1}H diffusion ordered spectroscopy (DOSY) was carried out. DOSY differentiates molecules by their diffusion rates in solution. By carrying out a pulse sequence of varying gradient strength signal intensity is expected to diminish. This loss is attributed to a lowering of T_1 relaxation and is affected intrinsically by the hydrodynamic radius of the molecule. Derived from the Stokes-Einstein equation (Equation 3.2), and assuming that the analyte behaves as a hard sphere in solution, a value of the diffusion coefficient of a given proton environment can be calculated. Due to this assumption and the influence of solvent interactions, viscosity, and convection, DOSY is not a truly quantitative technique and is utilised as a comparative tool in this study.

Equation 3.3. Stokes-Einstein equation for the calculation of diffusion coefficient.

$$D\,\frac{kT}{6\pi\eta R}$$

D = diffusion rate, k = Boltzmann constant
η = viscosity, R = hydrodynamic radii

In recent years the accuracy and precision of this technique has improved dramatically with notable worked by Morris and coworkers.[67–69] Using published protocols aimed at reducing the impact of convection (Chapter 6.2.1), a spectrum was obtained for {Sm(**1**)O^{i}Pr}$_2$ (Figure 3.14).[68,70] All assigned complex signals were shown to diffuse at the same rate (D = 5.89 × 10^{-10} m^2 s^{-1}) with faster moving signals of residual solvent (D_{sol} = 1.77 × 10^{-9} m^2 s^{-1}) which compared well with published values.[71]

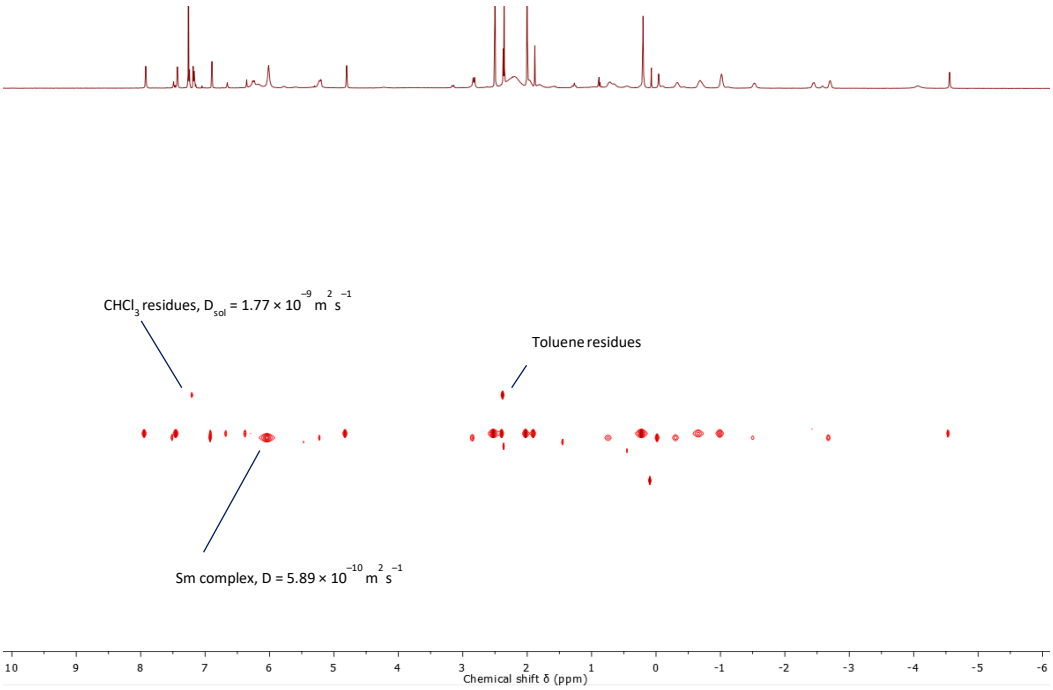

Figure 3.14. ^{1}H DOSY NMR (298 K, 500 MHz) spectra of {Sm(**1**)O^{i}Pr}$_2$ in $CDCl_3$.

Multiple adaptions of the Stokes-Einstein equation have since been derived for determination of the molecular weight of the solute.[72–74] Grubbs and co-workers highlighted how using very dilute solutions and external calibrants allowed determination of polymer molecular weight, with good agreement of SEC values up to 200 kg mol^{-1}.[73] In recent years, Morris and co-workers have developed an open access toolbox for the determination of molecular weight, without the use of external calibrants.[70,75] Using this GNAT (V1.1.1) toolbox the molecular weight of the Sm species in solution is estimated as 1270 g mol^{-1}. This value is in agreement with molecular weight of the solid-state structure of 1236 g mol^{-1} providing firm evidence that the complex is dimeric in solution. This result is in contrast to a report by Mountford and co-workers where it is hypothesised that a dimeric Sm complex bearing a tripodal ligand system is in equilibrium with the monomeric complex in solution.[33]

^{1}H NMR spectra of {Yb(**1**)O^{i}Pr}$_2$ showed significant positive and negative isotropic shift with signals seen between 120 and -70 ppm (Figure 3.15). In contrast to the Sm analogue, large shifting is seen for aromatic and 2,4-methyl substituted groups. Additionally, significant peak broadening is apparent, limiting integration of the signals. This same effect is seen with {Nd(**2**)O^{i}Pr}$_2$ with a very large degree of line broadening between 1.6 and 4.2 ppm preventing assignment of resonances. ^{1}H NMR spectra of {Yb$_2$(**2**)$_2$(O^{i}Pr)(OH)} showed low intensity signals between the range of 110 to -50 ppm regardless of solute concentration. Despite this, the position and integration of signals at 3.04 and 1.30 ppm indicate the presence of isopropoxide functional groups, with identification of ^{t}Bu– groups also possible. The

presence of an isopropoxide resonance suggests the molecule is dimeric with one alkoxide present in the complex. {Sm(**2**)O^{i}Pr}$_2$ was not produced in high enough yields to provide meaningful NMR analysis.

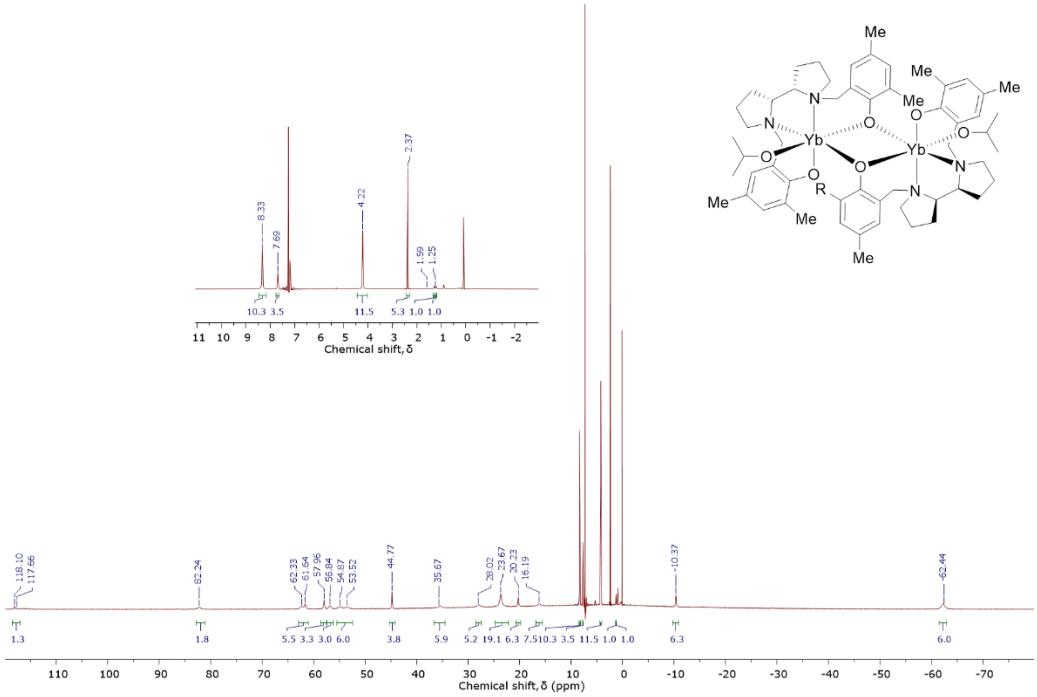

Figure 3.15. ^{1}H NMR (298 K, 500 MHz) spectra of {Yb(**1**)O^{i}Pr}$_2$ in $CDCl_3$.

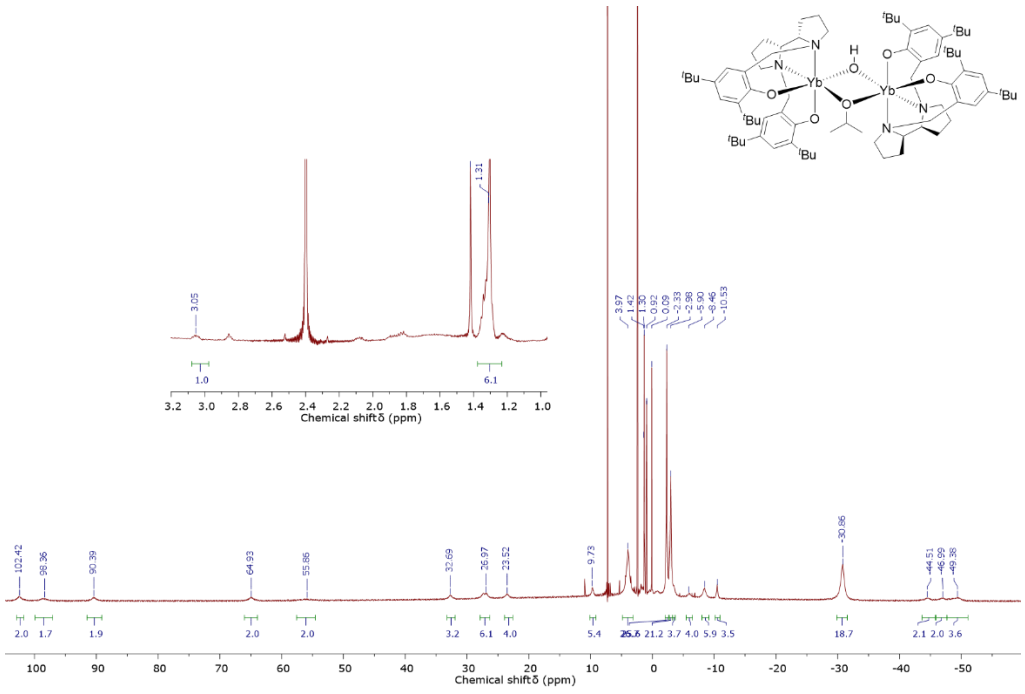

Figure 3.16. ^{1}H NMR (298 K, 500 MHz) spectra of {Yb$_2$(**2**)$_2$(O^{i}Pr)(OH)} in $CDCl_3$.

3.2.3. Synthesis and characterisation of hydrolytically degraded lanthanide complexes

Whilst reaction of $Nd(O^iPr)_3$ with **2**H_2 exclusively produced the di-alkoxide product, $\{Sm_2(\mathbf{2})_2(O^iPr)(OH)\}$ and $\{Yb_2(\mathbf{2})_2(O^iPr)(OH)\}$ were both isolated as crystalline products from their respective reaction mixtures in moderate yields (69% and 47% respectively) (Figure 3.17).

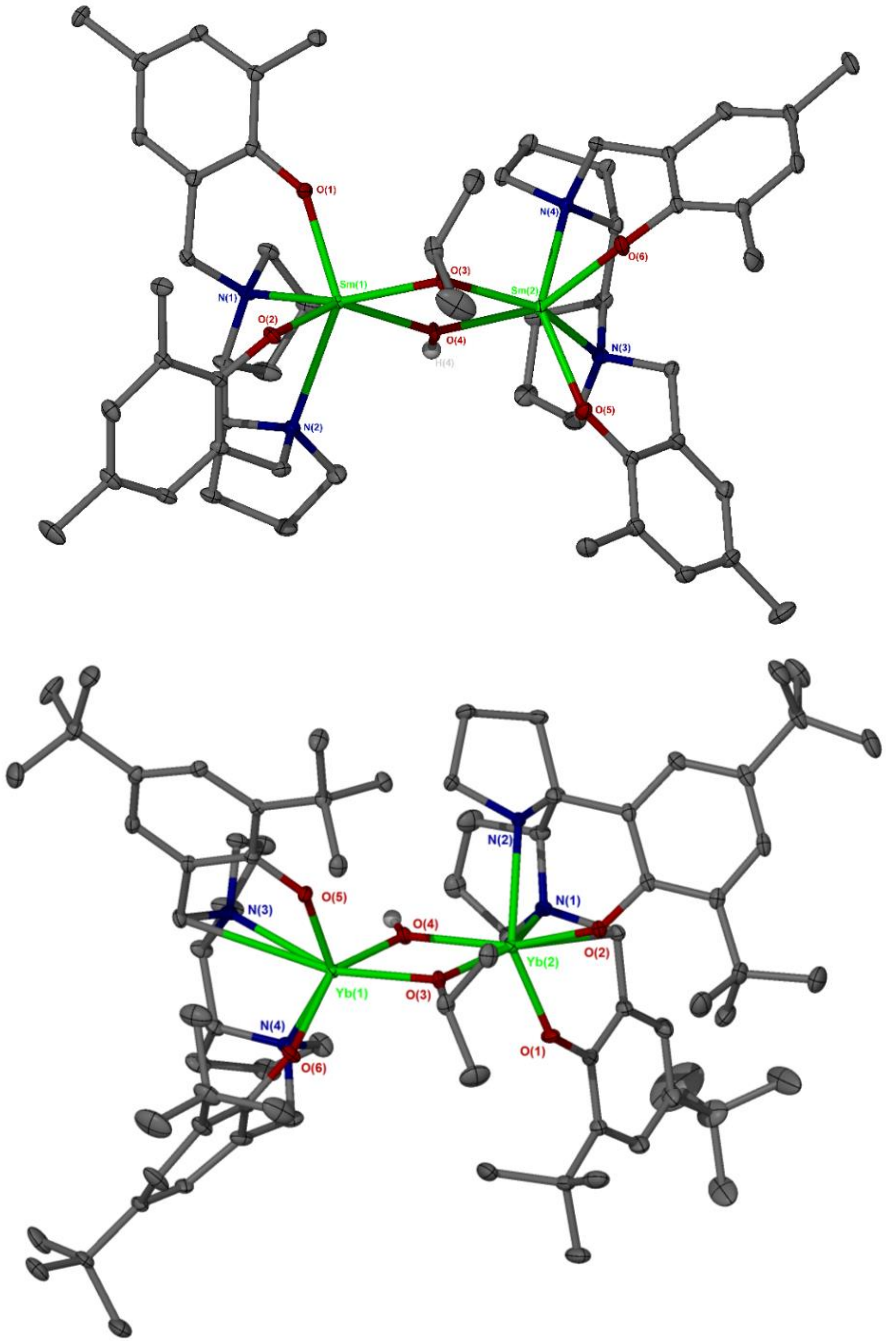

Figure 3.17. Solid-state structures for $\{Sm_2(\mathbf{2})_2(O^iPr)(OH)\}$ and $\{Yb_2(\mathbf{2})_2(O^iPr)(OH)\}$. All ellipsoids are at the 30% probability level with ^{t}Bu– replaced by Me– group in the case of Sm to improve clarity. All H atoms except bonded as an OH group have been removed for clarity

The formation of hydroxyl structures is likely the result of adventitious water in the starting $Ln(O^iPr)_3$ reagent. This is supported by the expectation that the larger ionic radii of Nd^{3+} would result in a greater sensitivity to residual water in the solvent or ligand system. Variation of reaction conditions including, solvent, temperature and rigorous schlenk line techniques failed to remove the formation of hydroxy bridged complexes. The formation of the hydroxyl-bridged Ln^{3+} systems is commonly reported in the literature yet very little work has been done to fully characterise or evaluate their activity for ROP.[29] Recent studies by Chen *et al.,* have shown how an air stable Y^{3+} complex (**47**) with significant hydrolytic degradation can be turned into a highly active moisture insensitive catalyst for the ROP of LA with addition of exogenous BnOH under elevated temperatures.[76]

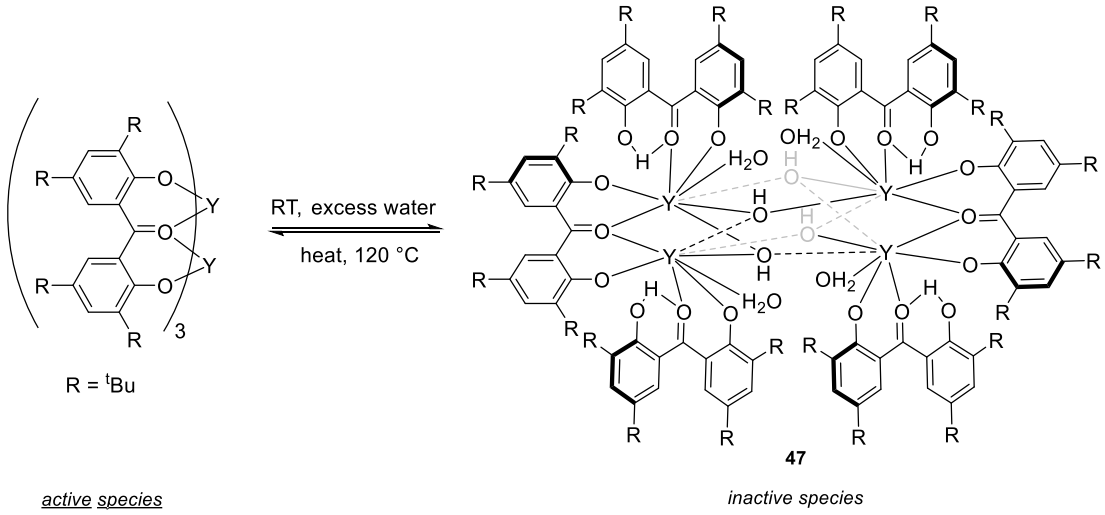

Scheme 3.3. Route to reversible multinuclear air stable Y^{3+} degradation species reported by Chen *et al*.[76]

In order to further explore the nature of hydrolytic decomposition of Ln^{3+} complexes and evaluate if an air-stable Ln^{3+} complex can be made active for ROP, the synthesis and characterisation of these products was further investigated. It could be expected that in cases where a mono hydroxide complex forms, further exposure could lead to formation of a bishydroxide complex or breakup of the ligand-metal framework. However, the ability to synthesise $\{Sm(\mathbf{1})O^iPr\}_2$ and $\{Yb(\mathbf{1})O^iPr\}_2$ cleanly with no evidence of hydrolytic degradation, suggests this bridging ligand structure is more resistant to adventitious water. If any moisture sensitivity is present it would likely lead to the formation of terminal hydroxides. To investigate this, $\{Ln(\mathbf{1})O^iPr\}_2$ in $CDCl_3$ in a J-Youngs NMR tube was exposed to a flow of compressed 'wet' air via a needle for 30 minutes, following which the ^1H NMR spectrum was measured periodically to monitor the release of ^{i}PrOH.

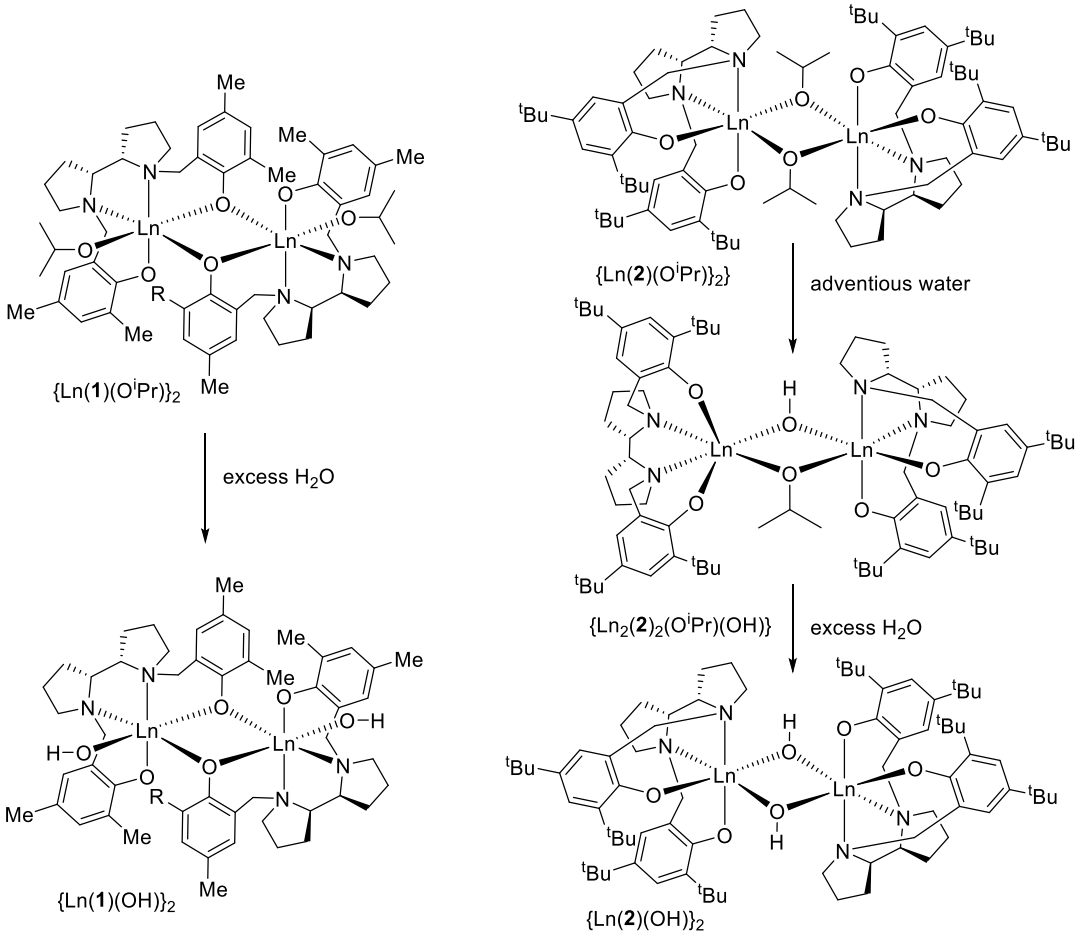

Scheme 3.4. Synthetic route to access hydrolytically degraded lanthanide complexes.

{Sm(**1**)O^{i}Pr}$_2$ was shown to completely hydrolytically degrade over the course of 36 hours with the clear release of ^{i}PrOH and shift of aromatic and NCH_2 signals in the ^{1}H NMR spectra (Figure 3.18). Over 120 hours no further change is observed. The retained presence of four aromatic signals and a presence of signals below 0 ppm suggests that the ligand framework remains intact and the complex exists as {Sm(**1**)OH}$_2$. DOSY analysis supports this with one diffusing species in solution with a diffusion constant very similar to the dialkoxide starting material (Table 3.3). In contrast {Yb(**1**)O^{i}Pr}$_2$ was shown to degrade completely within 5 hours to the pro-ligand and $Yb(OH)_3$. These results suggest the nature of the metal centre is significant in the rate of hydrolytic decomposition.

Table 3.3. Diffusion coefficients and calculated molecular weights for {Sm(**1**)OiPr}$_2$ and {Sm(**1**)OH}$_2$.

	D × 10^{-10} (m^2 s^{-1})	**D$_{sol}$ × 10^{-10} (m^2 s^{-1})**	**Calculated Mw (g mol^{-1})**	**Expected Mw (g mol^{-1})**
{Sm(**1**)O^{i}Pr}$_2$	5.89	1.77	1269	1236
{Sm(**1**)OH}$_2$	5.93	1.83	1212	1152

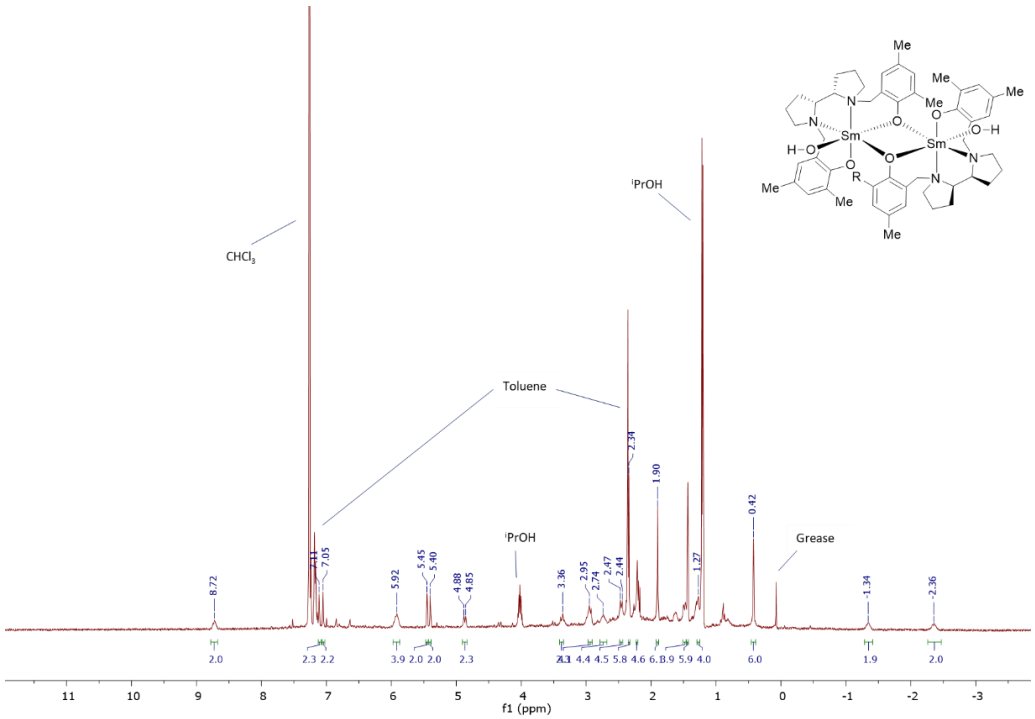

Figure 3.18. ^{1}H NMR (500 MHz, 298 K, $CDCl_3$) spectra of degradation product of {Sm(**1**)O^{i}Pr}$_2$ (Figure 3.13) after 120 hours exposure to air and proposed structure of degradation product, {Sm(**1**)OH}$_2$.

Due to the inability to clearly identify signals in the ^{1}H NMR spectra of {Ln(**2**)O^{i}Pr}$_2$ and {Ln$_2$(**2**)$_2$(OiPr)(OH)}, moisture sensitivity was analysed through the addition of 10 equivalents of water to the pure complex in toluene. After an hour of stirring the solvent was removed *in vacuo* and the solid was recrystallised in hexane. In agreement to conclusions from the methyl substituted complexes it was shown {Yb$_2$(**2**)$_2$(O^{i}Pr)(OH)} decomposed into the pro ligand, confirmed by ^{1}H NMR spectroscopy of the crude material. Conversely when the reaction was performed with {Sm$_2$(**2**)$_2$(O^{i}Pr)(OH)} a crystalline material was yielded. Single-crystal XRD analysis showed the solid state structure of the bimetallic bridged dihydroxide species {Sm(**2**)OH}$_2$ (Figure 3.19). Elemental analysis showed good agreement with the solid-state structure.

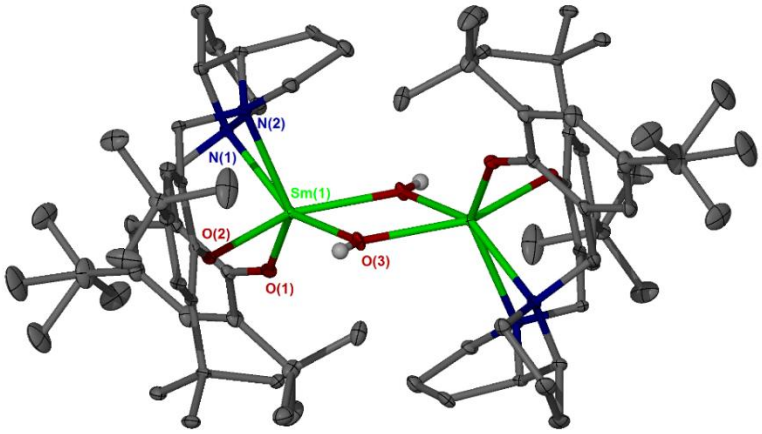

Figure 3.19. Solid state structure of {Sm(**2**)OH}$_2$. All ellipsoids are at the 30% probability level all hydrogen atoms except OH groups are removed for clarity.

^{1}H NMR spectroscopic analysis showed the complex to be clean with diagnostic signals of isotropic shifts between 23.0 and -8.0 ppm and the presence of 4 aromatic signals indicating inequivalent aryl rings around the metal centre with one trans to the –OH and one to the amine of the pyrrolidine ring (Figure 3.20). ^{13}C{^{1}H} NMR spectroscopy was facile, with signals corresponding to all carbon environments seen. In addition, diffusion experiments show one Sm species diffusing in solution with a diffusion coefficient of 4.69×10^{-10} m^2 s^{-1}. Estimation of the molecular weight of the species gives a value 1421 g mol^{-1}, in comparison to the expected value of 1488 g mol^{-1}.

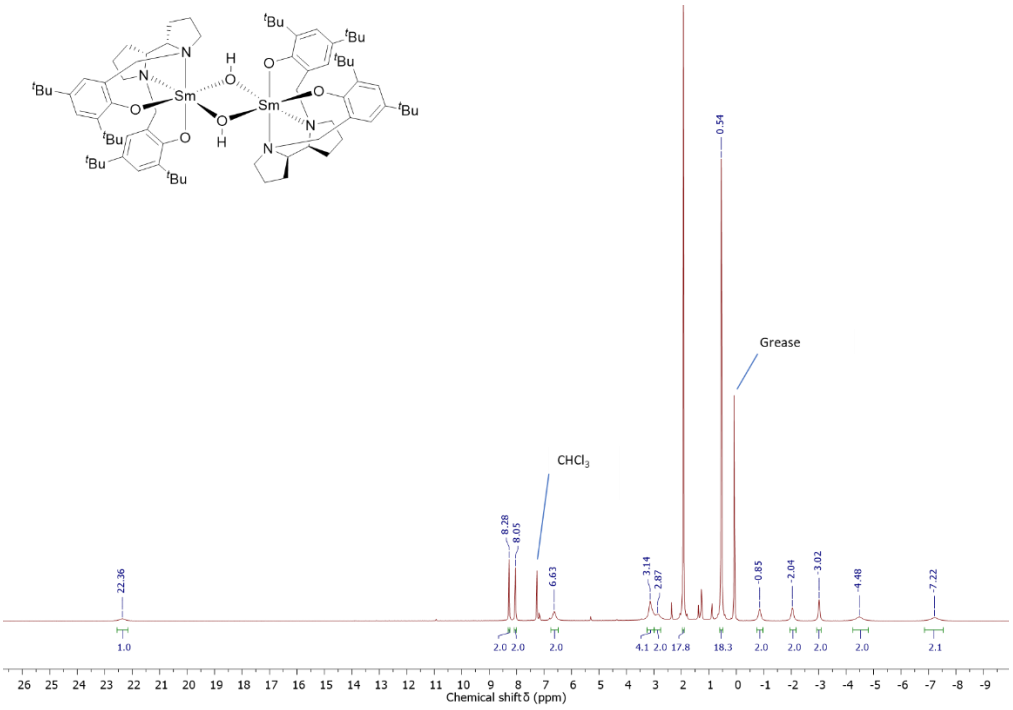

Figure 3.20. ^{1}H NMR (500 MHz, 298 K) spectra of {Sm(**2**)OH}$_2$ in $CDCl_3$.

3.3. Polymerisations using synthesised Ln^{3+} complexes

3.3.1. Polymerisations of *rac*-LA under mild conditions: CH_2Cl_2, 25 °C

Synthesised lanthanide complexes were initially tested as initiators for the ROP of *rac*-LA in CH_2Cl_2 at 25 °C. These relatively mild conditions are common for Ln systems, often yielding exceptional rates and resulting in high selectivity.[7,54] Unlike previously discussed group-13 metal chlorides, no exogenous alcohol was added to solutions and the ratio of monomer to catalyst is defined by the number of alkoxide initiating groups, with dialkoxides yielding two initiating groups. By varying the complex concentration an understanding of rate and control can be established.

Table 3.4.Polymerisation data for the polymerisation of *rac*-LA. $[LA]_0$ = 0.69 M, solvent = CH_2Cl_2, T = 25 °C.

Entry	Initiator	Ratio $[LA]_0:[I]_0$[a]	Time (min)	Conv.[b] %	M_n^{theo} [c] kg mol^{-1}	M_n^{SEC} [d] kg mol^{-1}	$Đ$ [d]	P_r [e]
1	{Nd(**2**)(O^{i}Pr)}$_2$	500	60	96	68.5	117.2	1.38	0.60
2	{Nd(**2**)(O^{i}Pr)}$_2$	1000	60	95	136.9	247.2	1.05	0.61
3	{Sm(**1**)(O^{i}Pr)}$_2$	150	120	40	8.7	5.8	1.03	0.58
4	{Sm(**1**)(O^{i}Pr)}$_2$	1000	120	5	-	-	-	-
5	{Yb(**1**)(O^{i}Pr)}$_2$	500	120	3	-	-	-	-
6	{Sm$_2$(**2**)$_2$(O^{i}Pr)(OH)}	300	120	95	41.1	41.9	1.51	0.60
7	{Sm$_2$(**2**)$_2$(O^{i}Pr)(OH)}	1000	120	95	136.9	92.9	1.51	0.59
8	{Yb$_2$(**2**)$_2$(O^{i}Pr)(OH)}	500	120	39	28.8	36.5	1.05	0.71
9	{Yb$_2$(**2**)$_2$(O^{i}Pr)(OH)}	1000	120	26	37.5	44.6	1.05	0.67

[a] Concentration of initiator based on per alkoxide initiating group. [b]Determined from analysis of the ^{1}H NMR spectrum by integration of the methine region (LA, 4.96 – 5.04 ppm; PLA, 5.10 – 5.22 ppm). [c]Theoretical M_n = (144.12 x $[LA]_0/[I]_0$) x (Conv. / 100) + Mw of end groups (O^{i}Pr + H). [d] As determined by SEC (THF) using triple detection methods. [e] As determined from ^{1}H{^{1}H} NMR from decoupling of the methine region using values predicted according to Bernoullian statistics.

Under these conditions, only {Nd(**2**)(O^{i}Pr)}$_2$ displayed high activity of the di-alkoxide complexes. With this system, high molecular weight polymer (247.2 kg mol^{-1}) with a low dispersity ($Đ$ = 1.05) was produced after 60 minutes (Entry 2, Table 3.4). Mono-alkoxide complexes were shown to be active with {Sm$_2$(**2**)$_2$(O^{i}Pr)(OH)} providing comparable rates to {Nd(**2**)(O^{i}Pr)}$_2$ under the tested timeframes and ratios (Entry 7, Table 3.4). The smaller Yb^{3+} analogue failed to reach high conversions after 120 minutes at a feed ratio of 500:1 {$[LA]_0:[I]_0$} (Entry 8, Table 3.3). This drop in activity is expected for the smaller Ln^{3+} metals and has previously been reported by Kerton, Carpentier, and Williams.[7,8,12]

It is commonly reported that the exceptionally small ionic radii of the latter Ln^{3+} ions results in an encapsulating ligand effect preventing access of the incumbent monomer to the metal centre. {Ln(**1**)(O^iPr)}$_2$ was not shown to be active under these conditions suggesting the terminal alkoxide is not an effective initiator compared to the bridging alkoxide analogue. Additionally, the complex structure is not found to have an impact on selectivity with only a mild heterotactic bias seen. The metal choice is shown to have only a small effect in enhancing this (Yb > Sm), far less pronounced than in comparable studies.[1,8,77] All complexes showed lower activity when tested under the commonly used conditions of THF at 40 °C, likely the result competitive coordination of monomer and solvent.

3.3.2. Polymerisations of *rac*-LA under moderate conditions: toluene, 80 °C

In order to generate a more comparative study, synthesised complexes were trialled for ROP activity under elevated conditions (toluene, 80 °C). Analogous to CH_2Cl_2 studies {Nd(**2**)(O^iPr)}$_2$ displayed the highest activity reaching near quantitative conversion within 10 minutes at feed ratios of 3000:1 {$[LA]_0$:$[I]_0$}, (Entry 3, Table 3.4). This result shows a huge reactivity improvement compared to similar dinuclear borohydride tripodal complexes published by Bonnet *et al.,* further highlighting the potential importance in the nature of the bridging group in initiator reactivity.[27,33,78] SEC analysis suggests the resultant polymer to be high molecular weight (370.3 kg mol^{-1}) with good agreement to the theoretically calculated value (410.5 kg mol^{-1}), whilst also having a low dispersity (*Đ* = 1.10). This control supports a 'living' nature of the polymerisation with little chain transfer.

Table 3.5.Polymerisation data for the polymerisation of rac-LA. $[LA]_0$ = 0.69 M, solvent = toluene, T = 80 °C.

Entry	Initiator [a]	Ratio {$[LA]_0$:$[I]_0$}[a]	Time (min)	Conv.[b] (%)	M_n^{theo} (kg mol^{-1})[c]	M_n^{SEC} (kg mol^{-1})[d]	*Đ* [d]
1	{Nd(**2**)(O^iPr)}$_2$	500	5	96	68.5	208.3	1.36
2	{Nd(**2**)(O^iPr)}$_2$	1500	5	95	205.3	156.3	1.30
3	{Nd(**2**)(O^iPr)}$_2$	3000	10	96	410.5	370.8	1.10
4	{Sm(**1**)(O^iPr)}$_2$	500	5	96	69.1	350.0	1.36
5	{Sm(**1**)(O^iPr)}$_2$	1500	10	96	207.4	169.4	1.23
6	{Sm_2(**2**)$_2$(O^iPr)(OH)}	1500	10	95	205.3	141.4	1.31
7	{Sm(**2**)(OH)}$_2$	1500	10	8	17.4	49.0	1.14
8	{Yb(**1**)(O^iPr)}$_2$	1500	10	80	173.0	101.3	1.07
9	{Yb_2(**2**)$_2$(O^iPr)(OH)}	500	10	95	68.5	69.0	1.11

[a] Concentration of initiator based on per alkoxide initiating group. [b] Determined from analysis of the ^{1}H NMR spectrum by integration of the methine region (LA, 4.96 – 5.04 ppm; PLA, 5.10 – 5.22 ppm). [c] Theoretical M_n = (144.12 x $[LA]_0/[I]_0$) x (Conv. / 100) + Mw of end groups (O^iPr + H). [d] As determined by SEC (THF) using triple detection methods.

Similar to trials under milder conditions, {Sm_2(**2**)$_2$(O^iPr)(OH)} is more active than {Yb_2(**2**)$_2$(O^iPr)(OH)} at elevated temperatures, albeit simultaneously sacrificing a degree of molecular control (Entry 6 *vs* 9, Table 3.4). This lower observed molecular weight seen in the Sm analogue is likely due to the possible reaction of the hydroxide acting as a chain-transfer agent. Di-hydroxide {Sm(**2**)OH}$_2$ showed very little activity with observed conversion likely the result of protic impurities present in the polymerisation mixture. These findings suggest that the hydroxide is not an effective initiating group for ring-opening but has the potential to generate unwanted transesterification. The increase in reaction temperature is shown to have a pronounced effect on the activity of terminal alkoxide complexes, {Ln(**1**)(O^iPr)}$_2$. Under comparable conditions to the bridging alkoxide motifs, excellent rates and good molecular control can be seen for {Sm(**1**)(O^iPr)}$_2$ (Entry 4 & 5, Table 3.4). The Yb^{3+} analogue produces low dispersity polymer yet a significant variance is seen between experimental and recorded molecular weights. Inability to reach theoretical molecular weights is likely the result of a degree of chain transfer.

3.3.3. Polymerisations of *rac*-LA under melt conditions: 130 °C

Whilst rarely reported for lanthanide systems, the ROP behaviour under melt conditions follows closely to commonly used industrial conditions for the production of PLA. These conditions can also highlight any thermal instability of the complex and so has become an integral test in testing a complexes industrial aptitude. From melting the *rac*-LA:initiator mixture at 130 °C, the polymerisation is monitored for 5 minutes or until gelation is apparent {$[LA]_0$:$[I]_0$ = 900:1}. Subsequent quenching by addition of excess CH_2Cl_2 allows extraction of the crude material.

All complexes were found to be highly active under melt conditions with highest conversions achieved for {Nd(**2**)(O^iPr)}$_2$. No significant difference in activity between Sm^{3+} and Yb^{3+} is seen, with {Yb(**1**)(O^iPr)}$_2$ and {Yb_2(**2**)$_2$(O^iPr)(OH)} both yielding lower dispersity polymer than the Sm^{3+} analogues (Entry 2–5, Table 3.5). This change in activity between solution and solvent free conditions has previously been shown for organocatalytic ROP of thioureas and bases and theorised to be due strong hydrogen bonding between the catalyst and incumbent monomer in solution.[79] Like in solution studies, {Nd(**2**)(O^iPr)}$_2$ produced exceptional control with a closeness of fit of theoretical and observed M_n values and very low dispersities (Entry 1, Table 3.5). No observed stereoselectivity was seen for all initiators under melt or high temperature solution conditions.

Table 3.6. Polymerisation data for the polymerisation of *rac*-LA at feed ratios of 900:1 {$[LA]_0$:$[I]_0$}. $[LA]_0$ = 0.69 M, T = 130 °C.

Entry	Initiator	Time (min)	Conv. (%)[a]	M_n^{theo} (kg mol^{-1})[b]	M_n^{SEC} (kg mol^{-1})[c]	$Đ$ [c]
1	{Nd(**2**)(O^{i}Pr)}$_2$	5	95	123.1	122.1	1.05
2	{Sm(**1**)(O^{i}Pr)}$_2$	5	74	96.0	136.4	1.45
3	{Sm$_2$(**2**)$_2$(OiPr)(OH)}	5	82	106.4	136.4	1.45
4	{Yb(**1**)(O^{i}Pr)}$_2$	5	91	118.1	128.8	1.24
5	{Yb$_2$(**2**)$_2$(O^{i}Pr)(OH)}	5	82	106.4	62.1	1.36

[a] Determined from analysis of the ^{1}H NMR spectrum by integration of the methine region (LA: 4.96 – 5.04 ppm; PLA: 5.10 – 5.22 ppm). [b] M_n^{theo} = (144.12 x $[LA]_0/[I]_0$) x (Conv. / 100) + Mw of end groups (O^{i}Pr + H). [c]As determined by SEC (THF) using triple detection methods.

3.3.4. Kinetic analysis of lanthanide initiators

With complete conversion seen in all closed vessel experiments where {Nd(**2**)(O^{i}Pr)}$_2$ was the chosen initiator it is likely completion is reached well before quenching. In order to fully test the activity of this catalyst kinetic analysis was performed. 'In-situ' ^{1}H NMR spectroscopic analysis allows the collection of significant data without disturbing the mixture. Whilst it is limited by a lack of stirring it is commonly used for the determination of rate data for catalytic reactions. Initially testing under mild conditions (CD_2Cl_2, 25 °C) a high catalyst loading was chosen {$[LA]_0$:$[I]_0$ = 150:1} to reduce the production of high molecular polymer which would ultimately lead to a mass transfer limited polymerisation. Under these conditions high conversions (95%) were achieved within 45 minutes (Figure 3.21). Linearisation of this data shows a pseudo-first order fit with an observed rate constant (k_{obs}) of 9.2 × 10^{-2} min^{-1}.

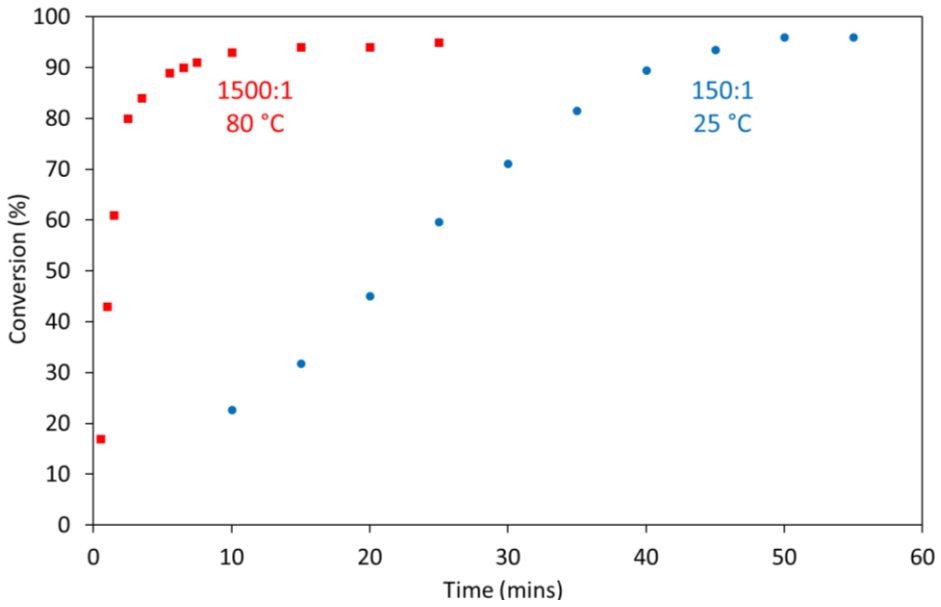

Figure 3.21. Conversion versus time for the polymerisation of *rac*-LA catalysed by {Nd(**2**)(O^iPr)}$_2$. ■ *ex-situ* sampling {[LA]$_0$:[I]$_0$ = 1500:1, [LA]$_0$ = 0.69 M, toluene, 80 °C}. ● *in-situ* ^{1}H NMR analysis {[LA]$_0$:[I]$_0$ = 150:1, [LA]$_0$ = 0.69 M, CD_2Cl_2, 25 °C}.

At 80 °C the high rate of polymerisation meant no data collection was possible on the NMR time-scale at low catalyst concentrations {[LA]$_0$:[I]$_0$ = 1500:1}. '*Ex-situ*' reaction monitoring was instead employed to extract aliquots of the stirred reaction mixture at set time intervals. This also allowed investigation of lower catalyst loadings and SEC analysis of the extracted samples. It is seen that within 4 minutes of addition of the reaction mixture to the oil bath set at 80 °C high conversion is reached (85%) with a plateau in the proceeding 20 minutes (Figure 3.22). Pseudo-first order plot of LA consumption shows a linear relationship under these conditions with a k_{obs}= 0.47 min^{-1} (Figure 3.22). This exceptional rate compares well with some of the most active lanthanide catalysts reported in the literature.[53,54,80] The non-origin intercept suggests a small induction period possibly highlighting the breakup of the dinuclear species upon initial ring-opening.

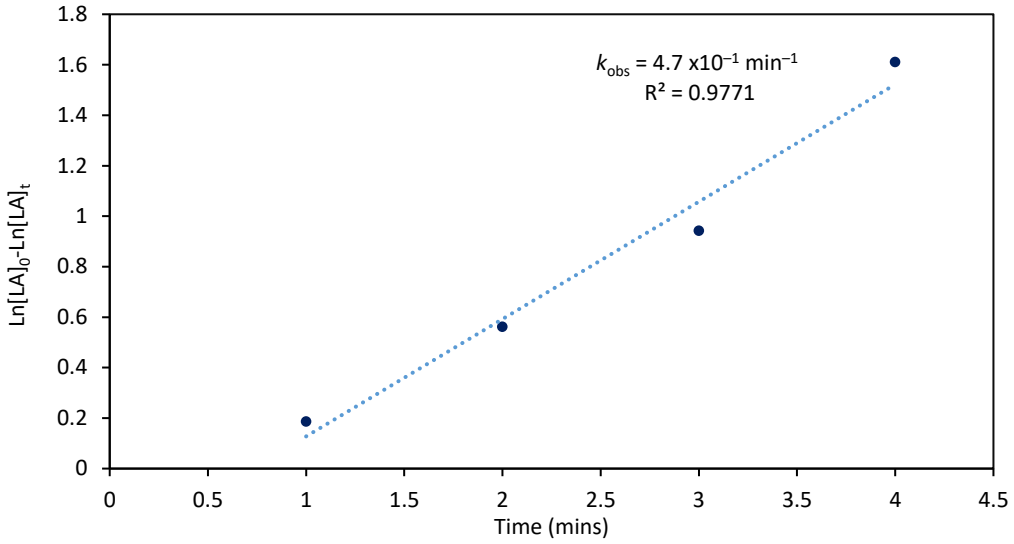

Figure 3.22. Pseudo first order plot for the polymerisation of *rac*-LA catalysed by {Nd(**2**)(O^{i}Pr)}$_2$, monitored via *ex-situ* sampling {[LA]:[I] = 1500:1, [LA]$_0$ = 0.69 M, toluene, 80 °C}.

SEC analysis of polymer extracted shows a linear increase in M_n reaching 160 kg mol^{-1} after 4 minutes (Figure 3.23). The resultant plateau showed no increase in polymer molecular weight or dispersity after 25 minutes. This highlights that at very low lactide concentration the catalytically active species does not participate in transesterification. Additionally, the agreement of this result to closed vessel methods, shows no significant impurities are added to the system upon sampling. A gradient of 1434 g mol^{-1} for the plot of M_n *vs* conversion relates closely to the expected value of 1500 based on the feed ratio, further supporting a well-controlled polymerisation with little deactivation or chain transfer (Figure 3.23).

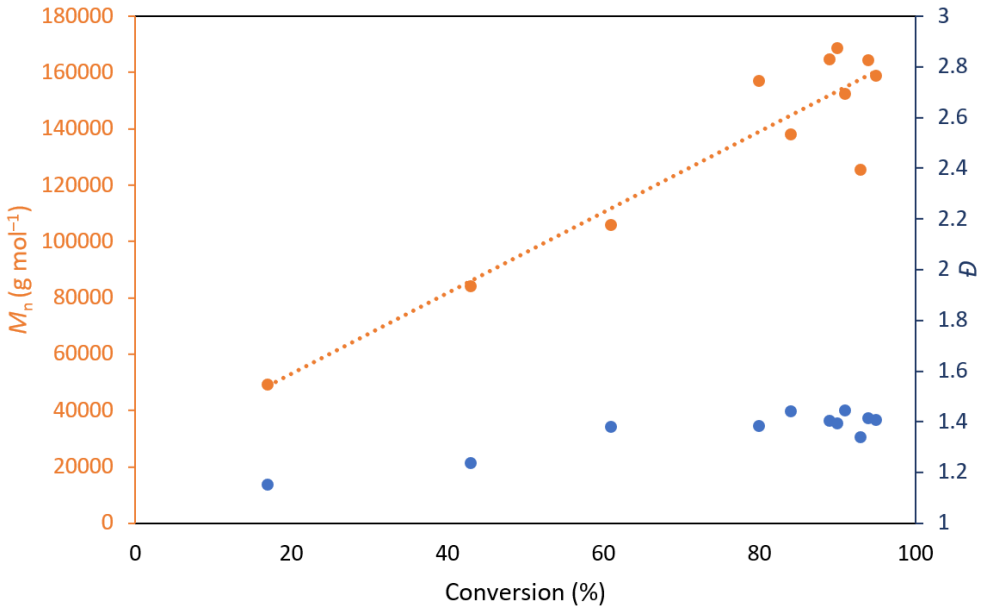

Figure 3.23. Plot of M_n^{SEC} and *Đ* versus conversion for the polymerisation of *rac*-LA catalysed by {Nd(**2**)(O^{i}Pr)}$_2$, monitored via *ex-situ* sampling {[LA]:[I] = 1500:1, [LA]$_0$ = 0.69 M, toluene, 80 °C}.

3.3.5. MALDI-ToF analysis

MALDI-ToF is a method of mass spectrometry commonly used to examine polymer microstructure. Between the plotted signals polymers of varying chain length the mass of the repeating unit can be established. In the case of PLA this is repeat units of 72.06 g mol^{-1} with transesterified polymer showing a 2n+1 (n = number of the repeat units) repeating unit (Figure 3.24). The residual mass is equivalent to the molecular weight of the end groups and a molecule of Na^+ or K^+. If a polymer is found to have no end groups, it is suggested to be cyclic in nature. MALDI-ToF performed on all PLA samples of suitable molecular weight produced from polymerisation with {Nd(**2**)(O^{i}Pr)}$_2$, {Ln(**2**)(O^{i}Pr)}$_2$ and {Ln$_2$(**2**)$_2$(O^{i}Pr)(OH)} were shown to be linear with end groups of –O^{i}Pr and H (Figure 3.24). All PLA species were found to contain a degree of transesterification resulting in polymer with a repeating unit of 72 g mol^{-1}.

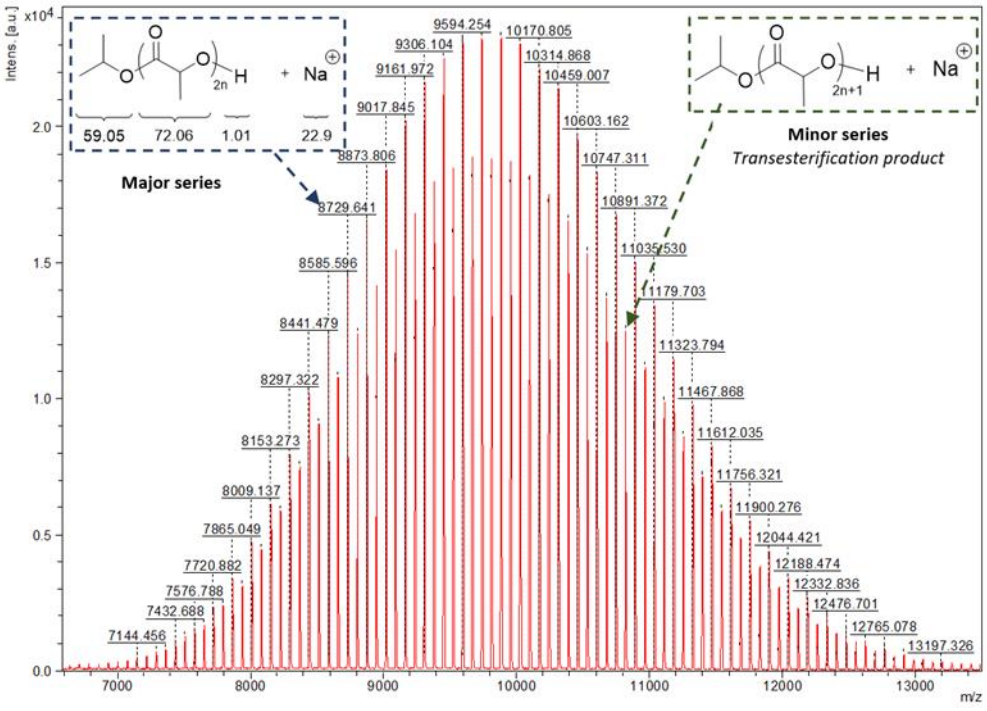

Figure 3.24. MALDI-ToF for PLA produced from the polymerisation of *rac*-LA with {Sm(**1**)(O^{i}Pr)}$_2$ at ratios of 150:1 ([LA]$_0$:[I]$_0$) in CH_2Cl_2, 25°C. M_n^{SEC}(kg mol^{-1}) = 5.8, M_n^{Theo}(kg mol^{-1}) = 8.7.

3.3.6. *'in-situ'* analysis of the catalytically active lanthanide species

The unprecedented ability to characterise certain synthesised lanthanide complexes in the solution state gives the opportunity to further probe the catalytically species through monitoring changes in the NMR spectra during polymerisation. Whilst all species were highly active under melt conditions, a stark difference in reactivity was shown under 'mild' conditions (CH_2Cl_2, 25 °C) between {Nd(**2**)(O^iPr)}$_2$ and {Sm(**1**)(O^iPr)}$_2$. This is potentially due to a stronger Ln–O^iPr bond when the alkoxide is terminal as opposed to being bridging. In order to investigate this further *'in-situ'* NMR spectroscopic studies were carried out on the polymerisation of *rac*-LA and {Sm(**1**)(O^iPr)}$_2$ in CD_2Cl_2 at 25 °C. After 24 hours a stoichiometric reaction {$[LA]_0 = [O^iPr]_0$} showed no further changes in the ^{1}H NMR spectra with the presence of LA, indicated by a quartet at 4.96 – 5.01 ppm still visible. Whilst the complex appears intact a small shift is observed in the aromatic signals. Additionally, the appearance of new resonances previously shown to be assigned to an isopropoxy lactate molecule are visible in equal ratio to that of residual lactide.[81] Due to turgid nature of this polymerisation the acquisition of DOSY data was possible (Figure 3.25). Diffusion constants of LA and signals equivalent to a ring opened lactate molecule were shown to diffuse at a similar rate to that of the shifted lanthanide complex. As these values are not similar to that of the solvent molecules of similar hydrodynamic radii it is hypothesised a coordination of both lactide and lactate to the Sm^{3+} species.

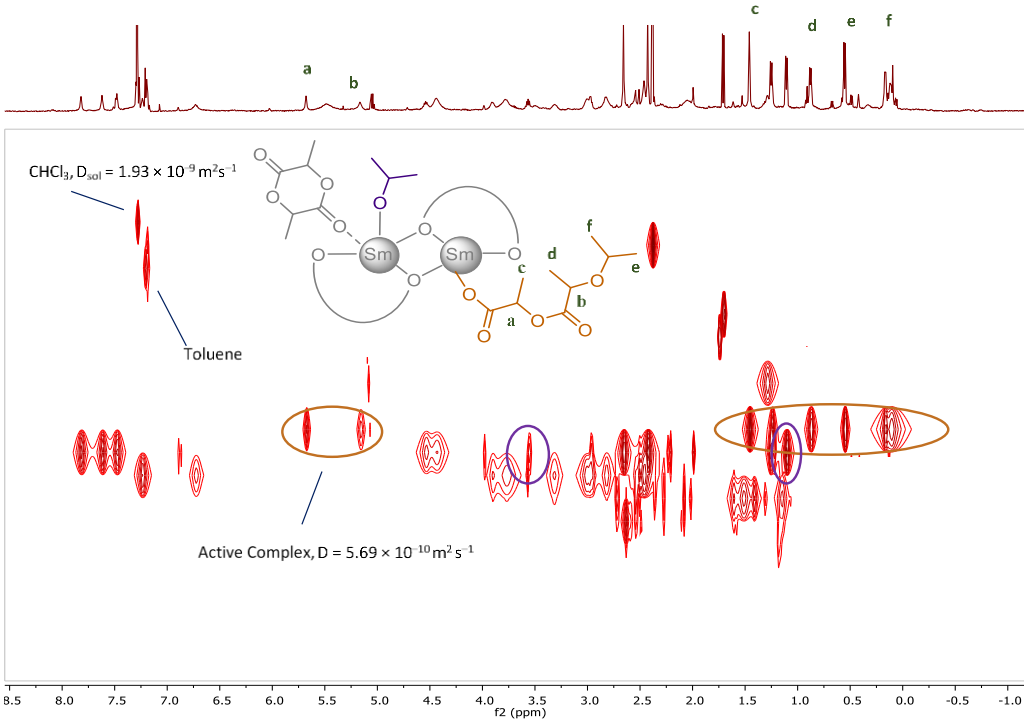

Figure 3.2528. ^{1}H DOSY NMR of a polymerisation of *rac*-LA initiated with {Sm(**1**)(O^{i}Pr)}$_2$ at a 2:1 ratio {[LA]$_0$:[{Sm(**1**)(O^{i}Pr)}$_2$]$_0$}, [LA]$_0$ = 0.069 M, 25 °C, 5 hours, $CDCl_3$.

Decreasing the catalyst loading to 20:1 {[LA]$_0$:[{Sm(**1**)(O^{i}Pr)}$_2$]$_0$} and leaving at temperature for the same time frame (24h, CD_2Cl_2, 25 °C), resulted in an increase in theoretical polymer weight with conversions of 73% seen. DOSY NMR of the spectra shows signals corresponding to the metal complex diffusing at a lower rate than what is seen from the pure complex or the stoichiometric reaction mixture (Figure 3.26). Additionally, diffusing at a similar rate are signals corresponding to the methine proton in PLA and a molecule of LA. Along with evidence of a bound lactide molecule from stoichiometric reactions it is possible to theorise the identification of a propagating species in solution along with the interaction of a LA molecule in the same coordination sphere. The resonances of metal bound isopropoxide seen in stoichiometric reactions also suggests this species retains one of the isopropoxide initiating groups. This agrees well with the variation in observed and calculated molecular weights as initial feed ratios are calculated per initiating group not per complex molecule. Due to an apparent plateau in LA conversion, it is proposed this complex becomes stable under these conditions, with the LA molecule coordinated to the 'unproductive' metal centre. It is probable that the metal centres are cooperative similar to mechanisms proposed for certain metal catalysts designed for ring-opening copolymerisation (ROCOP) of epoxides and CO_2, and cyclic carbonate synthesis.[82–85]

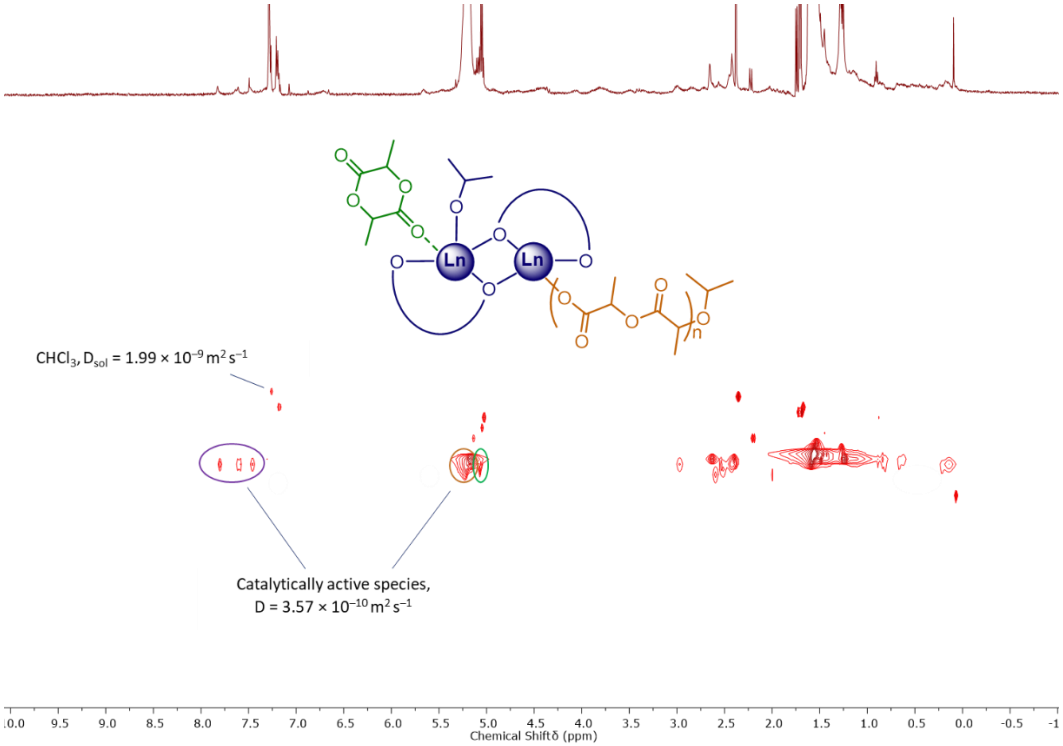

Figure 3.26. ^{1}H DOSY NMR of a polymerisation of *rac*-LA initiated with {Sm(**1**)(O^{i}Pr)}$_2$ at a 20:1 ratio {[LA]$_0$:[{Sm(**1**)(O^{i}Pr)}$_2$]$_0$}, [LA]$_0$ = 0.069 M, 25 °C, 5 hours, $CDCl_3$.

In order to validate this proposed mechanism as well as DOSY as a method of *in-situ* polymer analysis, M_n from diffusion coefficients was calculated and compared to the theoretical values. The effect of polymers in solution causes an increase in viscosity and a greater deviation from the hard-sphere of the Stokes-Einstein equation, decreasing the accuracy as molecular weight increases.[72,73,86]

Table 3.7. Reactivity of {Sm(**1**)(O^{i}Pr)}$_2$ with *rac*-LA, followed DOSY NMR spectroscopy

Entry	*rac*-LA equiv.	D[e] 10^{-9} m^2 s^{-1}	D_{sol}[e] 10^{-9} m^2 s^{-1}	DOSY M_n[f] g mol^{-1}	M_n^{theo} [g] g mol^{-1}	M_n^{SEC} [h] g mol^{-1}
1	-	0.589	1.77	1269	1236	-
2[b]	2	0.569	1.93	1371	1380	-
3[c]	20	0.357	1.99	4091	3830	-
4[c,d]	20	0.427	1.97	2668	2584	2800

{Sm(**1**)(O^{i}Pr)}$_2$ (I) in $CDCl_3$ (1 mL), [I]$_0$ = 2.4 mmol L^{-1}. [b] [I]$_0$ = 2.4 mmol L^{-1}, [*rac*-LA]$_0$ = 4.8 mmol L^{-1}, reaction left at 25 °C for 5 hours under Ar. [c] [I]$_0$ = 0.24 mmol L^{-1}, [*rac*-LA]$_0$ = 4.8 mM, reaction left at 25 °C for 24 hours under Ar. [d] After 24 h at 25 °C, the reaction was quenched by bubbling air through the system and the sample analysed. [e] Diffusion constants taken from the middle of the contour plot mapped using a peak heights fit method. [f] Estimated from the calculated hydrodynamic radii of the diffusing species.[68,74] [g] Calculated as: ([rac-LA]$_0$/[I]$_0$) × M_r(LA)× conversion/100) + M_r(I), where M_r = 1236.5 g mol^{-1}, conversion is taken from integration of the methine region of the ^{1}H NMR spectrum. [h] Determined by SEC in THF.

Whilst this is the case calculated M_n^{DOSY} values are in good agreement with calculated M_n^{theo} values (Table 3.7) assuming a bound species as proposed (Figure 3.26 & 3.27). Quenching of the solution through addition of air showed an increase in the diffusion rate of the polymeric species with molecular weight estimation closely aligning to the theoretical value of the free polymer. Isolation and SEC analysis of this polymer gave molecular weight values of 2800 g mol^{-1}. This agreement between the three methods of detection further highlights the potential of DOSY as a tool to calculate molecular weights, avoiding the use of external standards which are chemically dissimilar to the analyte such as in SEC. The quenching of the polymer and proceeding increase in diffusion rate further supports the identification of the catalytically active species and mechanism of propagation under these conditions, a phenomenon which has not previously been observed.

3.4. Ring-opening copolymerisations (ROCOP) using Ln^{3+} complexes

The dinuclearity and proposed binuclear mechanism of polymerisation makes synthesised lanthanide bipyrrolidine complexes ideal candidates for ring-opening copolymerisation studies.[82,85,87] The alternating co-polymerisation of epoxides and CO_2 or epoxide and anhydride as a method to produce polycarbonates and polyesters has long been discussed as an avenue of great potential in polymer synthesis.[88,89] Epoxide and CO_2 copolymerisation presents a method of CO_2 utilisation, whilst the great variability in epoxides and anhydrides presents an extensive range of potential polyesters as discussed in a seminal review by Williams and coworkers.[56] The innumerable range of potential epoxides which can be synthesised has allowed in recent years the exploitation of bio-renewable waste feedstocks to produced fully renewable polycarbonates and polyesters.[90–95]

In the field of ROCOP, monomer selectivity is highly prized, with the potential formation of cyclic carbonate synthesis or polyether mis-insertion limiting polymer properties.[96,97] Alongside this, stereoselectivity, like in ROP of LA, is shown to have pronounced impact on polymer properties, making catalyst choice highly significant.[93,98–100] In a recent study, supported by a combination of experimental and computational studies, the chemoselectivity of a dinuclear zinc catalyst (**48**) developed by Williams and co-workers was shown.[82,101] From a monomer mixture of phthalic anhydride, ε-caprolactone and epoxide the selectivity could be tuned by the addition of CO_2. Computational studies showed a higher activation barrier for the ROP of the epoxide, instead highlighting ROCOP as a lower energy pathway (Scheme 3.5). This level of control opens the opportunity for controlled block polymers, a highly attractive macrostructure in polymer chemistry.[88,102,103]

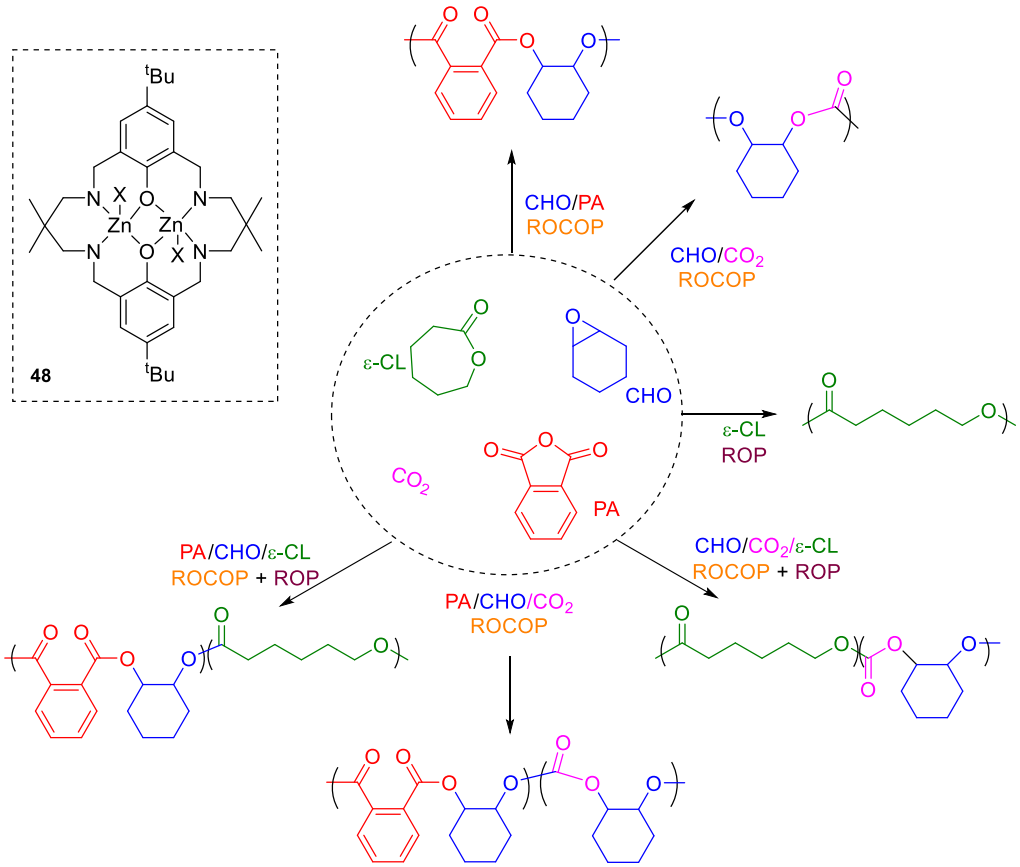

Scheme 3.5. Routes to a range of polyesters and polycarbonates synthesised by Williams and coworkers.[82]

In order to further test the versatility of our best performing rare earth bipyrrolidine complexes, initial investigations were performed on the copolymerisation of cyclohexene oxide (CHO) and phthalic anhydride (PA).

3.4.1. Copolymerisation of phthalic anhydride and cyclohexene oxide

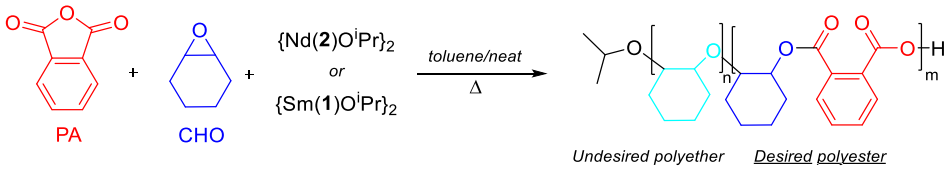

Scheme 3.6. ROCOP of phthalic anhydride and cyclohexene oxide using di-alkoxide initiators.

Initial ROCOP studies of PA and CHO were carried out in toluene at 100 °C using {Nd(**2**)O^{i}Pr}$_2$ or {Sm(**1**)O^{i}Pr}$_2$ (Scheme 3.6). High temperatures were required to dissolve the PA into the reaction mixture. At feed ratios of 300:300:1 {[CHO]$_0$:[PA]$_0$:[I]$_0$, [PA]$_0$ = 0.5 M} moderate activity is shown for both catalysts with {Sm(**1**)O^{i}Pr}$_2$ performing the best giving 70% conversion of PA after 24 hours (Table 3.6). Selectivities were able to be calculated from the signals corresponding to the (O)CH- group on the polyester and ester endgroup (4.8 – 5.2 ppm) against that of the polyether groups (3.41 – 3.60 ppm) (Figure 3.27).[87] Both catalysts

were shown to give good selectivities with a small degree of polyether enchainment (<10%). Bimodality in the SEC trace suggests a small degree of cyclohexenediol is present and has acted as a CTA, a common problem in this field.[104] A large discrepency between calculated and obsevered molecular weights supports this poor control, another feature not uncommon in ROCOP studies.[104–106]

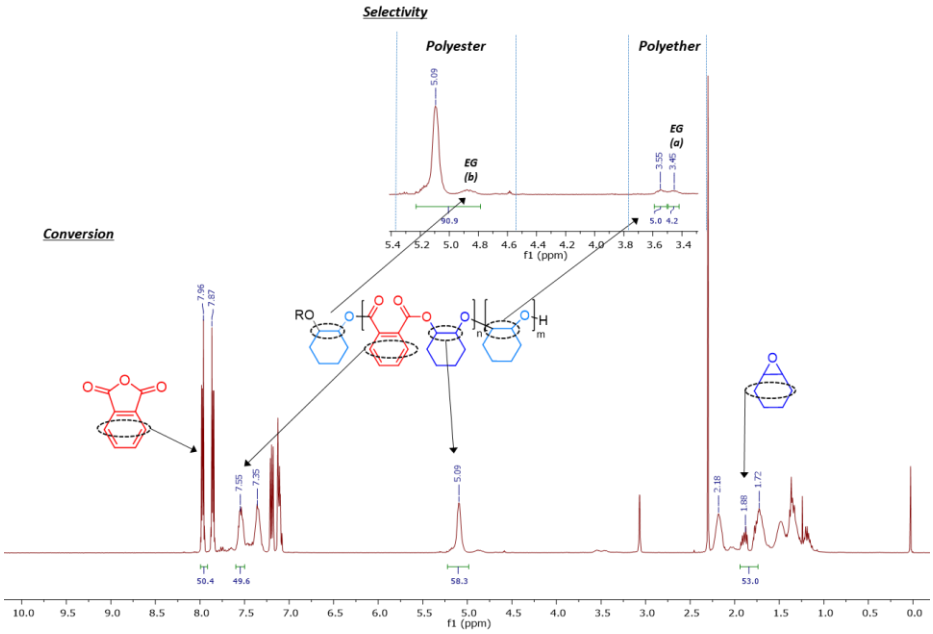

Figure 3.27. ^{1}H NMR spectra of the crude material from the solution polymerisation of PA and CHO using {Nd(**2**)O^{i}Pr}$_2$ as initiator.

Table 3.8. Solution state ROCOP polymerisation data in toluene.[a]

Entry	Initiator	PA Conv. (%)[b]	Select. (%)[c]	M_n^{theo} (kg mol^{-1})[d]	M_n^{SEC} (kg mol^{-1})	$Đ$
1	{Nd(**2**)O^{i}Pr}$_2$	50	91	20.9	5.6	1.21
2	{Sm(**1**)O^{i}Pr}$_2$	70	91	29.2	5.5	1.05

[a] 100 °C, 24 h, {[PA]:[CHO]:[I] = 300:300:1}, [PA] = 0.5M. [b] Conversion of PA from integration of the aromatic regions in the polymer (7.59 – 7.28 ppm) against the monomer region (7.80 – 8.02 ppm). [c] Derived from the ratio of C*H* groups on cyclohexene oxide units from polyester (5.01 – 5.38 ppm) *vs* polyether units (3.51 – 3.60 ppm). [d] Calculated based on the conversion of each monomer.

MALDI-ToF spectra of the purified polymer shows repeating units of 246 m/z indicative of the repeating unit of the polyester (Figure 3.28). The presence of other series supports the presence of small quantities of polyether in the copolymer as well as cyclic species. In order to increase conversion, the use of CHO as the neat solvent was used.[56,105] At feed ratios of 200:200:1 {[CHO]$_0$:[PA]$_0$[{Nd(**2**)O^{i}Pr}$_2$]$_0$} temperatures of 125 °C were required to fully dissolve the PA. Taking aliquots from the stirred mixture it was possible to track the initial

profile of polymerisation to investigate how monomer selectivity changes over time (Figure 3.29).

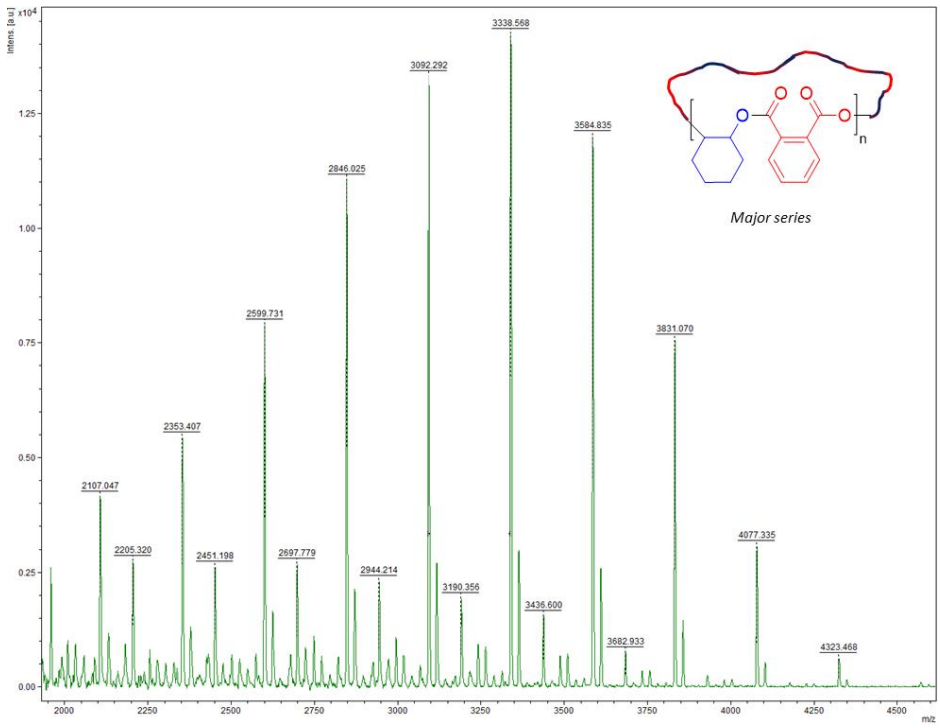

Figure 3.28. MALDI-ToF spectra for the ROCOP of phthalic anhydride and cyclohexene oxide using {Nd(**2**)O^{i}Pr}$_2$. Repeating units of 246.27 g mol^{-1} indicate the repeating unit of the polyester.

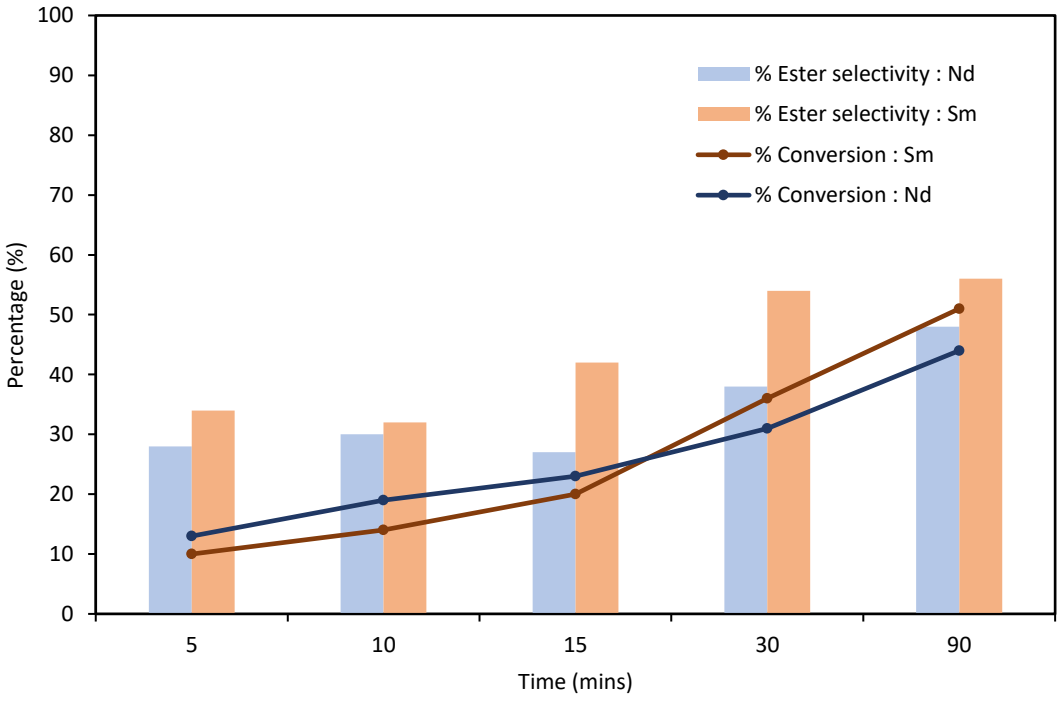

Figure 3.29. Conversion and Selectivity over time for the ROCOP of PA and CHO using {Nd(**2**)O^{i}Pr}$_2$ and {Sm(**1**)O^{i}Pr}$_2$ at feed ratios of 200:200:1 {[CHO]$_0$:[PA]$_0$:[I]$_0$}, 125 °C, no solvent.

After 5 minutes, low conversion of PA is recorded with very low ester selectivity (25 – 35 %). Over time the increase in conversion of PA is marked with an increase in the polyester selectivity. This suggests a large proportion of polyether is produced upon initial heating and a switch to ROCOP occurs as the PA dissolves. Whilst the catalytically active species is different this is supported by reported computational studies from Williams and co-workers, showing a lower energy barrier for ROCOP *vs* ROP of CHO.[82] Overall the bridging phenolate catalyst, {Sm(**1**)O^{i}Pr}$_2$ proved more selective and more reactive than {Nd(**2**)O^{i}Pr}$_2$. This contrast with results obtained for the ROP of LA where {Nd(**2**)O^{i}Pr}$_2$ consistently outperformed {Sm(**1**)O^{i}Pr}$_2$. At feed ratios of 800:100:1 {[CHO]$_0$:[PA]$_0$[{Nd(**2**)O^{i}Pr}$_2$]$_0$} it was possible to reduce the temperature required to dissolve PA to 80 °C. Under these conditions 83% conversion could be achieved within 90 minutes. Despite the reduced temperature the selectivity remained low throughout the study with a final selectivity of 50%. SEC analysis showed unimodal traces indicative of a copolymer containing both polyester and polyether units. Plotting M_n *vs* conversion a linear increase in M_n is seen suggesting controlled polymerisation. The non 0,0 intercept in M_n highlights a deviation from linearity in the initial minutes likely due to the significant quantity of polyether polymerisation seen. The increase in dispersity suggests that the polymerisation proceeds with a degree of chain transfer and deviates from the idealised propagation pathway at high conversion of PA.

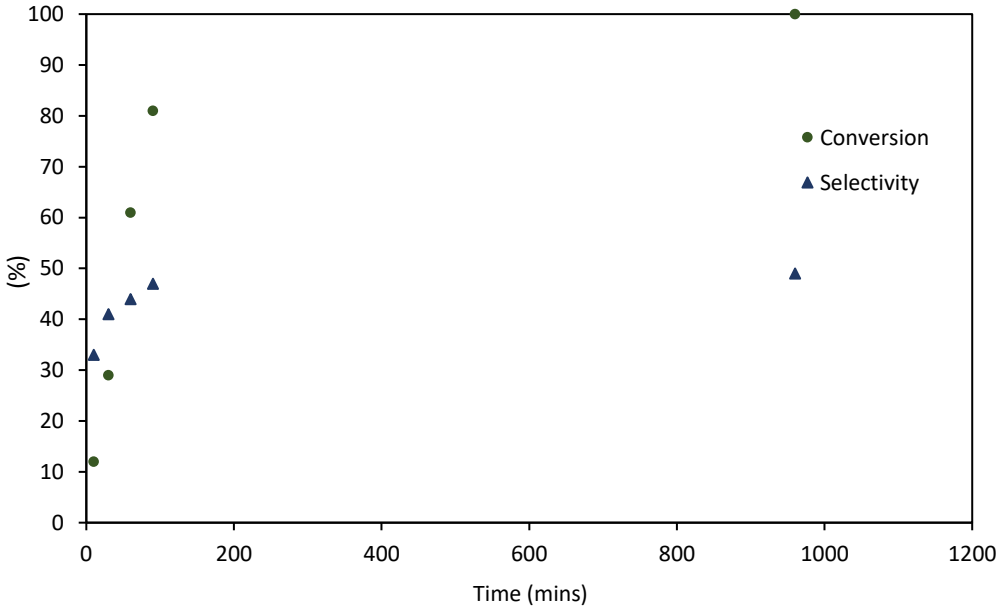

Figure 3.30. Conversion and selectivity over time for the ROCOP of PA and CHO using {Nd(**2**)O^{i}Pr}$_2$ at feed ratios of 800:100:1 {[CHO]$_0$:[PA]$_0$:[I]$_0$}, 80 °C, no solvent. Conversion is measured from [(1 - {[PA]$_t$/[PA]$_0$}) × 100].

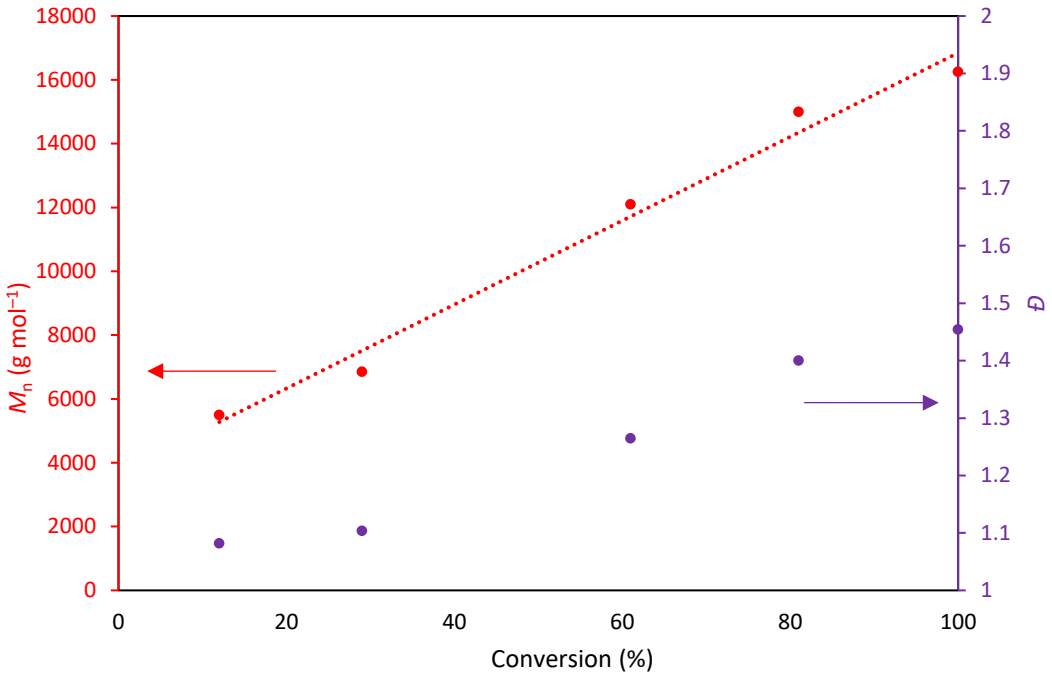

Figure 3.31. M_n^{SEC} and $Đ$ versus conversion for the ROCOP of PA and CHO using {Nd(**2**)O^{i}Pr}$_2$ at feed ratios of 800:100:1 {[CHO]$_0$:[PA]$_0$:[I]$_0$}, 80 °C, no solvent.

3.5. Conclusions and future work

In this chapter the synthesis of dinuclear bis(phenolate) lanthanide complexes of Nd^{3+}, Sm^{3+} and Yb^{3+} bearing different coordination spheres were reported. Extension to La^{3+}, Y^{3+} and Gd^{3+} reagents were unsuccessful. Solid state complexes were reported alongside solution state NMR analysis where possible, representing some of the first fully characterised Ln^{3+} complexes in the literature. Mild isotropic shifting in complexes of {Sm(**1**)O^{i}Pr}$_2$ allowed investigation into the hydrolytic sensitivity of synthesised complexes, another rarely reported feature with large significance in lanthanide chemistry. The synthesis and characterisation of mono, and di-hydroxide bound complexes in the solution state through the addition of water, gave an estimation for the degradation rates of each complexes. {Yb(**1**)O^{i}Pr}$_2$ was very sensitive to water, degrading completely to pro-ligand and Yb(OH)$_3$ over a 5 hour period, whilst the {Sm(**1**)O^{i}Pr}$_2$ degraded over a 36 hour period to {Sm(**1**)OH}$_2$.

Upon testing synthesised complexes for ROP of *rac*-LA it was shown the bridging dialkoxide species {Nd(**2**)O^{i}Pr}$_2$ was the most active under mild conditions. In contrast, {Sm(**1**)O^{i}Pr}$_2$ was less active under these conditions representing a potential energetic difference between the terminal- and bridging- alkoxide groups. This reactivity gap was bridged at elevated ROP conditions, with both di-alkoxides being highly active whilst maintaining a good control throughout propagation. '*Ex-situ*' kinetic investigations using {Nd(**2**)O^{i}Pr}$_2$ at loadings of 0.06 mol% showed complete conversion was achieved within 4 minutes, outperforming the industrial standard, tin(II)octanoate.[107] The lanthanide contraction resulted in a pronounced difference structurally, with Yb^{3+} complexes showing shorter Ln-μ-O bond distances than the analogous Sm^{3+} and Nd^{3+} complexes. In agreement with literature this resulted in a poorer ROP performance. Unlike many literature studies no selectivity switch was observed between the metals with the most selective {Yb(**1**)O^{i}Pr}$_2$ producing only mildly heterotactic PLA (P_r = 0.71). This lack of selectivity completes a story of serendipity with bipyrrolidine ligands, with judicial choice of metal centre leading to the generation of isotactic, heterotactic or atactic PLA.

Stoichiometric reactions monitored via diffusion NMR spectroscopy gave evidence behind a concerted polymerisation mechanism for {Sm(**1**)O^{i}Pr}$_2$, with both metal centres fielding different roles in polymerisation. Molecular weight estimations from diffusion rates were shown to be a complimentary technique to traditional SEC analysis supporting the theory of binuclear cooperativity. The potential use of polymer internal standards of well-defined molecular weights could be used to greater validate these DOSY molecular weights

measurements, further developing the technique which could act as a complimentary tool to researchers.

The ROCOP of cyclohexene oxide and phthalic anhydride was investigated to test the versatility of synthesised metal complexes to act as polymerisation catalysts. Both {Nd(**2**)O^{i}Pr}$_2$ and {Sm(**1**)O^{i}Pr}$_2$ displayed only mild activity in solution whilst maintaining high polyester selectivity. Higher temperature experiments in neat epoxide yielded an increase in activity albeit with a severe reduction in selectivity. Kinetic experiments suggest this selectivity issue is a product of the initial sequencing. Despite this, molecular weight was shown to increase linearly with conversion evidencing controlled ROCOP. Optimisation of these complexes for ROCOP could involve adaption of the backbone. Whilst this study has mainly focused on the effects of metal choice, it has been shown by Coates and co-workers that variation of the *para*-substituted group caused a significant variation in rate and selectivity of ROCOP.[98] In a follow up study using a di-acid chain transfer agent (CTA), excellent control over polymer growth was achieved with a variety of functional epoxides and anhydrides.[108] The addition of a di-acid CTA prevents unwanted bimodality appearing from unwanted acid monomer residues. This work could equally be applied to synthesised systems, emulating the bi-functional lanthanide arylalkoxides reported by Shen and coworkers.[37]

Recent literature advances have shown how well-defined ABA block copolymers of PLLA–*b*–{PA:PO}–*b*–PLLA could be produced from sequential addition and from monomer mixtures.[88] Using catalysis to this effect presents a large spectrum of possible polymer conformations and properties. With PLA coming under increasing scrutiny for its poor degradability it falls upon scientists to deliver alternatives.[109] Due to the variation in reactivity shown for ROCOP and ROP using {Nd(**2**)O^{i}Pr}$_2$ and {Sm(**1**)O^{i}Pr}$_2$ exploitation of the reaction conditions might equally yield controlled block copolymers from a monomer mixture.

Whilst this study focuses on the use of PA and CHO for comparison with literature catalysts, an expansion of this work could involve further screening with a variety of different epoxides and anhydrides.[98,110] To gain a further understanding of functional group tolerance of Ln catalysts ROCOP with more complex and 'bio-sourced' epoxides and anhydrides could be a potential avenue. This follows a current focus in literature aimed at exploiting alkene functionality in naturally occurring chemicals to produce epoxides and hence polymers.[90,92,104,111]

The ROP of 6-membered cyclic carbonates derived from sugars (Scheme 3.7) presents an opportunity to expand material properties through catalysis.[112–115] These systems are of interest within bio-medical engineering due their biocompatibility, facile degradation, and the possibility to carry out post polymerisation modification of functional groups on the polymer.[116] Whilst the ring opening of 6-membered cyclic carbonates is generally seen as facile, with many organo-catalysts producing poly(carbonates) to good effect, issues can occur with back biting and accessing high molecular weights. A metal-based system could potentially provide a more controlled and regio-selective polymerisation, as seen for the ROP of LA.

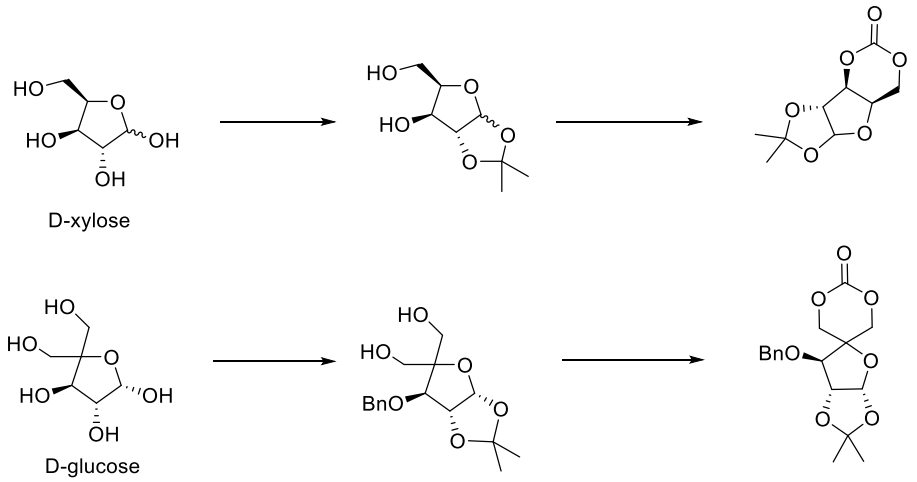

Scheme 3.7. Synthesis of 6-membered cyclic carbonates from *D*-xylose and *D*-glucose.[115]

Using a novel cyclic carbonate based around D-mannose as reported by Gregory *et al*, initial investigations were carried out using $\{Nd(\mathbf{2})O^{i}Pr\}_2$ as an initiator under mild conditions (Scheme 3.8).[117] Complete conversion was seen within 5 minutes at a ratio of 50:1 and 500:1 $\{[M]_0:[I]_0\}$. This result is significantly faster than the previously examined organocatalytic and metal based initiators (Table 3.9). In addition, higher molecular weights were achieved in comparison to the reported organocatalysts, indicating a lower degree of backbiting.

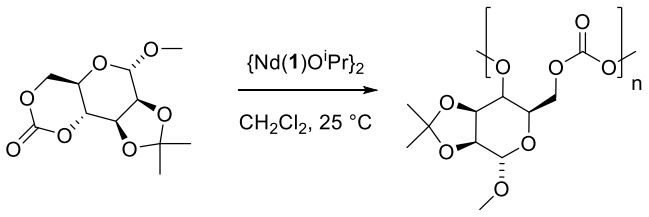

Scheme 3.8. Ring opening polymerisation of *D*-mannose derived cyclic carbonate.[117]

Table 3.9. Polymerisation data for the ROP of synthesised *D*-mannose cyclic carbonate, CH_2Cl_2, 25 °C.

Entry	Catalyst	$[M]_0:[I]_0$	Time (hours)	Conv. (%) [b]	M_n^{theo} (kg mol^{-1})	M_n^{SEC} (kg mol^{-1})	$Đ$ [c]
1	{Nd(**2**)O^{i}Pr}$_2$	50:1	0.08	100	13.1	17.5	1.33
2	{Nd(**2**)O^{i}Pr}$_2$	500:1	0.08	100	130.1	48.6	1.17
3[117]	TBD	50:1[a]	1	100	13.0	13.6	1.17
4[117]	TBD	150:1[a]	3	98	38.3	33.4	1.19

[a] In addition to an equivalent of TBD, 4-MeBnOH was added as co-initiator,[117] [b] Conversion is calculated from 1H NMR spectra of the crude material, [c] Theoretical molecular weight calculated from the conversion ((Conv. × $([M]_0/[I]_0)$ + Mw of end group), [d] Determined from SEC in $CDCl_3$ using RI methods.

MALDI-ToF experiments of polymer obtained at a ratio of 50:1 showed a gaussian distribution with a peak separation of 260.12 m/z indicating the desired repeating unit. A minor series (<4%) was apparent showing evidence of a small degree of backbiting. Alongside this, the poor molecular weight control at low catalyst loading indicates transesterification might be prevalent (Entry 2, Table 3.9). Further optimisation of the reaction conditions to facilitate the sampling and collection of M_n and $Đ$ data versus time could identify if deviation from the expected molecular weights is a result of transesterification/back-biting upon complete conversion. Furthermore, operating the polymerisation at lower temperature might reduce deviations from linear propagation whilst still maintaining an appreciable rate. In keeping with the search for more degradable PLA based polymers, copolymers of cyclic carbonate sugars and LA could provide enhanced degradation kinetics. The exceptionally high T_g reported for sugar based homopolymers could improve the thermal properties of PLA without the need for the development of the elusive stereo-block isotactic PLA.[116]

Overall, an extensive investigation into the versatility of the synthesised lanthanide complexes for polymerisation of a variety of monomers seems the next logical step, having already shown efficacy for the model system of LA. Initial tests have been very promising with preliminary studies showing potential applicability within the polymerisation of 6-membered cyclic carbonates and co polymerisations with epoxide and anhydride. Future

work around this area should be a high priority, looking to optimise the reaction conditions and expand on the current monomers used. This will allude to the impact of structural variations in the catalyst and ultimately provide a feedback system for continual improvement in catalyst design.

3.6. References

1 M. D. Jones, L. Brady, P. McKeown, A. Buchard, P. M. Schäfer, L. H. Thomas, M. F. Mahon, T. J. Woodman and J. P. Lowe, *Chem. Sci.*, 2015, **6**, 5034–5039.

2 M. D. Jones, S. L. Hancock, P. McKeown, P. M. Schafer, A. Buchard, L. H. Thomas, M. F. Mahon and J. P. Lowe, *Chem. Commun.*, 2014, **50**, 15967–15970.

3 J. Beament, M. F. Mahon, A. Buchard and M. D. Jones, *New J. Chem.*, 2017, **41**, 2198–2203.

4 R. H. Platel, L. M. Hodgson and C. K. Williams, *Polym. Rev.*, 2008, **48**, 11–63.

5 F. T. Edelmann, *Coord. Chem. Rev.*, 2017, **338**, 27–140.

6 A. Amgoune, C. M. Thomas and J.-F. Carpentier, *Pure Appl. Chem.*, 2007, **79**, 2013–2030.

7 J.-F. F. Carpentier, *Organometallics*, 2015, **34**, 4175–4189.

8 C. Bakewell, A. J. P. White, N. J. Long and C. K. Williams, *Angew. Chemie - Int. Ed.*, 2014, **53**, 9226–9230.

9 X. Zou, M. Li, P. Yan, J. Zhang, G. Hou and G. Li, *Dalton Trans.*, 2013, **42**, 9482–9.

10 P. Chen, H. Chen, P. Yan, Y. Wang and G. Li, *CrystEngComm*, 2011, **13**, 6237.

11 M. Seitz, A. G. Oliver and K. N. Raymond, *J. Am. Chem. Soc.*, 2007, **129**, 11153–11160.

12 F. M. Kerton, A. C. Whitwood and C. E. Willans, *Dalton. Trans.*, 2004, 2237–2244.

13 S. M. Guillaume and J.-F. Carpentier, *Catal. Sci. Technol.*, 2012, **2**, 898.

14 Y. Chapurina, J. Klitzke, O. D. L. Casagrande Jr, M. Awada, V. Dorcet, E. Kirillov and J.-F. Carpentier, *Dalton Trans.*, 2014, **43**, 14322–14333.

15 M. Bouyahyi, N. Ajellal, E. Kirillov, C. M. Thomas and J. F. Carpentier, *Chem. - A Eur. J.*, 2011, **17**, 1872–1883.

16 A. Amgoune, C. M. Thomas, T. Roisnel and J. F. Carpentier, *Chem. - A Eur. J.*, 2005, **12**, 169–179.

17 N. Ajellal, J.-F. Carpentier, C. Guillaume, S. M. Guillaume, M. Helou, V. Poirier, Y. Sarazin and A. Trifonov, *Dalton Trans.*, 2010, **39**, 8363–8376.

18 A. Amgoune, C. M. Thomas and J. F. Carpentier, *Macromol. Rapid Commun.*, 2007, **28**, 693–697.

19 W. Guerin, A. K. Diallo, E. Kirilov, M. Helou, M. Slawinski, J. M. Brusson, J. F. Carpentier and S. M. Guillaume, *Macromolecules*, 2014, **47**, 4230–4235.

20 M. Hong and E. Y. X. Chen, *Nat. Chem.*, 2016, **8**, 42–49.

21 W. H. Carothers, G. L. Borough, F. J. van Natta, G. L. Dorough and F. J. van Natta, *J. Am. Chem. Soc.*, 1932, **54**, 761–772.

22 D. Myers, A. Cyriac and C. K. Williams, *Nat. Chem.*, 2015, **8**, 3–4.

23 A. Buchard, R. H. Platel, A. Auffrant, X. F. Le Goff, P. Le Floch and C. K. Williams, *Organometallics*, 2010, **29**, 2892–2900.

24 J. Wang, Y. Yao, Y. Zhang and Q. Shen, *Inorg. Chem.*, 2009, **48**, 744–751.

25 J.-F. Gromada, J.; Mortreux, A.; Chenal, T.; Ziller, J. W.; Leising, F.; Carpentier, *Chem.;Eur. J.*, 2002, **8**, 3773–3778.

26 J. G. Barnhart,D.M.; Clark, D. L.;Huffman, J. C.; Vincent, R. L.; Watkin, *Inorg. Chem*, 1993, **32**,

4077–4083.

27 F. Bonnet, A. R. Cowley, P. Mountford, M. Road and O. Ox, *Inorg. Chem.*, 2005, **44**, 9046–9055.

28 T. P. Spaniol, J. Okuda and H. Ma, *Angew. Chemie - Int. Ed.*, 2006, **118**, 7982–7985.

29 K. Nie, L. Fang, Y. Yao, Y. Zhang, Q. Shen and Y. Wang, *Inorg. Chem.*, 2012, **51**, 11133–11143.

30 F. Bonnet, M. Visseaux, A. Pereira, F. Bouyer and D. Barbier-Baudry, *Macromol. Rapid Commun.*, 2004, **25**, 873–877.

31 S. M. Guillaume, M. Schappacher and A. Soum, *Macromolecules*, 2003, **36**, 54–60.

32 Y. Yang, K. Lv, L. Wang, Y. Wang and D. Cui, *Chem. Commun.*, 2010, **46**, 6150–6152.

33 H. E. Dyer, S. Huijser, N. Susperregui, F. Bonnet, A. D. Schwarz, R. Duchateau, L. Maron and P. Mountford, *Organometallics*, 2010, **29**, 3602–3621.

34 F. Bonnet, A. R. Cowley and P. Mountford, *Inorg. Chem.*, 2005, **44**, 9046–9055.

35 W. Zhao, C. Li, B. Liu, X. Wang, P. Li, Y. Wang, C. Wu, C. Yao, T. Tang, X. Liu and D. Cui, *Macromolecules*, 2014, **47**, 5586–5594.

36 W. Zhao, Y. Wang, X. Liu, X. Chen and D. Cui, *Chem. - An Asian J.*, 2012, **7**, 2403–2410.

37 K. Nie, T. Feng, F. Song, Y. Zhang, H. Sun, D. Yuan, Y. Yao and Q. Shen, *Sci. China Chem.*, 2014, **57**, 1106–1116.

38 X. Q. Lü, W. X. Feng, Y. N. Hui, T. Wei, J. R. Song, S. S. Zhao, W. Y. Wong, W. K. Wong and R. Jones, *Eur. J. Inorg. Chem.*, 2010, **2**, 2714–2722.

39 S. Liao, X. Yang and R. Jones, *Cryst. Growth Des.*, 2012, **12**, 970–974.

40 Y.-B. Shu and W.-S. Liu, *Dalton. Trans.*, 2015, **44**, 6353–6357.

41 W.-B. Sun, B.-L. Han, P.-H. Lin, H.-F. Li, P. Chen, Y.-M. Tian, M. Murugesu and P.-F. Yan, *Dalton Trans.*, 2013, **42**, 13397–403.

42 W. Gu, K. Nie, Q. Shen, Y. Yao and Y. Zhang, *Organometallics*, 2013, **32**, 2608–2617.

43 E. M. Broderick and P. L. Diaconescu, *Inorg. Chem.*, 2009, **48**, 4701–4706.

44 X. Liu, X. Shang, T. Tang, N. Hu, F. Pei, D. Cui, X. Chen and X. Jing, *Organometallics*, 2007, **26**, 2747–2757.

45 A. Alaaeddine, C. M. Thomas, T. Roisnel and J. F. Carpentier, *Organometallics*, 2009, **28**, 1469–1475.

46 Z. Zhuo, C. Zhang, Y. Luo, Y. Wang, Y. Yao, D. Yuan and D. Cui, *Chem. Commun.*, 2018, **54**, 11998–12001.

47 Q. Nie, K. Gu, X. Yao, Yingming. and Shen, *Dalton. Trans.*, 2010, **39**, 6832–6840.

48 W. Li, Z. Zhang, Y. Yao, Y. Zhang and Q. Shen, *Organometallics*, 2012, **31**, 3499–3511.

49 J. Wang, X. Hu, J. Jiang, S. Gou, X. Huang, X. Liu and X. Feng, 2007, 8468–8470.

50 Z. Zhang, X. Xu, W. Li, Y. Yao, Y. Zhang, Q. Shen and Y. Luo, *Inorg. Chem.*, 2009, **48**, 5715–5724.

51 M. Zhang, X. Ni and Z. Shen, *Organometallics*, 2014, **33**, 6861–6867.

52 T. P. A. Cao, A. Buchard, X. F. Le Goff, A. Auffrant and C. K. Williams, *Inorg. Chem.*, 2012, **51**, 2157–2169.

53 C. Bakewell, T. Cao, X. F. Le Goff, N. J. Long, A. Auffrant and C. K. Williams, *Organometallics*, 2013, **2**, 1–15.

54 C. Bakewell, T. P. A. Cao, N. Long, X. F. Le Goff, A. Auffrant and C. K. Williams, *J. Am. Chem. Soc.*, 2012, **134**, 20577–20580.

55 D. Myers, A. J. P. White, C. M. Forsyth, M. Bown and C. K. Williams, *Angew. Chemie - Int. Ed.*, 2017, **56**, 5277–5282.

56 S. Paul, Y. Zhu, C. Romain, R. Brooks, P. K. Saini and C. K. Williams, *Chem. Commun.*, 2015, **51**, 6459–6479.

57 H. Ouyang, D. Yuan, K. Nie, Y. Zhang, Y. Yao and D. Cui, *Inorg. Chem.*, 2018, **57**, 9028–9038.

58 F. Gendron, K. Sharkas and J. Autschbach, *J. Phys. Chem. Lett.*, 2015, **6**, 2183–2188.

59 W. Schilf, C. J. Jameson, S. Kuroki, K. Kamienska-Trela, R. Ludwig, R. V Law, H. Kurosu, M. J. W. Prior, T. Watanabe, L. Paduano and others, *Nuclear Magnetic Resonance*, Royal Society of Chemistry, 2011.

60 R. H. Contreras, *High Resolution NMR Spectroscopy: Understanding Molecules and their Electronic Structures*, Elsevier Science, 2013.

61 J. Novotný, M. Sojka, S. Komorovsky, M. Nečas and R. Marek, *J. Am. Chem. Soc.*, 2016, **138**, 8432–8445.

62 M. Kruck, C. Sauer, M. Enders, H. Wadepohl and L. Gade, *Dalton. Trans.*, 2011, **40**, 10406–10415.

63 A. Mondal, M. W. Gaultois, A. J. Pell, M. Iannuzzi, C. P. Grey, J. Hutter and M. Kaupp, *J. Chem. Theory Comput.*, 2018, **14**, 377–394.

64 W. D. Horrocks and J. P. Sipe, *J. Am. Chem. Soc.*, 1971, **93**, 6800–6804.

65 C. C. Hinckley, *J. Am. Chem. Soc.*, 1969, **91**, 5160–5162.

66 R. E. Rondeau and R. E. Sievers, *J. Am. Chem. Soc.*, 1971, **93**, 1522–1524.

67 R. Huo, R. Wehrens and L. M. C. Buydens, *J. Magn. Reson.*, 2004, **169**, 257–269.

68 R. Evans, G. Dal Poggetto, M. Nilsson and G. A. Morris, *Anal. Chem.*, 2018, **90**, 3987–3994.

69 I. Swan, M. Reid, P. W. A. Howe, M. A. Connell, M. Nilsson, M. A. Moore and G. A. Morris, *J. Magn. Reson.*, 2015, **252**, 120–129.

70 M. Nilsson, *J. Magn. Reson.*, 2009, **200**, 296–302.

71 H. Kato, T. Saito, M. Nabeshima, K. Shimada and S. Kinugasa, *J. Magn. Reson.*, 2006, **180**, 266–273.

72 J. G. Rosenboom, J. De Roo, G. Storti and M. Morbidelli, *Macromol. Chem. Phys.*, 2017, **218**, 1–10.

73 W. Li, H. Chung, C. Daeffler, J. A. Johnson and R. H. Grubbs, *Macromolecules*, 2012, **45**, 9595–9603.

74 R. Evans, Z. Deng, A. K. Rogerson, A. S. McLachlan, J. J. Richards, M. Nilsson and G. A. Morris, *Angew. Chemie - Int. Ed.*, 2013, **52**, 3199–3202.

75 R. Evans, G. D. Poggetto, M. Nilsson and G. A. Morris, *Anal. Chem.*, 2018, **90**, 3987–3994.

76 C. Chen, Z. Bai, Y. Cui, Y. Cong, X. Pan and J. Wu, *Macromolecules*, 2018, **51**, 6800–6809.

77 C. X. Cai, A. Amgoune, C. W. Lehmann and J. F. Carpentier, *Chem. Commun.*, 2004, **4**, 330–331.

78 I. Yu, A. Acosta-Ramírez and P. Mehrkhodavandi, *J. Am. Chem. Soc.*, 2012, **134**, 12758–12773.

79 J. U. Pothupitiya, N. U. Dharmaratne, T. M. M. Jouaneh, K. V. Fastnacht, D. N. Coderre and M.

K. Kiesewetter, *Macromolecules*, 2017, **50**, 8948–8954.

80 M. Deng, F. Chen, J. Chen and Y. Luo, *J. Organomet. Chem.*, 2016, **808**, 117–121.

81 C. Bakewell, A. J. P. White, N. J. Long and C. K. Williams, *Inorg. Chem.*, 2015, **54**, 2204–2212.

82 C. Romain, Y. Zhu, P. Dingwall, S. Paul, H. S. Rzepa, A. Buchard and C. K. Williams, *J. Am. Chem. Soc.*, 2016, **138**, 4120–4131.

83 J. Castro-Osma, M. North and X. Wu, *Chem. - A Eur. J.*, 2014, **20**, 15005–15008.

84 A. Thevenon, C. Romain, M. S. Bennington, A. J. P. White, H. J. Davidson, S. Brooker and C. K. Williams, *Angew. Chemie - Int. Ed.*, 2016, **55**, 8680–8685.

85 J. A. Garden, P. K. Saini and C. K. Williams, *J. Am. Chem. Soc.*, 2015, **137**, 15078–15081.

86 P. Lewinski, S. Sosnowski, S. Kazmierski and S. Penczek, *Polym. Chem.*, 2015, **6**, 4353–4357.

87 P. K. Saini, C. Romain, Y. Zhu and C. K. Williams, *Polym. Chem.*, 2014, **5**, 6068–6075.

88 C. K. Williams, T. Stoesser and D. Mulryan, *Angew. Chemie Int. Ed.*, 2018, **57**, 16893–16897.

89 T. Stößer, T. T. D. Chen, Y. Zhu and C. K. Williams, *Phil. Trans. R. Soc. A*.

90 A. W. Kleij, *ChemSusChem*, 2018, **11**, 2842–2844.

91 M. Winkler, C. Romain, M. A. R. Meier and C. K. Williams, *Green Chem.*, 2015, **17**, 300–306.

92 N. J. Van Zee and G. W. Coates, *Angew. Chem Int. Ed.*, 2015, **54**, 2665–2668.

93 F. Auriemma, C. De Rosa, M. R. Di Caprio, R. Di Girolamo, W. C. Ellis and G. W. Coates, *Angew. Chemie - Int. Ed.*, 2015, **54**, 1215–1218.

94 C. Tang and C. Y. Ryu, *Sustainable Polymers from Biomass*, Wiley, 2017.

95 T. Stößer, C. Li, J. Unruangsri, P. K. Saini, R. J. Sablong, M. A. R. Meier, C. K. Williams and C. Koning, *Polym. Chem.*, 2017, **8**, 6099–6105.

96 X. Zhang, M. Fevre, G. O. Jones and R. M. Waymouth, *Chem. Rev.*, 2018, **118**, 839–885.

97 D. J. Darensbourg, A. I. Moncada and S. H. Wei, *Macromolecules*, 2011, **44**, 2568–2576.

98 A. M. Diciccio, J. M. Longo, G. G. Rodríguez-Calero and G. W. Coates, *J. Am. Chem. Soc.*, 2016, **138**, 7107–7113.

99 X. B. Lu, L. Shi, Y. M. Wang, R. Zhang, Y. J. Zhang, X. J. Peng, Z. C. Zhang and B. Li, *J. Am. Chem. Soc.*, 2006, **128**, 1664–1674.

100 M. R. Kember, A. Buchard and C. K. Williams, *Chem. Commun.*, 2011, **47**, 141–163.

101 Y. Zhu, C. Romain and C. K. Williams, *J. Am. Chem. Soc.*, 2015, **137**, 12179–12182.

102 Y. Zhu, M. R. Radlauer, D. K. Schneiderman, M. S. P. Shaffer, M. A. Hillmyer and C. K. Williams, *Macromolecules*, 2018, **51**, 2466–2475.

103 T. T. D. Chen, Y. Zhu and C. K. Williams, *Macromolecules*, 2018, **51**, 5346–5351.

104 E. H. Nejad, A. Paoniasari, C. G. W. W. Van Melis, C. E. Koning and R. Duchateau, *Macromolecules*, 2013, **46**, 631–637.

105 H. Li, H. Luo, J. Zhao and G. Zhang, *Macromolecules*, 2018, **51**, 2247–2257.

106 M. Pepels, M. Bouyahyi, A. Heise and R. Duchateau, *Macromolecules*, 2013, **46**, 4324–4334.

107 D. Garlotta, *J. Polym. Environ.*, 2001, **9**, 63–84.

108 M. J. Sanford, N. J. Van Zee and G. W. Coates, *Chem. Sci.*, 2017, **9**, 134–142.

109 T. Haider, C. Völker, J. Kramm, K. Landfester and F. R. Wurm, *Angew. Chem Int. Ed.*, 2018, **58**, 50–62.

110 D. Liu, X. Zhang, L. Zhu, J. Wu and X. Lü, *Catal. Sci. Technol.*, 2015, **5**, 562–571.

111 G. X. De Hoe, M. T. Zumstein, B. J. Tiegs, J. P. Brutman, K. McNeill, M. Sander, G. W. Coates and M. A. Hillmyer, *J. Am. Chem. Soc.*, 2018, **140**, 963–973.

112 R. Kumar, W. Gao and R. a. Gross, *Macromolecules*, 2002, **35**, 6835–6844.

113 X. Chen and R. Gross, *Macromolecules*, 1999, **32**, 308–314.

114 X. Hu, X. Chen, Z. Xie, H. Cheng and X. Jing, *J. Polym. Sci. Part A Polym. Chem.*, 2008, **46**, 7022–7032.

115 S. Tempelaar, L. Mespouille, O. Coulembier, P. Dubois and A. P. Dove, *Chem. Soc. Rev.*, 2013, **42**, 1312–1336.

116 G. L. Gregory, E. M. López-Vidal and A. Buchard, *Chem. Commun.*, 2017, **53**, 2198–2217.

117 G. L. Gregory, L. M. Jenisch, B. Charles, G. Kociok-Köhn and A. Buchard, *Macromolecules*, 2016, **49**, 7165–7169.

Chapter 4

Aluminium Monopyrrolidine Complexes for the Controlled ROP of Lactide

ORGANOMETALLICS Article
Cite This: Organometallics 2018, 37, 1719−1724

Aluminum Complexes of Monopyrrolidine Ligands for the Controlled Ring-Opening Polymerization of Lactide

James Beament, Mary F. Mahon, Antoine Buchard,* and Matthew D. Jones*

Department of Chemistry, University of Bath, Claverton Down Bath BA2 7AY, U.K.

Supporting Information

ABSTRACT: In this paper we report the full characterization (solution-state NMR spectroscopy and solid-state structures) of a series of Al(III) half-salan complexes and their exploitation for the ring-opening polymerization of *rac*-lactide. Depending on the ligand employed and stoichiometry of the complexation, structures of the form $Al(\mathbf{X})_2Me$ or $Al(\mathbf{X})Me_2$ were isolated. Interestingly $Al(\mathbf{2})_2Me$ and $Al(\mathbf{2})Me_2$ produce PLA with a strong isotactic bias (P_m up to 0.80), whereas all other complexes produced atactic PLA. This is in contrast to recent studies on similar salan ligand systems. PLAs with predictable molecular weights and narrow distributions were achieved. The results are discussed in terms of steric and electronic properties of the ligands.

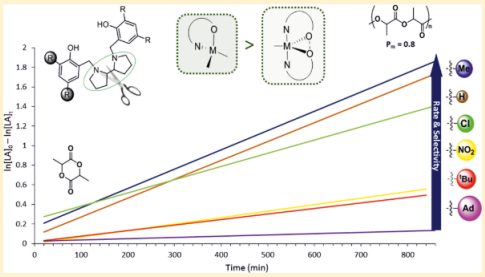

INTRODUCTION

Currently, there is a tremendous desire to develop new polymeric materials that are biodegradable and are sourced from annually renewable raw materials.[1] Unquestionably one of the most important polymers that fulfills these criteria is polylactide (PLA). PLA is prepared from the ring-opening polymerization (ROP) of a cyclic ester monomer, lactide (LA). LA is typically utilized as either the enantiomerically pure L-LA or as a racemic mixture of D and L monomers (*rac*-LA). When *rac*-LA is utilized, atactic, heterotactic, or isotactic PLA can be prepared, with the physical properties of the polymer being intrinsically linked to the polymer's microstructure. The microstructure can be controlled by the judicious choice of metal center and ligand. For example, there are many elegant stereoselective polymerizations employing group 1−4 metal centers,[2] lanthanides,[3] indium,[4] zinc,[5] and (pertinent to this study) aluminum.[6] This follows on from seminal contributions by Feijen,[6h] Chisholm,[7] Gibson[8] and Coates[2p,9] in the early part of this century. More recently, a tremendous amount of effort has been focused on understanding the subtle interplay between the metal center and ligand and the consequence this has on the stereochemistry of the resulting polymer.[2o,v] Subtle changes in selectivity have been observed by Williams for phospha-salen lanthanide complexes and by Ma for a series aminophenolate Zn(II)/Mg(II) complexes.[2o,10] However, it is fair to say that there is a degree of serendipity in the stereochemical outcome of the polymerization, with unpredictable tacticities achieved from metal−ligand combinations. Furthermore, subtle changes to the ligand can significantly alter the rate of polymerization.[6f] In this regard we have shown that simply reducing a salalen to a salan dramatically increases the rate of ROP of *rac*-LA.[6f] Tolman and co-workers have demonstrated, with a series of Al(III)-salen complexes, that the ortho substituent on the phenyl ring of the salen can induce distortions which can have a massive effect on the rate of polymerization of caprolactone. In this case it is shown that bulky substituents distort the geometry around the Al(III) center, which is believed to be responsible for the observed increase in polymerization rate.[11]

Recently, we have demonstrated the importance of bipyrrolidine-derived salan ligands for controlling the stereochemical outcome for *rac*-LA polymerization.[2u,v] For example, when a *meso*-bipyrrolidine salan ligand (Scheme 1) is complexed to Zr(IV), the resulting initiator shows a high isotactic tendency (P_m up to 0.86).[2u] Interestingly, when the same ligand is complexed to Al(III), highly heterotactic PLA is produced (P_r up to 0.87).[2v] Moreover, for the tBu analogue, atactic PLA was produced in the melt (130 °C) after 48 h and it was shown that the complex was inactive in solution.[2v] The In(III) complex of the meso tBu bipyrrolidine produced heterotactic PLA in solution (P_r up to 0.84).[4b] The exact reasons for these dramatic switches in selectivity and activity are still open to debate. Kol has also successfully shown the importance of the these pyrrolidine rings in salalen complexes of Al(III) for the controlled isotactic selective polymerization of *rac*-LA.[2s,12] As part of ongoing studies in the area of pyrrolidine systems we have prepared a series of monopyrrolidine ligands and their respective Al(III) complexes. These were screened for the ROP of *rac*-LA to further investigate how the ligand affects the stereochemical outcome of the polymerization. Moreover, the ligand framework could provide a more rigid environment

Received: March 19, 2018
Published: May 22, 2018

DOI: 10.1021/acs.organomet.8b00161
Organometallics 2018, 37, 1719−1724

4. Aluminium Monopyrrolidine Complexes for the Controlled ROP of Lactide

4.1. Introduction

Aluminium complexes supported by bidentate ligands represent another avenue in catalyst synthesis, with growing attention due to their activity for ROP.[1] Behavioural differences are often explained through a greater exposure of the metal centre within the coordination sphere in comparison to the tetradentate bisphenolate motif.

4.1.1. Phenoxy-imine aluminium alkyl complexes

Gibson and co-workers first explored these systems through the synthesis of a series of monoligated phenoxy-imine or ('half-salen') complexes and their conversion to a mono-alkyl aluminium cationic species through the reaction with $B(C_6F_5)_3$, although they were not tested for ROP.[2] Often applied to the ROP of ε-CL, half-salen complexes have focused iteratively on varying the bulk around the imine centre to generate differences in reactivty.[3–5] Reasonable molecular weight control is often achieved from the exogenous addition of one equivalent of alcohol, supporting the formation of *in-situ* alkoxide complexes, although the true nature of the catalytically active species is poorly understood. When applied to the ROP of *rac*-LA these systems typically fail to meet the same degree of rate or selectivity shown for the 7-membered ε-caprolactone.

Early work by Nomura and co-workers, focused on changes to the *para*-substituted analogues of Gibson's complexes (**49**, Figure 4.1).[3,6] These systems were seen to be active for the ROP of ε-CL in the presence of ^{n}BuOH. A general rate increase is seen from using the electron withdrawing $–C_6F_5$ group attached to the imine nitrogen in comparison to the bulky adamantyl and $–^{t}$Bu substituents. Applied to the ROP of *rac*-LA, only atactic PLA was yielded, achieving complete conversion after 24h {$[LA]_0$:$[I]_0$:$[BnOH]_0$ =100:1:1, 80 °C, toluene}. Zhang and co-workers expanded on this finding, with a wide range of complexes surrounding an aryl bound imine motif with varying ortho- and para- substituents on the phenoxy and iminium aromatic groups (**50**).[7] Despite this, no notable improvement in rate or selectivity is seen. The lack of selectivity these systems exhibit is not uncommon, yet raises questions about the nature of the catalytically active species and if it possess the same metal-ligand framework as the initiator. Later work within the group utilised a imidazole ring as source of the coordinating nitrogen atom (**52**).[8] The decrease in basicity caused a marked increase in activity, although no selectivity was seen.

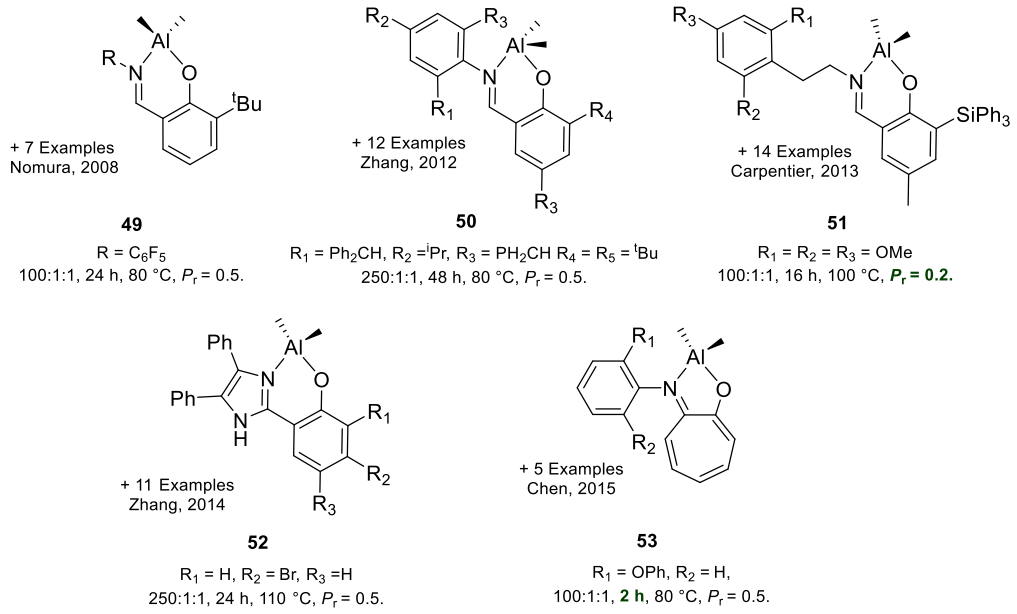

Figure 4.1. phenoxy-imine 'half-salen' aluminium complexes reported for the polymerisation of *rac*-LA in toluene with the addition of exogenous alcohol.[6–10]

Carpentier and co-workers have investigated one of the most iso-selective initiators of this series (P_r = 0.2) achieved with significantly bulky ligand-coordination sphere achieved through the use of *ortho* substituted –$SiPh_3$ group around the metal centre (**51**).[9] When indium is used as the central metal a significantly more active system was generated albeit with no stereoselective control. This finding further highlights the aforementioned importance in the choice of metal ion in comparison to tuning the ancillary ligand. Chen and co-workers have shown how changing the metallacycle ring size lead to a dramatic effect on the rate of ROP of ε-CL and *rac*-LA.[5,10] The 5-membered metal coordination ring, **53**, imparting a tighter coordination motif, was shown to be significantly more active that the corresponding 6-membered system for the ROP of ε-CL (k_{obs} = 15.9 × 10^{-3} min^{-1} *vs* 5.5 × 10^{-3} min^{-1} respectively).

4.1.2. Bis-amido aluminium alkyl complexes

Aluminium bis-amido complexes have similarly been utilised for ROP of *rac*-LA with notable work by Ma and co-workers (**54–55**, Figure 4.2).[11,12] Tuning the pendent phenyl group and nature of the coordinated cyclic amine had no significant impact on rate or selectivity. MALDI-ToF end group analysis showed these systems to be capped with the bis-amido ligand, proposing the propagating species as having an active –$AlMe_2$ chain end. Whilst narrow dispersities and good molecular weight control are seen, this system highlights the importance in fully understanding the catalytically active species in being able to further design new systems which can impart stereocontrol at appreciable rates.

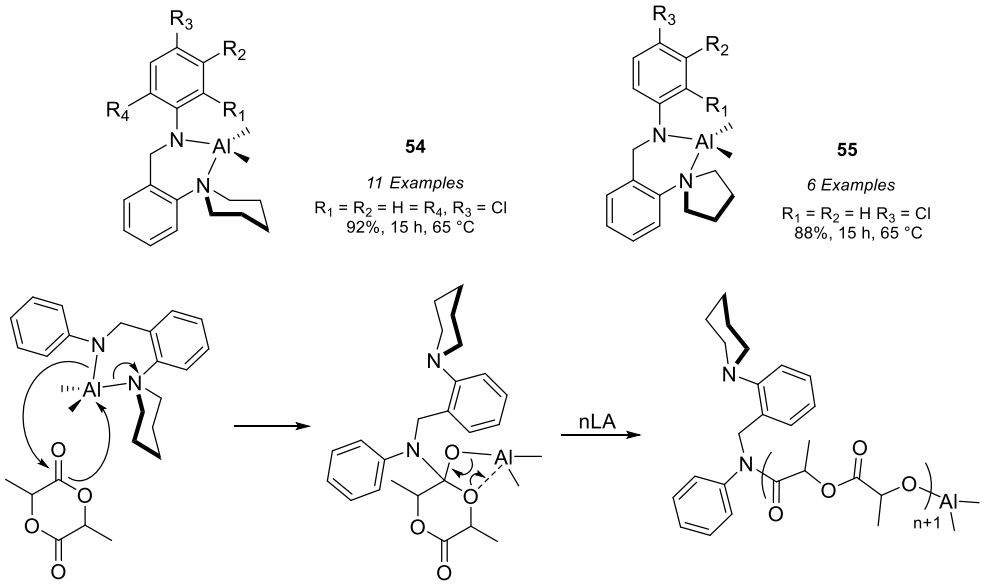

Figure 4.2. Bis-amido aluminium complexes reported by Ma and co-workers. Scheme showing proposed mechanism of initiation.[11,12]

4.1.3. Amino phenolate aluminium alkyl complexes

'Half-salan' or amino phenolate complexes have also been realised for the ROP of ε-CL and *rac*-LA. Ma, Chakraborty and Shen have all reported variants of these monoligated system with varying steric characteristics on the amine and phenolate groups (Figure 4.3).[13–15] Ma and co-workers first reported these systems, however only mild activity was seen with essentially atactic PLA (P_r = 0.45) produced after 48 hours {$[LA]_0$:[**56a**]$_0$ = 100:1, $[LA]_0$ = 1 M, toluene, 90 °C}.[15] The poor activity is likely due to the lack of alcohol co-initiator commonly used, further evidenced by poor molecular weight control. It was seen that increasing the bulk on the *ortho* position had a slight reduction in the activity with no increase in

stereoselectivity. Chakraborty showed improvement to these results by reporting similar structures which were moderately hetereoselective for ROP of *rac*-LA (P_r = 0.75). These were relatively active for aluminium catalysts, achieving complete conversion within 26 hours at ratios of 200:1 {$[LA]_0$:[**57a**]$_0$}, in the absence of alcohol, albeit under intensive conditions (100 °C, toluene).[13] This rate increase is suggested to be the result of weaker steric interactions from the coordinating nitrogen moieties. As both studies do not use classical alkoxide initiation the amine group likely has a role in the initiation step, evidenced by MALDI-ToF investigations which highlight residues of ligand at the chain-end.

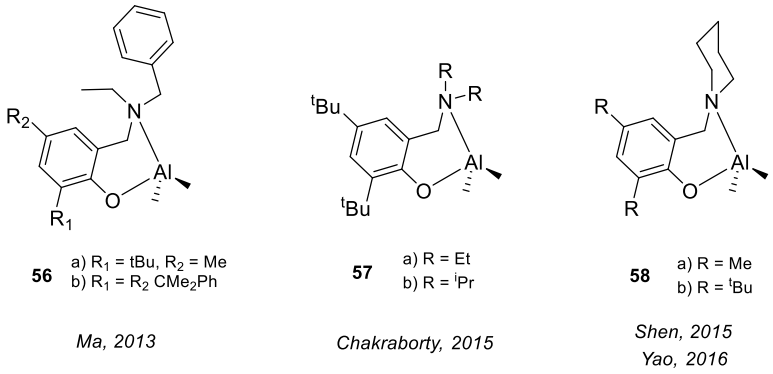

Figure 4.3. Half-salan monoligated aluminium phenolate complexes reported for ROP.[13–16]

For the polymerisation of ε-CL, Shen and co-workers reported a series of cyclic aminophenolate aluminium complexes, **58a–b.** Under similar conditions to **57** {[ε-CL]$_0$:[I]$_0$ = 200:1}, significantly lower activity was seen. This can be explained due to the lower rate associated with ligand initiation from the cyclic amine group. This poor activity was resolved with the addition of ethanol as a coinitiator, ultimately achieving quantitative conversion in 6 hours at ratios of 2000:2:2 {[ε-CL]$_0$:[I]$_0$:[EtOH]$_0$}. Alkoxide initiation was shown through MALDI-ToF analysis showing exclusively ethoxide end groups. This switch in reactivity from the addition of a more nucleophilic initiating group although expected, provides insight into the role and lability of aluminium-alkyl groups as precursors for generating effective *in-situ* alkoxide complexes.

4.1.4. Bisligated amino-phenolate aluminium alkyl complexes

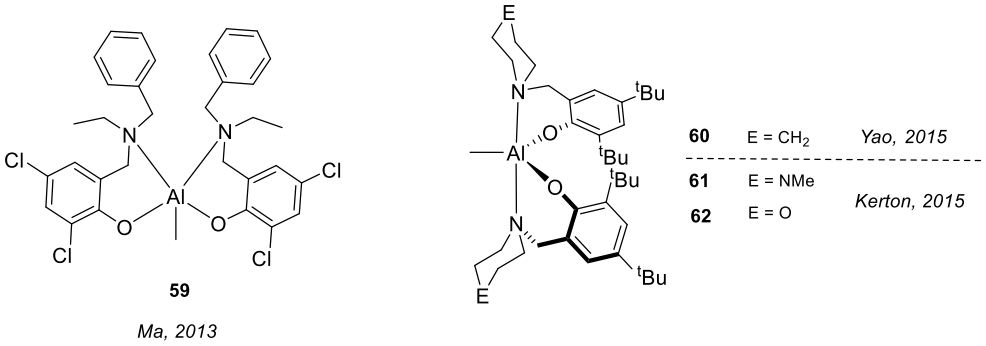

Figure 4.4. Bis-ligated half-salan aluminium complexes reported for ROP.[14,15,17,18]

Nomura *et al.,* reported excellent activity for the ROP of ε-CL when $AlEt_3$ and 2 equivalents of phenoxy-imine ligands were mixed *in-situ* in the presence of BnOH.[19] Whilst the catalytically active species were not isolated, it is expected that bisligation occurs around one metal centre. With a single aluminium alkyl species acting as the labile group for reaction with BnOH from which coordination-insertion mechanism operates. In comparison to the highly heterotactic (P_r = 0.96) tetradentate salan complex **11b**, shown by Gibson and co-workers (Figure 2.4), the bis-ligated bidentate analogue reported by Ma produced only atactic PLA at a significantly lower rate (**59**, Figure 4.4).[15,20] This reduction in rate is not unexpected as a result of the added degrees of freedom effectively shielding the active coordination site. Whilst the loss of selectivity is not commented on, it can be postulated this is a structural effect of the active species with Al centres effectively in identical electronic environments.

Yao and Kerton have further explored this ligation effect with a piperazine bidentate ligand, similarly yielding mono aluminium alkyl complexes (**60–62**).[14,17,18] Kerton and co-workers, show a substantial ROP rate increase to previously reported mono-ligated complexes, contrasting with other literature comparisons.[17,18] The effect of group trans to the amine in the piperazine ring was probed showing significance in activity. When an ether group was adopted (**62**) a much higher activation energy is seen for ROP of ε-CL in comparison to the tertiary amine structure (**61**). This is explained due to the stronger basicity of the pendant amine group in activating the monomer and the possible coordination of the ether to the aluminium centre, effectively blocking coordination.[21]

4.1.5. Dinuclear aluminium amino phenolate complexes

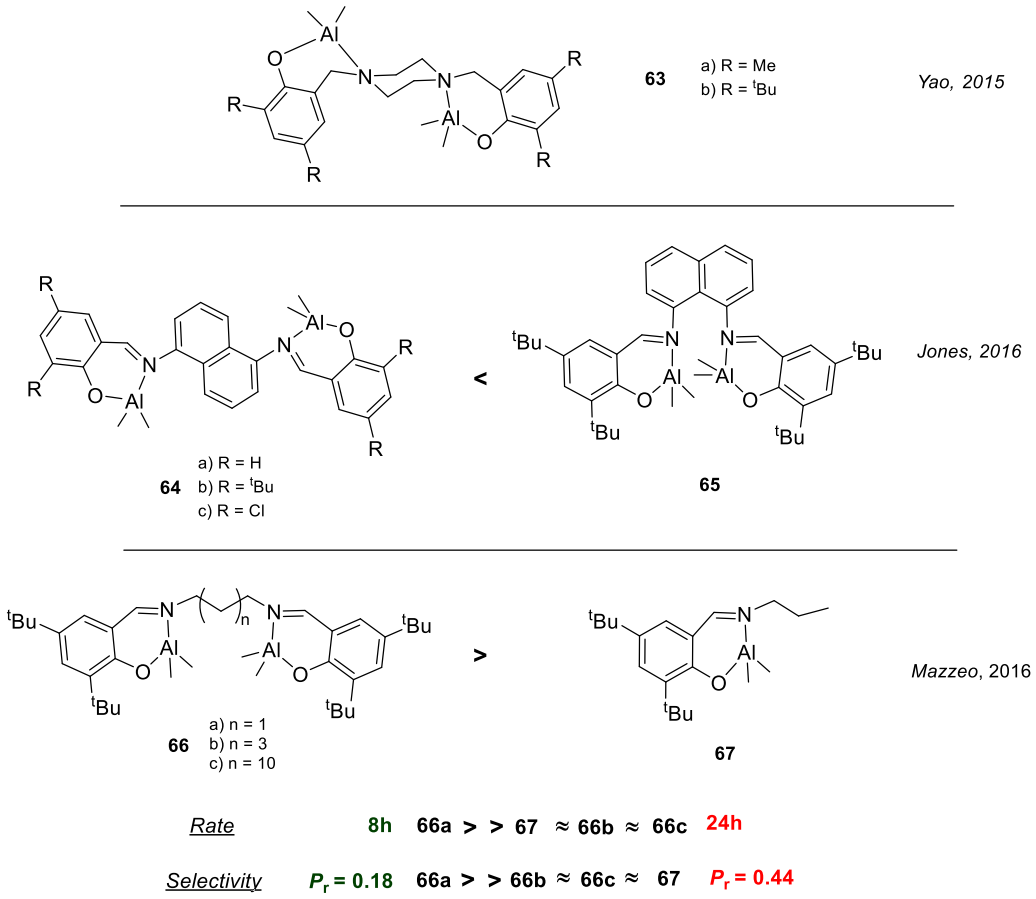

Figure 4.5. Dinuclear aluminium complexes investigated by Yao, Jones and Mazzeo.[14,22,23]

Multinuclear aluminium complexes have been isolated and investigated for ROP, often yielding a substantial increase in activity compared to the mononuclear analgoues.[14,17,23–27] To yield comparison to mononuclear complexes, Yao and co-workers reacted a piperazine bridged bisphenol ligand with 2 equivalents of aluminium trialkyl yielding the binuclear adduct (**63a–b**, Figure 4.5) instead of the mono nuclear bisligated complex (Figure 4.4).[14] The reduced rotation of the phenolate groups around the cyclic amine bridge is an explanation for this structure despite the possible entropic gain associated from the ligand binding in tetradentate fashion to one aluminium centre. In comparison to **58**, the dinuclear species **63a** was significantly more active for the ROP of ε-CL, leading to the proposal of a cooperative aluminium mechanism. This mechanism can be supported by literature work surrounding how flexibility in the ligand can be used to initiate a cooperative effect.[9,28,29] Jones and co-workers further explored this with a series of dinuclear cis/trans naphthalene complexes.[22] **65** was shown more active for the ROP of *rac*-LA than **64a–c**, similarly explained due to a coordination of metal centres which is not possible in **64a–c**. A slight improvement in the activity is seen by employing low steric bulk and deactivating groups on the phenolate

substituent. The effect of electronic and steric considerations when tuning activity, for bidentate aluminium systems, is well known to display significant differences. An extensive kinetic study on ketimine aluminium complexes showed how deactivating groups with low bulk in the ortho- position were more active for ROP, highlighting an avenue of future investigation.[30]

Mazzeo and co-workers used an increase in carbon chain length between imine groups on a dinuclear salen complex to show the effect of cooperative metal centres (**66a–c**, Figure 4.5).[23] **66a** showed good activities and a high degree of iso-selectivity (P_r = 0.18) for the ROP of *rac*-LA, which was interpreted in terms of cooperation between the aluminium centres. Increasing the carbon linker (**66b–c**) was met with a reduction in rate and selectivity in line with the monomeric species **67** suggesting no cooperative behaviour is seen.

4.1.6. Chapter aims

Previous studies on the synthesis of aluminium monophenolate complexes have highlighted the accessibility and versatility of aluminium. The wide variability of possible coordination modes, initiating sites, and tuneable ligand effects has in recent years, been a focus for researchers looking to further explore the efficacy of Al^{3+} initiators. Whilst it is proposed the coordination site is more accessible for polymerisation, monophenolate complexes often fail to reach the same degree of activity and selectivity as the analogous tetradentate bisphenolate structures.

It has reported both in this thesis and previous publications that the bipyrrolidine backbone can be used to generate highly selective and active initiators by control of the metal centre and ligand chirality. Herein, this chapter evaluates whether the 'half-salan' analogue, based around a pyrrolidine monophenol ligand, can be coordinated to aluminium and can produce structures which are distinctly different in their activity and mechanism of polymerisation. In addition, this chapter aims to further explore the nature of the catalytically active species as well as the impact of ligand functional groups on the ROP of LA.

4.2. Synthesis of aluminium mono pyrrolidine complexes

4.2.1. Synthesis of monopyrrolidine ligands

In order to create a suitable array of monopyrrolidine ligands which could be complexed to aluminium, three synthetic routes were required. As in the synthesis of bipyrrolidine ligands, discussed previously, a modified 'Mannich' reaction was shown to be suitable for the reaction of pyrrolidine with 2,4 substituted phenols **15-17**H (Route 1, Scheme 4.1). Through this route good yields were obtained (66 – 86%). When testing with 2,4-dichlorophenol the reaction yielded a mixture which was not facile to purify. Condensation of pyrrolidine with the corresponding salicylaldehyde, followed by reduction with $NaBH_4$ yielded **14** and **18**H in high purity in moderate yields (Route 2, Scheme 4.1). Due to the commercial unavailability of 4-nitro-substituted salicylaldehyde, a nucleophilic substitution of the synthesised 2-(bromomethyl)-4-nitrophenol with pyrrolidine yielded **19**H in moderate yields (Route 3, Scheme 4.1).

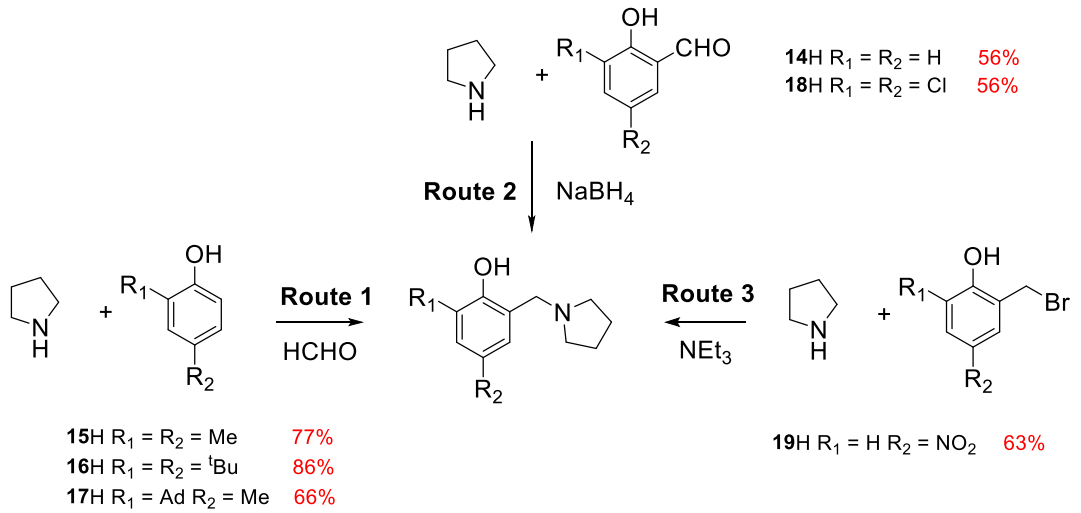

Scheme 4.1. Synthetic routes to access mono-pyrrolidine ligands **14–18**H.

Interestingly, using 2 or more equivalents of $NaBH_4$ in the reduction of the Schiff-base intermediate for **14**H, yielded a product with split methylene resonances in the ^{1}H NMR spectra, indicative of an inequivalent environment (Figure 4.7). ESI-MS showed a peak of 205.16 m/z in comparison to the expected 193.15 m/z. Recrystallisation in hexane yielded a crystalline product allowing identification of the solid-state structure as B(**14**)H_2 (Figure 4.6). ^{11}B NMR spectroscopy showed the presence of a triplet indicative of the coupling of the B to the bound hydrogens (Figure 3.8). This complex was inert to hydrolysis under basic and acidic conditions tested (1 M NaOH/HCl) and was shown to be moisture and air stable. Despite the addition of an excess of $NaBH_4$ to the intermediary of **18**H no indicative signals of borohydride complexation were seen.

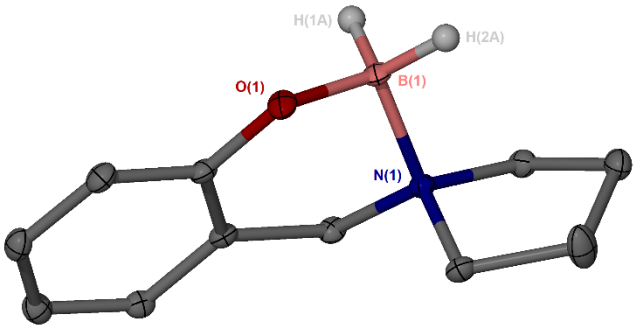

Figure 4.6. Solid-state structure of B(**14**)H_2. Ellipsoids are at the 30% probability level. Ancillary hydrogen atoms are removed for clarity.

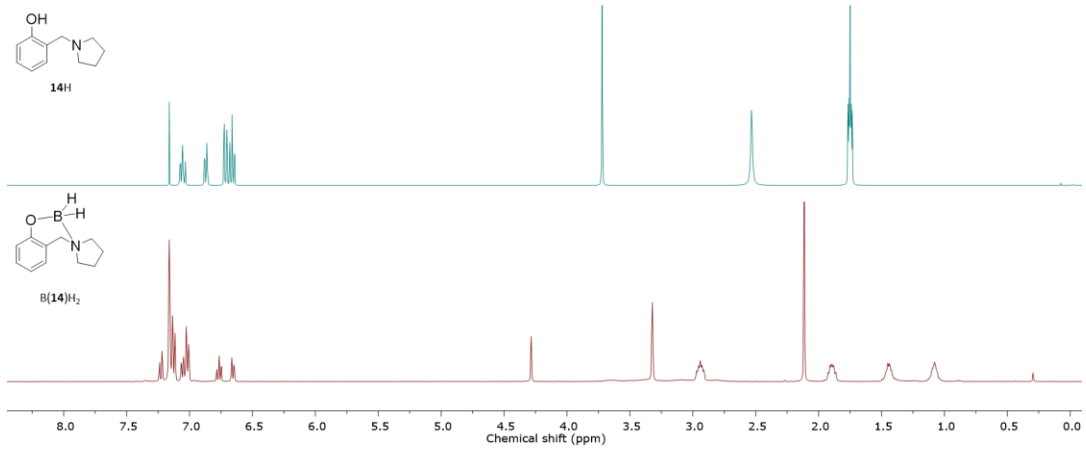

Figure 4.7. Stacked ^{1}H NMR (400 MHz, 298 K) spectra of **14**H and B(**14**)H_2 in C_6D_6.

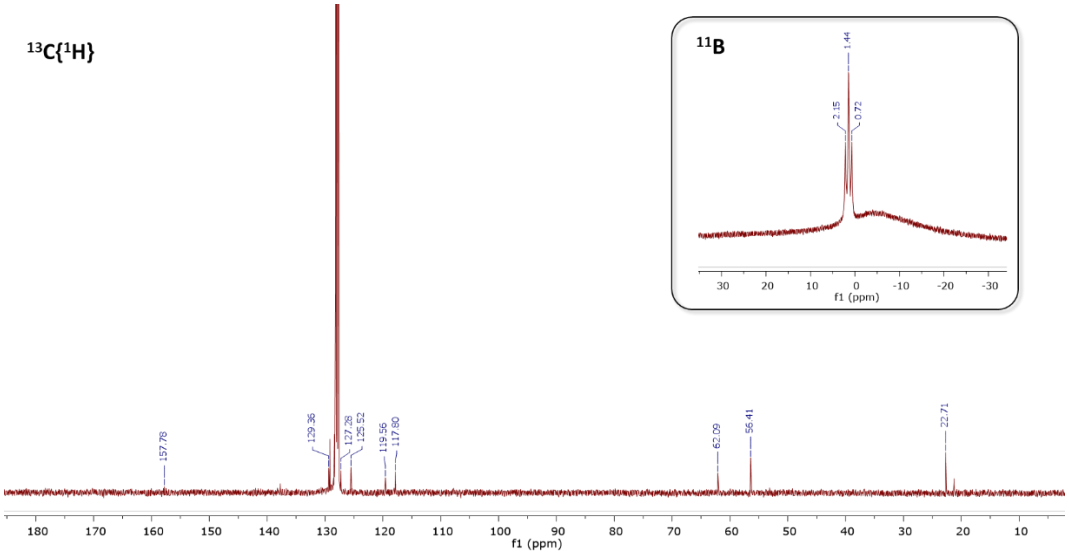

Figure 4.8. $^{13}C\{^{1}H\}$ and ^{11}B NMR spectra (298 K, C_6D_6) for B(**14**)H_2.

4.2.2. Synthesis of bisligated aluminium pyrrolidine complexes

To create complexes comparable to Al(**2**)Cl and Al(**2**)Me, **14-19**H were reacted in a 2:1 stoichiometric ratio with $AlMe_3$ (Scheme 4.2).[31] Trimethylaluminium was chosen due to the greater lability of the Al–CH_3 bond compared to the Al–Cl bond, in theory reducing the initiation period in the formation of the *in-situ* metal alkoxide. Whilst this means direct structural comparison with M(**2**)Cl complexes is not possible, comparison with Al(**2**)Me reported by Jones and co-workers provides an analogous comparison.[32]

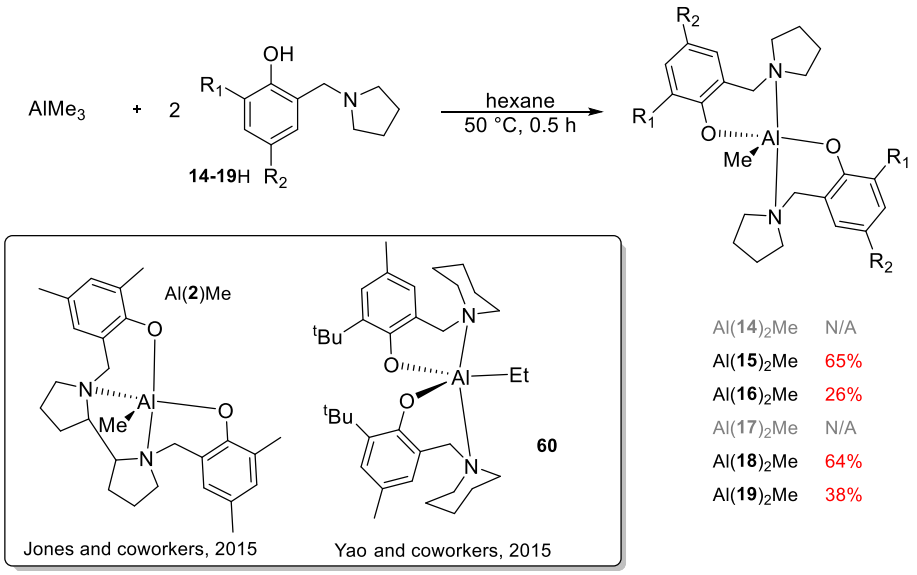

Scheme 4.2. Synthesis of bisligated Al(**X**)$_2$Me complexes. Literature complexes by Jones and co-workers and Kerton and co-workers are presented for comparison.[18,32]

Reaction in hexane followed by recrystallisation in a hexane/toluene mixture yielded a crystalline material which was suitable for single-crystal XRD analysis, confirming the structures of Al(**15-19**)$_2$Me (Figure 4.9). Structures were pseudo-trigonal bipyramidal, as observed by their calculated τ values being greater than 0.5 (Table 4.1). This is in agreement with other bisligated 'ON' Al complexes in the literature.[18] All complexes had nitrogen groups trans in pseudo axial positions, indicated by N(1)–Al–N(2) bond angles being in the range 169.29(7) – 172.06(7)°. This differs significantly from bipyrrolidine and other tetradentate 'salan' systems where the nitrogen atoms are forced to be cis to each other.[31–34] Metric data highlights there is little difference on the Al–O (1.770(2) – 1.792(2) Å) and Al–C (1.973(3)–1.987(4) Å) bond distances between the bidentate and tetradentate analogues.[32]

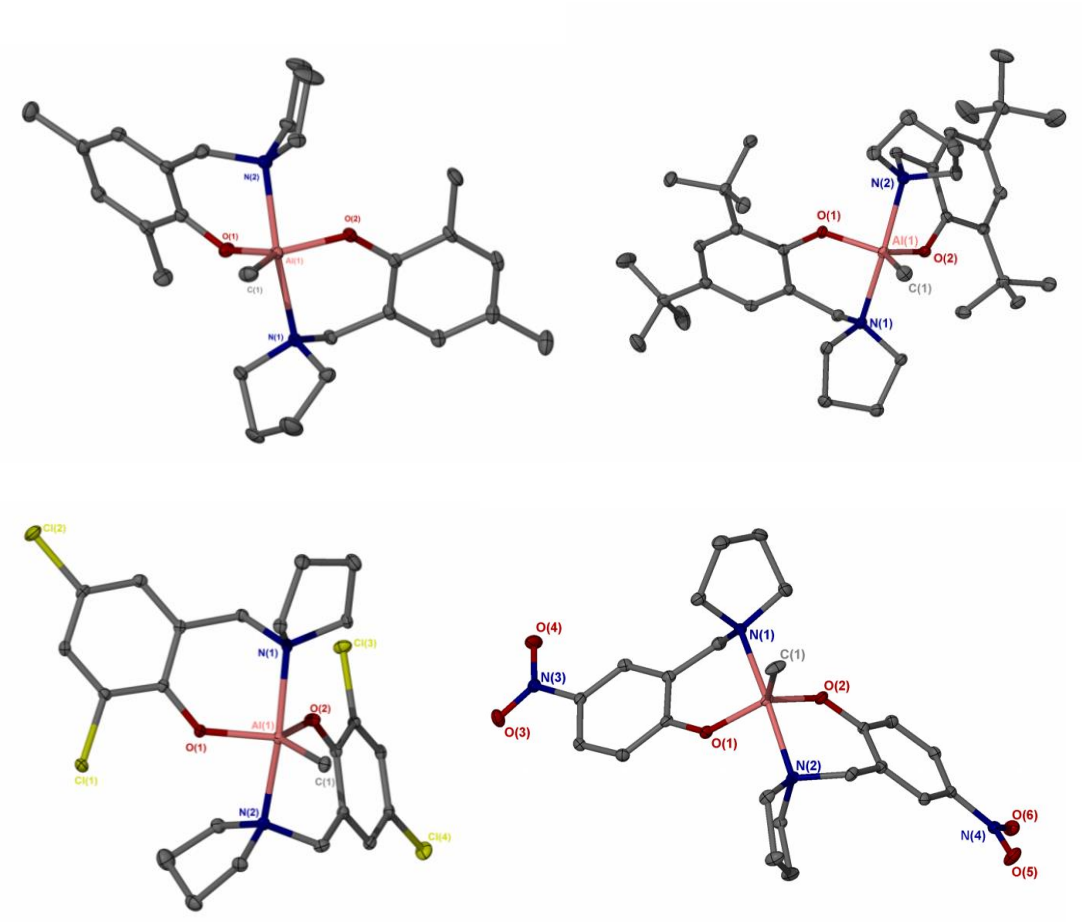

Figure 4.9. Solid state structures for Al(**14**)$_2$Me, Al(**15**)$_2$Me, Al(**18**)$_2$Me and Al(**19**)$_2$Me. Ellipsoids are at the 30% probability level. All hydrogen atoms have been removed for clarity, as have all solvent molecules.

Table 4.1. Comparative information on the bond angles, bond lengths and τ values of Al(**14**–**19**)$_2$Me complexes.

	Al(**14**)$_2$Me	Al(**15**)$_2$Me	Al(**18**)$_2$Me	Al(**19**)$_2$Me
Al(1)–O(1)	1.770(2)	1.792 (1)	1.787(2)	1.785(2)
Al(1)–O(2)	1.770(2)	1.787(1)	1.783(1)	1.792(2)
Al(1)–N(1)	2.139(3)	2.126(2)	2.125(2)	2.113(2)
Al(1)–N(2)	2.132(3)	2.138(2)	2.125(2)	2.139(2)
Al(1)–C(1)	1.987(4)	1.981(2)	1.973(2)	1.983(2)
O(1)–Al(1)–N(1)	87.77(11)	87.85(6)	89.55(7)	89.48(7)
N(1)–Al(1)–N(2)	170.41(11)	172.06(7)	167.88(8)	169.29(7)
O(1)–Al(1)–O(2)	118.98(13)	117.28(7)	118.46(8)	119.41(7)
C(1)–Al(1)–O(1)	118.66(15)	121.52(9)	119.08(9)	120.77(10)
τ	0.81	0.84	0.77	0.81

^{1}H NMR spectra of Al(**15**)$_2$Me in C_6D_6 at 298 K confirmed the presence of Al–Me at (-0.5 ppm) and four aromatic protons split over 2 environments (Figure 4.10). All bisligated complexes exhibited broad signals between 2.5 – 4.0 ppm which were assigned to NCH_2 indicating the complexes display a degree of fluxionality at 298 K. Low-temperature ^{1}H NMR spectroscopy (218 K – 298 K) generated splitting in aromatic and Al-Me resonances, indicating that multiple coordination motifs were present in solution upon cooling. Returning to 298 K restored the initial spectrum showing any changes to the complex are in thermodynamic equilibria. At higher temperatures, the signals were sharper and clarity of the NCH_2 environments made full assignment possible (Figure 4.11). ^{13}C{^{1}H} and HSQC NMR analysis confirmed the complex as pure with retention of the solid-state structure in solution.

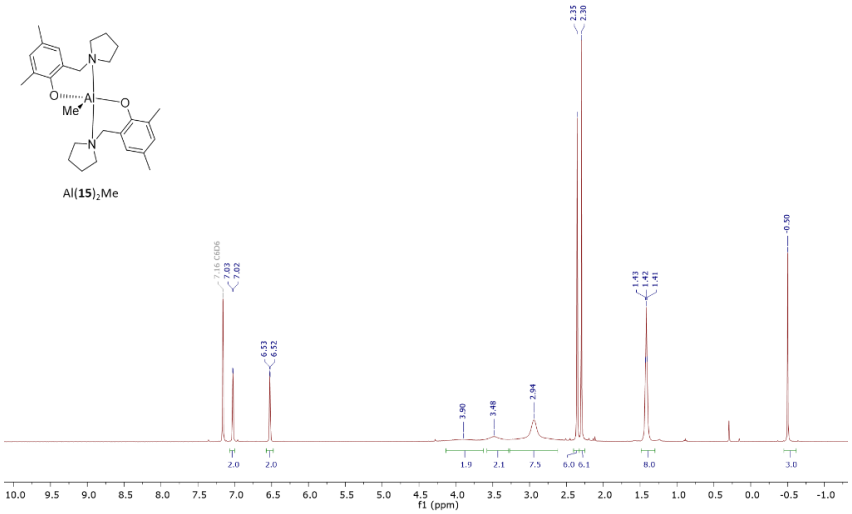

Figure 4.10. ^{1}H NMR spectra (400 MHz, C_6D_6) of Al(**15**)$_2$Me at 298 K.

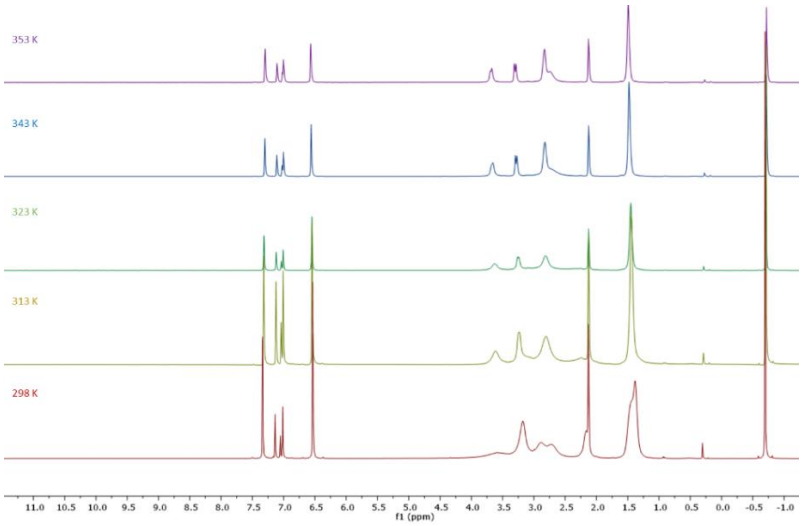

Figure 4.11. Stacked ^{1}H NMR (400 MHz, toluene-d_8) spectra of Al(**18**)$_2$Me at varying temperatures between 353 K and 298 K).

It was not possible to isolate Al(**17**)$_2$Me, with evidence of starting material present in the ^{1}H NMR spectrum. Varying the reaction temperature and reagent stoichiometry failed to yield any evidence of the bisligated product. This is likely due to the large steric hindrance of the adamantyl groups preventing bisligation around the aluminium centre. In contrast, the formation of Al(**14**)$_2$Me was visible in the ^{1}H NMR spectra, albeit in a 1:2 mixture with the Al(**14**)Me$_2$ (Figure 4.12). Repeated syntheses under a variety of conditions yielded the same complex ratio suggesting a ligand-complex exchange equilibrium maybe in operation. Due to the similar solubilities of the complexes it was not possible to isolate Al(**14**)$_2$Me or Al(**14**)Me$_2$ cleanly.

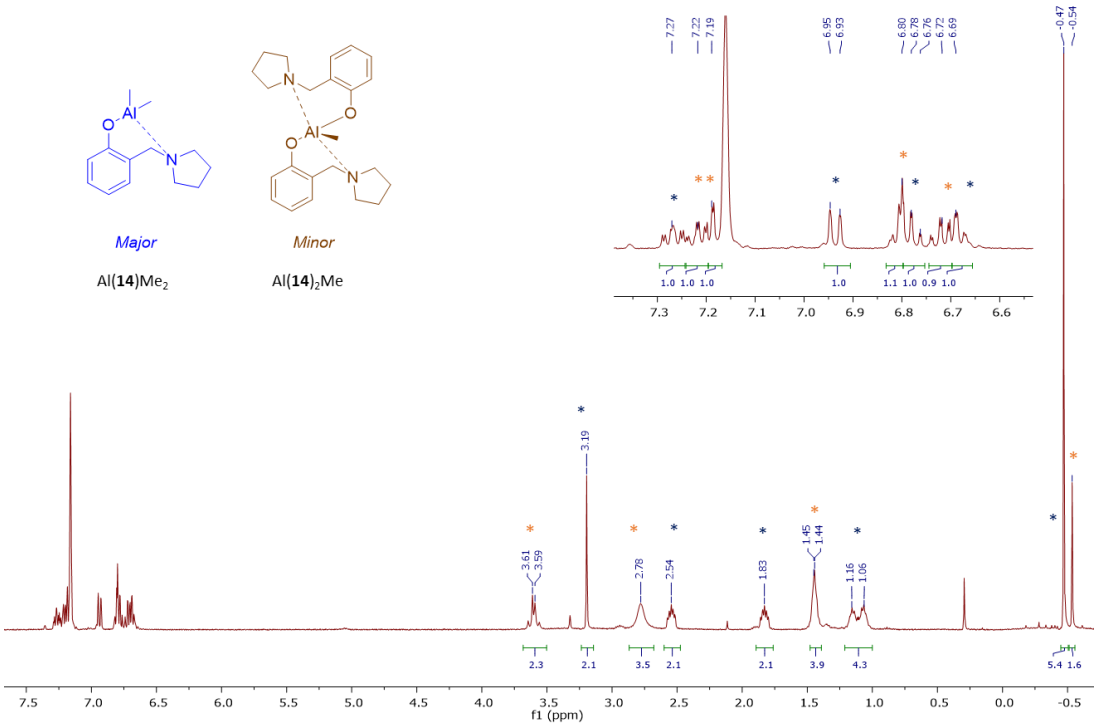

Figure 4.12. ^{1}H NMR spectrum (400 MHz, C_6D_6) of the 1:2 mixture of Al(**14**)$_2$Me and Al(**14**)Me$_2$ at 298 K.

4.2.3. Synthesis of monoligated aluminium pyrrolidine complexes

Synthesising four-coordinate monoligated pyrrolidine complexes follows the direction of Carpentier and Shen, providing a structural comparison to the five-coordinate bisligated complexes (Scheme 4.3).[14,35] Experiments to prepare Al(**14–19**)Me_2 were carried out under mild temperatures and a 1:1 stoichiometry to prevent bisligation, driven by the entropic release of methane.

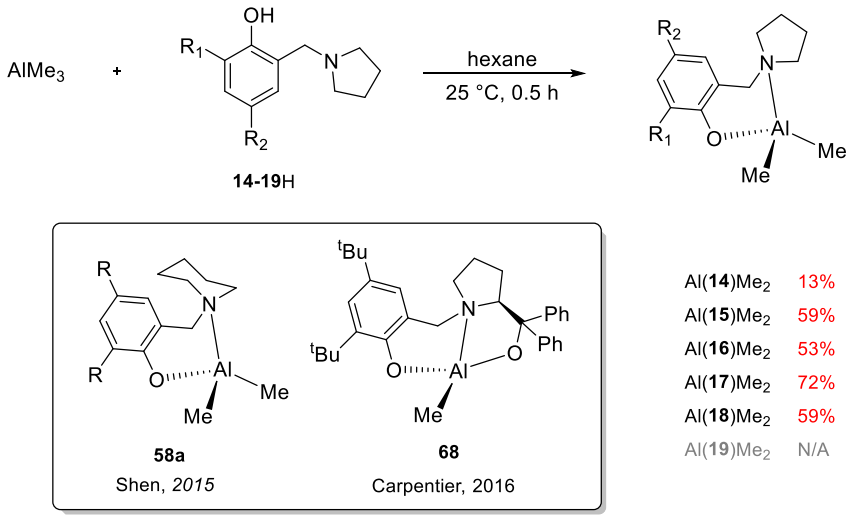

Scheme 4.3. Synthetic route to synthesis Al(**14-19**)Me_2 complexes. Literature complexes shown by Shen and co-workers, and Carpentier and co-workers, are provided for comparison.[14,35]

Recrystallisation in hexane yielded crystals which were analysed by X-ray diffraction. The solid-state structure of all complexes display a pseudo-tetrahedral geometry around the aluminium centre with each aluminium ion bonded to two methyl groups (Figure 4.13). Similarly to bisligated complexes no distinct variation in Al–C or Al–O metric data exists, with a distortion from the idealised 109.5 ° angle for the ligand-metal interactions, O(1)-Al(1)-N(1) (95.58° – 98.13°) (Table 4.2). This data agrees well with similar bidentate 'half-salan' Al complexes previously reported.[14,36] In all cases ^{1}H NMR spectra showed the presence of one sharp 6H resonance in the Al-Me region (-0.51 – -0.76 ppm) and a doublet for NCH_2 protons, indicative of a "locked" coordination of the pyrrolidine ring in solution (Figure 4.14). Al(**14**)Me_2 and Al(**19**)Me_2 were not cleanly prepared with the presence of Al(**14**)$_2$Me and Al(**19**)$_2$Me increasing upon recrystallisation. Whilst the bisligated product of **17**H could not be synthesised, Al(**17**)Me_2 was cleanly produced in high yields. $^{13}C\{^1H\}$ and HSQC NMR spectroscopy allowed full assignment of carbon environments. Slight variance in the carbon content from elemental analysis between observed and expected values highlights the high sensitivity of the Al-Me bonds upon data collection.

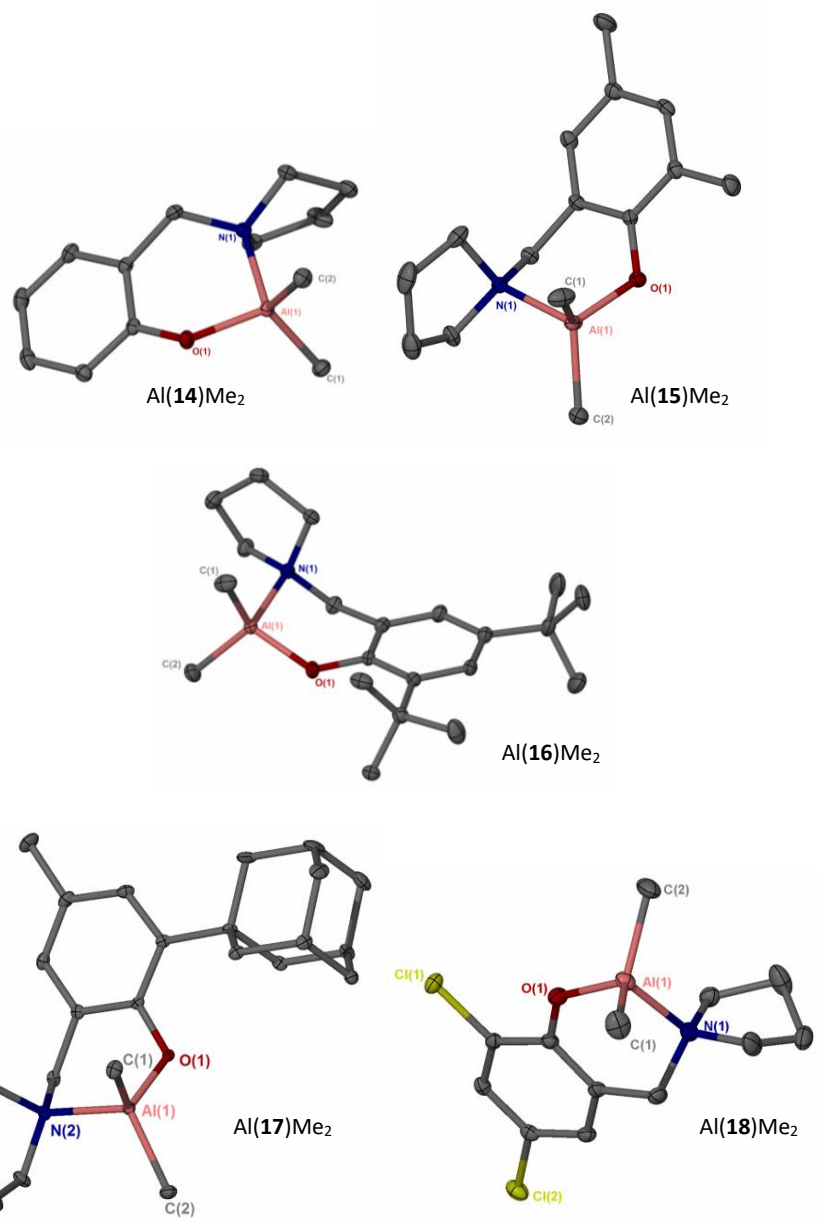

Figure 4.13. Solid state structures of Al(**14–18**)Me_2. Ellipsoids are at the 30% probability level. All hydrogen atoms are removed for clarity.

Table 4.2. Comparative information on the bond angles and bond lengths for Al(**14-18**)Me_2 complexes.

	Al(**14**)Me_2	Al(**15**)Me_2	Al(**16**)Me_2	Al(**17**)Me_2	Al(**18**)Me_2
Al(1)-O(1)	1.775(1)	1.764(2)	1.760(2)	1.777(2)	1.761(1)
Al(1)-N(1)	2.030(1)	2.040(2)	2.029(2)	2.047(2)	1.997(2)
Al(1)-C(1)	1.964 (1)	1.954(3)	1.963(3)	1.964(3)	1.964(2)
Al(1)-C(2)	1.958(1)	1.956(3)	1.956(3)	1.952(3)	1.956(2)
O(1)-Al(1)-N(1)	98.13(4)	97.43(8)	97.46(9)	97.45(8)	95.58(7)
C(1)-Al(1)-O(1)	112.06(9)	111.22(11)	112.37(13)	111.88(10)	112.27(9)

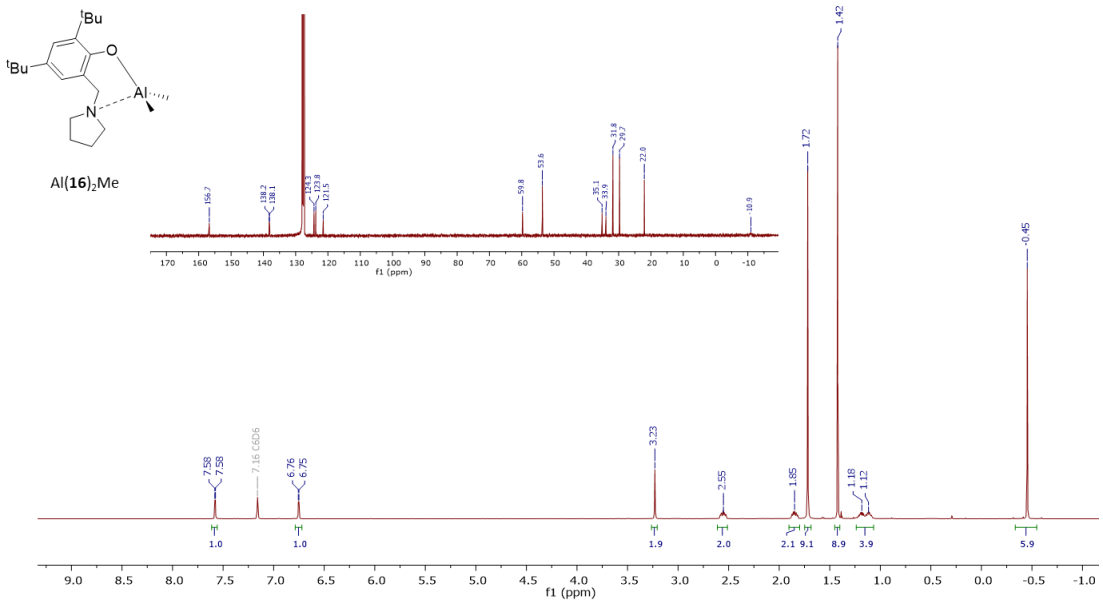

Figure 4.14. ^{1}H and $^{13}C\{^{1}H\}$ NMR spectra of Al(**3**)Me_2 in C_6D_6 at 298 K.

As expected DOSY NMR spectroscopy showed a lower diffusion coefficient for the larger Al(**15**)$_2$Me (D = 7.01 × 10^{-10} m^2s^{-1}) in comparison to Al(**15**)Me_2 (D = 9.9 × 10^{-10} m^2s^{-1}), confirming the monoligated complex does not rearrange in solution. It is expected the addition of exogenous alcohol generates an *in-situ* alkoxide species from which it can then act as the initiator for polymerisation. With the possibility of an alkoxide bridging two aluminium centres, it is important to understand the nature of this species so appropriate catalyst loadings can be established.[37] As there are two methyl groups on the synthesised monoligated structures it is possible both will be removed and hence the aluminium centre will have two alkoxides, altering the nature of catalytically active species in solution. To investigate this further, stoichiometric reactions of Al(**15**)Me_2 with 1 and 2 equivalents of BnOH were carried out and monitored via ^{1}H NMR spectroscopic analysis (Figure 4.15).

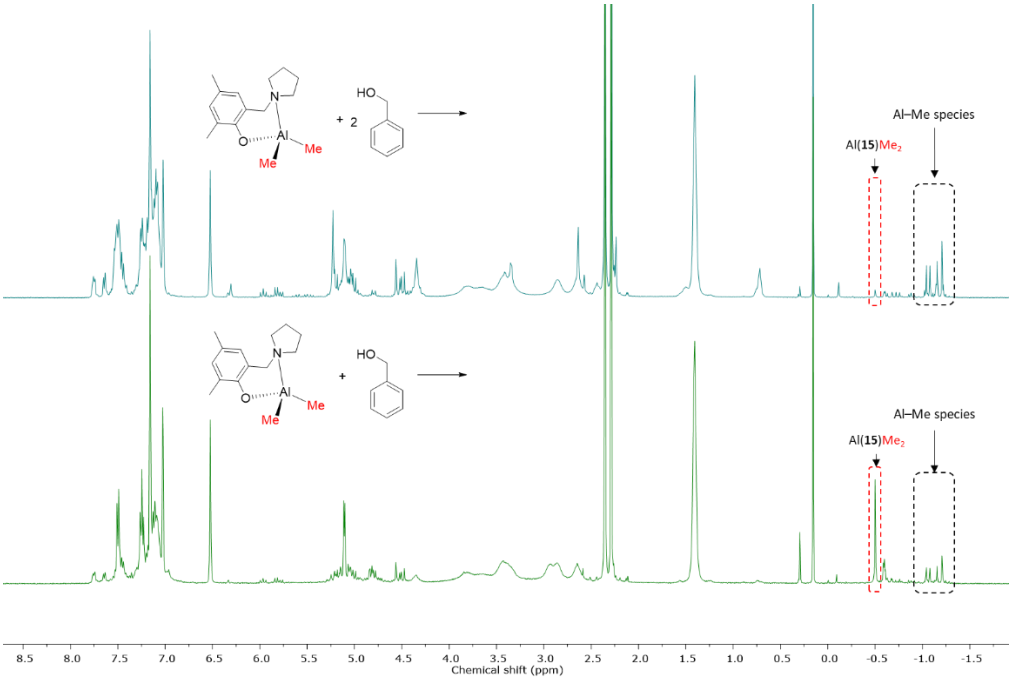

Figure 4.15. Stacked ^{1}H NMR (400 MHz, 298 K) spectra for the reaction of Al(**15**)Me_2 with BnOH in C_6D_6.

Al(**15**)Me_2 was reacted with 1 equivalent of BnOH. There was a reduction in the number of Al-Me signals of Al(**15**)Me_2 after 10 minutes, with the appearance of new resonances in the range of -0.5 ppm and 1.5 ppm, possibly indicating the formation of Al(**15**)Me(BnO). Under the same time frame, reaction of Al(**15**)Me_2 with 2 equivalents of BnOH shows the complete release of Al-Me groups assigned to Al(**15**)Me_2, with a small range of resonances assigned as Al-Me in a different coordination sphere (-1.0 – -1.3 ppm). Hypothetically, if both equivalents of BnOH reacted, no resonances should be seen for M-CH_3. ^{1}H DOSY analysis of these species does not show a significant reduction in diffusion rate for either species indicating that neither species had dimerised under these conditions.

4.2.4. Synthesis of dinuclear monoligated aluminium pyrrolidine complexes

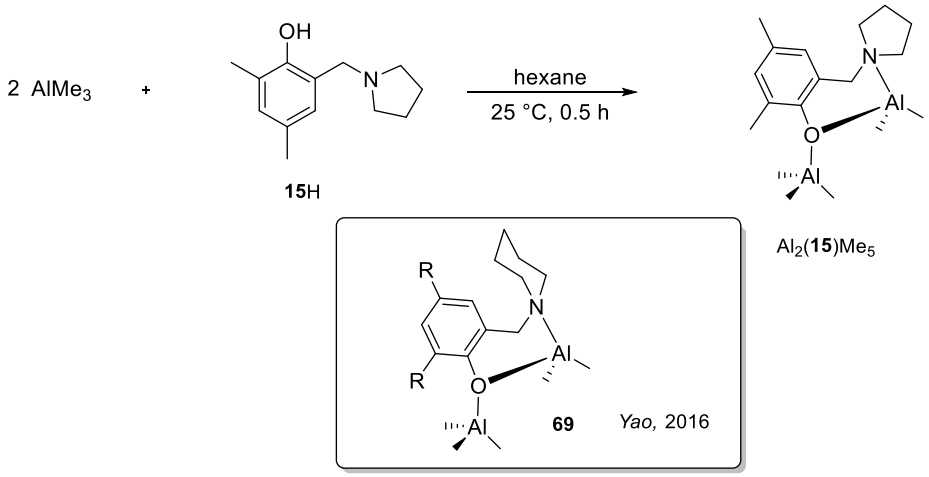

Scheme 4.4. Synthesis of dinuclear monoligated aluminium pyrrolidine complex (Al_2(**2**)Me_5), and comparative piperidine literature complex.[16]

In a separate study the equivalents of $AlMe_3$ in the reaction mixture were increased to 2:1 {[$AlMe_3$]$_0$:[**15**H]$_0$}, in order to see if a dinuclear species could be isolated following the direction of similar studies in literature (Scheme 4.4).[16] These systems report a substantial rate increase when applied to ROP, explained due to possible cooperative effects between the metal centres. Following the same synthetic protocol as for Al(**X**)Me_2 it was possible to obtain a crystalline material for reaction with **15**H. Single-crystal XRD analysis confirmed the bulk structure as Al_2(**15**)Me_5 with coordination of the bridging phenolate oxygen to two aluminium centres (Figure 4.16).

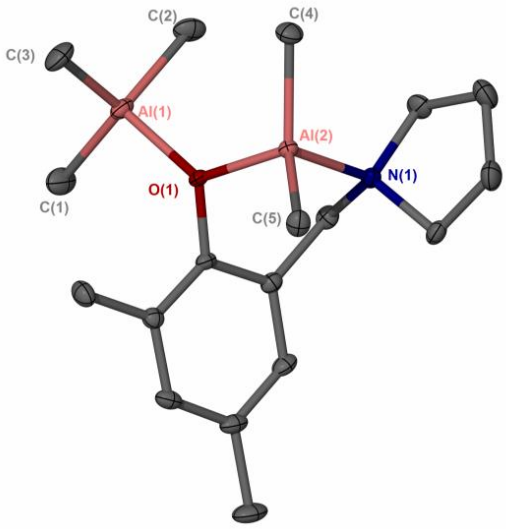

Figure 4.16. Solid-state structure of Al_2(**15**)Me_5. Ellipsoids are at the 30% probability level. Hydrogens are removed for clarity.

Table 4.3. Comparative information on the bond angles (°), bond lengths (Å) of Al_2(**15**)Me_5 and Al(**15**)Me_2.

	Al_2(**15**)Me_5	Al(**15**)Me_2
Al(2)–O(1)	1.843(1)	1.764(2)
Al(2)–N(1)	2.05(1)	2.040(2)
Al(1)–O(1)	1.932(1)	-
O(1)–Al(2)–N(1)	95.92(5)	97.43(8)
Al(1)–O(1)–Al(2)	128.38(5)	-

The solid-state structure of Al_2(**15**)Me_5 shows similarities with the monoligated Al(**15**)Me_2 with a similar Al-N bond lengths and O(1)–Al(2)–N(1) bond angles (Table 4.3). A difference in the Al–O bond length for the nitrogen bound aluminium highlights a possible reduction in the Lewis basicity of the phenolate oxygen, as a result from coordination to multiple Lewis acidic centres. The longer bond length in Al_2(**15**)Me_5 could lead to poorer activity of this aluminium centre upon initiation. The side chain -$AlMe_3$ can be seen to be datively coordinated to the ligand with a longer Al–O bond distance (Al(1)–O(1) = 1.932(1) Å *vs* Al(2)–O(1) = 1.843(1) Å). For the ROP of epoxides, Yao and co-workers suggest these systems behave cooperatively with retention of both aluminium centres coordinated to the ligand framework.[16] This is supported by MALDI-ToF analysis where only polymeric series are seen suggesting only one type of active species in solution.

^{1}H NMR spectroscopy shows this compound as pure with retention of the solid-state structure in solution (Figure 4.17). Three Al-Me resonances are seen (-0.17, -0.24, -1.04 ppm), with integration as 9H at -0.24 ppm, indicative of equivalent Al-Me groups on the datively coordinated metal centre. An integration of 3H each for the remaining Al-Me resonances shows the compound as distinctively different to Al(**15**)Me_2 (6H, -0.45 ppm). Due to the highly solubility the material in non-polar solvents such as hexane and diethyl ether, only low yields were isolated (0.17 mmol, 17%).

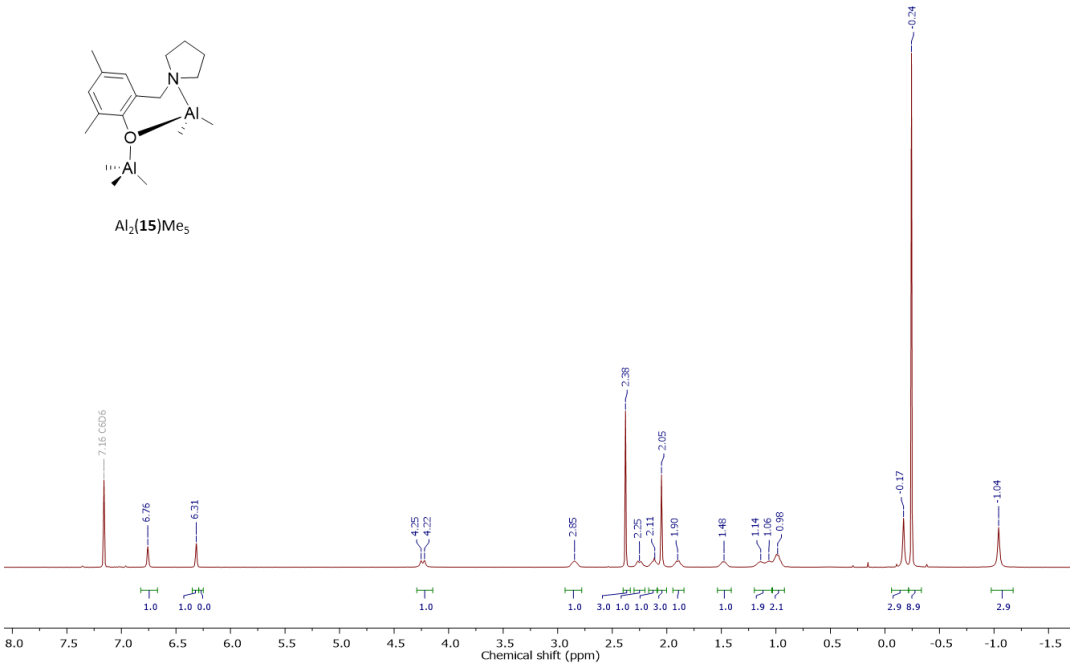

Figure 4.17. ^{1}H NMR (400 MHz, 298 K) of Al_2(**15**)Me_5 in C_6D_6.

4.3. Polymerisation of *rac*-LA using aluminium monopyrrolidine complexes

Monoligated and bisligated complexes were tested in solution (80 °C, toluene, $[LA]_0$ = 0.69 M) and melt conditions (130 °C, no solvent) for the polymerisation of *rac*-LA (Table 4.4). With exceptions, BnOH was added as a co-initiator to generate the *in-situ* alkoxide initiator. In order to compare with bulk activity, reactions were generally carried out at feed ratios of 100:1:1 {$[LA]_0$:$[I]_0$:$[BnOH]_0$} with variation of the timeframe of polymerisation indicating the activity.

Table 4.4. Polymerisation data for the ROP of *rac*-LA with Al(**X**)Me_2, Al(**X**)$_2$Me and Al_2(**15**)Me_5

Entry	Initiator	$[LA]_0$:$[I]_0$:$[BnOH]_0$	Temp (°C)	Time (h)	Conv. (%)[e]	M_n^{theo} (kg mol^{-1})[f]	M_n^{SEC} (kg mol^{-1})[g]	$Đ$ [g]	P_r [h]
1[32]	Al(**2**)Me	100:1:1	80[a]	120	86	12.5	21.6[d]	1.05	0.87
2	Al(**15**)$_2$Me	100:1:1	80[a]	6	38	5.6	4.2	1.02	0.28
3	Al(**15**)$_2$Me	100:1:1	80[a]	24	95	13.8	8.8	1.04	0.29
4	Al(**15**)$_2$Me	100:1:0	130[b]	0.25	60	8.8	18.5	1.24	0.38
5	Al(**15**)$_2$Me	100.1:1	130[b]	0.25	94	13.7	14.9	1.10	0.42
6	Al(**15**)$_2$Me	100:1:1	25[c]	120	17	2.6	-	-	-
7	Al(**16**)$_2$Me	100:1:1	80[a]	48	32	4.7	4.5	1.28	0.48
8	Al(**18**)$_2$Me	100:1:1	80[a]	6	36	5.3	4.6	1.18	0.39
9	Al(**18**)$_2$Me	100:1:1	80[a]	24	96	13.9	12.0	1.17	0.41
10	Al(**19**)$_2$Me	100:1:1	80[a]	6	48	6.9	4.4	1.07	0.51
11	Al(**19**)$_2$Me	100:1:1	80[a]	24	72	10.4	12.8	1.10	0.52
12	Al(**14**)Me_2	100:1:1	80[a]	6	84	12.2	8.25	1.06	0.47
13	Al(**15**)Me_2	100:1:1	80[a]	6	73	10.6	9.3	1.05	0.20
14	Al(**15**)Me_2	100:1:2	80[a]	6	52	7.4	6.1	1.06	0.22
15	Al(**15**)Me_2	100:1:0	80[a]	6	23	3.4	-	-	-
16	Al(**15**)Me_2	100:1:1	130[b]	0.16	73	10.6	12.6	1.23	0.39
17	Al(**15**)Me_2	1000:1:10	130[b]	0.5	92	13.3	18.2	1.10	0.44
18	Al(**16**)Me_2	100:1:1	80[a]	24	16	2.4	-	-	-
19	Al(**17**)Me_2	100:1:1	80[a]	24	12	1.9	-	-	-
20	Al(**18**)Me_2	100:1:1	80[a]	6	74	10.7	8.8	1.06	0.39
21	Al(**18**)Me_2	100.1.2	80[a]	6	68	5.0	5.3	1.07	0.45
22	Al_2(**15**)Me_5	100:1:1	80[a]	6	95	13.8	4.6	1.38	0.47

[a] 80 °C, toluene, $[LA]_0$ = 0.69 M, [b] 130 °C, no solvent, [c] 25 °C, CH_2Cl_2, $[LA]_0$ = 0.69 M. [d] Calculated via RI methods using a polystyrene standard. [e] Determined from analysis of the ^{1}H NMR spectrum. [f] Theoretical molecular weight calculated from conversion { $[LA]_0/[BnOH]_0$ × (conversion × 144.13) + 108.14)}, [g] Determined by SEC (THF) calibrated using RI, viscometer, and light scattering detectors using the universal calibration method via multi-detection software. [h] Determined from ^{1}H{^{1}H} NMR spectrum.

All the initiators were shown to display mild to moderate isotactic bias (Figure 4.18). This is the reverse to the very strong heteroselectivity (P_r = 0.87) seen with the bipyrrolidine system Al(**2**)Me realised by Jones and coworkers.[32] The Al(**X**)$_2$Me bisligated systems show a substantial rate increase from the previously reported system, achieving high conversions over 24 hours in comparison to the 120 hours required for Al(**2**)Me (Entry 3, Table 4.4).[32] Jones and co-workers rationalise their selectivity bias with the influence of the chirality of the bipyrrolidine backbone, with the *meso*- version yielding the stated heterotactic behaviour and the homo chiral versions yielding atactic PLA. As the synthesised bisligated complexes contain no ligand chirality, it can be assessed this difference in activity is the result of variation in geometry between these two systems, altering the polymerisation direction of the incumbent monomer unit. Moreover, the *sii*, *iis* and *isi* tetrads are present in a ratios of approximately 1:1:1 indicative that a chain-end mechanism is in operation.

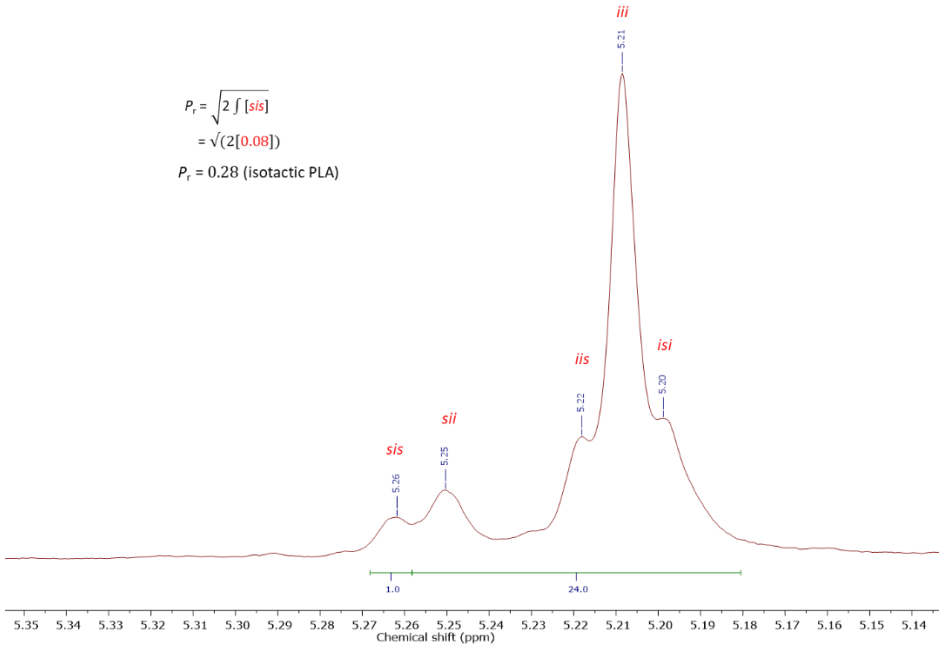

Figure 4.18. $^1H\{^1H\}$ NMR spectrum of isotactic polymer produced from Al(**2**)$_2$Me (Entry **2**, Table 3.4).

As expected increasing the bulk around the metal decreased the activity, with ^{t}Bu and Ad-complexes showing a significant reduction in conversion compared to Me substituted complexes. Contrary to the literature expectation, this reduction in rate was not met with an increase in selectivity with Al(**16**)$_2$Me, Al(**16**)Me$_2$ and Al(**17**)Me$_2$ all yielding atactic PLA. Deactivating substituents were more active with good iso-selectivity, as seen for Al(**18**)Me$_2$ (Entry 9 *vs* 10, Table 4.4). This monoligated system also displayed a greater activity and good molecular control in comparison to the bisligated analogue (Entry 20 *vs* 8, Table 4.4). As both these studies were carried out with feed ratios of 100:1:1 {[LA]$_0$:[I]$_0$:[BnOH]$_0$}, results support

that monoligated complexes with two Al–CH_3 groups, only undergo 1 alkoxide addition with the polymerisation proceeding as expected upon initiation. Increasing the feed ratio of BnOH to 100:1:2 {$[LA]_0$:$[I]_0$:$[BnOH]_0$} yielded a similar rate and selectivity, with a concomitant reduction in observed molecular weights according to the addition of multiple chain transfer agents (Entry 12–13 and 19–20, Table 4.4). Di-nuclear mono phenolate Al_2(**2**)Me_5 appeared similarly active to mononuclear complexes albeit with no stereoselectivity and poor molecular weight control. It is expected this is the result of unpredictable initiation caused by multiple metal centres with $AlMe_3$ and Al(**2**)Me_2 likely to be existing in solution prior to initiation.

Al(**15**)Me_2 is the best performing catalyst combining the highest rates (73% in 6 hours) and greatest isoselectivities (P_r = 0.2) with excellent agreement between observed and calculated M_n values (M_n^{SEC} = 9.3 kg mol^{-1}, M_n^{theo} = 10.6 kg mol^{-1}, $Đ$ = 1.05) (Entry 13, Table 4.4). Low activity was seen without the addition of BnOH showing the poor initiation ability of the methyl groups. It is likely the observed conversion is due to a low concentration of protic impurities in the reaction mixture. *In-situ* ^{1}H NMR kinetics with the enantiomers of LA show a faster rate for the polymerisation of *L*-LA compared to *rac*-LA as expected with an isoselective catalyst (Figure 4.19). From the difference in observed rate constants it is possible to calculate P_r = 0.78 as detailed in literature.[38]

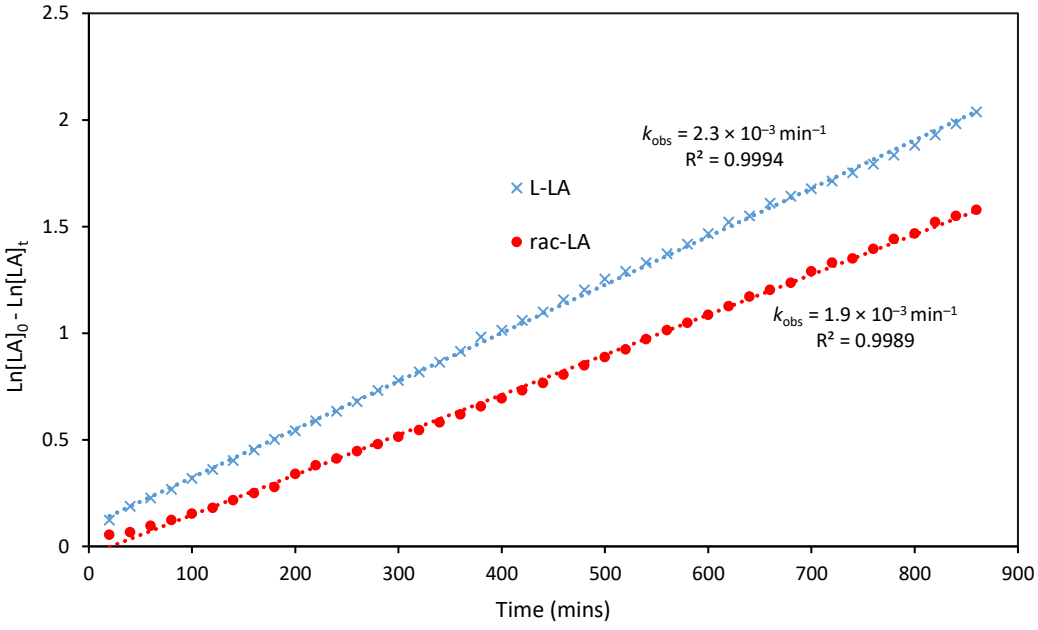

Figure 4.19. Pseudo logarithmic plot for the polymerisation of LA using Al(**15**)Me_2 at 80 °C in toluene, {$[LA]_0$:$[I]_0$:$[BnOH]_0$ = 100:1:1}, $[LA]_0$ = 0.69 M. • = *rac*-LA, x = L-LA.

To further investigate the controlled nature of polymerisation with Al(**15**)Me_2 multiple reactions were run in batch with quenching at regular time intervals {100:1:1 $[LA]_0$:[Al(**15**)Me_2]$_0$:$[BnOH]_0$, $[LA]_0$ = 0.69 M, toluene, 80 °C}. Plotting the observed molecular weight over conversion yields a linear relationship with a gradient of ≈ 144 g mol^{-1} indicative of one chain growing per metal centre (Figure 4.20). The dispersity remained low (Đ < 1.10) confirming a well-controlled process.

Testing this system under more industrially relevant melt conditions (130 °C, no solvent) showed a reduction in selectivity with a notable increase in rate, with mass transport limited viscosity achieved within 10 minutes. Bisligated Al(**15**)$_2$Me showed similar behaviour, achieving high conversions (94%), albeit after a longer reaction time (15 minutes) (Entry 16, Table 3.4). Under 'immortal' conditions of 1000:1:10 {$[LA]_0$:[Al(**15**)Me_2]$_0$:$[BnOH]_0$} predictable molecular weights were achieved with high conversions obtained after 30 minutes (Entry 17, Table 4.4).[39,40] This immortal behaviour is desired industrially with control of the molecular weight varied by addition of alcohol.

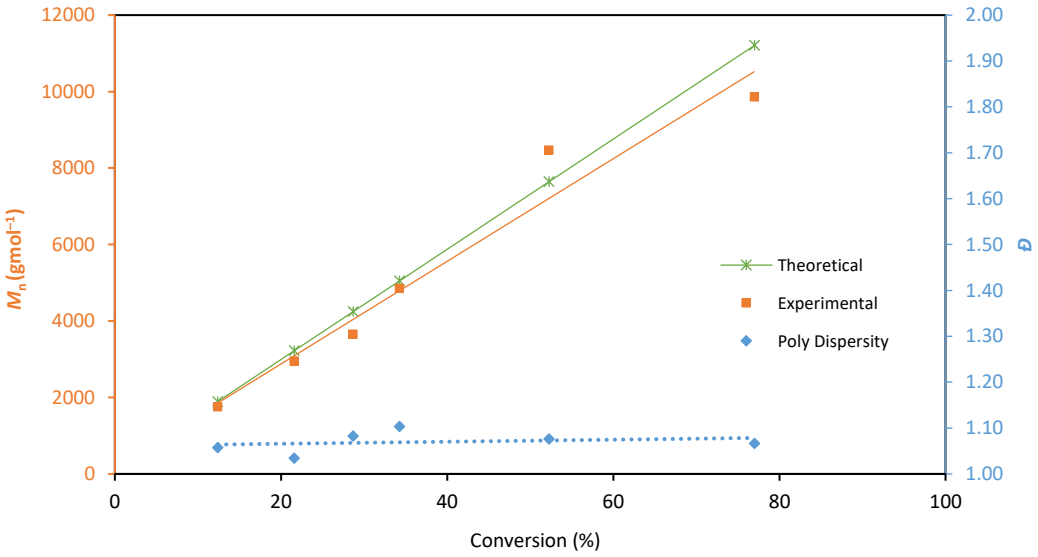

Figure 4.20. Plot of M_n^{SEC} and *Đ* versus conversion for the polymerisation of *rac*-LA with Al(**15**)Me_2 at feed ratios of 100:1:1 {$[LA]_0$:[Al(**2**)Me_2]$_0$:$[BnOH]_0$}, $[LA]_0$ = 0.69 M, toluene, 80 °C).

In order to further probe differences in the activity between synthesised initiators, '*in-situ*' ^{1}H NMR spectroscopic kinetic experiments were carried out with *rac*-LA (Figure 4.21). Linearisation of the data shows a pseudo-first order behaviour for all complexes. In agreement with batch polymerisations, comparable mono ligated complexes Al(**X**)Me$_2$, polymerise at a significantly faster rate than bisligated Al(**X**)$_2$Me systems. This is exemplified by Al(**15**)Me$_2$ and Al(**15**)$_2$Me (k_{obs} = 18.8 × 10^{-4} min^{-1} *vs* k_{obs} = 6.5 × 10^{-4} min^{-1} respectively).

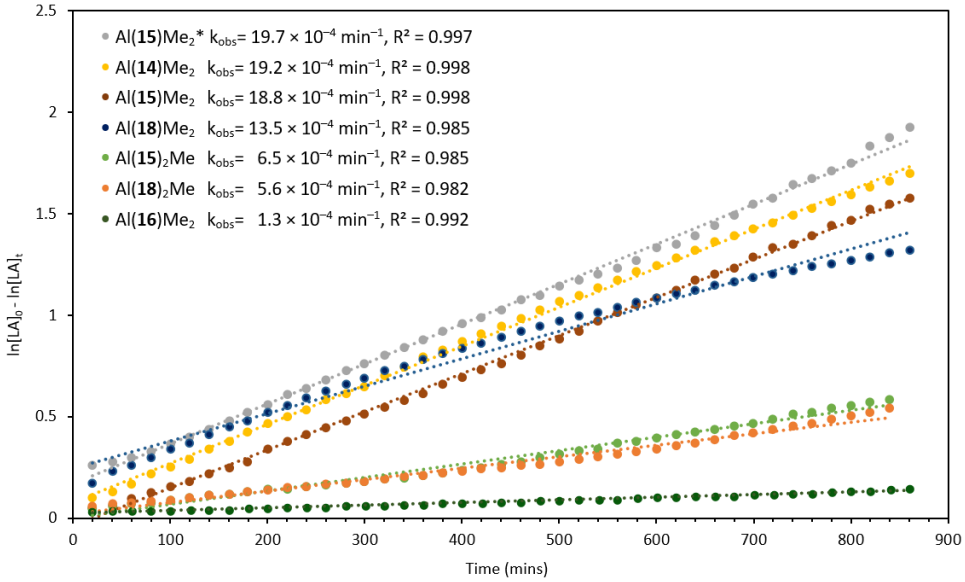

Figure 4.21. Stacked kinetic plots for the ^{1}H NMR monitored polymerisation of *rac*-LA with synthesised mono and bisligated complexes {100:1:1 = [LA]$_0$:[I]$_0$:[BnOH]$_0$}, [LA]$_0$ = 0.69 M, toluene, 80 °C).* {[LA]$_0$:[I]$_0$:[BnOH]$_0$} = 100:1:2.

Whilst it was not possible to synthesise sufficient quantities of Al(**14**)Me$_2$ to carry out batch scale testing, kinetic analysis shows this system to have the fastest observable rate at feed ratios of 100:1:1 {[LA]$_0$:[I]$_0$:[BnOH]$_0$}. At feed ratios of 100:1:2 {[LA]$_0$:[Al(**15**)Me$_2$]$_0$:[BnOH]$_0$} a slightly faster observable rate constant is observed than at 100:1:1. This is likely due to a reduction in the initiation period in agreement with stoichiometric reactions carried out. This is also possibly supported an expected reduction in viscosity of the polymeric sample from a lowering in molecular weight. Further probing the nature of the polymerisation process, MALDI-ToF analysis was performed on polymer produced from 100:1:1 and 100:1:2 {[LA]$_0$:[Al(**2**)Me$_2$]$_0$:[BnOH]$_0$} experiments (Figure 4.22). Both polymers show a degree of transesterification evidenced by a minor series with repeating units of 72 g mol^{-1}. Both series show linear polymer with end groups calculated as that of BnO– and H– end groups.

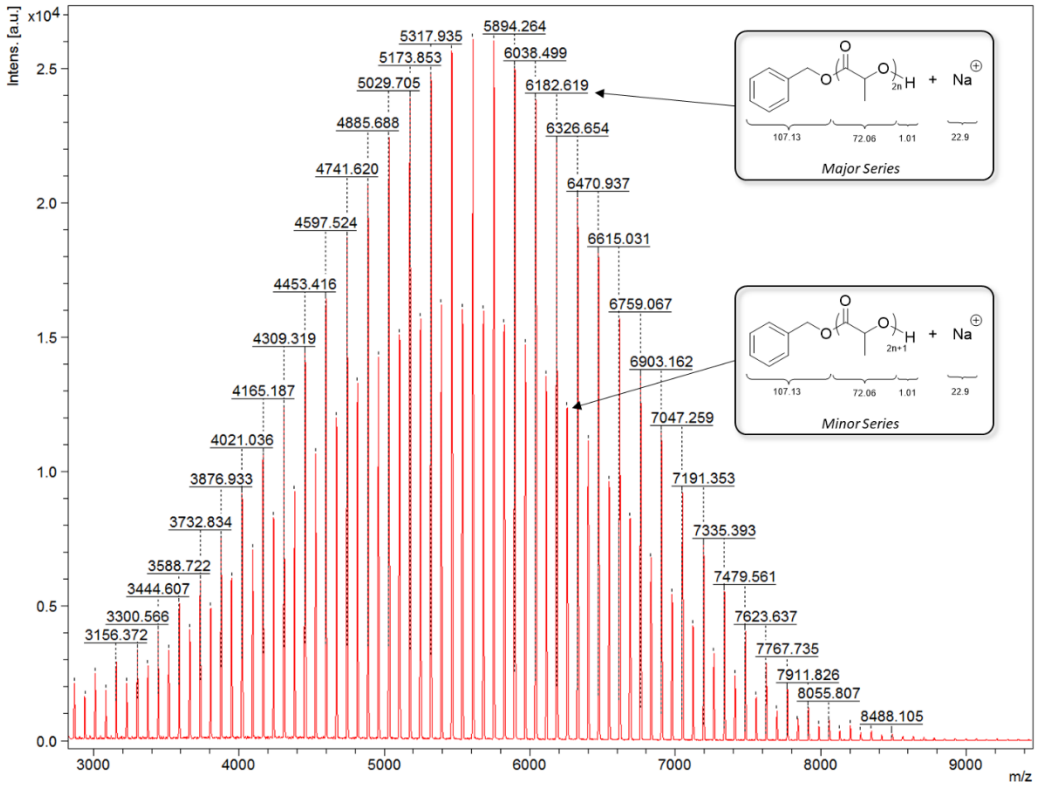

Figure 4.22. MALDI-ToF spectrum for polymer produced with Al(**15**)Me_2 at feed ratios of 100:1:1 {$[LA]_0$:[Al(**2**)Me_2]$_0$:$[BnOH]_0$} (Entry 13, Table 3.4). Conversion = 73%. Time = 6 hours. M_n^{SEC} (kg mol^{-1}) = 9.3, M_n^{theo}(kg mol^{-1}) = 10.6. Linear polymer with BnO + H end groups. The presence of a minor series of indicates a degree of transesterification is present.

4.4. Conclusions and future work

A series of bidentante amino-phenol ligands with varying steric and electronic substituents were complexed to aluminium. Depending on the stoichiometric ratio of the reagents and reaction conditions it was possible to isolate and fully characterise complexes with a 2:1, 1:1 and 1:2 ratio of ligand to metal centre. Bisligated complexes were similar in structure to piperazine complexes previously reported, occupying a distorted trigonal bipyramidal structure with nitrogen groups trans to each other.[14,18] This is the opposite conformation of previous bipyrrolidine complexes where nitrogen atoms exist cis to each other.[32,41,42] Stoichiometric reactions with BnOH showed these complexes likely form alkoxide species prior to ROP, with evidence to suggest that during polymerisation Al(**X**)Me_2 species undergo only one alkoxide substitution, with the other aluminium alkyl bond existing in a meta-stable state. Further investigation should consider efforts to isolate aluminium alkoxide complexes. It has previously been shown by Romain and co-workers that isolation of similar species shows the complex exists as a binuclear aluminium dialkoxide complex in the solid state.[37] These complexes were shown to be substantially more active than the monomeric aluminium alkyl complex. As DOSY spectroscopic studies carried out on synthesised mono pyrrolidine complexes suggest the complexes are monomeric in the presence of BnOH, isolation of these structures in the solid-state could be in a different coordination motif, supplying information on the initiation mechanisms of these alkoxide species.

When applied to the polymerisation of *rac*-LA the complexes were active in toluene at 80 °C with narrow dispersities and good molecular weight control seen throughout. In addition, an isoselective bias was seen, presenting a selectivity switch from the highly heterotactic bipyrrolidine analogue, Al(**2**)Me.[32] Such a switch has not been previously realised for analogous bidentate and tetradetante complexes, with only a reduction in reactivity and selectivity when the bisligated bidentate complexes have been previously tested for ROP.[15] Monoligated complexes appeared more active than the bisligated systems likely due to the larger coordination sphere available. This was supported by kinetic analysis showing distinct difference in rate between analogous Al(**X**)$_2$Me and Al(**X**)Me_2. Unexpectedly this rate improvement was coupled with a selectivity improvement with high isotacticities being seen (P_r = 0.20). These results make these systems the fastest and most selective bidentate aluminium species to date.[1,43]

Such as in the stoichiometric reactions with exogenous alcohol, the addition of multiple equivalents of BnOH only reduced the initiation period during ROP with similar reactivity and selectivity seen. The effect of steric and electronic substituents on the polymerisation was seen to be most significant in determination of rate, with bulky Ad– and ^{t}Bu– complexes being significantly less active. Electronic variation showed that the mildly donating methyl substituted ligands performed best in rate and selectivity in contrast to previous kinetic studies on the impact of substituent groups.[30]

Future work surrounding these species should be expanding their adoption as catalysts for less facile monomers. The good stereo-selectivities, high rates and narrow dispersities make these system excellent candidates for the polymerisation of 5 membered lactones, and the ROP of cyclic carbonates. To this end the bisligated aminophenolate aluminium complexes **59-62**, have been explored for ROP of CHO and the ROCOP of CO_2 and CHO.[17] In these examples variation on the piperazine ring proved important in unlocking copolymerisation activity. Issues in polycarbonate selectivity means these systems are shown as highly active examples of polyether catalysts at loadings as low as 0.001 mol %. Initial investigations with Al(**15**)Me_2 has shown at loadings of 0.01 mol % CHO can be converted to polyether at high conversion (89%) after 10 minutes stirring neat at 25 °C. This result clearly shows the favouring of ROP rather than ROCOP for this system. However, higher activity and selectivity for polycarbonate synthesis has been reported for bidentate aluminium methyl complexes, making further investigation into the selectivities of bisligated and monoligated complexes pertinent.[44–47]

4.5. References

1 Y. Wei, S. Wang and S. Zhou, *Dalton. Trans.*, 2016, **45**, 4471–4485.

2 P. A. Cameron, V. C. Gibson, C. Redshaw, J. A. Segal, G. A. Solan, A. J. P. White and D. J. Williams, *Dalton. Trans.*, 2001, **119**, 1472–1476.

3 J. Liu, N. Iwasa and K. Nomura, *Dalton. Trans.*, 2008, **3**, 3978–3988.

4 N. Iwasa, S. Katao, J. Liu, M. Fujiki, Y. Furukawa and K. Nomura, *Organometallics*, 2009, **28**, 2179–2187.

5 C. L. Lee, Y. F. Lin, M. T. Jiang, W. Y. Lu, J. K. Vandavasi, L. F. Wang, Y. C. Lai, M. Y. Chiang and H. Y. Chen, *Organometallics*, 2017, **36**, 1936–1945.

6 N. Iwasa, J. Liu and K. Nomura, *Catal. Commun.*, 2008, **9**, 1148–1152.

7 W. Zhang, Y. Wang, L. Wang, C. Redshaw and W. H. Sun, *Dalton. Trans.*, 2012, **41**, 11587.

8 W. Zhang, Y. Wang, L. Wang, C. Redshaw and W. H. Sun, *J. Organomet. Chem.*, 2014, **750**, 65–73.

9 M. Normand, V. Dorcet, E. Kirillov and J. F. Carpentier, *Organometallics*, 2013, **32**, 1694–1709.

10 M. Li, M. Chen and C. Chen, *Polymer* , 2015, **64**, 234–239.

11 J. Liu and H. Ma, *Dalton. Trans.*, 2014, **43**, 9098–9110.

12 J. Liu and H. Ma, *J. Polym. Sci. Part A Polym. Chem.*, 2014, **52**, 3096–3106.

13 S. K. Roymuhury, D. Chakraborty and V. Ramkumar, *Eur. Polym. J.*, 2015, **70**, 203–214.

14 L. Chen, W. Li, D. Yuan, Y. Zhang, Q. Shen and Y. Yao, *Inorg. Chem.*, 2015, 150428135954005.

15 Y. Wang and H. Ma, *J. Organomet. Chem.*, 2013, **731**, 23–28.

16 W. Li, H. Ouyang, L. Chen, D. Yuan, Y. Zhang and Y. Yao, *Inorg. Chem.*, 2016, **55**, 6520–6524.

17 H. Plommer, I. Reim and F. M. Kerton, *Dalton. Trans.*, 2015, **44**, 12098–12102.

18 N. Ikpo, S. M. Barbon, M. W. Drover, L. N. Dawe and F. M. Kerton, *Organometallics*, 2012, **31**, 8145–8158.

19 N. Nomura, T. Aoyama, R. Ishii and T. Kondo, *Macromolecules*, 2005, **38**, 5363–5366.

20 P. Hormnirun, E. L. Marshall, V. C. Gibson, a. J. P. White and D. J. Williams, *J. Am. Chem. Soc.*, 2004, **126**, 2688–2689.

21 H. C. Hsiao, A. Datta, Y. F. Chen, W. Chang, T. Y. Lee, C. H. Lin and J. H. Huang, *J. Organomet. Chem.*, 2016, **804**, 35–41.

22 S. M. Kirk, H. C. Quilter, A. Buchard, L. H. Thomas, G. Kociok-Kohn and M. D. Jones, *Dalton. Trans.*, 2016, **45**, 13846–13852.

23 F. Isnard, M. Lamberti, L. Lettieri, I. D'auria, K. Press, R. Troiano and M. Mazzeo, *Dalton. Trans.*, 2016, **45**, 16001–16010.

24 D. Alhashmialameer, N. Ikpo, J. Collins, L. N. Dawe, K. Hattenhauer and F. M. Kerton, *Dalton. Trans.*, 2015, **44**, 20216–20231.

25 M. Normand, T. Roisnel, J. F. Carpentier and E. Kirillov, *Chem. Commun.*, 2013, **49**, 11692–11694.

26 A. Arbaoui, C. Redshaw and D. L. Hughes, *Chem. Commun.*, 2008, 4717–4719.

27 A. Arbaoui and C. Redshaw, *Polym. Chem.*, 2010, **1**, 801–826.

28 X. Pang, R. Duan, X. Li and X. Chen, *Polym. Chem.*, 2014, **5**, 3894–3900.

29 X. F. Yu and Z. X. Wang, *Dalton. Trans.*, 2013, **42**, 3860–3868.

30 H.-C. Tseng, M. Y. Chiang, W.-Y. Lu, Y.-J. Chen, C.-J. Lian, Y.-H. Chen, H.-Y. Tsai, Y.-C. Lai and H.-Y. Chen, *Dalton Trans.*, 2015, **44**, 11763–73.

31 J. Beament, M. F. Mahon, A. Buchard and M. D. Jones, *New J. Chem.*, 2017, **41**, 2198–2203.

32 M. D. Jones, L. Brady, P. McKeown, A. Buchard, P. M. Schäfer, L. H. Thomas, M. F. Mahon, T. J. Woodman and J. P. Lowe, *Chem. Sci.*, 2015, **6**, 5034–5039.

33 H. Du, A. H. Velders, P. J. Dijkstra, J. Sun, Z. Zhong, X. Chen and J. Feijen, *Chem. - A Eur. J.*, 2009, **15**, 9836–9845.

34 K. Press, I. Goldberg and M. Kol, *Angew. Chemie - Int. Ed.*, 2015, **54**, 14858–14861.

35 N. Maudoux, E. Tan, Y. Hu, T. Roisnel, V. Dorcet, J. F. Carpentier and Y. Sarazin, *Main Gr. Met. Chem.*, 2016, **39**, 131–143.

36 S. Dagorne, L. Lavanant, R. Welter, C. Chassenieux, P. Haquette and G. Jaouen, *Organometallics*, 2003, **22**, 3732–3741.

37 S. Gesslbauer, H. Cheek, A. J. P. White and C. Romain, *Dalton. Trans.*, 2018, **47**, 10410–10414.

38 N. Nomura, R. Ishii, Y. Yamamoto and T. Kondo, *Chem. - A Eur. J.*, 2007, **13**, 4433–4451.

39 L.-E. Chile, T. Ebrahimi, A. Wong, D. C. Aluthge, S. G. Hatzikiriakos and P. Mehrkhodavandi, *Dalton. Trans.*, 2017, **46**, 6723–6733.

40 T. Ebrahimi, D. C. Aluthge, B. O. Patrick, S. G. Hatzikiriakos and P. Mehrkhodavandi, *ACS Catal.*, 2017, **7**, 6413–6418.

41 J. Beament, M. F. Mahon, A. Buchard and M. D. Jones, *New J. Chem.*, 2017, **41**, 2198–2203.

42 M. D. Jones, S. L. Hancock, P. McKeown, P. M. Schafer, A. Buchard, L. H. Thomas, M. F. Mahon and J. P. Lowe, *Chem. Commun.*, 2014, **50**, 15967–15970.

43 A. Routaray, N. Nath, T. Maharana and A. K. Sutar, *Catal. Sci. Technol.*, 2015, 1–68.

44 W. Clegg, R. W. Harrington, M. North and R. Pasquale, *Chem. - A Eur. J.*, 2010, **16**, 6828–6843.

45 M. North, R. Pasquale and C. Young, *Green Chem.*, 2010, **12**, 1514.

46 S. H. Kim, D. Ahn, M. J. Go, M. H. Park, M. Kim, J. Lee and Y. Kim, *Organometallics*, 2014, **33**, 2770–2775.

47 R. M. Haak, S. J. Wezenberg and A. W. Kleij, *Chem. Commun.*, 2010, **46**, 2713–2723.

Chapter 5

Catalytic synthesis of Lactide – Phosphonate Copolymers for the enhancement of degradation and thermal accessibility

Relating Publication

Macromolecules

Article

Cite This: *Macromolecules* 2019, 52, 1220−1226

pubs.acs.org/Macromolecules

Copolymerization of Cyclic Phosphonate and Lactide: Synthetic Strategies toward Control of Amphiphilic Microstructure

James Beament,[§] Thomas Wolf,[‡] Jens C. Markwart,[‡] Frederik R. Wurm,*[,‡] Matthew D. Jones,*[,§] and Antoine Buchard*[,§]

[§]Department of Chemistry, University of Bath, Claverton Down, Bath BA2 7AY, U. K

[‡]Max Planck Institute for Polymer Research, Ackermannweg 10, D-55128 Mainz, Germany

Supporting Information

ABSTRACT: Controlling the microstructure of polymers through chemical reactivity is key to control the material properties of synthetic polymers. Herein we investigate the ring-opening copolymerization of a mixture of lactide and 2-ethyl-2-oxo-1,3,2-dioxaphospholane, promoted by an aluminum pyrrolidine monophenolate complex or 1,8-diazabicyclo[5.4.0]undec-7-ene (DBU). This monomer mixture provides fast access to amphiphilic copolymers. The reaction conditions control the copolymer microstructure, which has been determined via a combination of ^{1}H and ^{31}P NMR spectroscopy. The choice of initiator has a profound impact: both initiators produce tapered block copolymers but with reverse monomer selectivity. While the aluminum initiator favors the cyclic phosphonate monomer, DBU favors lactide polymerization. Moreover, a sequential control of temperature facilitates the preparation of block copolymers in one pot. Thermal properties measured by TGA and DSC correlate to copolymer architectures. This methodology is the first report of copolymerization between cyclic phosphonates and lactide and opens the possibility to tune the thermal properties, solubility, and degradation rates of the resulting materials.

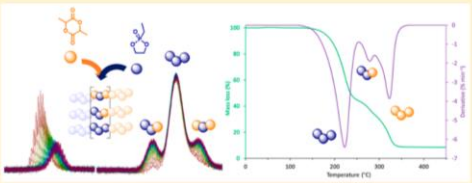

INTRODUCTION

Poly(lactic acid) (PLA) is arguably one of the most promising commodity plastics derived from renewable feedstocks and industrially compostable, which has penetrated a highly unsustainable market of nondegradable polymers based around crude-oil feedstocks.[1−3] The production of PLA was close to 220 000 tonnes in 2017 and is predicted to increase by 50% by 2022.[4] Much research has been directed toward improving the thermal properties of PLA, in particular through the development of stereoselective ring-opening polymerization (ROP) catalysts for lactide.[5] In parallel, increasing efforts have focused on improving the biodegradability of PLA and its composites in natural and landfill environments.[6−8] Notable strategies have included the development of PLA-based polymer blends,[9−14] as well as copolymerization methods to incorporate more degradable linkages into the PLA polyester backbone.[15,16]

In that regard, phosphorus(V)-based monomers, such as phosphoesters {P(═O)(OR)$_2$OR′}, phostones, or phosphonates {P(=O)(OR)$_2$R′}, are of interest due to their low toxicity and facile hydrolysis. Furthermore, while they have been polymerized via step-growth esterification and acyclic diene metathesis,[17,18] cyclic phosphoesters, phostones, and phosphonates are also amenable to ROP,[19,20] which allows copolymerization with lactide.

Penczek and co-workers first investigated polyphosphoesters (−[P(=O)(OR′)ORO]$_n$−) in 1976, as precursors for polyelectrolytes.[21] Since then, these polymers and related polyphosphates have been widely studied for biomedical applications and as flame retardants.[20,22−24] Catalytic ROP of five-membered cyclic phosphoesters has been demonstrated to produce well-defined polyphosphoesters,[25,26] with recent catalyst development (e.g., the combination of thioureas (TUs) and 1,8-diazabicyclo[5.4.0]undec-7-ene (DBU))[27−30] overcoming the broad molecular weight distributions from initial studies.[31−36] Block copolymers of cyclic phosphoesters and lactide synthesized via sequential addition have been studied and applied for tissue engineering and drug delivery,[37−40] these systems showing high rates of enzymatic degradation under physiological conditions.[37]

Polyphosphonates (−[P(=O)R′ORO]$_n$−) are another class of phosphorus(V)-based polymers which differ from polyphosphates in their alkyl side arm (R′), which alters polymerization kinetics and degradation rates compared to phosphates analogues.[41−43] Wurm and co-workers have thus recently synthesized copolymers of phosphonates (PPn) with hydrophilic and hydrophobic segments, which have both lower and upper critical solution temperatures, yielding a route to self-assembled and degradable polymersomes.[44] Compared to polyphosphates, polyphosphonates are less susceptible to transesterification, so that simple ROP initiating systems

Received: November 7, 2018
Revised: January 11, 2019
Published: January 30, 2019

DOI: 10.1021/acs.macromol.8b02385
Macromolecules 2019, 52, 1220−1226

5. Catalytic Synthesis of Lactide–Phosphonate Copolymers for the Enhancement of Degradation and Thermal Accessibility

5.1. Introduction

Despite the significant research effort to improve the thermal properties of PLA, and hence improve its status as a commodity plastic, the recent awakening to the persistence of plastics in the ecosystem has highlighted a potentially drawback in describing PLA as a 'green' alternative.[1–5] Despite being long accepted as compostable under controlled conditions, the leaching of plastic out of the controlled waste system is currently inevitable, with 32% of plastic produced ending up in the environment.[6]

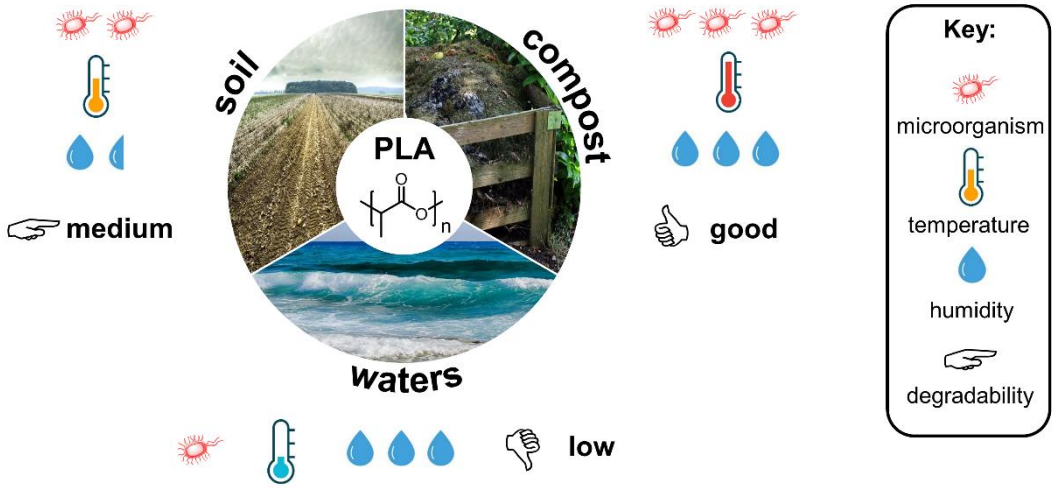

Figure 5.1. Different end of life environments for leeched PLA and their effect on degradability, adapted from Wurm and co-workers.[1]

PLA which ends its life in the world's oceans is exposed to significantly lower temperatures and lower concentrations of microorganisms than the controlled conditions of industrial compostatories (Figure 5.1).[1] Bagheri *et al.* showed that under conditions that closely mimic natural sea water, PLA and many other "biodegradable" plastics showed less than 1% weight loss after 1 year.[2] In a similar study, a yearlong simulation carried out by the California Department of Resources, Recycling and Recovery found that PLA did not meet the American Society of Testing and Materials (ASTM) standards on biodegradation. Only a 8% mass loss after a year exposure to the marine environment was reported, a rate comparable with the negative control, LDPE.[7]

To address this research efforts have focused around blends,[8–11] and co-polymers of as a way of incorporating more degradable units into the bulk material.[3,12–18] Controlled copolymerisation offers an opportunity to tune the properties of polymers, with their development being seen as one of the most significant in the future exploitation of bioplastics.[19] Miller and co-workers, showed how the random copolymerisation of *L*-LA with 1,3-dioxolan-4-one resulted in a polyesteracetal with an enhanced marine degradation profile, reducing M_n by 16% within the first 46 days in a pH 7 salt water solution at an acetal incorporation rate of only 4% (Scheme 5.2).[3,20] Whilst initial degradation is seen, it is not reported whether this is an autocatalytic profile. The break-up to smaller microplastics is more likely with a mass loss of only 1.8% showing limited metabolic degradation to CO_2 and H_2O. In order to produce a 'biodegradable' PLA based polymer with a degradation rate in line with global standards a greater research effort is required.[21,22] Herein this review aims to showcase how phosphorous based monomers could provide a solution as the co-monomer choice and how the microstructure effects the degradation rate of PLA based copolymers.

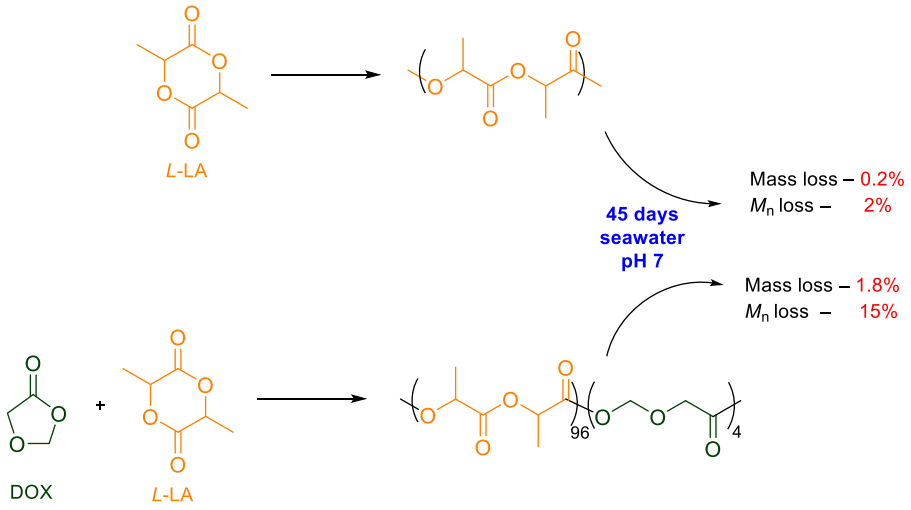

Scheme 5.1. Seawater degradation rates of PLLA and a polyesteracetal synthesised from PLLA and dioxolan-4-one reported by Miller and co-workers.[3,20]

5.1.1. Polyphosphates

Widely studied within literature, with a strong focus as halogen-free flame retardants and biomedical delivery systems, polyphosphates represent a matured area of science with great applicability.[23–28] First explored by Penczek and co-workers as a way of mimicking the ribose backbone of DNA and RNA, poly(phosphoesters) (PPE) dominate this field. From this a range of examples have since been shown, detailing how the thermal and mechanical properties of the polymer can be tuned based on the monomer make-up.[29]

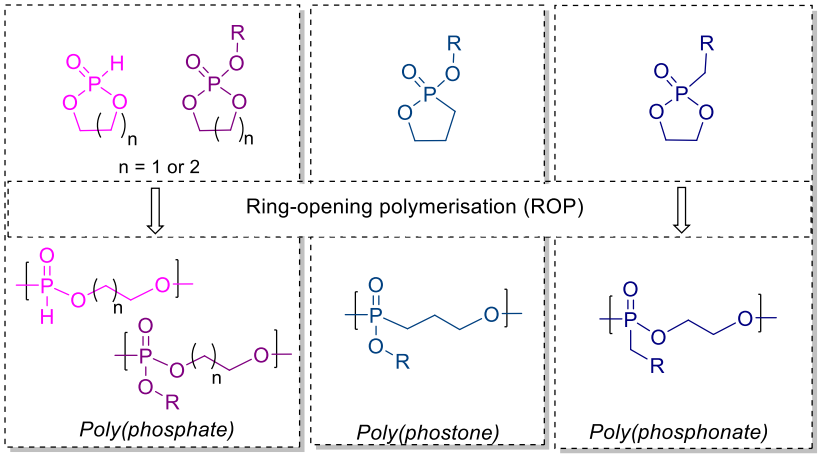

Figure 5.2. Cyclic phosphates, phosphonates and phostones and their ring-opened repeat units.

PPE synthesis can be carried out by either a condensation reaction of the phosphoric acid reagent with the chosen diol, or *via* ROP of the analogous cyclic monomer, with the latter providing a more facile route to high molecular weight polymers (Figure 5.2).[26] Due to the presence of the -OR side group, these systems are reported to undergo significant transesterification during propagation, broadening the molecular dispersity and hence limiting their processability. Catalysts tested for ROP of the cyclic monomer have focused around the use of $Sn(Oct)_2$ or DBU, with exogenous alcohol as the co-initiator, providing a robust and cheap approach. However the additional alcohol is thought to be a major contributing factor in the transesterification process.[25–30] Subsequent generations of catalysts have since reduced this effect by using a DBU/TU co-catalyst system.[31–34] However, toxic residues of thiourea based systems could limit further development within bio-medical fields.[35]

5.1.2. Phosphoester-lactide copolymers

Alongside other noteworthy copolymer studies,[28,30–36] Wang and co-workers, described how a poly(*L*-lactic acid)-*b*-poly(ethyl ethylene phosphate) block copolymer showed promising results in the field of tissue engineering, applied for the proliferation of osteoblasts (Scheme 5.2).[37] The amphiphilicity of these copolymers has recently been extended by Wooley and co-workers, reported that upon functionalisation of the phosphoester block, fully degradable block co-polymers were produced.[33] Due to the hydrophobic/hydrophilic character of the individual blocks the copolymers were tested as nucleic acid carriers. In order to generate block copolymers, the sequential addition of monomers or macro-initiation from a polymeric end group is common. This method facilitates the facile production of copolymers which can express a variety of properties under different conditions. Due a to lack of catalyst development in this area of polymer synthesis, chemo-specific propagation from a monomer mixture has not yet been realised. Achieving this selectivity provides many synthetic advantages, including the ability to manipulate the polymer nature without concerning the addition of external reactants during polymerisation.

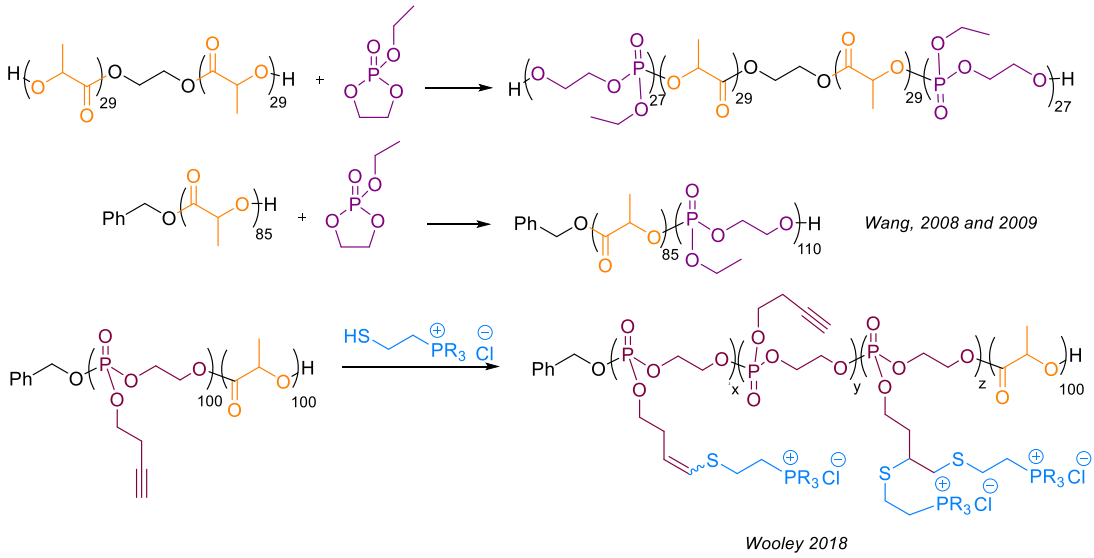

Scheme 5.2. Block copolymers of PLLA and polyphosphoesters reported by Wang and co-workers,[34,37] and Wooley and co-workers.[33]

5.1.3. Poly(phostones)

The high rate of hydrolytic degradation shown for synthetic poly(phosphoesters) often means they are difficult to manipulate and as such are not commercially viable for packaging or storage applications.[38] As hydrolytic degradation is known to occur across the P–O phosphoacyl bond, research efforts have focused on switching this functionality for the more stable P–C bond. To this effect, poly(phostones) have recently been explored as a PPE analogue with the aim of reducing degradation rates.[38,39] Initially produced via diene-metathesis polymerisation, high molecular weight polymer has been shown to be achieved with a variety of alkyl chain lengths. Whilst subsequent hydrogenation is required to yield the comparable alkyl chain polymer, post-polymerisation modification on the polymer alkene functionality could be used to tune the properties (Scheme 5.3).

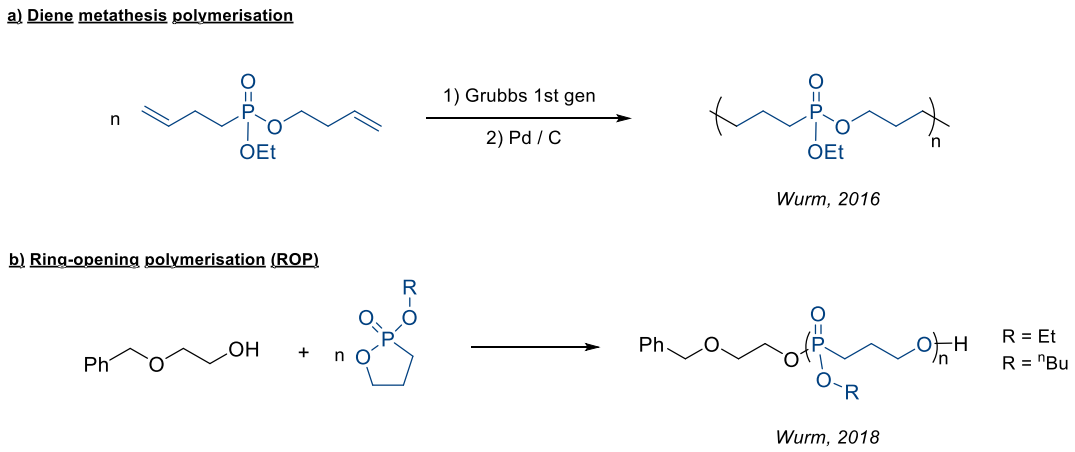

Scheme 5.3. Routes to the production of in-chain P–C polymers poly(phostones).[38,39]

Later work highlighted the possibility to prepare the cyclic phostone monomers, avoiding the multiple steps required in the production of the acyclic diene monomer.[38] ROP of the cyclic phostone was slower than analogous cyclic phosphate, explained due a reduction in ring strain (2.14 *vs* 3.69 kcal mol^{-1} respectively). The choice of the ROP initiator was explored with triazabicyclodecene (TBD) affording the highest conversion of 87% in 270 minutes {$[M]_0$:$[I]_0$:$[BnOH]_0$ = 100:20:1, $[M]_0$ = 2 M, toluene, 0 °C}. Despite the perceived stability of the P-C bond, dispersities were high (*Đ* = 1.56) likely due to transesterification facilitated by the strong Lewis basic initiator used. Degradation studies monitored via ^{1}H NMR analysis showed a reduction in polymer resonances by 40% after 12 days when dispersed in a highly basic solution (pH 12). In comparison, under these conditions, the poly(phosphate) analogue achieved complete degradation in 2 days. Under highly acidic and neutral conditions degradation was extremely low with only <4% conversion after 40 days. Whilst none of the

tested conditions represent realistic environments, the influence of the bonding around the phosphorous is shown to be extremely important on the degradation kinetics.

5.1.4. Poly(phosphonates)

In recent years, Wurm and co-workers have developed poly(phosphonates) (PPn), a poly(phosphoester) motif bearing a terminal alkyl moiety as a way of inherently lowering transesterification in polyphosphates, as well as allowing facile functionalisation of the side arm for specific applications (Figure 5.3).[40–43] Utilising DBU as the catalyst, reasonable degrees of polymerisation were achieved with minimal discrepancy between theoretical and observed molecular weight values.[41] It is noted that intramolecular transesterification at high molecular weights is believed to cause an increase in *Đ*, rationalised due to the high basicity of DBU. High water-solubility was seen for all polymer systems except the cyclohexyl polymer. Linear alkyl side-arms were shown to yield polymers with a range of T_g between -35 and -50 °C, with a general decrease in T_g upon increasing chain length of the terminal alkyl group (Table 5.1). Cyclohexyl substituted analogue (CyPPn) exhibited a relatively high T_g (16 °C) compared to other reported poly(phostones) and poly(phosphonates).

Table 5.1. Glass transition and degradation data for linear poly(phosphonates) reported by Wurm and co-workers.[40,41,43]

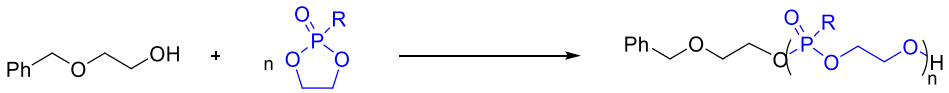

R =	T_g (°C)	Degradation Time (days) (pH 9, 37.5 °C)	Drop in M_n (%)
$-CH_3$ (MePPn)	-35	2	100
$-C_2H_5$ (EtPPn)	-46	14	60
$-CH_2(CH_3)CH_3$ (^{i}PrPPn)	-41	21	48
$-C_4H_{11}$ (^{n}BuPPn)	-50	28	0
$-C_6H_{11}$ (CyPPn)	16	28	0

Hydrolytic degradation of these polymers is shown to occur via second order kinetics with nucleophilic attack of hydroxide ions on the phosphorous centre, with the steric bulk around the phosphorous shown to be highly important. Poly(ethylene methyl phosphonate)(pMePPn) lost monomodality in the SEC trace within 4 hours, with complete degradation in 2 days (pH 9, 37.5 °C) whereas poly(ethylene ethyl phosphonate)(pEtPPn) was

significantly more resistant, with 60% M_n loss seen after 2 weeks under analogous conditions.[41] Further increases to the chain length resulted in very low degradation rates, observed over 4 weeks. Showing low cytotoxicity, poly(phosphonate) architectures have been targeted for encapsulation and drug delivery.[44]

Expanding their accessible properties, Wurm and co-workers recently showed copolymers of phosphonates with hydrophilic and hydrophobic characteristics (Figure 5.3). Controlling the feeds and substituents, copolymers exhibiting both lower critical solution temperatures (LCST) and upper critical solution temperatures (UCST) were produced. This enabled the self-assembly into degradable polymersomes, an important step in designing drug delivery devices.[42,45]

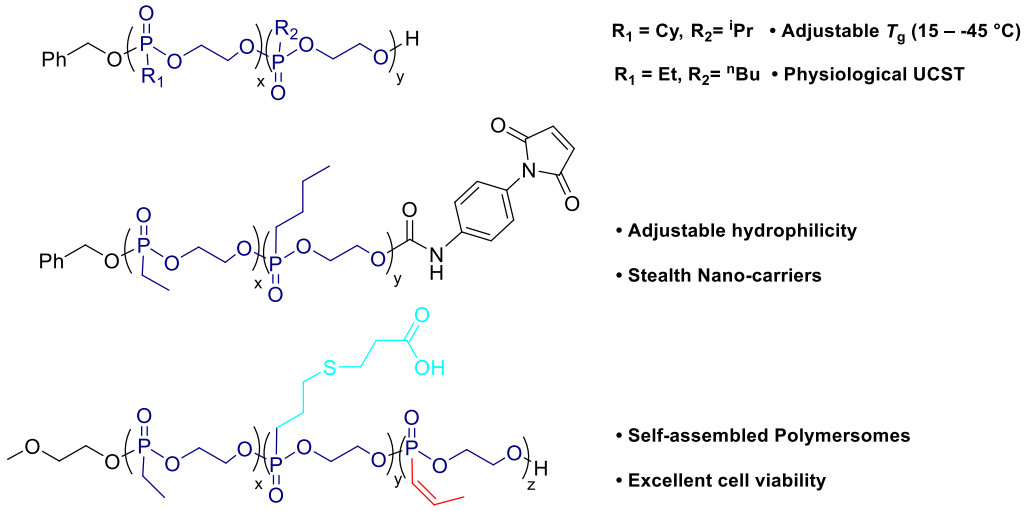

Figure 5.3. Phosphonate copolymers reported by Wurm and co-workers.[42,44–46]

Due to their promising properties, poly(phosphonates) have begun to see increasing attention aimed at the optimisation of the catalysis process, with significant contributions by Shaver and Nifant'ev, testing a range of different initiators for ROP (Figure 5.4).[47,48] Shaver and co-workers showed how pK_a and ring strain played an important role with organocatalytic initiators. Initiators with pK_a <14 showing no activity for the polymerisation of 2-methyl-1,3,2-dioxaphosphalone-2-oxide (MePPn).[47] The highest pKa base tested, triazabicyclodecene (TBD), yielded 91 % conversion in 4 hours at room temperature {$[M]_0$:$[I]_0$:$[Cat]_0$ = 100:1:5}. Narrow dispersities and molecular weights fitted closely to those theoretically calculated. Alongside this, an organometallic aluminium 'ONNO' salen initiator (**71**), tested under similar conditions yielded complete conversion within 6 hours whilst maintaining narrow dispersities ($Đ$ = 1.06).

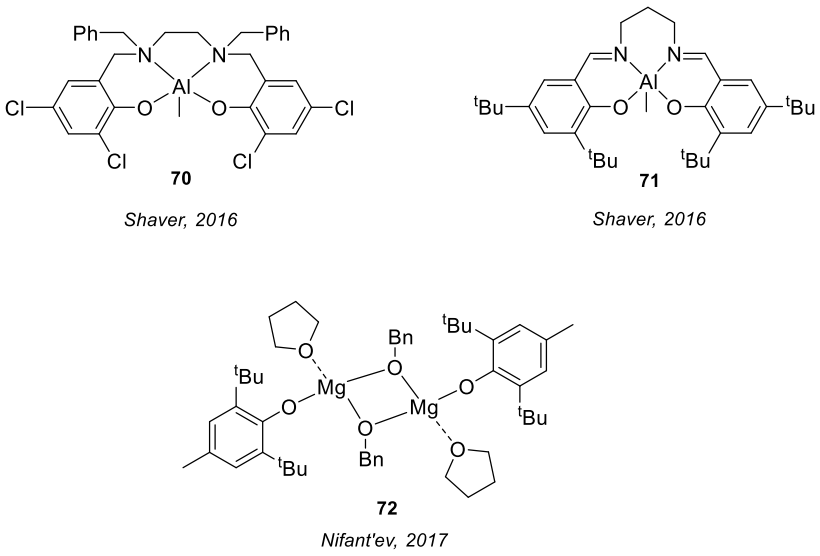

Figure 5.4. metal catalysts previously reported for the ROP of phosphonates.[47,48]

Nifant'ev and co-workers since presented a heteroleptic $[(BHT)Mg(OBn)(THF)]_2$ catalyst (**72**) which was tested for a range of phosphates, phosphonates and phosphoramidates.[48] When tested with EtPPn, (**72**) high molecular weight polymer was produced within 1 hour at -20 °C without the need for exogeneous alcohol, albeit with a moderately high dispersity ($Đ$ = 1.46) and under concentrated conditions {$[EtPPn]_0$:[**72**]$_0$ = 100:1, $[EtPPn]_0$ = 2 M in THF}. The prevalence of transesterification has since limited the adoption of these initiators in comparison to the well-established organocatalysts currently used.

Herein this chapter reports the further optimisation of ROP catalysis of cyclic phosphonates, with a focus on EtPPn. Through exploring the importance of the catalytic system used, the case of how further contributions in catalysis can play a key role in the of emergence new polymers is presented. Following in the analogous work by Wooley and co-workers surrounding lactide-phosphoester copolymers,[31,33] the production of the first lactide-phosphonate copolymers is investigated. In addition, the development of analytical methods for monitoring monomer reactivity, copolymer composition, and polymer microstructure are investigated. This study also shows how catalyst choice, temperature sequencing and staggered additions can be exploited to develop a range of well-defined copolymers. Physical analysis shows how these microstructures have a pronounced impact on the thermal and chemical properties of the macromolecule.

5.2. Results and discussion

5.2.1. Homopolymerisation of EtPPn

Initial work into the homopolymerisation of EtPPn was carried out by testing initiators developed during this project, which performed exceptionally for the polymerisation of *rac*-LA. With the aim to be able to produce well-defined copolymers of LA and EtPPn, the initiator is required to show excellent control for the homopolymer units as copolymerisations often leads to a broadening in molecular weights from intramolecular cyclisation and transesterification.

{Nd(**2**)O^{i}Pr}$_2$ had been found to combine very high activity and excellent control for the ROP of *rac*-LA under mild conditions (CH_2Cl_2, 25 °C). This activity provides a potential opportunity for co-polymerisation under ambient conditions, mimicking those previously tested for EtPPn. Conversely, Al(**15**)Me$_2$ provides a synthetically more accessible initiator which was shown to deliver good control and an iso-selective bias for the polymerisation of *rac*-LA, albeit under more moderate conditions (toluene, 80 °C). For this study EtPPn was received from the Max-Planck Institute for Polymer Research synthesised by Dr Thomas Wolf, following published synthetic procedures and was twice freeze dried under vacuum prior to usage.[41]

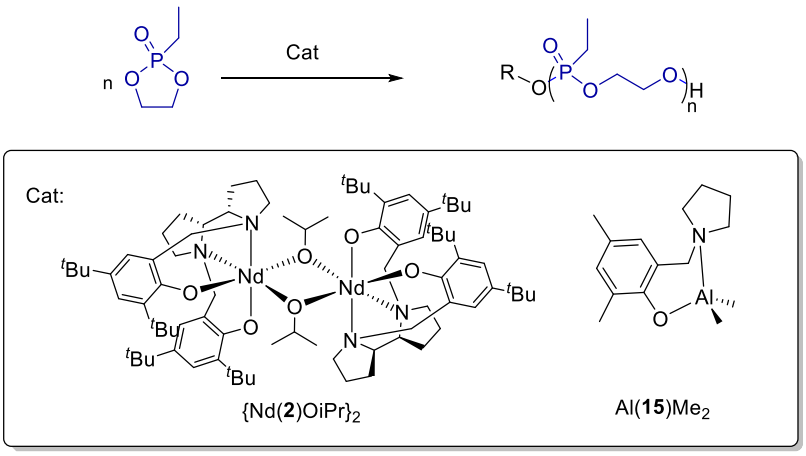

Scheme 5.4. Scheme for the ROP of EtPPn initiated by {Nd(**2**)O^{i}Pr}$_2$ and Al(**15**)Me$_2$.

Under solvent free conditions, addition of a catalytic quantity of Al(**15**)Me$_2$ to a stirred mixture of EtPPn and BnOH yielded 90% conversion within 5 minutes at 20 °C {[EtPPn]$_0$:[BnOH]$_0$:[Al(**15**)Me$_2$]$_0$ = 50:1:1} (Figure 5.5). Following literature assignments, conversion was measured from the proton-coupled ^{31}P NMR spectra by integration of polymer resonances (34.5 – 36.0 ppm) over corresponding monomer resonances (52.5 – 53.5 ppm).[41] Quantification of ^{31}P NMR spectra was improved by running samples over 64 scans

with a large pulse delay to ensure complete magnetic relaxation. The values obtained with ^{31}P NMR spectroscopy compared within a ~2% range of conversions with those calculated through ^{1}H NMR spectra. Due to the insolubility of poly(EtPPn) aka (pEtPPn) in THF, SEC analysis was performed in DMF at 60 °C providing direct comparison with previously reported results by Wurm and coworkers.[41] The high activity in bulk using Al(**15**)Me$_2$ as the initiator is complemented with a low dispersity and molecular weights close to the theoretical values (Entry 1, Table 5.2). ^{31}P NMR spectroscopy shows only one signal in the previously reported polymeric range of (34.0 – 37.0 ppm) indicating no protic impurities or oligomerisations. ^{1}H DOSY experimentation identified aromatic signals of BnO– end groups diffusing at the same rate as polymer species, suggesting a linear chain growth with *in-situ* alkoxide formation prior to chain initiation.

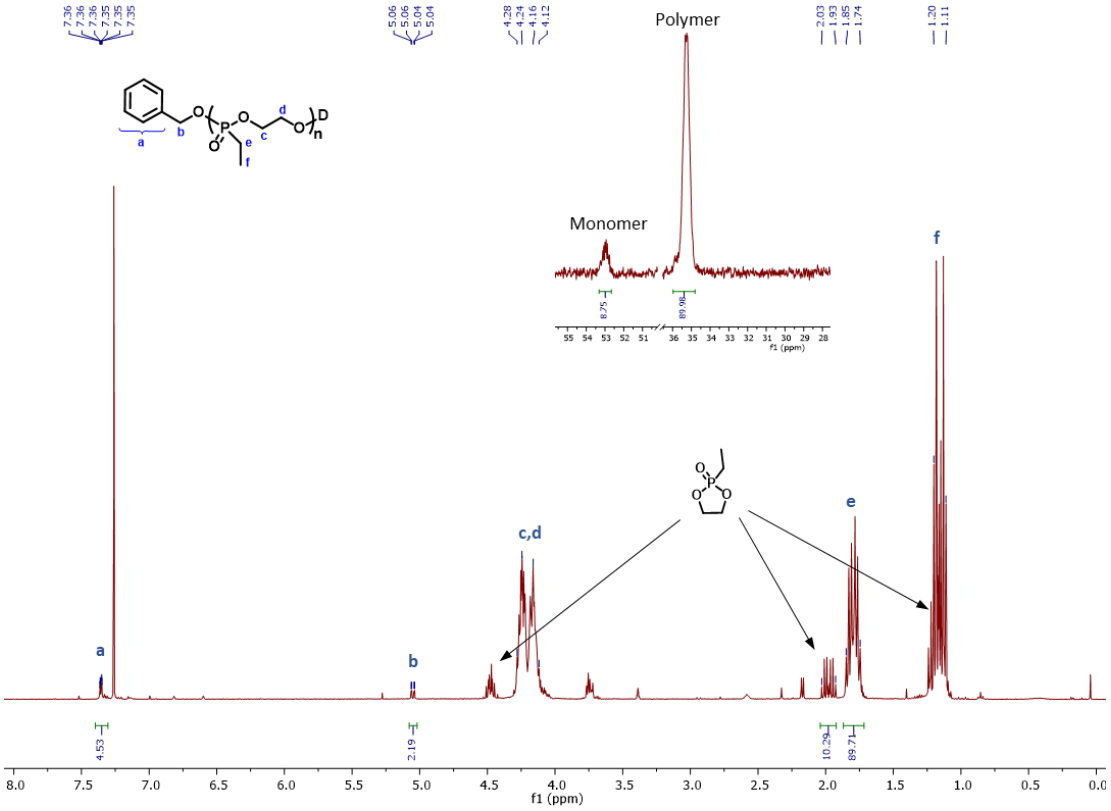

Figure 5.5. Crude ^{1}H and ^{31}P NMR spectra of pEtPPn synthesised using Al(**15**)Me$_2$ {[EtPPn]$_0$:[I]$_0$:[BnOH]$_0$ 50:1:1, 20 °C, 5 minutes, 90% conv.} (Entry 1, Table 5.2).

Table 5.2. Polymerisation data for the ROP of EtPPn at ratios of 50:1:1 {$[EtPPn]_0$:$[I]_0$:$[BnOH]_0$}.

Entry	Catalyst	Temp °C	Solvent	Time (hours)	Conc M	Conv %[b]	M_n^{theo} (kg mol^{-1})[c]	M_n^{SEC} (kg mol^{-1}) {Đ}[d]
1	Al(**15**)Me_2	20	N/A	0.08	Bulk	90	6.2	4.3{1.11}
2	Al(**15**)Me_2	20	CH_2Cl_2	3	0.35	96	6.6	5.3{1.14}
3	Al(**15**)Me_2	20	Tol	3	0.35	83	5.7	5.6{1.10}
4	Al(**15**)Me_2	20	Tol	120	0.35	94	6.5	3.3{1.42}
5	Al(**15**)Me_2	20	Tol	24	0.7	99	6.8	4.8{1.38}
6	Al(**15**)Me_2	80	Tol	2	0.35	49	3.4	2.8{1.26}
7	Al(**15**)Me_2	80	Tol	4	0.35	55	3.8	3.1{1.20}
8	Al(**15**)Me_2	80	Tol	16	0.35	81	5.4	7.6{1.17}
9	Al(**15**)Me_2	80	Tol	4	0.7	90	6.2	5.3{1.21}
10[a]	{Sm(**1**)O^{i}Pr}$_2$	20	CH_2Cl_2	1	0.35	9	1.3	3.2{1.21}
11[a]	{Sm(**1**)O^{i}Pr}$_2$	80	Tol	1	0.35	95	13.0	9.6{1.32}
12[a]	{Nd(**2**)O^{i}Pr}$_2$	20	CH_2Cl_2	1	0.35	100	13.7	10.5{1.21}
13	DBU[36]	25	CH_2Cl_2	16	4	90	6.3	5.4{1.07}
14[a]	**72**[30]	-20	THF	1	2	89	12.2	14.2{1.46}

Reactions were quenched with addition of excess formic acid. [a] Feed ratios of 100:1 {$[EtPPn]_0$:$[I]_0$} with the assumption both alkoxides act as initiating groups. [b] Calculated by integration of polymer resonances in the ^{31}P NMR spectra (34.5 – 36.0 ppm) over corresponding monomer resonances (52.5 – 53.5 ppm). Calculated from the crude ^{31}P NMR spectra {($[EtPPn]_0/[I]_0$ × Conv. × 136.03) + Mw of end group}. [d] SEC carried out in DMF at 60 °C, using RI methods with a PEG standard.

Solution polymerisations with Al(**15**)Me_2 were carried out under comparatively dilute conditions compared to literature reports due to the desire to align conditions with those already proven effective for ROP of LA.[41,48–50] In CH_2Cl_2, at monomer concentrations of 0.35 mol L^{-1}, high conversion is achieved within 3 hours. Under comparable time frames, experiments run at 80 °C showed lower conversions than at 25 °C and increasing initial monomer concentration from 0.35 to 0.7 mol L^{-1}, increased conversion (Table 5.2, Entry 3-9). This result supports that conversion is governed by the monomer thermodynamics and not by catalyst deactivation with a potential monomer equilibrium in effect. Transesterification is shown to occur at low monomer concentrations with an increase in dispersity seen upon increasing reaction times (Table 5, Entry 3-5).

{Sm(**1**)O^{i}Pr}$_2$ and {Nd(**2**)O^{i}Pr}$_2$ were tested at initial monomer ratios of 100:1 {[EtPPn]$_0$:[I]$_0$}. In this scenario the terminal and bridging alkoxides coordinated to the metal are assumed to both be able to initiate giving two initiators per complex. Whilst spectral evidence suggests only one initiating group is active for the polymerisation of LA at 25 °C when {Sm(**1**)O^{i}Pr}$_2$ is the initiator (Chapter 3.3), it is presumed EtPPn might activate the complex differently. A higher feed ratio is required when using these systems due to the high molecular weight of Ln complexes, resulting in a mass intensive catalyst feed. As shown in chapter 4, for the ROP of *rac*-LA, {Sm(**1**)O^{i}Pr}$_2$ was inactive under mild conditions (Table 5.2, Entry 10). Similarly, it is probable that only one alkoxide initiates as evidenced by a large discrepancy in experimental molecular weights from those estimated from NMR spectroscopy. At elevated temperatures, this behaviour is lost with high conversions seen after 60 minutes (Entry 11, Table 5.2). Under the mild conditions which {Sm(**1**)O^{i}Pr}$_2$ was inactive, {Nd(**2**)O^{i}Pr}$_2$ achieved quantitative conversion (Table 5.2, Entry 12), following the reactivity relationship drawn for the ROP of *rac*-LA. In comparison to the bimetallic Mg complex (**72**), previously reported by Nifant'ev and co-workers, shows a similar reactivity under more dilute conditions albeit with different solvent and temperatures used (Entry 12 and 14, Table 5.2).[48]

Screening of synthesised complexes for the ROP of EtPPn has yielded results comparable to that seen for LA polymerisation. The high activity associated for Ln^{3+} complexes makes them the fastest tested initiators for the ROP of EtPPn under the trialled conditions. However, the high costs associated with ligand and catalyst preparation limits these systems for future utilisation in copolymerisation with LA. Conversely, Al(**15**)Me$_2$ showed excellent activity under a range of conditions with good control of molecular weights. This control is imperative in generating well defined copolymers and as a result, Al(**15**)Me$_2$ was chosen as the primary initiator for further investigation.

5.2.2. Copolymerisation of EtPPn and LA

The production of block copolymers from 'click' chemistry is long famed to hold huge importance in the development of designer polymers with ability to control architecture and physical properties. Work carried out by Yang *et al.,* on phosphoester-*b*-lactide copolymers, show how this material exhibits biphasic properties in polar solvents, with the hydrophobic LA phase maintaining immiscibility in water.[37] A few methods of block copolymer formation are known, including the sequential addition of reagents to a one pot system, macro-initiation starting from an active polymeric chain or selective enchainment of monomers from a mixed monomer solution. Whilst more challenging from a catalysis perspective, selective enchainment offers notable benefits from being synthetically more facile to access copolymers in closed systems. Initial studies for the copolymerisation of LA and phosphonates was carried out sequentially with the aim of generating block copolymers, testing the possibility of co-enchainment.

5.2.3. Sequential addition of monomers

A stirred solution of PLLA was prepared from the ROP of *L*-LA with Al(**15**)Me_2 and BnOH at feed ratios of 50:1:1 {$[L\text{-LA}]_0$:$[BnOH]_0$:$[Al(\mathbf{15})Me_2]_0$, [*L*-LA] = 0.35 $molL^{-1}$} in toluene at 80 °C. Near complete conversion (96%) was confirmed after 24 hours. To this solution, 50 equivalents of EtPPn in toluene {[EtPPn] = 0.35 mol L^{-1}} were added and the solution was left to stir at 80 °C for a further hour. Quenching the reaction with a few drops of MeOH and removal of the solvent yielded a white gel. ^{31}P NMR spectroscopy showed a main signal in the range of the homopolymer with 2 smaller signals either side. Copolymers of EtPPn (P) and LA (L) can be expressed as three possible (P) centred triads which could be active in the ^{31}P NMR, these are P-P-P, P-P-L, and L-P-L (Figure 5.6). With a pure block expected to have only P-P-P and one-unit of P-P-L, signals corresponding to L-P-L can be indicative of the degree of randomness in the final copolymer. With three signals seen in this region it is expected a tapering of blocks is observed. This is possibly due to intermolecular transesterification seen at low monomer conversions and high temperatures.

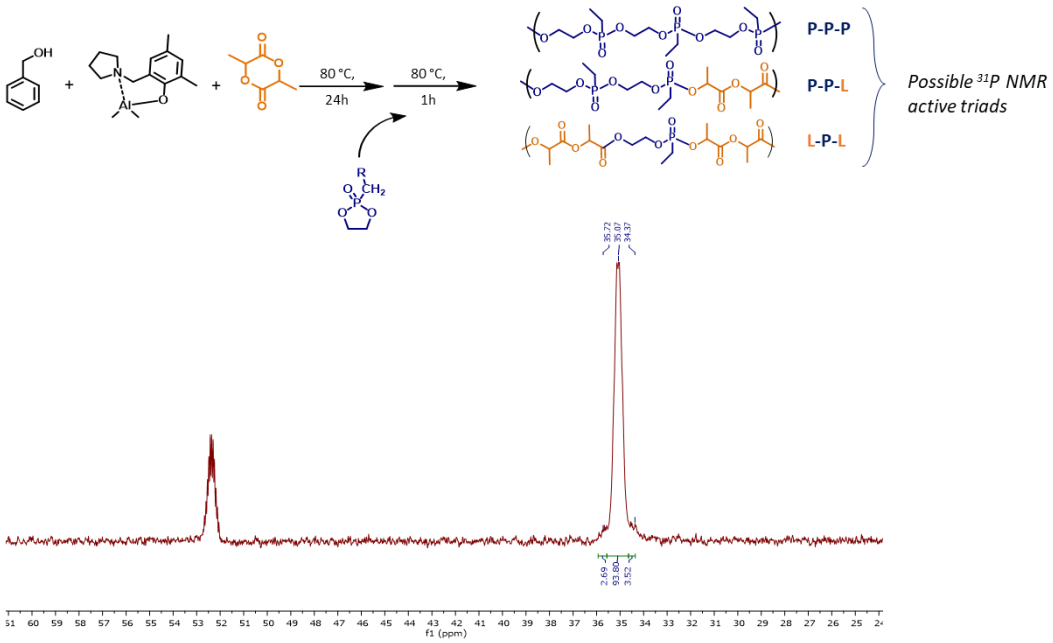

Figure 5.6. ^{31}P NMR of the copolymer of L-LA and EtPPn formed from sequential addition, showing assignments to ^{31}P NMR triads.

As reducing the temperature greatly reduces the activity of the active species towards propagation of LA, the temperature of the polymer solution was reduced to (25 °C) prior to sequential addition of EtPPn. This yielded a polymer with only 2 signals in the ^{31}P NMR spectra, 34.8 – 35.5 ppm (98%) and 35.5 ppm (2%), which arise from PPP and PPL linkages respectively. This percentage corresponds to clean block formation at the feed ratios of 50:50:1:1 {$[LA]_0$:$[EtPPn]_0$:$[I]_0$:$[BnOH]_0$}. Copolymerisation enchainment was confirmed through ^{1}H and ^{31}P DOSY which shows only one diffusing polymer species (Figure 5.7). In agreement with homopolymerisation data, BnO– signals are seen to diffuse at the same rate indicating the copolymer is linear with end groups of BnO– and –H. SEC analysis in DMF yielded a monomodal chromatogram (M_n^{SEC} = 11.2 kg mol^{-1}, $Đ$ = 1.15). Differential scanning calorimetry (DSC) confirmed a biphasic copolymer with two distinct T_g of in the range of the individual homopolymers (-48.0 °C and 63.9 °C). In the trace a small endothermic peak can be seen on heating (95 – 110 °C) indicative of the semi-crystalline nature of the PLLA block. When the initial polymerisation step was carried out with EtPPn as monomer, the final copolymer yielded a greater proportion of L-P-L (34.0 – 34.8 ppm) and P-P-L (35.5 – 36.0 ppm) resonances in the polymer region of the ^{31}P NMR spectra.

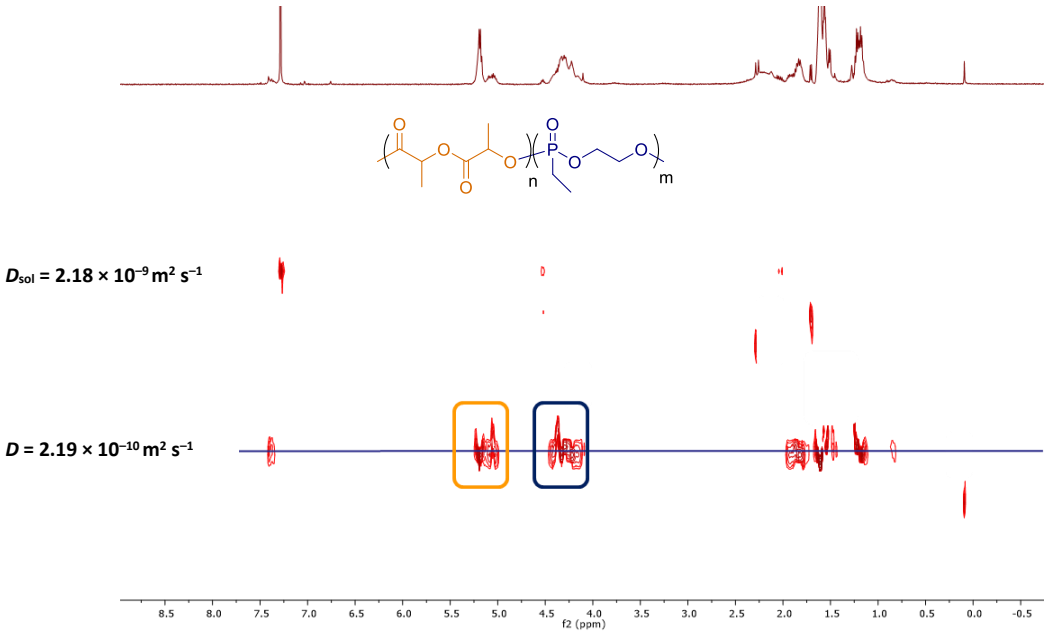

Figure 5.7. ^{1}H DOSY (400 MHz, 298 K) spectra of block copolymer {*L*-lactide-*b*-EtPPn} in $CDCl_3$.

5.2.4. Copolymerisations from monomer mixtures

Arguably a more rigorous test of catalyst efficacy is to display selective control of monomers from a mixed solution. Variances in the ring strain, bond enthalpies, steric hindrance, and Lewis basicity between the monomers provides potential for selective enchainment from the catalysis process. From a mixed monomer solution of EtPPn, *L*-LA and BnOH in toluene at a feed ratio of 50:50:1 {$[LA]_0$:$[EtPPn]_0$:$[BnOH]_0$, [LA] = 0.35 M}, 1 equivalent of Al(**15**)Me_2 was added and the solution was heated to 80 °C for 16 hours. Conversions of 75% and 100% of *L*-LA and EtPPn respectively were obtained, giving an incorporation of 58% phosphonate into the final polymer (Entry 1, Table 5.3). SEC analysis shows a monomodal chromatogram with high molecular weights and a low dispersity (M_n^{SEC} = 21.0 kg mol^{-1}, $Đ$ = 1.12). ^{31}P NMR spectroscopy showed three distinct signals in the polymer region with a triad ratios of 62:21:17 (PPP:PPL:LPL). The high ratio of PPP to PPL and LPL suggests a tapering of repeating units. Whilst largely tapered, the randomness of the polymer is expressed thermally with only one T_g being present in the DSC chromatogram at (18.7 °C). A T_g between the two transitions of the homopolymers is expected for random systems with T_g estimated to be proportional to the mole fraction (ω) of the co-monomer units inside the copolymer, as dictated by the Fox Equation (Equation 5.1).

Equation 5.1. Fox equation for the prediction of glass transition temperature in statistical copolymers.

$$\frac{1}{T_g} = \frac{\omega_1}{T_{g,1}} + \frac{\omega_2}{T_{g,2}}$$

This effect is highlighted by altering the feed ratio of *L*-LA:EtPPn to 100:50 with respect to initiator resulting in a polymer of 40% poly(phosphonate) and a higher T_g = 23.3 °C (Entry 2, Table 5.3). Conversely conversions remained the same in this experiment and showed a closer fit of molecular weights calculated from SEC to those calculated theoretically from conversions (M_n^{SEC} = 20.6 kg mol^{-1}, M_n^{theo} = 21.0 kg mol^{-1}) whilst maintaining a narrow distribution ($Đ$ = 1.06). Varying the enantiomeric feed of LA from semi-crystalline *L*-LA to the racemic mixture yielded the expectedly lower T_g, with no observable hindrance on conversion. Whilst Al(**15**)Me$_2$ showed an *iso*-selective bias for the homopolymerisation of *rac*-LA, this is not of high enough proportion to observe thermal transitions similar to PLLA. Good agreement between the feed percentage and percentage incorporation in the polymer was seen, giving the ability to produce copolymers with a range of mole fractions of poly(lactic acid) and poly(phosphonate).

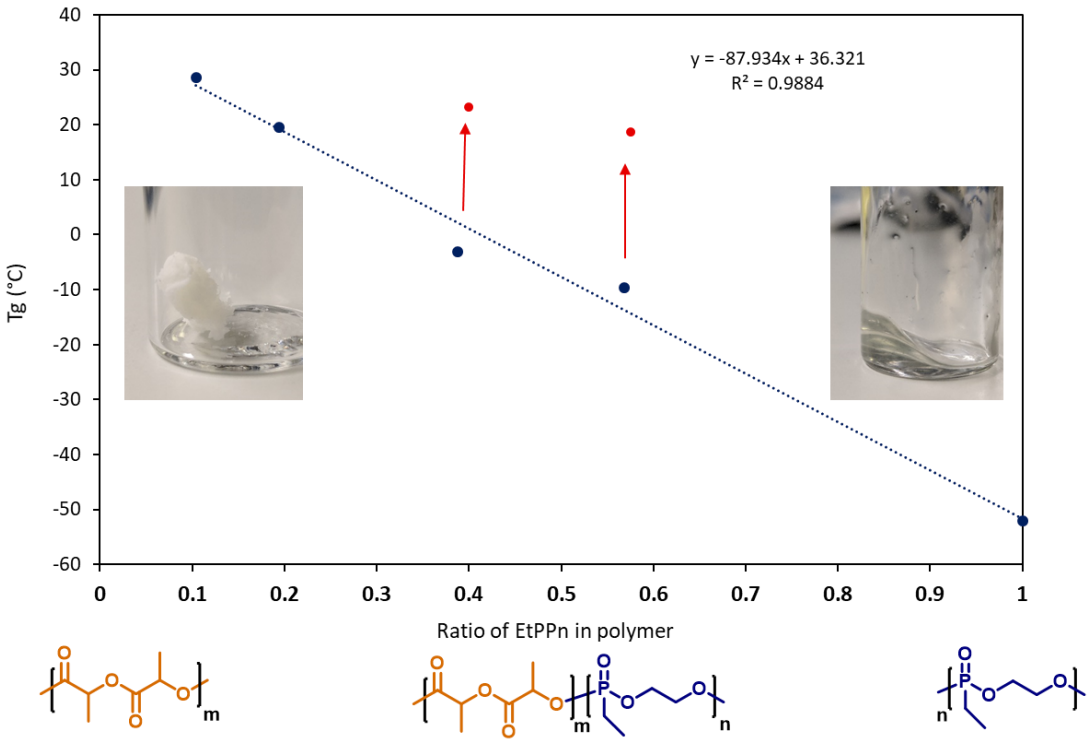

Figure 5.8. Plot of T_g versus ratio of EtPPn incorporated into the polymer. ● *rac*-LA, ● *L*-LA.

Plotting the observed T_g versus the ratio of EtPPn in the polymer gives a linear fit with a range of ~88 °C (Figure 5.8). The effect of the having a thermal transition in the range of ambient conditions can be seen physically with the physical behaviour of the polymer changing through working temperatures, varying from a white elastic solid to a viscous gel, an effect common for thermoplastic elastomers. Whilst the degree of randomness can be expected to influence the T_g of copolymers, no significant difference is seen in the triad ratio to draw comparison. A tapering of chains is at feed ratios as low as 100:20:1:1 {$[LA]_0$:$[EtPPn]_0$:$[BnOH]_0$[Al(**15**)$Me_2]_0$}, with feeds of 100:10:1:1 resulting in a highly random distribution of phosphonate units (15:44:41, PPP:PPL:LPL). As $[LA]_0 > [EtPPn]_0$ it is likely insertion is dependent on monomer concentration rather than catalyst selectivity.

Table 5.3. Polymerisation data for copolymerization of LA and EtPPn from monomer mixtures.

Entry	Init	Feed ratio $[LA]_0$:$[EtPPn]_0$:$[I]_0$:$[BnOH]_0$	Conv. LA (%)	Conv. EtPPn (%)	EtPPn (%)	M_n^{SEC} {$Đ$} (kg mol^{-1})	M_n^{NMR} (kg mol^{-1})	M_n^{theo} (kg mol^{-1})	T_g (°C)	Triad ratio PPL:PPP:LPL
1	Al(**15**)Me_2	50:50:1:1	75	100	57	15.6{1.06}	13.3	12.3	-9.7	22:55:27
2	Al(**15**)Me_2	100:50:1:1	77	98	39	12.5{1.02}	8.6	18.0	-3.1	28:59:13
3	Al(**15**)Me_2	100:20.1:1	83	100	19	16.3{1.27}	16.6	14.8	19.6	28:45:27
4	Al(**15**)Me_2	100:10.1:1	95	100	11	12.9{1.23}	11.7	15.2	27.4	44:15:41
5[a]	Al(**15**)Me_2	50:50.1:1	73	100	58	21.0{1.12}	9.5	12.2	18.7	21:62:17
6[a]	Al(**15**)Me_2	100:50:1:1	75	100	40	20.6{1.06}	20.1	17.6	23.3	29:38:33
7[b]	Al(**15**)Me_2	50:50:1:1	30	96	76	2.1{1.31}*	7.7	8.8	35.8	8:87:5
8[a]	DBU	50:50:1:1	85	67	45	4.3{1.10}	8.6	10.5	2.9	30:45:25
9[c]	DBU	50:50:1:1	80	80	35	4.8{1.18}	8.6	9.4	7.9	32:35:34
10[c,d]	DBU	50:50:1:1	91	18	17	3.2{1.10}	7.2	7.9	18.1	40:14:46

Toluene at 80 °C for 16h, $[rac\text{-}LA]_0 = [EtPPn]_0 = 0.7$ mol L^{-1}. [a] *L*-LA. [b] *L*-LA, T = 25 °C, time = 120 h, $[EtPPn]_0 = [LA]_0 = 0.35$ mol L^{-1}. [c] *L*-LA, $[M]_0 = 0.35$ mol L^{-1}. [d] CH_2Cl_2, T = 25 °C. M_n^{SEC} data was obtained from SEC analysis in THF using Triple detection methods. *SEC analysis carried out in DMF using RI detection methods with a poly(ethylene glycol) standard.

When DBU was tested as an initiator, a slightly lower activity is seen under the same conditions with both monomers not being fully converted (Entry 8, Table 5.3). The presence of multiple quartets in the methine region of the polymer ^{1}H NMR spectrum highlights the presence of epimerisation of *L*-LA, a common side reaction when utilising strong Lewis base organocatalysts.[51] Quenching of the solution with methanol or ethanoic acid afforded an additional resonance at 37.0 – 38.0 ppm which was not seen with Al(**15**)Me$_2$. ^{31}P^{1}H COSY NMR analysis showed this signal to be the ring-opened product of EtPPn with quenching agent, with no evidence of propagation from this site. After purification, the product was physically not as viscous as those at similar conversion produced when Al(**15**)Me$_2$ was the initiator. The material was insoluble in THF and poorly soluble in DMF, making SEC analysis not possible. Diluting the monomer solution to 0.35 mol L^{-1} yielded similar physical properties with an even larger ratio of PPL units to PPP and LPL triads. Whilst in literature it is common to use acids to quench DBU polymerisation, it is likely the methanol acted as a nucleophilic source to ring-open any residual EtPPn, yielding insoluble oligomers.[41]

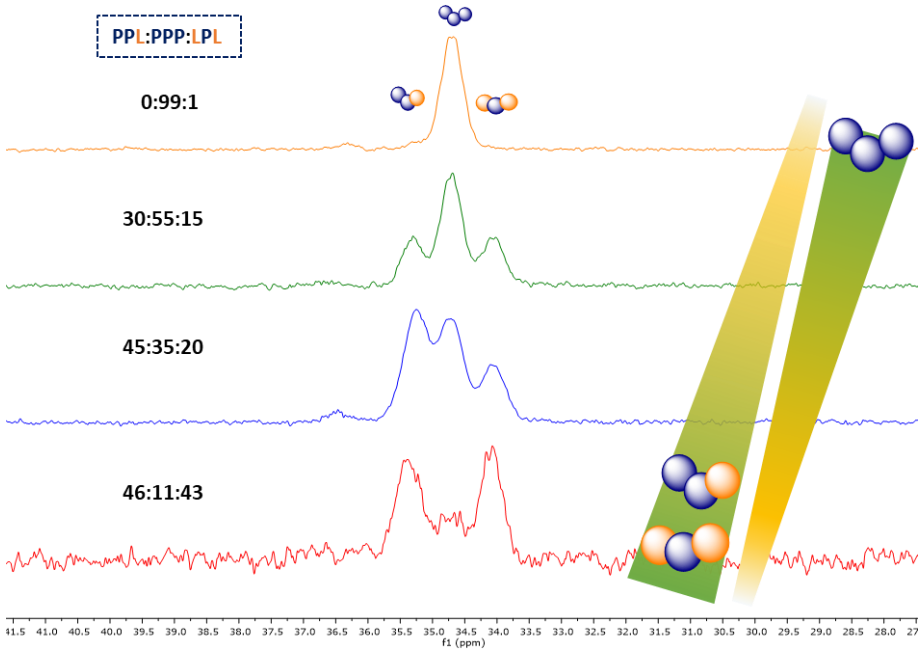

Figure 5.9. Stacked ^{31}P NMR spectra of copolymers with different triad ratios.

When DBU was used as the initiator, the ^{31}P NMR spectrum of the polymer showed triad proportions with a greater proportion of PPL to PPP triads. This lower degree of phosphonate block units compared to Al(**15**)Me$_2$, indicates a more random and tapered incorporation of phosphorous in the copolymer (Figure 5.9). To further investigate how variation in triad ratio is affected by the choice of initiator, polymerisation kinetics were carried out via *in-situ* NMR experimentation, monitoring both ^{1}H and ^{31}P nuclei.

5.2.5. Kinetics and *in-situ* monitoring of mixed monomer copolymerisations

In-situ kinetic analysis was performed in toluene-d_8 at 80 °C with monomer concentrations of 0.35 mol L^{-1} to reduce viscosity at high monomer conversions. The changing nature of the solution during polymerisation, long relaxation times of macromolecules, and high reaction temperatures resulted poor homogenisation of the magnetic field and broad resonances during data collection. Further to this, an overlap of signals in the methine region of PLA/LA and the C*H*$_2$ groups in the phosphonate is seen in tol-d_8. The side chain C*H*$_2$ of EtPPn and the methyl groups of LA were sufficiently resolved to integrate separately, forming the integral monomer/polymer pair for calculation of conversion. Due to the time delay between sample preparation to magnetic equilibration the initial minutes at elevated temperatures are not recorded limiting the ability to monitor initial rates. When Al(**15**)Me_2 was used as the initiator this was found to have a pronounced effect, with the first measurement times at 30 minutes of sample preparation showing 43% and 19% conversion of EtPPn and *L*-LA respectively (Figure 5.10).

Over the subsequent 300 minutes an increase in conversion of both monomers suggests a random incorporation during this sequence. A plateau in conversion of EtPPn is seen at 85% with propagation only apparent for LA after this time frame. It is likely that this plateau is due to the rise in viscosity of the solution and the aforementioned monomer equilibrium at low monomer concentration. LA conversion is apparent until the reaction was terminated after 16 hours, with final conversions of 85% EtPPn and 79% *L*-LA. ^{1}H DOSY analysis of the purified polymer in $CDCl_3$ confirmed a single species diffusing in solution. This suggests a 'living' growth of molecular weights where the profile of conversion is related to the macrostructure changing over time. A preferred enchainment of EtPPn is seen with conversion of LA dominant at low [EtPPn].

When DBU was tested under the same conditions a switch in selectivity is seen. A high rate of LA incorporation is observed reaching 90% within the first 300 minutes (Figure 5.11). A significantly slower rate of propagation for EtPPn is seen with DBU at low LA concentration leading to a final conversion of 24% EtPPn and 94% *L*-LA. Linearisation of the initial conversion data yields a straight line for all monomers with both DBU and Al(**15**)Me_2, suggesting the propagation is first order with respect to monomer (Figure 5.12). A comparatively low R^2 is seen for $\ln[EtPPn]_0/\ln[EtPPn]_t$ when DBU was used due to the inherent error of integrating at low conversion.

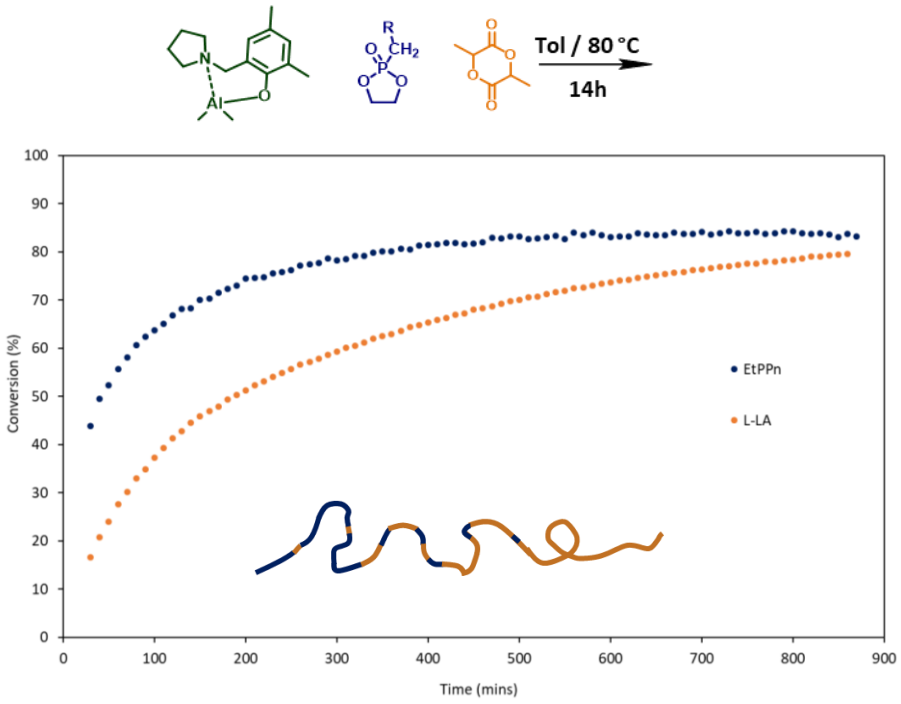

Figure 5.10. Conversion versus time graph for the copolymerisation of *L*-LA with EtPPn initiated with Al(**15**)Me_2, monitored via *in-situ* ^{1}H NMR spectroscopy. $[EtPPn]_0$:$[L\text{-}LA]_0$:$[I]_0$:$[BnOH]_0$ = 50:50:1:1, $[EtPPn]_0$ = 0.35 mol L^{-1}.

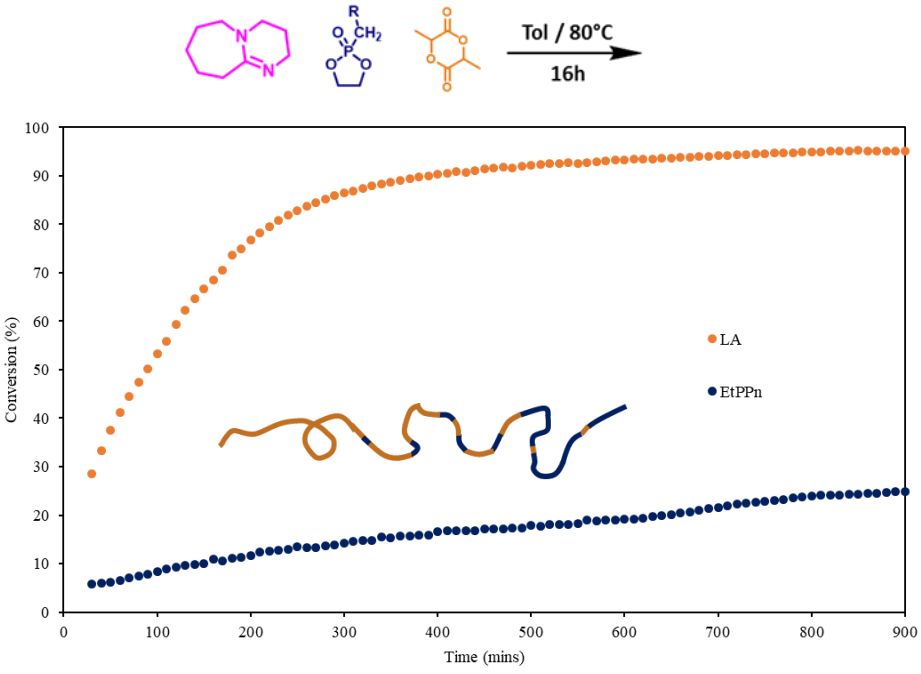

Figure 5.11. Conversion versus time graph for the copolymerisation of *L*-LA with EtPPn initiated with DBU, monitored via *in-situ* ^{1}H NMR spectroscopy. $[EtPPn]_0$:$[L\text{-}LA]_0$:$[I]_0$:$[BnOH]_0$ = 50:50:1:1, $[EtPPn]_0$ = 0.35 mol L^{-1}

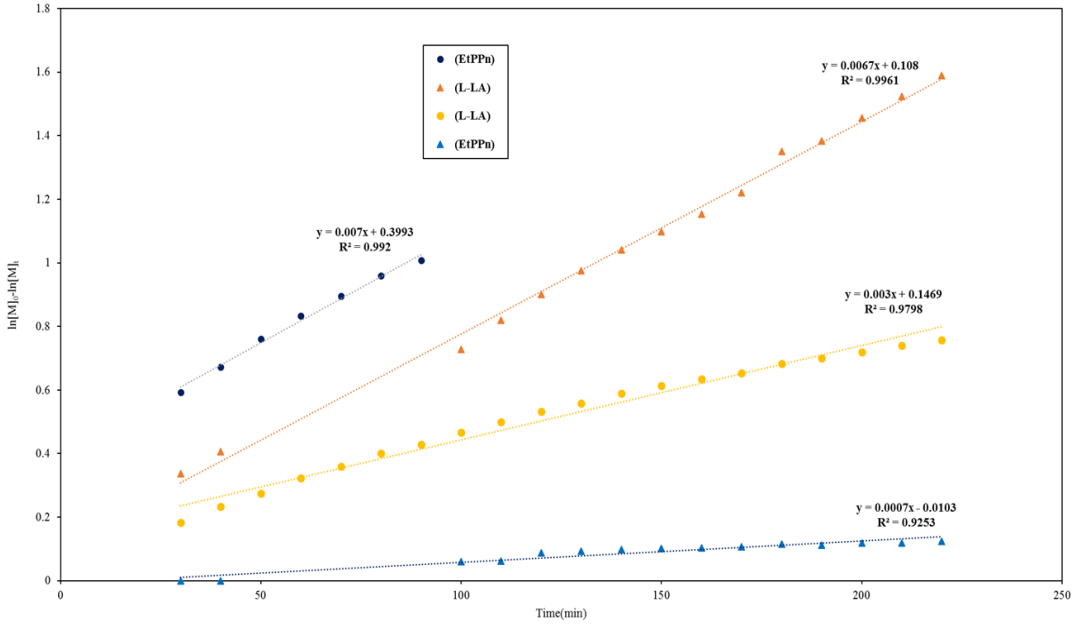

Figure 5.12 Linearised pseudo-first order plot of EtPPn and *L*-LA over time when Al(**15**)Me_2 (●) and DBU (▲) are used as initiators in the presence of BnOH as co-initiator. $[EtPPn]_0$:$[L\text{-}LA]_0$:$[I]_0$:$[BnOH]_0$ = 50:50:1:1, $[EtPPn]_0$ = 0.35 mol L^{-1}.

Due to the plateau in conversion, only a small number of plots can be fitted for EtPPn with Al(**15**)Me_2 as initiator. Despite this an observed rate constant (k_{obs}) equal to 7.0×10^{-3} min^{-1} is obtained, an order of magnitude faster than when DBU is used as the initiator. With a non-origin intersection through the y-axis it is likely the initial rate of EtPPn is greater than that recorded with conversion occurring directly after the addition of the catalyst in the ambient temperatures of the glovebox. Conversely, the propagation of *L*-LA shows a faster observed rate when DBU is used with a $k_{obs} = 6.7 \times 10^{-3}$ min^{-1}. The observed rate for LA when Al(**15**)Me_2 is used is similar to those recorded for the homopolymerisation of *L*-LA suggesting there is no kinetic difference in propagating a lactide molecule into a EtPPn or LA chain-end.[50]

During kinetic experimentation, parallel acquisition of ^{31}P NMR spectra was undertaken to identify how the peak structure and hence triad ratios changed over time (Figure 5.13). In agreement with batch analysis, after 16 hours, *in-situ* polymerisations with Al(**15**)Me_2 analysed by ^{31}P NMR spectroscopy show a tapering effect with triad ratios of 21:66:13 (PPL:PPP:LPL) agreeing with the profile of conversions seen from plotted ^{1}H NMR conversion data. Overlaying the triad ratio onto a conversion *vs* time graph this can be emphasised, quantifying the change, as a result of conversion (Figure 5.14 and Figure 5.15).

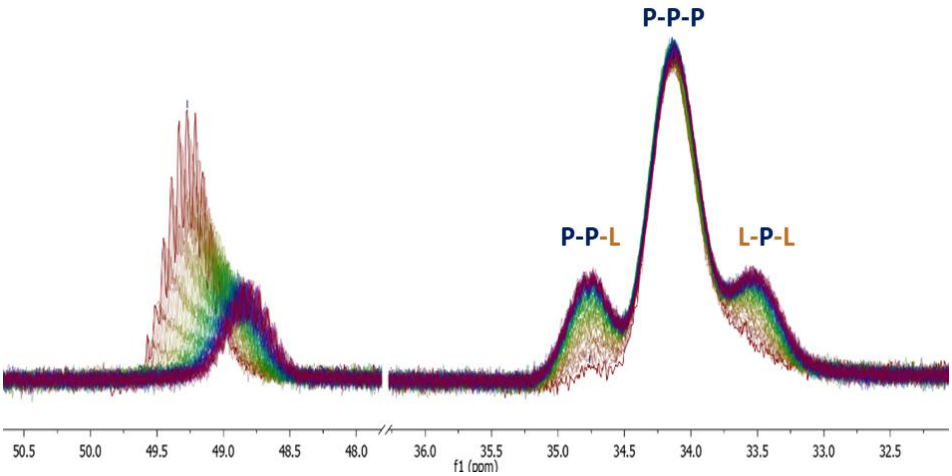

Figure 5.13. Overlay of ^{31}P NMR spectra generated from *in-situ* monitoring of the copolymerisation of EtPPn and *L*-LA, initiated by BnOH and Al(**15**)Me_2, monitored via *in-situ* ^{31}P NMR spectroscopy. $[EtPPn]_0$:$[L\text{-}LA]_0$:$[Al(\mathbf{15})Me_2]_0$:$[BnOH]_0$ = 50:50:1:1, $[EtPPn]_0$ = 0.35 mol L^{-1}.

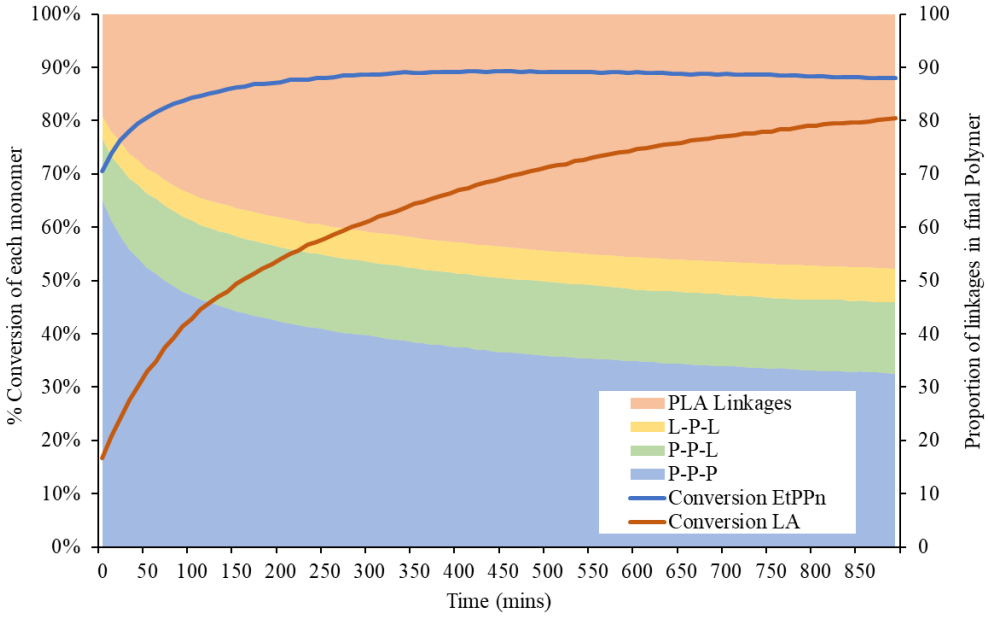

Figure 5.14. Plot of conversion and proportion of triad linkages against time for copolymerisation of EtPPn and *L*-LA with Al(**15**)Me_2 and BnOH, monitored via *in-situ* ^{1}H and ^{31}P NMR spectroscopy. $[EtPPn]_0$:$[L\text{-}LA]_0$:$[Al(\mathbf{15})Me_2]_0$:$[BnOH]_0$ = 50:50:1:1, $[EtPPn]_0$ = 0.35 mol L^{-1}.

As it is not possible to identify the PLA centred triads (PLP and LLP) from the obtained spectra, PLA linkages are represented by the conversion of LA from the methine region of the ^{1}H NMR spectrum and fitted to a 100% stacked area graph. From this approach an idea of the total contribution of each monomer and linkage to the final architecture can be gained. It can be seen that with Al(**15**)Me_2 the initial entries show a degree of random incorporation of LA into the poly(phosphonate) chain. Over time the propagation rate of LA supersedes that of EtPPn,

leading to an increase in the proportion of LA, PPL, and LPL linkages in the overall polymer. After 300 minutes it can be seen the ratio of phosphonate triads does not change with the overall proportion of LA and EtPPn linkages coming to around 50 % each, in agreement with single analysis stirred polymerisations. In contrast, the proportion graph for the polymerisation with DBU shows the polymer exists as primarily LA linkages with an even distribution of PPP, PPL and LPL linkages throughout (Figure 5.15). Statistical enchainment of EtPPn into *L*-LA, with DBU as initiator, gives a potential method for the distribution of theoretically hydrolytically more susceptible units throughout the polymer, potentially providing a route to enhanced degradation kinetics.

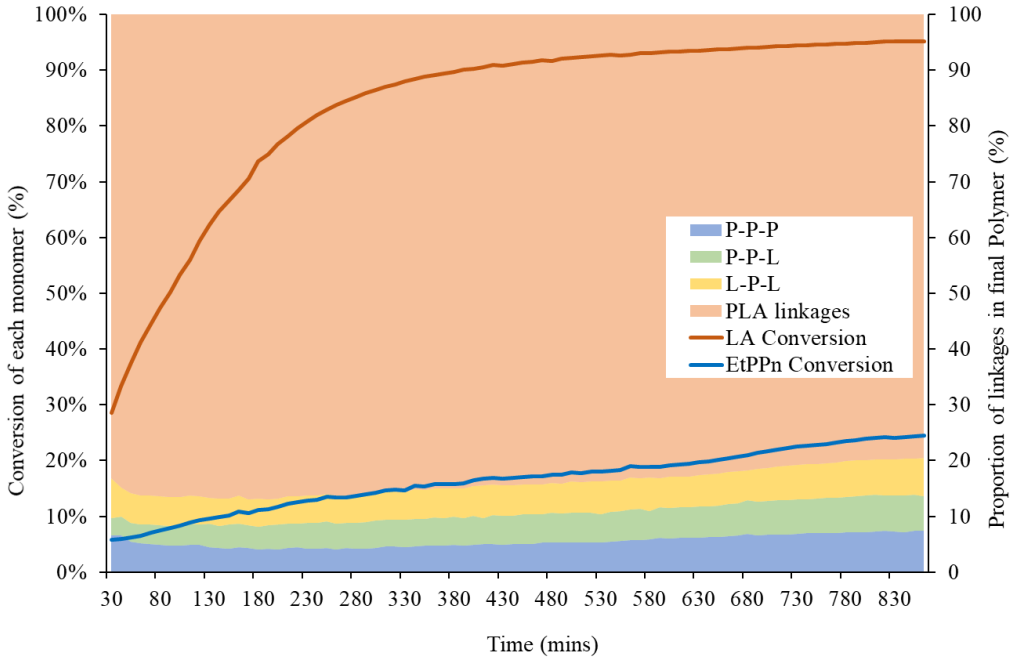

Figure 5.15. Plot of conversion and proportion of triad linkages against time for copolymerisation of EtPPn and *L*-LA with DBU and BnOH at 80 °C, monitored via *in-situ* ^{1}H and ^{31}P NMR spectroscopy. $[EtPPn]_0$:$[L\text{-}LA]_0$:$[DBU]_0$:$[BnOH]_0$ = 50:50:1:1, $[EtPPn]_0$ = 0.35 mol L^{-1}.

5.2.6. Reactivity Ratios

The nature of the microstructure of a copolymer synthesised from monomer mixtures is often defined by the reactivity ratios of each monomer. The rates of propagation cannot be measured independently due to the presence of multiple propagation reactions during the polymerisation. For the copolymerisation of LA and EtPPn there are four potential chain extension reactions, each with a propagation rate constant (Equation 5.2). As each propagation has a separate rate law, the rate of change of each monomer can be defined by a combination of the propagation rates (Equation 5.3). Due to the steady state approximation the rate of change of active LA* and EtPPn* chain ends is equal to zero, thus removing these terms from the equation. From this assumption the rate laws are converted into the Mayo-Lewis equation for a copolymerisation (Equation 5.4).[52]

Equation 5.2. Possible propagation reactions for the copolymerisation of EtPPn and LA.

$$LA* + LA \rightarrow LALA* \quad (k_{LALA})$$

$$LA* + EtPPn \rightarrow LAEtPPn* \quad (k_{LAEtPPn})$$

$$EtPPn* + LA \rightarrow EtPPnLA* \quad (k_{EtPPnLA})$$

$$EtPPn* + EtPPn \rightarrow EtPPnEtPPn* \quad (k_{EtPPnEtPPn})$$

Equation 5.3. Propagation rate laws for the copolymerisation of EtPPn and LA

$$-\frac{d[LA]}{dt} = k_{LALA}[LA]\sum[LA*] + k_{EtPPnLA}[LA]\sum[EtPPn*]$$

$$-\frac{d[EtPPn]}{dt} = k_{EtPPnEtPPn}[EtPPn]\sum[EtPPn*] + k_{LAEtPPn}[EtPPn]\sum[LA*]$$

Equation 5.4. Mayo-Lewis Equation for copolymerisation.[53]

$$\frac{d[LA]}{d[EtPPn]} = \frac{[LA](r_1[LA] + [EtPPn])}{[EtPPn]([LA] + r_2[EtPPn])} \qquad \text{Where } r_1 = \frac{k_{LALA}}{k_{LAEtPPn}} \text{ and } r_2 = \frac{k_{EtPPnEtPPn}}{k_{EtPPnLA}}$$

With r_1 and r_2 referring to the reactivity ratios, expressing the likelihood of insertion of EtPPn into metal-PLA bond over the homo insertion of another LA (r_1), and vice versa for the second reactivity ratio r_2. The ratio of these values refers to the expected macrostructure of the copolymer:

$r_1 = r_2 >> 1$ – Shows the mixture has very little preference for co-enchainment with homo insertion into the active chain end. This would result in a mixture of two homopolymers.

$r_1 = r_2 > 1$ – A preference for homopolymerisation with the rare insertion of the other monomer resulting in propagation of that new chain end. This behaviour is seen for during the ROP of *rac*-LA using highly-isoselective catalysts, resulting in stereoblock copolymers.

$r_1 = r_2 \approx 1$ – There is no preference of either monomer inserting into the active centre generating a random copolymer system.

$r_1 = r_2 \approx 0$ – A strong preference for co-enchainment suggesting propagation of a monomer has to be proceeded by insertion of the other monomer. This behaviour is expected for alternating copolymerisation such as the ROCOP of CO_2 and epoxides using a highly polycarbonate selective catalyst.

$r_1 \gg 1 \gg r_2$ – A wide discrepancy in the value of each reactivity ratio either side of 1 indicates a tapered block copolymer is favoured. As co-insertion is still possible it is likely that concentration of each monomer will affect the macrostructure.

Using multiple linear plots and expressing one monomer as a function of another, Mayo and Lewis were able to experimentally calculate the reactivity ratios from a co-monomer mixture (Equation 5.5).[53] Where f_{LA} = the ratio of LA in the initial feed and F_{LA} equates to the corresponding copolymer composition at low conversions (<15%). An initial guess is required for r_1 which can later be defined by an intersection method to more accurately define the values.

Equation 5.5. Equation for the calculation of reactivity ratios from a monomer mixture.[53]

$$r_2 = \frac{f_{LA}\,(1 + r_1 f_{LA})}{F_{LA}} - f_{LA}$$

This method has formed the basis of multiple derivations of this equation and with an increase in computing power more accurate methods have been developed, notably Meyer-Lowry, Jaacks, and Direct Numerical integration methods.[54–58] Using kinetic data obtained from analysis of *in-situ* ^{1}H NMR experimentation, these methods were applied for the copolymerisation of EtPPn and L-LA using both Al(**15**)Me_2 and DBU by Jens C. Markwart at the Max Planck Institute for Polymer research (Figure 5.14 and Figure 5.15). As these methods are only applicable at low monomer conversion (<40%), when the rate is not defined by variation in monomer concentration a fit of the data to t = 0 is applied for the polymerisation of EtPPn using Al(**15**)Me_2 (Figure 5.16).[54]

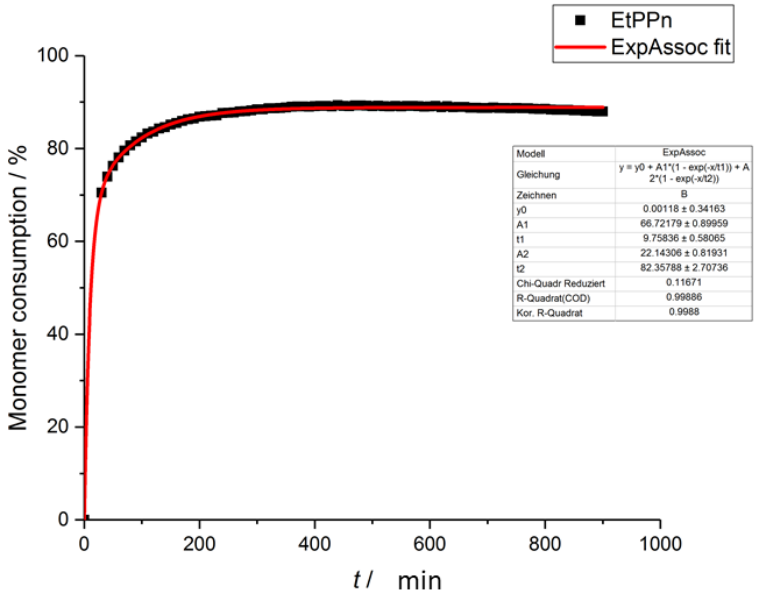

Figure 5.16. Fit of the real-time ^{1}H NMR data of EtPPn using Al(**15**)Me$_2$ at feed ratios 50:50:1:1 {[EtPPn]$_0$:[LA]$_0$:[BnOH]$_0$:[Al(**15**)Me$_2$]$_0$}, 80 °C, 16h to t = 0.

Applying the Meyer-Lowry model, reactivity ratios at low to moderate conversions can be obtained. This is done by fitting the experimental composition drift (f_1) against the total conversion, defining r_1 = EtPPn and r_2 = LA (Figure 5.17). When Al(**15**)Me$_2$ is used as the initiator, reactivity values of r_1 and r_2 (18.41 and 0.83 respectively) show a tapered structure with a large EtPPn block followed by a tapering into a LA block. Plotting the kinetic data for when DBU is the initiator the reverse selectivity is seen, with r_1 and r_2 value of 0.20 and 19.74 respectively.

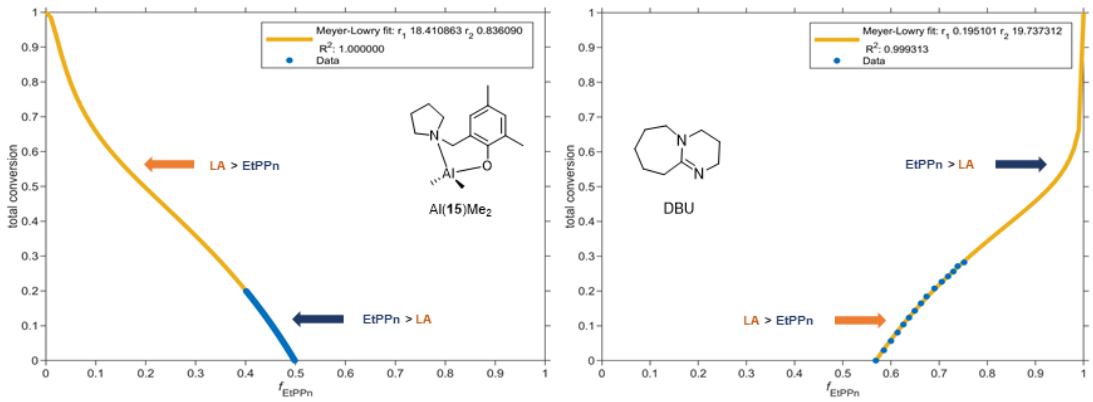

Figure 5.17. Meyer-Lowry fits from the real-time NMR data of EtPPn (r_1) and LA (r_2) using Al(**15**)Me$_2$ and DBU at feed ratios 50:50:1:1 {[EtPPn]$_0$:[L-LA]$_0$:[BnOH]$_0$:[I]$_0$}, 80 °C, 16h.

Using the reactivity ratios values obtained via Meyer-Lowry methods it is possible to calculate the mean composition as a function of conversion (Figure 5.18).[58] Whilst this plot is only valid for data at low to moderate conversions it is possible to see during this phase the copolymer composition shows a high selectivity for EtPPn in the case of Al(**15**)Me_2 and LA in the case of DBU.

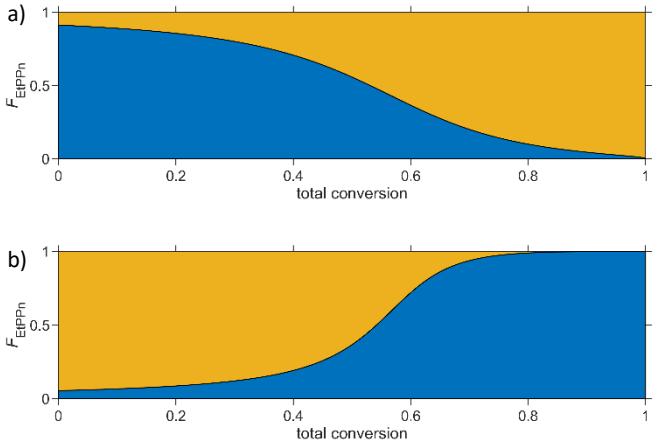

Figure 5.18. Mean composition (*F*) of EtPPn and LA using a) Al(**15**)Me_2 or b) DBU at feed ratios 50:50:1:1 {$[EtPPn]_0$:$[L\text{-}LA]_0$:$[BnOH]_0$:$[I]_0$}, 80 °C, 16h versus the total conversion determined using the r parameters estimated by the Meyer-Lowry fit.

Direct numerical integration methods show very similar reactivity ratios values to that of Meyer-Lowry methods for Al(**15**)Me_2 and DBU providing increased validation of these findings (Figure 5.19). Whilst Jaacks methodologies support the observation of a tapered system with a selectivity switch between the two initiators, a reduction in both r_1 and r_2 is seen (Figure 5.20). This is a common feature of this methodology as it estimates reactivity ratios under the assumption of an ideal copolymerisation ($r_1 \times r_2 = 1$).[56,59]

Whilst these calculations are estimations, with a degree of inaccuracy in the methodologies, they serve as good support for the identifying the nature of the synthesised LA:EtPPn copolymers. In agreement with other spectroscopic investigations it can be seen that selectivity is monomer concentration dependent under the tested conditions, with the choice of the initiator having a profound impact on the microstructure.

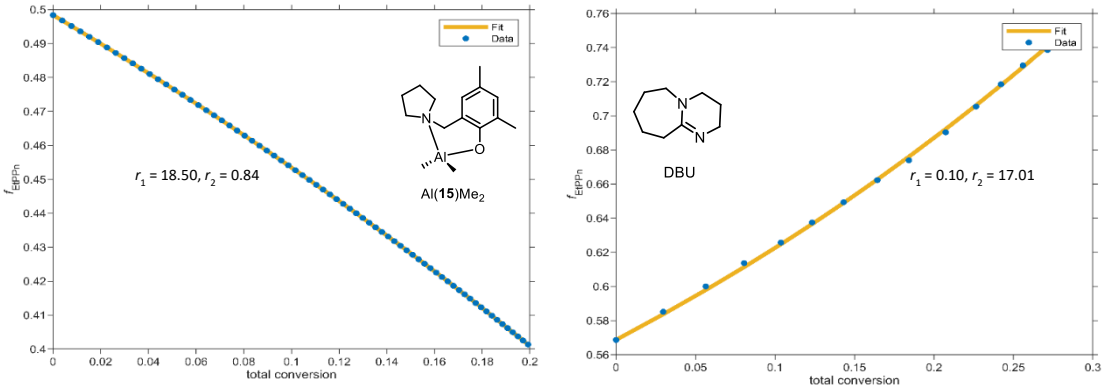

Figure 5.19. Direct numerical integration of the real-time NMR data of EtPPn (r_1) and LA (r_2) using Al(**15**)Me_2 and DBU at feed ratios 50:50:1:1 {$[EtPPn]_0$:$[L\text{-}LA]_0$:$[BnOH]_0$:$[I]_0$}, 80 °C, 16h.[57]

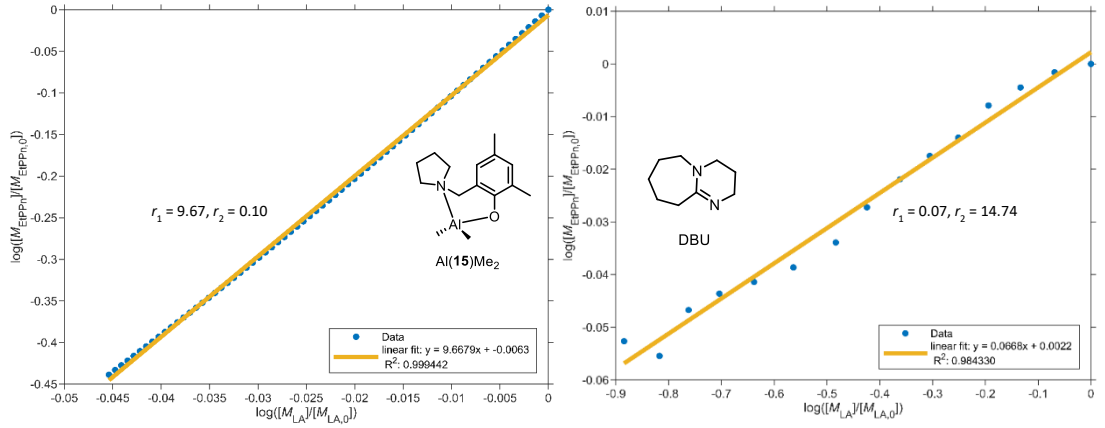

Figure 5.20. Jaacks plot of the real-time NMR data of EtPPn (r_1) and LA (r_2) using Al(**15**)Me_2 and DBU at feed ratios 50:50:1:1 {$[EtPPn]_0$:$[L\text{-}LA]_0$:$[BnOH]_0$:$[I]_0$}, 80 °C, 16h.[56]

5.2.7. Calculation of molecular weights from *In-situ* kinetic analysis

Analysing the conversions of each monomer over time allows the estimation of molecular weight of the polymer at a given conversion following the calculation for M_n^{theo}. Plotting this 'ideal fit' against conversion yields a straight line with a gradient equal to the molecular weight of an averaged copolymer unit ({136.03(EtPPn) + 144.12(LA)}/ 2) with an intercept which is equal to the mass of residual end groups. Assuming linear growth, perfect dispersity, and alternating sequence of copolymer repeating units, it can be used to show any deviation of experimental results from the 'ideal' (Figure 5.16).

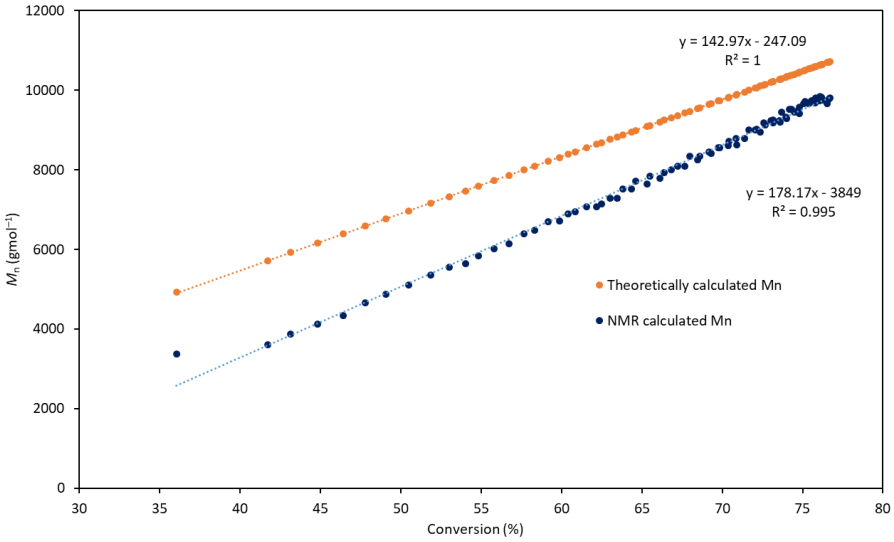

Figure 5.21. Plot of theoretically calculated molecular weight (M_n^{theo}) and NMR calculated molecular weight (M_n^{NMR}) against total combined monomer conversion for the copolymerisation of *L*-LA with EtPPn initiated with Al(**15**)Me_2, monitored via ^{1}H NMR spectroscopy. $[EtPPn]_0$:$[L\text{-}LA]_0$:$[I]_0$:$[BnOH]_0$ = 50:50:1:1, $[EtPPn]_0$ = 0.35 M.

With *in-situ* analysis it was possible to identify the aromatic resonances assigned to the BnO– end group. Throughout the kinetic run, the integral of aromatic resonances remained constant relative to the combined monomer and polymer integrals. Through normalisation of the BnO– resonances it is possible to calculate a value for the repeating unit of each monomer relative to a single BnO– end group. Multiplying this by the molecular weight of each monomer yields a molecular weight estimate of each monomer contribution in the copolymer at a given time, or M_n^{NMR} (Figure 5.21).

This calculation is only appropriate as an estimate and assumes all aromatic benzyl alcohol signals are end groups which remain attached to one individual linear chain. Plotting the calculated M_n^{NMR} against the combined monomer conversion yields a straight line with a gradient of 178.17 g mol^{-1} and an R^2 = 0.995. This value is significantly greater than the theoretical (142.97 g mol^{-1}) showing a degree of transesterification or catalyst deactivation

is present. Comparing this to M_n^{SEC} values obtained after the reaction was quenched, a close fit to is obtained via ^{1}H NMR analysis (M_n^{theo} = 9.5 kg mol^{-1}, M_n^{NMR} = 10.8 kg mol^{-1}, M_n^{SEC} = 8.7 kg mol^{-1}, $Đ$ = 1.27). The accuracy of this measurement could be improved through the introduction of internal standards in the NMR tube allowing a more accurate integration of BnO– and polymer units to a known quantity.

5.2.8. Temperature sequencing for block enhancement

Optimisation of the temperature sequence and concentration of solution could lead to an enhancement in the 'block' nature of the copolymer from a monomer mixture. The gradient sequence seen through kinetic experimentation at 80 °C, when Al(**15**)Me$_2$ is chosen as the initiator, shows a slight preference for the propagation of EtPPn over LA at high [M]. Additionally, for the homopolymerisation reactions of EtPPn in toluene high conversions could be achieved within 3 hours at 25 °C (Entry 2, Table 5.2), whereas LA shows poor solubility and reactivity with Al(**15**)Me$_2$ under these conditions. Exploiting this, an *in-situ* NMR experiment was performed to see if an initial low temperature sequence promoting EtPPn propagation, followed by a second, high temperature sequence favouring the polymerisation of the LA could lead to enhancement of the block-like nature of the copolymer.

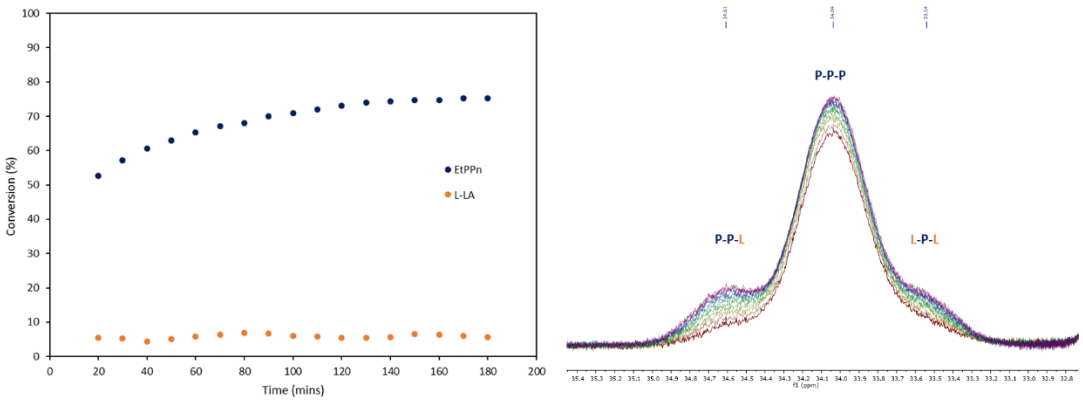

Figure 5.22. ^{1}H and ^{31}P NMR monitored copolymerisation of EtPPn and *L*-LA at 25 °C {[LA]$_0$:[EtPPn]$_0$:[Al(**15**)Me$_2$]$_0$:[BnOH]$_0$ = 50:50:1:1, [LA]$_0$ = 0.35 M}. a) Conversion over time graph. b) Stacked ^{31}P NMR spectra of polymer region (red – 20 minutes, purple 180 minutes).

Initial testing of the monomer mixture at 25 °C in toluene-d_8 {$[LA]_0$:$[EtPPn]_0$:$[Al(\mathbf{15})Me_2]_0$:$[BnOH]_0$ = 50:50:1:1, $[LA]_0$ = 0.35 M} showed that conversion of EtPPn after 3 hours is similar to that achieved at 80 °C (Figure 5.22). No appreciable increase in conversion of *L*-LA occurs during the experiment with low conversion (5 – 10%) seen in the initial stages. ^{31}P NMR showed a slight increase of PPL and LPL units as reaction time proceeds showing that even at reduced temperature, a small degree of "mis-insertion" is seen.

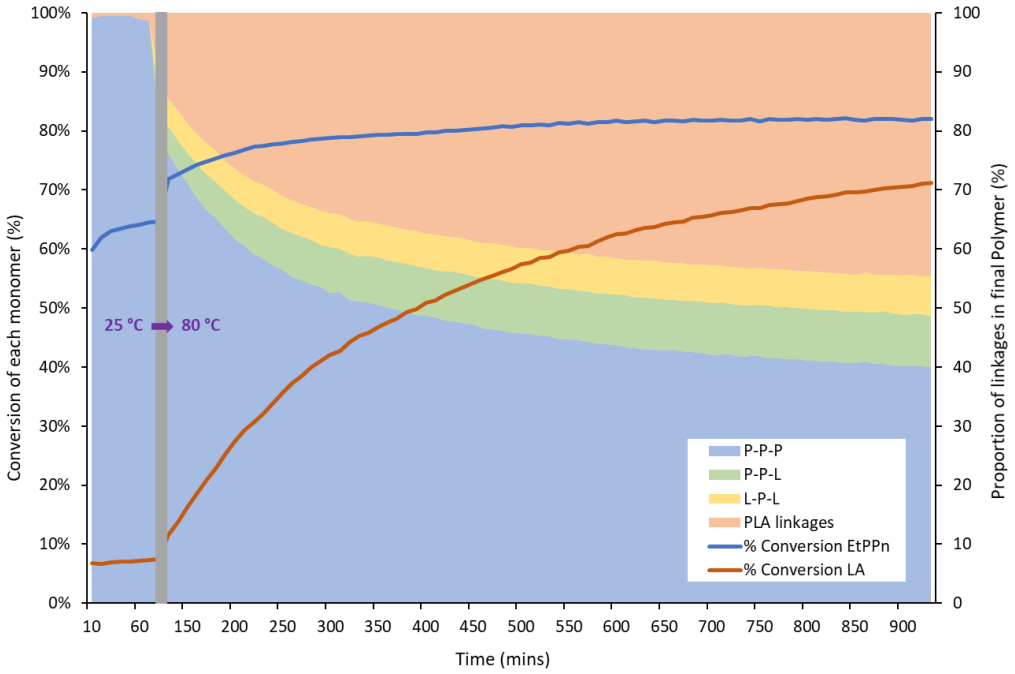

Figure 5.23. Plot of conversion and proportion of triad linkages against time for copolymerisation of EtPPn and L-LA with Al(**15**)Me_2 and BnOH at 25 °C for 80 minutes followed by 80 °C for a further 900 minutes, {$[LA]_0$:$[EtPPn]_0$:$[Al(\mathbf{15})Me_2]_0$:$[BnOH]_0$ = 50:50:1:1, $[LA]_0$ = 0.35 M}.

In an analogous experiment, temperature sequencing was used, increasing the temperature of the sample to 80 °C after 90 minutes at 25 °C (Entry 2, Table 5.4). Whilst not all the EtPPn had converted in this time, a plateauing in conversion was seen, similar to experimentation at 25 °C (Figure 5.18). Due to the time taken to perform the temperature ramp and equilibrate the sample, data between 80 – 100 minutes was not collected. Following equilibration, an increase in both LA and EtPPn conversion is seen, as well as the proportion of random PPL and LPL triad linkages. A steady rise in LA and EtPPn conversion is seen for the next 100 minutes with $k_{obs} = 2.7 \times 10^{-3}$ min^{-1} and $k_{obs} = 2.3 \times 10^{-3}$ min^{-1} respectively. Hereafter, a plateau of phosphonate conversion is observed at 82%, with a steady increase in LA conversion, reaching 72% after 14 hours. ^{1}H DOSY analysis of the purified polymer showed only one species diffusing in solution with a diffusion constant, equal to 2.3×10^{-10} m^2 s^{-1} (D_{sol} = 2.3×10^{-9} m^2 s^{-1}). Propagation of both monomers between 100 – 200 minutes *via* the represents a reduced co-enchainment timeframe to experiments ran solely at 80 °C. As a

result, an enhancement of homopolymer (PPP) units is seen, with phosphonate triad ratios of 73:15:12 (PPP:PPL:LPL) for temperature sequencing in comparison to ratios of 56:25:19 (PPP:PPL:LPL) seen for polymerisation just at 80 °C. DSC traces show only one glass transition temperature at 5.3 °C suggesting the polymer was not significantly 'blocky' at this degree of copolymerisation to express the biphasic behaviour as seen *via* sequential addition.

Wurm and co-workers reported that for the polymerisation of cyclic phosphates high concentration was required to achieve high conversions and limit molecular weight distribution. Unlike the previous reported initiators, high concentrations were shown not to be a necessity for Al(**15**)Me_2 to achieve high molecular weights and narrow dispersities in both homo and copolymerisations. However a plateau of conversions for EtPPn (80 – 90%) is seen during the *in-situ* monitored experiments carried out under low monomer concentration (0.35 mol L^{-1}). As seen above, homopolymerisations of EtPPn with Al(**15**)Me_2 under bulk conditions, yielded high molecular weight polymer in a matter of minutes, a rate not seen before in literature (Entry 1, Table 5.2).[41,47,48] In order to test if concentration plays a role in monomer selectivity, a stirred copolymerisation experiment at 20 °C was set up with total monomer concentrations of 3.6 mol L^{-1} in toluene (Entry 1, Table 5.4).

Table 5.4. Polymerisation data for the copolymerisation of *L*-LA and EtPPn with Al(**15**)Me_2 via temperature sequencing.

Entry	Sequence 1 T (°C), t (h)	Sequence 2 T (°C), t (h)	Conc. (mol L^{-1})	Conv. LA (%)	Conv. EtPPn (%)	EtPPn (%)	T_g (°C)	Triads ratio PPP-PPL-LPL
1	20, 0.16	80, 1	3.6	60	100	62.5	1.0	85:11:4
2[a]	25, 1.5	80, 16	0.35	71	82	53.6	5.3	73:12:15
3[a]	80, 16	25, 0.5	0.35	81	95	54	-	61:25:14

$[EtPPn]_0$:$[L\text{-LA}]_0$:$[Al(\mathbf{15})Me_2]_0$:$[BnOH]_0$ = 50:50:1:1 in toluene, $[EtPPn]_0 = [L\text{-LA}]_0$. [a] Experiment carried out *in-situ* in an NMR spectrometer in toluene-d_8.

Aided by high solubility of LA in EtPPn, a homogenous solution was generated prior to addition of Al(**15**)Me_2 and BnOH. Following catalyst addition, the polymerisation was allowed to stir at temperature for 10 minutes to force EtPPn conversion as high as possible. Subsequently, the solution was heated at 80 °C for a further hour to promote conversion of *L*-LA. Quenching and NMR analysis showed complete conversion of EtPPn and 60% conversion of LA. A much improved triad ratio of 85:11:4 (PPP:PPL:LPL) is seen, with a single glass transition seen at 1.0 °C. Due to the high monomer concentrations it is likely that 'mis-

insertion' might have occurred during the initial temperature sequence where it is expected the complete conversion of EtPPn would be seen. This follows kinetic analysis showing a small degree of LA (<5%) converted at 25 °C from the co-monomer mixture under dilute conditions (Figure 5.22). Due to the high conversions and near block microstructure this copolymer was not soluble in THF, meaning SEC analysis could only be carried out in DMF at 60 °C using RI measurements. Relatively narrow molecular dispersities and a closeness to expected molecular weights was seen indicating low degrees of transesterification (M_n^{theo} = 11.3 kg mol^{-1}, M_n^{SEC} = 9.9 kg mol^{-1}, $Đ$ = 1.26).

5.2.9. Thermal Gravimetric Analysis (TGA)

Analysis of the thermal decomposition profiles through TGA is an important aspect when dealing with new polymeric systems. The onset of degradation issues the lower limit of commercial processability of the pure material, with systems likely to not be commercialised if they fail to have a high thermal stability.[60] The profile of decomposition can elude to the stability of linkages, interactions and bonds as the mass is measured as a function of temperature. Measuring the point of fastest decline (T_{inf}) from the derivative curve and comparing with the onset of degradation can give information into the uniformity of the sample. A large variance between the two highlights a lack of uniformity in bond strengths. TGA of pEtPPn shows a single derivative signal with a onset of 136 °C and a T_{inf} of 210 °C with no further degradation seen after 300 °C (Figure 5.24). The 10% of residual mass is in keeping with previous reports for polyphosphonates, where significantly lower char quantities are recorded than the higher oxidation number in poly(phosphoesters).[25] This sort of behaviour has recently been explored in the application of flame retardancy, for which phosphorous compounds are becoming increasingly popular.[25,26,61] In comparison, measurements for the degradation of PLLA show a higher temperature degradation profile with a T_{inf} in the range of 330 – 340 °C. The large gap between this degradation temperature and the melt temperature of the crystalline PLLA (T_m = 180 °C) is one of the reasons for its emminence in the plastic packaging market, allowing thermal processing of the bulk polymer.[62]

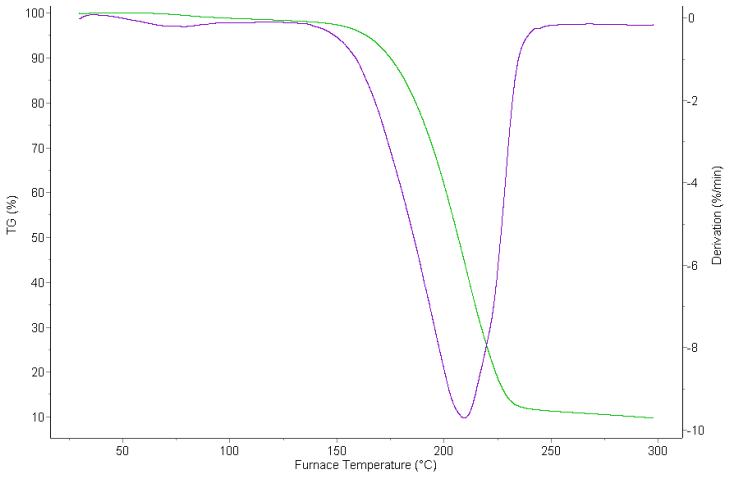

Figure 5.24. TGA trace for pEtPPn synthesised from the bulk polymerisation of EtPPn using Al(**15**)Me_2 as initiator (Entry 1, Table 5.2).

TGA of the synthesised copolymers show decomposition graphs with T_{inf} between the two homopolymers. The profile is shown to be dependent on the microstructure, with a number of derivative peaks seen (Figure 5.25). These derivatives highlight the different linkages shown through ^{31}P NMR spectroscopy, with T_{inf} between 200 – 220 °C showing PPP in the copolymer and T_{inf} between 300 – 350 °C showing LLL in the copolymer. Depending on the extent of tapering between the blocks, the size of the derivative is shown to vary, with a broadening between the decomposition onset and T_{inf}.

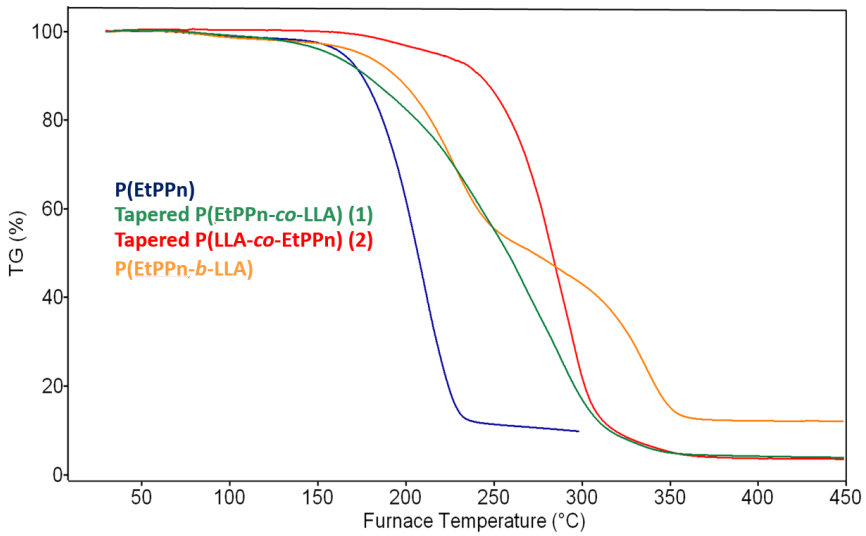

Figure 5.25. Stacked TGA curves of homopolymer of EtPPn, Tapered copolymer synthesised from using Al(**15**)Me_2 as initiator (Entry 5, Table 5.3), Tapered copolymer synthesised from using DBU as initiator (Entry 8, Table 5.3) and block copolymer synthesised from sequential addition using Al(**15**)Me_2.

Copolymers with low tapering, synthesised from the sequential addition of EtPPn (96:3:1, PPP:PPL:LPL) show three distinct derivatives clearly indicating the pure blocks with a small derivative at 272 °C between the two (Figure 5.26).

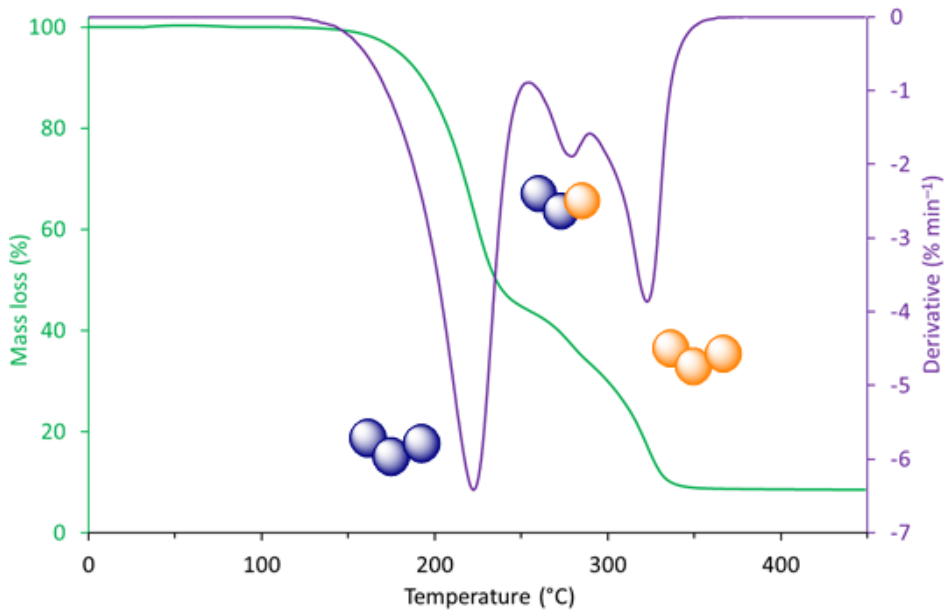

Figure 5.26. TGA graph of copolymer synthesised from sequential addition of EtPPn to a stirred PLLA mixture at 80 °C (96:3:1, PPP:PPL:LPL).

Block copolymer synthesised from polymerisation of LA at 80 °C and then addition of EtPPn at 25 °C (PPP:PPL:LPL, 98:2:0), showed a reduction in this signal as expected with two distinct derivatives seen (Figure 5.27). Performing a subtraction of the derivative baseline it is possible to carry out a peak separation calculation to estimate the integral of each peak as a percentage of total weight lost during decomposition. This calculation shows a 39.2% loss at the phase of the curve responsible for pEtPPn block with a 41.7% for the PLLA section. Converting this into percentages in the total polymer shows a 49% of EtPPn is estimated in the polymer, a value which aligns closely with the 47% shown by ^{1}H NMR spectroscopy of the purified polymer.

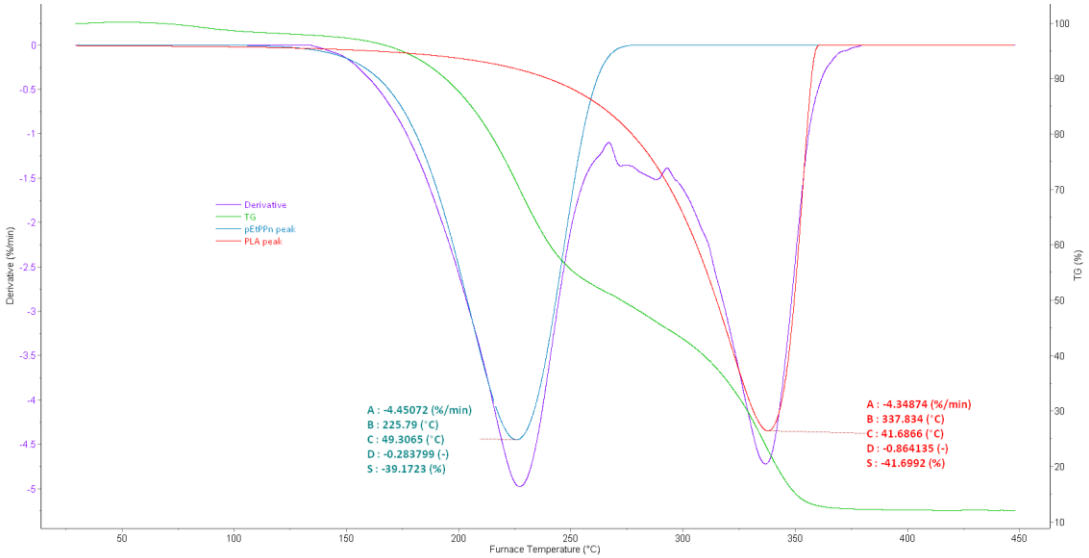

Figure 5.27. TGA curve for p(EtPPn-*b*-LLA) block copolymer showing the derivative signal, with overlaid peak separation curves and calculated integrals.

Whilst this approach is not quantitative due to a large error in the estimation, it provides supporting evidence in the copolymer composition, as well as insight into the thermal stability of different linkages and microstructures. For systems with multiple derivative maxima this approach offers a way of adding clarity to an otherwise complicated trace.

5.2.10. MALDI-ToF analysis

Alongside these techniques, MALDI-ToF is commonly reported for copolymer systems.[63] Whilst commonly employed to identify end groups and chain length, it has also been explored for statistical copolymers to calculate reactivity ratios and chain length distributions.[64,65] In order to further explore LA and phosphonate copolymers, MALDI-ToF was attempted on copolymers from monomer mixtures (Entry 1 – 5, Table 5.3). All obtained mass spectra show a trailing series from 1000 – 3000 g mol^{-1} with no gaussian distribution of peaks, but a consistent distribution between envelopes (Figure 5.28).

It is possible to obtain integer units for each monomer by calculating each series with no end groups (indicative of a cyclic polymer) with a sequence transesterified units of PLA between envelopes. Between each envelope a repeating unit of transesterified PLA is seen, with series in each envelope having a matrix association of the two monomers, with decreasing EtPPn and increasing PLA units upon increasing m/z. Whilst variations in peak envelopes are seen between different copolymer compositions, the trend is consistent throughout.

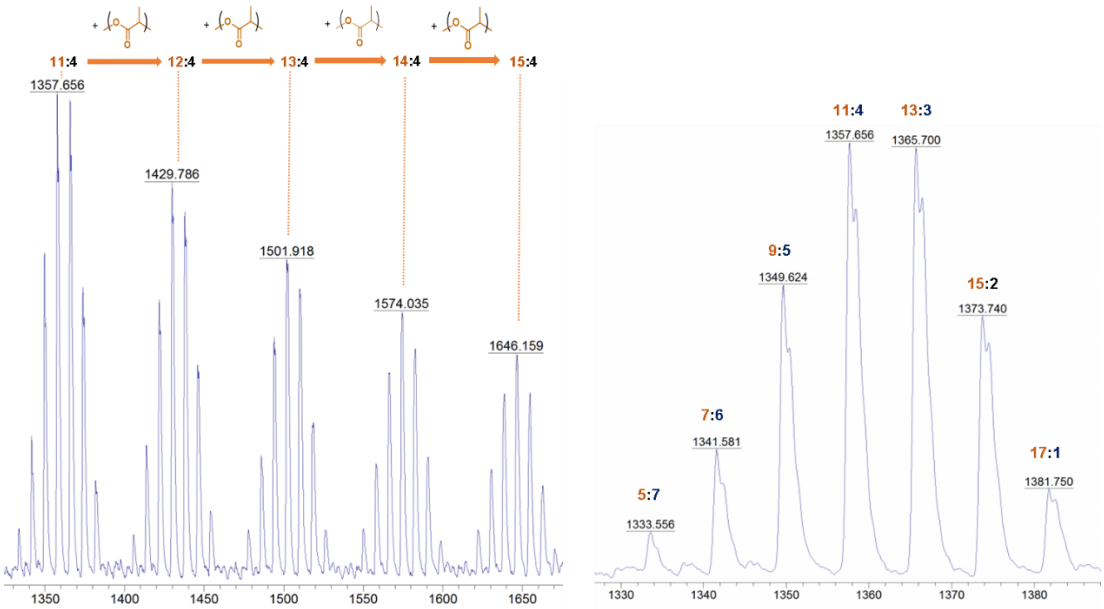

Figure 5.28. MALDI-ToF mass spectra of a LA-EtPPn copolymer (Entry 2, Table 5.3). EtPPn incorporation = 39% and M_n^{SEC} = 12.5 kg mol^{-1}. Associated X:X ratios represent the integer value of repeating units of transesterified PLA with repeating units of 77.06 g mol^{-1} and pEtPPn with repeating units of 136.03 g mol^{-1}.

The presence of low molecular weight species in the MALDI-ToF spectra is in contrast to results from SEC where high molecular weights were calculated with narrow distributions. Additionally, the identification of cyclic species with no benzyl end group is in disagreement with the ^{1}H DOSY analysis which shows the end group diffusing at a similar rate to the polymer signals. This variation is could be due to the intensive ionisation process of the sample causing scission of bonds, with only the resultant low molecular weight chains being able to fly sufficiently through the spectra to be recorded. High molecular weight suppression is common with samples that are carried out in reflector positive mode, where the ions are ran in multiple loops through the spectrometer prior to data collection, often leading to a dampening in the signal strength of higher molecular weight samples (> 10 kDa).[66,67] In addition, it is likely that the recipe which has previously been optimised for the PLA is not suitable for the phosphorous containing copolymers. This follows that MALDI-ToF spectra were poorer in resolution and observable molecular weights with increasing EtPPn content as shown via ^{1}H NMR spectroscopy.

5.3. Conclusions and future work

This chapter has detailed the expansion of the ROP catalysis of cyclic phosphosphonates, with a focus on EtPPn due to its favourable hydrolytic degradation and applications in biomedical delivery systems. Al(**15**)Me_2 was shown to be highly active for this polymerisation under a variety of conditions, yielding well defined molecular weights close to that of expected values. Solvent-free polymerisation was shown to reach high conversions (90%) within 5 minutes, a rate previously not been seen by either organic or organometallic initiators, albeit under slightly different conditions.[41,48] The effect of concentration and temperature was explored, leading to the identification of a possible ceiling point for productive propagation. Despite this, under dilute conditions and high temperatures, synonymous to those previously tested for LA, high conversions could be obtained (81%) within 16 hours.[50]

Sequential addition of EtPPn into a stirred PLLA mixture at 25 °C was shown to yield the desired block copolymer {P(LLA-*b*-EtPPn)}, with co-enchainment confirmed through unimodal SEC traces, ^{31}P NMR spectroscopy, and two distinct thermal transitions in the DSC trace. This copolymer held amphiphilic properties, swelling in polar solvents in alignment with phosphoester-*b*-PLLA block copolymers observed by Wang and coworkers.[37] From co-monomer mixtures, additional resonances in the ^{31}P NMR spectra were identified as phosphorous based EtPPn-LA linkages. Quantification of these showed the copolymer produced was tapered in macrostructure. ^{1}H and parallel ^{31}P NMR kinetics showed a tapering effect from the homopolymerisation of EtPPn (PPP) to a LA block in real time giving information on the reverse selectivity seen between DBU and Al(**15**)Me_2. This selectivity was quantified through calculated reactivity ratios using a variety of methodologies.

In addition, the kinetic data obtained from *in-situ* experiments was used to plot the calculated end group molecular weights *vs* conversion, observing a linear growth close to that of the theoretical values. The slight deviation from this ideal growth can be used as evidence of some cyclic species in the polymer. Comparison with SEC obtained molecular weights show close agreement with this *in-situ* calculated approach.

Temperature sequencing as a method of block enhancement was employed for comonomer mixtures with Al(**15**)Me_2 as initiator. Kinetic data showed whilst low temperatures (25 °C) promoted high conversion of EtPPn, upon an increase in the reaction temperature (80 °C), tapering was still observed. Best results were achieved under highly concentrated conditions where high activity and low tapering were achieved (Entry 1, Table 5.4). This data supports

homopolymerisation data obtained for EtPPn, that at high temperatures and low concentrations that a monomer equilibrium is in place, limiting manipulation of the microstructure. Despite a reduction in the length of the tapered sequence, the copolymers produced from this methodology were not sufficiently 'blocky' to possess biphasic properties.

Future work regarding the ROP of cyclic phosphonates should encompass a screening of different catalytic systems. It has been shown in this study that catalyst selection has a pronounced effect on the achievable rates and control for this monomer. In addition, it would be pertinent to explore Al(**15**)Me_2 with more lipophilic phosphonates such at ^{n}BuPPn and alkene functionalised systems. If proved an effective initiator for these monomers, the possibility to access a great range of LA:phosphonate copolymers will allow a more wide spread investigation into their properties and applications. To this end, ongoing work at the Max Planck Institute for Polymer Research looks to fully evaluate LA based phosphonate copolymers for drug delivery applications, with cell viability studies in progress.

Whilst this study explores how through kinetic analysis, the nature of the microstructure can be identified, further work should be done to explore more accurate methods of analysis. '*On-line'* or flow NMR spectroscopy, could give faster and more representative kinetic data. If initial data (0 – 20 minutes) could be obtained, obtaining low conversion data might be possible. This would allow calculation of initial rates and greater accuracy in calculation of the reactivity ratios. Expanding the analytical methods available is also a focus of polymer chemists. To this end, TGA and MALDI-ToF analysis have a lot of potential. In addition, to giving thermal stability data of the copolymer, it was shown through TGA of block copolymers that distinct decomposition phases could be integrated to give estimations of the copolymer microstructure. Further work testing a variety of molecular weights and block microstructures should be carried to further explore the accuracy of this method. MALDI-ToF analysis clearly identifies the co-enchainment of EtPPn and LA, with ability to identify the presence of transesterification and cyclisation of the polymers. With these results conflicting with other forms of analysis, the optimisation of the recipe and methodology should be a priority.

Hydrolytic degradation was not fully explored with initial investigations showing little change in molecular weights or mass of polymer when immersed in deionised water (30 °C, pH 5.6) for 20 days. Further investigation should consider using accelerated degradation methods, such as testing in strongly basic solutions. Whilst not a realistic representation, this would

provide insight into whether the microstructure has a significant impact on the degradation kinetics, exploring the theory that dispersing the more 'degradable' phosphonate units throughout the chain will encourage a more complete degradation profile. In addition, the more degradable MePPn could also be adopted in the comonomer feed, to further tune the degradation properties of the resultant polymer.

5.4. References

1 T. Haider, C. Völker, J. Kramm, K. Landfester and F. R. Wurm, *Angew. Chem Int. Ed.*, 2018, **58**, 50–62.

2 A. R. Bagheri, C. Laforsch, A. Greiner and S. Agarwal, *Glob. Challenges*, 2017, **1**, 1700048.

3 R. T. Martin, L. P. Camargo and S. A. Miller, *Green Chem.*, 2014, **16**, 1768–1773.

4 California Department of Resources Recycling and Recovery, 2012, 38.

5 H. S. Yang, J. S. Yoon and M. N. Kim, *Polym. Degrad. Stab.*, 2005, **87**, 131–135.

6 World Economic Forum. and Ellen MacArthur Foundation., *The New Plastics Economy: Rethinking the future of plastics*, 2016.

7 R. Pradhan, M. Reddy, W. Diebel, L. Erickson, M. Misra and A. Mohanty, *Int. J. Plast. Technol.*, 2010, **14**, 45–50.

8 A. Ostafinska, I. Fortelny, M. Nevoralova, J. Hodan, J. Kredatusova and M. Slouf, *RSC Adv.*, 2015, **5**, 98971–98982.

9 F. Yemisci and A. Aytac, *Fibers Polym.*, 2017, **18**, 1445–1451.

10 J. Muller, C. González-Martínez and A. Chiralt, *Materials* , 2017, **10**, 1–22.

11 P. Chaiwutthinan, V. Pimpan, S. Chuayjuljit and T. Leejarkpai, *J. Polym. Environ.*, 2015, **23**, 114–125.

12 S. M. S. Corneillie, *Polym. Chem.*, 2015, **6**, 850.

13 D. Cohn and H. Younes, *J. Biomed. Mater. Res.*, 1988, **22**, 993–1009.

14 D. J. Darensbourg and G. P. Wu, *Angew. Chemie - Int. Ed.*, 2013, **52**, 10602–10606.

15 K. J. Pepper, T. Masson, D. De Focatiis and S. M. Howdle, *J. Supercrit. Fluids*, 2018, **133**, 343–348.

16 F. Sadeghi, F. Hadizadeh, S. Sazmand, S. Shahrokhi, M. Seifi and M. Alibolandi, *Int. J. Pharm. Investig.*, 2015, **5**, 134.

17 L. Yang, A. El Ghzaoui and S. Li, *Int. J. Pharm.*, 2010, **400**, 96–103.

18 L. Wang, Z. Zhang, H. Chen, S. Zhang and C. Xiong, *J. Polym. Res.*, 2010, **17**, 77–82.

19 M. A. Hillmyer, *Science*, 2017, **358**, 868–870.

20 S. A. Miller, *ACS Macro Lett.*, 2013, **2**, 550–554.

21 C. Bastioli and R. T. Limited, *Handbook of Biodegradable Polymers*, Rapra Technology, 2005.

22 J. H. Song, R. J. Murphy, R. Narayan and G. B. H. Davies, *Philos. Trans. R. Soc. B Biol. Sci.*, 2009, **364**, 2127–2139.

23 J. Pretula, K. Kaluzynski, B. Wisniewski, R. Szymanski, T. Loontjens and S. Penczek, *J. Polym. Sci. Part a-Polymer Chem.*, 2008, **46**, 830–843.

24 T. S. Stukenbroeker, D. Solis-Ibarra and R. M. Waymouth, *Macromolecules*, 2014, **47**,

8224–8230.

25 M. M. Velencoso, A. Battig, J. C. Markwart, B. Schartel and F. R. Wurm, *Angew. Chemie Int. Ed.*, 2018, **130**, 10608–10626.

26 K. N. Bauer, H. T. Tee, M. M. Velencoso and F. R. Wurm, *Prog. Polym. Sci.*, 2017, **73**, 61–122.

27 Y. Y. T. Tsao, T. H. Smith and K. L. Wooley, *ACS Macro Lett.*, 2018, **7**, 153–158.

28 T. Steinbach, R. Schröder, S. Ritz and F. R. Wurm, *Polym. Chem.*, 2013, **4**, 4469.

29 P. Klosiński and S. Penczek, *Macromolecules*, 1983, **16**, 316–320.

30 D. P. Chen and J. Wang, *Macromolecules*, 2006, **39**, 473–475.

31 Y. H. Lim, G. S. Heo, S. Cho and K. L. Wooley, *ACS Macro Lett.*, 2013, **2**, 785–789.

32 G. Becker, Z. Deng, M. Zober, M. Wagner, K. Lienkamp and F. R. Wurm, *Polym. Chem.*, 2018, 315–326.

33 Y. P. Borguet, S. Khan, A. Noel, S. P. Gunsten, S. L. Brody, M. Elsabahy and K. L. Wooley, *Biomacromolecules*, 2018, **19**, 1212–1222.

34 X.-Z. Yang, Y. Wang, L.-Y. Tang, H. Xia and J. Wang, *J. Polym. Sci. Part A Polym. Chem.*, 2008, **46**, 6425–6434.

35 G. Becker, T. A. Marquetant, M. Wagner and F. R. Wurm, *Macromolecules*, 2017, **50**, 7852–7862.

36 G. Becker, L. Vlaminck, M. M. Velencoso, F. E. Du Prez and F. R. Wurm, *Polym. Chem.*, 2017, **8**, 4074–4078.

37 X.-Z. Yang, T.-M. Sun, S. Dou, J. Wu, Y.-C. Wang and J. Wang, *Biomacromolecules*, 2009, **10**, 2213–2220.

38 K. N. Bauer, L. Liu, D. Andrienko, M. Wagner, E. K. Macdonald, M. P. Shaver and F. R. Wurm, *Macromolecules*, 2018, **51**, 1272–1279.

39 K. N. Bauer, H. T. Tee, I. Lieberwirth and F. R. Wurm, *Macromolecules*, 2016, **49**, 3761–3768.

40 T. Steinbach, S. Ritz and F. R. Wurm, *ACS Macro Lett.*, 2014, **3**, 244–248.

41 T. Wolf, T. Steinbach and F. R. Wurm, *Macromolecules*, 2015, **48**, 3853–3863.

42 T. Wolf, T. Rheinberger and F. R. Wurm, *Eur. Polym. J.*, 2017, **95**, 756–765.

43 T. Wolf, J. Naß and F. R. Wurm, *Polym. Chem.*, 2016, **7**, 2934–2937.

44 J. Simon, T. Wolf, K. Klein, K. Landfester, V. Mailänder and F. R. Wurm, *Angew. Chemie Int. Ed.*, 2018, **57**, 5548–5553.

45 T. Wolf, T. Rheinberger, J. Simon and F. R. Wurm, *J. Am. Chem. Soc.*, 2017, **139**, 11064–11072.

46 T. Wolf, J. Hunold, J. Simon, C. Rosenauer, D. Hinderberger and F. R. Wurm, *Polym. Chem.*, 2018, **9**, 490–498.

47 E. K. Macdonald and M. P. Shaver, *Green Mater.*, 2016, **4**, 81–88.

48 I. E. Nifant'ev, A. V. Shlyakhtin, V. V. Bagrov, P. D. Komarov, M. A. Kosarev, A. N. Tavtorkin, M. E. Minyaev, V. A. Roznyatovsky and P. V. Ivchenko, *Polym. Chem.*, 2017, **8**, 6806–6816.

49 J. Beament, G. Kociok-Köhn, M. D. Jones and A. Buchard, *Dalton. Trans.*, 2018, **47**, 9164–9172.

50 J. Beament, M. F. Mahon, A. Buchard and M. D. Jones, *Organometallics*, 2018, **37**, 1719–1724.

51 A. Dove, H. Sardon and S. Naumann, *Organic Catalysis for Polymerisation*, Royal Society of Chemistry, 2018.

52 F. R. Mayo and F. M. Lewis, *J. Am. Chem. Soc.*, 1944, **66**, 1594–1601.

53 T. Rooney, O. Monyatsi and R. A. Hutchinson, *Macromolecules*, 2017, **50**, 3, 784–795.

54 N. Kazemi, T. A. Duever and A. Penlidis, *Macromol. React. Eng.*, 2011, **5**, 385–403.

55 H. Patino-Leal, P. M. Reilly and K. F. O'Driscoll, *J. Polym. Sci. Polym. Lett. Ed.*, 1980, **18**, 219–227.

56 V. Jaacks, *Macromol. Chem. Phys.*, 1972, **161**, 161–172.

57 E. Hauch, X. Zhou, T. A. Duever and A. Penlidis, *Macromol. Symp.*, 2008, **271**, 48–63.

58 P. C. Painter and M. M. Coleman, *Essentials of Polymer Science and Engineering*, DEStech Publications, Incorporated, 2008.

59 F. T. Wall, *J. Am. Chem. Soc.*, 1941, **63**, 1862–1866.

60 T. Mekonnen, P. Mussone, H. Khalil and D. Bressler, *J. Mater. Chem. A*, 2013, **1**, 13379–13398.

61 S. Yu, H. Xiang, J. Zhou and M. Zhu, *Fibers Polym.*, 2017, **18**, 1098–1105.

62 H. Tsuji, *Macromol. Biosci.*, 2005, **5**, 569–597.

63 G. Montaudo, F. Samperi and M. S. Montaudo, *Prog. Polym. Sci.*, 2006, **31**, 277–357.

64 R. X. E. Willemse, B. B. P. Staal, E. H. D. Donkers and A. M. Van Herk, 2004, 5717–5723.

65 S. Huijser, G. D. Mooiweer, R. Van Der Hofstad, B. B. P. Staal, J. Feenstra, A. M. Van Herk, C. E. Koning and R. Duchateau, *Macromolecules*, 2012, **45**, 4500–4510.

66 H. Pasch and W. Schrepp, *MALDI-TOF Mass Spectrometry of Synthetic Polymers*, Springer Berlin Heidelberg, 2013.

67 J. Blais, A. Caminade, J. Majoral and M. Curie, *Anal. Chem.*, 2000, **72**, 5097–5105.

Chapter 6

Experimental

6. Experimental

6.1. General considerations

Complex preparations and characterisations were performed under an inert gas atmosphere (Ar) using standard Schlenk line and glove box techniques. Dry solvents for the handling of and preparation of metal complexes and polymerisations was collected from an MBraun solvent purification syste m (SPS) and kept under argon. Laboratory reagent grade solvents were used for the preparation of ligands and purification of polymers. Chemicals were purchased from Sigma-Aldrich and used without further purification unless stated except for monomers. *rac*-, *L*-LA and phthalic anhydride were crystallised twice from high purity toluene obtained from an MBraun SPS. Cyclohexene oxide was dried over $MgSO_4$ and twice distilled. All monomers were stored under inert atmosphere in a glove box. Lanthanide reagents including $(Ln(O^iPr)_3$, $Ln(N(Si(CH_3)_3)_2)_3$ were purchased from Strem and used as received. 2-ethyl-1,3,2-dioxaphospholane 2-oxide (EtPPn) was received from collaborators Dr. Thomas Wolf and Dr. Frederik Wurm from the Max Planck Institute of Polymer Research and stored under argon at 253 K. 3,5-di-tert-*butyl*-2-hydroxybenzylbromide, 3-(1-adamantyl)-5-methylsalicylaldehyde, 2-(chloromethyl)-4,6-dimethylphenol, were prepared according to literature methods.[1–3] 1-O-methyl-α-mannose was purchased from Carbosynth and used as received, the synthesis of the mannose based cyclic carbonate was carried out by Dr. Georgina Gregory following literature procedures.

6.2. Instrumentation and Analysis

6.2.1. NMR Spectroscopy

^1H, $^1H\{^1H\}$, ^{11}B, and $^{13}C\{^1H\}$ NMR spectra were recorded with a Bruker 400 MHz instrument and referenced to residual solvent resonances. NMR spectroscopic analysis was conducted in $CDCl_3$, THF-d_8, C_6D_6 or $C_6D_5CD_3$ at 298 K unless stated otherwise. For the analysis of organometallic complexes dry NMR solvents were dried and degassed over molecular sieves before use with metal complexes. NMR tubes fitted with Young's taps were utilised for analysis of metal complexes and variable temperature experiments. Coupling constants are given in Hertz.

For the polymerisation of LA: Calculation of conversion when carried out in $CDCl_3$ was determined from the integration of the methine region of the polymer (5.12 – 5.20 ppm) against that of the monomer (4.94 – 5.01 ppm). Homonuclear decoupled ^1H NMR spectra was carried out to calculate tacticity by decoupling of the methine region.

For the polymerisation of mannose derived cyclic carbonate: Calculation of conversion was carried out in $CDCl_3$ from the integration of methine protons neighbouring the methoxy side chain in the monomer (4.99 ppm) and the polymer (4.85 – 4.90ppm).

For the copolymerisation of PA and CHO: Calculation of conversion when carried out in $CDCl_3$ was determined from the integration of the Ar protons in the polymer for PA (7.50 – 7.53 ppm) against the PA monomer (7.95 – 8.01 ppm). Ester bond selectivity was taken from the resonances of polyester CHO (4.82 – 5.22 ppm) and polyether CHO resonances (3.40 – 3.58 ppm).

For the copolymerisation of EtPPn and LA: Calculation of conversion when carried out in $CDCl_3$ was determined from the integration of the methine region of the polymer (5.12 – 5.20 ppm) against that of the monomer (4.94 – 5.01) in the case of LA and (1.74 – 1.85 ppm) for the polymer and (1.93 – 2.03 ppm) for the monomer in the case of EtPPn, unless stated otherwise.[4] Conversions of EtPPn were also taken and compared from integration of all polymer signals in the ^{31}P NMR spectra {number of scans (ns) = 64, D1 = 5 seconds)}, *i.e.* in $CDCl_3$ polymer signals (34.0 – 36.0 ppm) against the monomer signals (53.0 – 53.5 ppm) or in the case of toluene-d_8 (33.0 – 35.1 ppm) for the polymer and (48.2 – 49.6 ppm) for the monomer. Triad ratios were calculated from integration of the 3 triad sequences observable in the ^{31}P NMR spectra {number of scans (ns) = 64, D1 = 5 seconds} and are assigned as P–P–L (35.2 – 36.0 ppm), P–P–P (34.3 – 35.2 ppm) and L–P–L (33.0 – 34.3 ppm) respectively in $CDCl_3$. In the homopolymerisation of EtPPn a small quantity of ring-opened methoxy terminated side product was seen (37.0 ppm in $CDCl_3$) upon quenching with methanol. When this side product was apparent, conversion was taken from integration of the polymer signals over that of the sum of the monomer and side-product signals. Expected % EtPPn in the copolymer was calculated from conversion and feed ratios from the crude product. Molecular weight measurements obtained from NMR analysis were carried out by comparing the integral of the aromatic signals of BnO- end group (7.28 – 7.43 ppm) with the EtPPn polymer backbone signal (4.13 – 4.39 ppm) and the methine region of the PLA unit. In the case of using 1,4-benzenedimethanol as an initiator polymers were integrated against the singlet aromatic signal at 7.30 ppm. *In-situ* NMR experiments were carried out in J-Young's NMR tubes in 0.7 mL toluene-d_8. Timings were recorded from sample preparation. Upon heating to elevated temperatures the sample was allowed to stabilise for 10 minutes prior to manual shimming. Successive ^{1}H (ns = 16) and ^{31}P (ns = 32, D1 = 5s) NMR spectra were acquired every 10 minutes via a staggering run sequence.

Diffusional ordered spectroscopy (DOSY): ^{1}H and ^{31}P DOSY experiments were carried out on a Bruker Avance III 500 MHz spectrometer and samples were equilibrated at the measurement temperature of 298 K for 5 min before data collection. Spinning was deactivated to avoid convection. For polymer analysis the NMR tube was filled with 0.7 mg mL^{-1} of polymer in 1 mL deuterated $CDCl_3$ to reduce the impact of polymer viscosity and molecular interactions.[5,6] 1D ^{1}H spectra were acquired with the zg30 pulse program from the Bruker library. 2D DOSY spectra were acquired using a double stimulated echo sequence ("dstegp2s") for convection compensation and with monopolar gradient pulses. D1 was set to 5 seconds, collecting 64k data points and 16 scans per gradient level. Ten gradient strengths were used between 2 and 95 %. The spectra were multiplied with an exponential window function before Fourier transformation (xf2), and subsequently phase corrected. The diffusion coefficients were obtained on MestReNova processing software by fitting a peak heights fit method to the spectra.

6.2.2. Single crystal X-ray diffraction

X-ray diffraction data was collected on either a Supernova or Excallibur, EOS detector diffractometer using radiation CuKα (λ= 1.54184 Å) or Mo-Kα (λ= 0.71073 Å) all recorded at 150(2) K. Data was collected and solved by Dr. Matthew Jones and Dr. Paul McKeown with assistance from Dr. Mary Mahon and Dr. Gabrielle Kociok-Köhn. All structures were solved by direct methods and refined on all F^2 data using the SHELXL-2014 suite of programs. All hydrogen atoms were included in idealized positions and refined using the riding model.

6.2.3. CHN microanalysis

All analysis was performed by Mr. Stephen Boyer at the Science Centre, London Metropolitan University.

6.2.4. Size-Exclusion Chromatography

Chromatographic molecular weight data for PLA polymers, polyesters of phthalic anhydride and cyclohexene oxide, mannose polycarbonates and phosphonate copolymers was carried on a Agilent 1260 Infinity series instrument with THF eluent at 1 mL min^{-1} at 35 °C using a PLgel 5 µm MIXED-D 300 × 7.5 mm column. Detection was carried out using triple detection methods, using a differential refractive index detector (referenced to 11 polystyrene standards of narrow molecular weight, ranging from M_w 615 – 568000 Da), a viscometer detector and a light scattering detector (90 °, with a calculated dn/dc range = 0.095-0.11 g^{-1} mL, as calculated from the RI). Multi analysis software was used to process the data. For

polyphosphonates and selected polyphosphonate copolymers, which were not soluble in THF, SEC analysis was carried out at the Max Planck Institute for Polymer Research in DMF (containing 0.25 g L^{-1} of lithium bromide as an additive) at 60 °C at a flow rate of 1 mL min^{-1} with an Agilent 1100 Series as an integrated instrument, including a PSS HEMA column (106 /105 /104 g mol^{-1}) and a refractive index (RI) detector. Calibration was carried out using poly(ethylene glycol) standards provided by Polymer Standards Service.

6.2.5. Differential Scanning Calorimetry

Thermal transitions were recorded on a Thermal analysis Q20 DSC from TA instruments, equipped with a Thermal Advantage Cooling System-90 under nitrogen. Samples were measured from –70 °C to 150 °C with 10 °C min^{-1} heating and 10 °C min^{-1} cooling, following a standard heating-cooling-heating-sequence. T_g data that is presented is that obtained from the second cycle upon heating and compared to the same transition during the cooling cycle.

6.2.6. Thermal-Gravimetric Analysis

Thermal gravimetric analysis (TGA) was carried out on a Setsys Evolution TGA 16/18. Calisto software was employed to collect and process the data. The sample was loaded onto a pre-weighed 170 µL alumina crucible. Following a 30 minute purge at 30 °C under argon flow at 20 mL min^{-1} the sample was heated at a rate of 20 °C a minute to the required temperature. The degradation maxima was taken from steepest point in the first derivative curve, calculated from the mass loss curve. For the semi-quantitative analysis of copolymer composition a subtraction of the derivative base line is performed followed by a deconvolution of peaks and optimisation of the separated peaks.

6.2.7. Matrix Assisted Laser Desorption Ionisation Time of Flight (MALDI-ToF)

Mass spectra were obtained on a Bruker Autoflex speed instrument using DCTB (trans-2-[3-(4-tert-butylphenyl)-2-methyl-2-propenylidene]malononitrile) as the matrix and ionized using NaTFA. For the analysis of PLA, 2 µL of a homogenised solution of DCTB (10 µL, 10 mg mL^{-1} in THF), NaTFA (2 µL, 0.1 M in THF) and polymer (10 µL, 5 mg mL^{-1} in THF) is placed on the ionisation plate for analysis.

6.2.8. Reactivity Ratio analysis

Reactivity ratios were calculated at the Max Planck Institute for polymer research by Mr. Jens Markwart using kinetic data collected at the University of Bath. Since most methods for estimating reactivity ratios are only applicable to low to medium conversions it was necessary to fit the real-time NMR data to t = 0 for the reaction using Al(**15**)Me_2.[7]

Computational modelling allowed the projection of graphical data displaying the equation results from which the reactivity ratios was calculated.[8–12]

6.3. Polymerisation Methods

Polymerisations were carried out in a Young's ampoule under inert argon conditions. For a typical solution polymerisation, *rac*-lactide (1.0 g, 0.69 mmol), initiator (typically $[LA]_0$:$[I]_0$ = 100:1) are dissolved in dry toluene (10 mL). If a co-initiator is required, benzyl alcohol typically in a stoichiometric ratio ($[I]_0$:$[BnOH]_0$ = 1:1, 7.26 µL) is added to the flask. The flask is then placed into a preheated oil bath (80 °C) and stirred for a set time. After polymerisation the solvent is removed *in vacuo* and a crude ^{1}H NMR recorded. The polymer was then purified by dissolution in methanol from a concentrated solution of polymer in dichloromethane (apart from Ln synthesised polymers, which were not purified prior to analysis). Solvent free or melt lactide polymerisations were usually carried out at a higher ratios ($[LA]_0$:$[I]_0$ = 300:1) in the absence of solvent at 130 °C. Upon gelation the polymerisation was stopped and the solid was quenched through the addition of DCM and a few drops of methanol. ^{1}H NMR kinetics were carried out in a J-Young's tube in d_8-toluene (0.6 mL, 6.9 mM).

The ROP of 1-O-methyl-α-mannose derived cyclic carbonate was carried out in dry CH_2Cl_2 using a stock solution of the catalyst in CH_2Cl_2. Quenching of the reaction was carried out through the addition of excess benzoic acid in CH_2Cl_2 (20 mgml^{-1}). The co-polymerisation of epoxides and anhydrides was carried out in either neat conditions {$[CHO]_0$:$[PA]_0$:$[I]_0$ = 800:100:1, $[PA]_0$ = 1 M, 130 °C} or in a toluene solution {$[CHO]_0$:$[PA]_0$:$[I]_0$ = 200:200:1, $[PA]_0$ = 1 M, 80 °C}. Cooling the mixture down and exposing to air quenched the reaction prior to purification of the polymer via precipitation in hexane. The ROP of D-mannose based 6-membered cyclic carbonate was carried out in CH_2Cl_2 at 25 °C {$[M]_0$ = 0.5 M}. Quenching was carried out by addition of a few drops of MeOH to the reaction mixture prior to ^{1}H NMR analysis of the crude polymer. Precipitation from a concentrated mixture of the crude product in diethyl ether yielded the pure polymer. The homopolymerisation of EtPPn is carried out as detailed (Chapter 5.2.1) following published reaction procedures for purification.[4] Copoylmerisation reactions were carried out as detailed (Chapter 5.2.3 and Chapter 5.2.4). Purification was carried out through precipitation in diethylether and centrifugation of the resultant suspension to yield the solid product.

6.4. Ligand synthesis and characterisation

6.4.1. Synthesis of tetradentate bisphenolate bipyrrolidine ligands

1H_2 and **2**H_2 were synthesised via modified procedures adapted from previously published procedures and compared to literature spectra.[13–15] The following procedures are adapted "mannich" reactions, reported in context of the newly synthesised **3-5**H_2. *meso*-bipyrrolidine (6.14 mmol) was added dropwise to a stirred solution of p-formaldehyde (12.3 mmol) in methanol (100 mL) at 40 °C. After 10 minutes, 2,5-dichlorophenol (12.3 mmol), was added and the solution was heated to reflux. After 3 hours the reaction was cooled to room temperature and the precipitate was collected via filtration and washed with hot methanol (4 × 30 mL). The solid precipitate was dissolved in DCM (30 mL) and extracted with 7 wt % NaOH solution (3 × 20 mL). Drying over $MgSO_4$ and *in vacuo* removal of the solvent yielded the pure product (2.74 mmol, 44%).

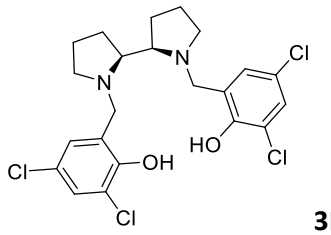

3H_2: Red solid (2.74 mmol, 44%). ^{1}H NMR (400 MHz, 298 K, $CDCl_3$, δ_H, ppm); 7.25 (2H, d, J = 2.3 Hz, Ar), 6.89 (2H, d, J = 2.3 Hz, Ar), 4.30 (2H, d, J = 13.5 Hz, CH*H*), 3.47 (2H, d, J = 13.5 Hz, C*H*H), 3.04 – 2.98 (2H, quin, C*H*H), 2.90 – 2.85 (2H, quin, NCH*H*), 2.42 – 2.36 (2H, m, C*H*H), 2.18 – 2.11 (2H, m, CH*H*), 1.88 – 1.83 (6H, m, CH_2); ^{13}C{^{1}H} NMR (100 MHz, 298 K, $CDCl_3$, δ_C, ppm); 152.3 (*C*-O), 128.6 (Ar), 126.4 (Ar), 124.4 (Ar), 123.4 (Ar), 121.4 (Ar), 68.1 (N*C*H_2), 59.8 (N*C*H_2), 54.4 (N*C*H) 25.6 (*C*H_2), 23.0 (*C*H_2). m/z [$C_{22}H_{24}Cl_2N_2O_2$ + H]$^+$: Calculated: 489.0652 g mol^{-1}, Experimental 489.0645 g mol^{-1}.

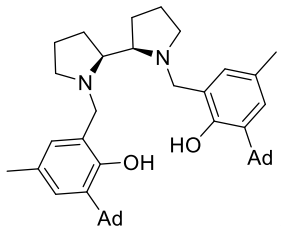

4H_2: White solid (12.3 mmol, 58%). ^{1}H NMR (400 MHz, 298 K, $CDCl_3$, δ_H, ppm); 10.78 (2H, s, OH), 6.90 (2H, d, J = 2.2 Hz, Ar), 6.63 (2H, d, J = 2.2 Hz, Ar), 4.31 – 4.34 (2H, d, J = 13.6 Hz, CH*H*), 3.39 – 3.43 (2H, d, J = 13.5 Hz, C*H*H), 2.98 – 3.01 (2H, m, C*H*H), 2.81 – 2.85 (2H, m, C*H*), 2.33 – 2.39 (2H, m, C*H*H), 2.23 (6H, s, CH_3), 2.13 (12H, m, CH_2), 2.02 (6H, m, CH_2) 1.75 (12H, m, CH_2); ^{13}C{^{1}H} NMR (100 MHz, 298 K, $CDCl_3$, δ_C, ppm); 154.5 (*C*-O), 136.3

(Ar), 126.8 (Ar), 126.5 (Ar), 126.1 (Ar), 122.5 (Ar), 67.8 (N*C*H_2), 60.7 (N*C*H_2), 54.3 (N*C*H), 40.2 (CH_2), 37.2 (*C*H(CH_2)$_3$), 36.6 (*C*(CH_2)$_3$), 29.2 (*C*H_2), 28.1 (*C*H), 25.6 (*C*H_2), 23.0 (*C*H_2). m/z [$C_{44}H_{60}N_2O_2$ + H]$^+$: Calculated: 649.4734 g mol^{-1}, Experimental 649.4715 g mol^{-1}.

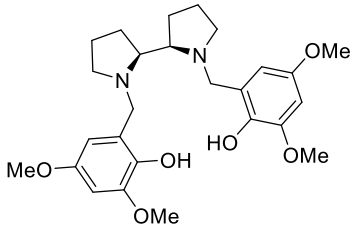

5H_2: orange solid (^{1}H NMR (400 MHz, 298 K, $CDCl_3$, δ_H, ppm); 9.18 (2H, s, OH), 7.02 (2H, d, J = 2.3 Hz, Ar), 6.62 (2H, d, J = 2.3 Hz, Ar), 4.8 (6H, s, OCH_3), 4.76 (6H, s, OCH_3), 4.23 (2H, d, J = 13.1 Hz, CH*H*), 3.65 (2H, d, J = 13.1 Hz, C*H*H), 2.84 – 2.98 (4H, m, C*H*H), 2.36 – 2.40 (2H, m, C*H*$_2$), 1.61 – 1.86 (8H, m, C*H*$_2$); ^{13}C{^{1}H} NMR (100 MHz, 298 K, $CDCl_3$, δ_C, ppm); 150.9 (*C*-O), 124.2 (Ar), 124.0 (Ar), 121.8 (Ar), 121.0 (Ar), 118.4 (Ar), 73.4 (OCH_3), 62.5 (OCH_3), 59.8 (N*C*H_2), 55.8 (N*C*H_2), 54.2 (N*C*H) 25.4 (*C*H_2), 21.5 (*C*H_2). m/z [$C_{26}H_{36}73.N_2O_2$ + H]$^+$: Calculated: 472.2611 g mol^{-1}, Experimental 472.2599 g mol^{-1}.

6.4.2. Synthesis of tetradentate bisphenolate ethylenediamine ligands.

N,N'-Dimethyl ethylenediamine ligands were synthesised according to previously reported procedures.[16,17] *p*-formaldehyde (34.5 mmol) was suspended into a solution of the diamine (15.6 mmol) in methanol (70 mL) stirred and heated to reflux for 30 minutes. To this solution 2,4 di-substituted phenol (31.4 mmol) was added and the solution was stirred and heated to reflux for 3 hours. Upon cooling, a precipitate was formed which was collected via filtration and washed with cold methanol (3 x 30 mL). Drying *in vaccuo* at 40 °C for 16 hours yielded the corresponding tetradentate ligand. Detailing of the yields and ^{1}H NMR spectra are presented for comparison.

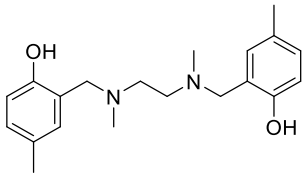

6H_2: white powder (4.1 g, 36 % yield). ^{1}H-NMR (400 MHz, $CDCl_3$, δ_H, ppm); 10.31 (2H, s, OH), 6.98 (2H, d, 8.3 Hz, Ar), 6.76 (2H, d, 8.3 Hz, Ar), 6.74 (2H, s, Ar), 3.65 (4H, s, NCH_2), 2.65 (4H, m, NC*H*$_2$), 2.28 (6H, s, CH_3) 2.24 (6H, s, CH_3).

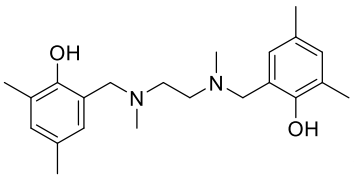

7H_2: white powder (7.1 g, 73% yield). ^{1}H-NMR (400 MHz, $CDCl_3$, δ_H, ppm); 10.6 (2H, s, OH), 6.85 (2H, s, Ar), 6.60 (2H, s, Ar), 3.62 (4H, s, CH_2), 2.65 (4H, m, NC*H*$_2$), 2.25 (6H, s, CH_3) 2.20 (6H, s, CH_3) 2.18 (6H, s, CH_3).

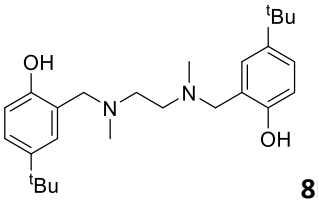

8H_2**:** white powder (4.8 g, 53% yield). ^{1}H-NMR (400 MHz, $CDCl_3$, δ_H, ppm); 9.83 (2H, s, OH), 7.22 - 7.24 (2H, dd, J = 8.70 Hz, J = 2.5 Hz, Ar), 7.01 (2H, d, J = 2.5 Hz, Ar), 6.81 – 6.83 (2H, d, J_{ba} = 8.7 Hz, Ar), 3.73 (4H, s, CH_2), 2.72 (4H, s, NC*H*$_2$), 2.32 (6H, s, CH_3) 1.33 (18H, s, ^{t}Bu).

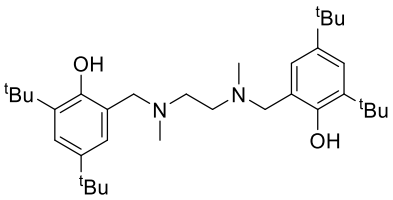

10H_2: white powder (8.91 g, 68% yield). ^{1}H-NMR (400 MHz, $CDCl_3$, δ_H, ppm); 10.61 (2H, s, OH), 7.13 (2H, s, Ar), 6.72 (2H, s, Ar), 3.59 (4H, s, CH_2), 2.56 (4H, s, NC*H*$_2$), 2.19 (6H, s, CH_3) 1.33 (18H, s, ^{t}Bu), 1.20 (18H, s, ^{t}Bu).

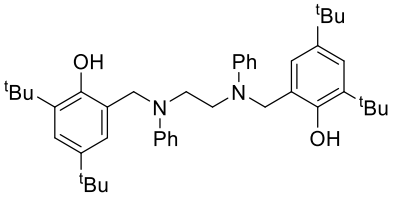

11H_2: yellow powder (2.2 g, 68% yield). ^{1}H-NMR (400MHz, $CDCl_3$, δ_H, ppm); 8.79 (2H, s, OH), 7.30 (2H, d, J = 2.9 Hz, Ar), 7.13 – 7.17 (4H, t, J = 7.9 Hz ,Ar), 6.92 – 6.96 (2H, t, J = 7.9Hz, Ar), 6.87 (2H, d, J = 2.9 Hz, Ar), 6.81 – 6.83 (4H, d, J = 8.0 Hz, Ar), 4.25 (4H, s, NC*H*$_2$), 3.22 (4H, s, CH_2) 1.41 (18H, s, ^{t}Bu), 1.29 (18H, s, ^{t}Bu).

All ligands with the exception of **17**H have previously been reported.[18–20] Experimental adaptations of previously reported synthetic methods, is reported to expand the routes available to each compound.

6.4.3. General Procedure for the synthesis of 14H and 18.

1H was prepared according to previously reported synthesis.[18] **5**H: Pyrrolidine (1.86 g, 26 mmol) was added to a stirred suspension of 3,5-dichloro-2-hydroxybenzaldehyde (5.0 g, 26 mmol) in ethanol (50 mL). The red solution was left to stir for 1 hour. $NaBH_4$ (2.0 g, 52 mmol) was added in small portions. The mixture was quenched with water (5 mL), filtered and the solvent was removed *in vacuo*. The resultant solid was extracted from CH_2Cl_2 (30 mL) with 1M HCl (3 × 30 mL), Brine (3 × 30 mL) and H_2O (3 × 30 mL), before being dried with $MgSO_4$. *In vacuo* removal of solvent yielded a cream solid, (56%, 14.6 mmol).

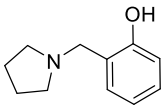

14H : Colourless liquid (14.6 mmol, 56%). ^{1}H NMR (400 MHz, 298 K, $CDCl_3$, δ_H, ppm); 10.73 (1H, s, OH), 7.14 – 7.18 (1H, t, J = 7.9 Hz, Ar*H*), 6.96 – 6.98 (1H, d, J = 7.6 Hz, Ar*H*), 6.81 – 6.83 (1H, d, J = 7.9 Hz, Ar*H*), 6.75 – 6.78 (1H, t, J = 7.6 Hz, Ar*H*), 3.82 (2H, s, CH_2) 2.63 (4H, m, NCH_2), 1.83 – 1.87 (4H, m, CH_2). m/z $[C_{11}H_{15}NO + H]^+$: Calculated: 178.1232 g mol^{-1}, Experimental 178.1240 g mol^{-1}.

6.4.4. General Procedure for the synthesis of 15-17H.

p-formaldehyde (2.00 g, 70 mmol) was dissolved in MeOH (60 mL). To this pyrrolidine (4.00 g, 56 mmol) and 2,4-di-tert-butlyphenol (11.5 g, 56 mmol) were added and the solution was heated to reflux for 16 hours. After the solvent was removed *in-vacuo*, the product was solubilised in DCM (20 mL) and the filtered. The filtrate was then extracted with deionised water (3 × 30 mL) and 7% NaOH (3 × 30 mL), stirred over $MgSO_4$ and filtered. *In-vacuo* removal 2of the solvent yielded a white solid (86 %, 48 mmol). **16**H was compared to similar reported synthesises of these compounds.[19]

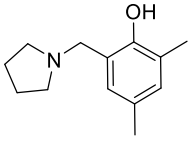

15H : Orange Liquid (77%). ^{1}H NMR (400 MHz, 298 K, $CDCl_3$, δ_H, ppm); 6.86 (1H, d, J = 1.3 Hz, Ar*H*), 6.63 (1H, d, J = 1.35 Hz, Ar*H*), 3.76 (2H, s, CH_2), 2.63 (4H, m, NCH_2), 2.22 (3H, s, CH_3), 2.20 (3H, s, CH_3), 1.83 - 1.86 (4H, m, CH_2), OH signal not observed; ^{13}C{^{1}H} NMR (100 MHz, 298 K, $CDCl_3$, δ_C, ppm); 153.9 (*C*-O), 130.4 (Ar), 127.4 (Ar), 126.0 (Ar), 124.5 (Ar), 121.6 (Ar), 59.0 (*C*H_2), 53.6 (N*C*H_2), 23.9 (N*C*H_2), 20.6 (*C*H_3), 15.7 (*C*H_3). FT-IR (cm^{-1}) 2966.6 (C-H, aromatic), 2809.5 (C-H, alkane), 1619.6 (C=C, aromatic), 1480.3 (C-H, bend) 1245.4 (C-N), 1155.9 (C-O), m/z $[C_{13}H_{19}NO + H]^+$ Calculated: 206.1545 g mol^{-1}, Experimental 206.1543 g mol^{-1}.

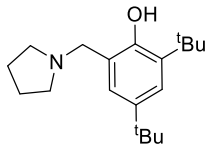

16H : White Solid (48 mmol, 86%) ^{1}H NMR (400 MHz, 298 K, $CDCl_3$, δ_H, ppm); 7.21 (1H, d, J = 2.5 Hz, Ar*H*), 6.84 (1H, d, J = 2.5 Hz, Ar*H*), 3.80 (2H, s, CH_2), 2.63 (4H, m, NCH_2), 1.83 - 1.86 (4H, m, CH_2), 1.43 (9H, s, (C(CH_3)$_3$)), 1.29 (9H, s, (C(CH_3)$_3$)) OH signal not observed; ^{13}C{^{1}H} NMR (100 MHz, 298 K, $CDCl_3$, δ_C, ppm); 154.4 (*C*-O), 140.0 (Ar), 135.2 (Ar), 122.6 (Ar), 122.5 (Ar), 121.8 (Ar), 59.6 (N*C*H$_2$), 53.3 (N*C*H$_2$), 34.8 (*C*(CH$_3$)$_3$), 34.1 (*C*(CH$_3$)$_3$), 31.6 (C(*C*H$_3$)$_3$) 29.5 (C(*C*H$_3$)$_3$), 23.7 (*C*H$_2$). FT-IR (cm^{-1}) 2966.4 (C-H, aromatic), 2807.4 (C-H, alkane), 1601.8 (C=C, aromatic) 1474.2 (C-H, bend), 1247.3 (C-N), m/z: [$C_{19}H_{31}NO$ + H]$^+$ Calculated: 290.2484 g mol^{-1}, Experimental 290.2490 g mol^{-1}.

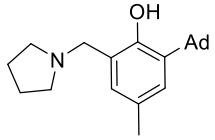

17H : White solid (66%). ^{1}H NMR (400 MHz, 298 K, $CDCl_3$, δ_H, ppm); 6.93 (1H, d, J = 2.9 Hz, Ar*H*), 6.65 (1H, d, J = 2.1 Hz, Ar*H*), 3.75 (2H, s, CH_2), 2.60 (4H, m, NCH_2), 2.24 (3H, s, CH_3), 2.16 (6H, d, J = 3.2, CH_2), 2.07 (3H, m, C*H*), 1.84 (4H, m, CH_2), 1.79 (6H, d, J = 2.9, CH_2) OH signal not observed; ^{13}C{^{1}H} NMR (100 MHz, 298 K, $CDCl_3$, δ_C, ppm); 154.8 (*C*-O), 136.2 (Ar), 126.8 (Ar), 126.3 (Ar), 126.1 (Ar), 122.6 (Ar), 59.3 (N*C*H$_2$), 53.2 (N*C*H$_2$), 40.4 (*C*H$_2$), 37.2 (*C*H$_2$) 36.7 (*C*H) 29.2 (*C*H$_2$) 23.6 (*C*H$_2$) 20.7 (*C*H$_3$). FT-IR (cm^{-1}) 3010.4 (C-H, aromatic), 2875.4 (C-H, alkane), 1455.9 (C=C, aromatic), 1344.1 (C-N), 1117.7 (C-O). m/z [$C_{22}H_{31}NO$ + H]$^+$ Calculated: 326.2484 g mol^{-1}, Experimental 326.2498 g mol^{-1}.

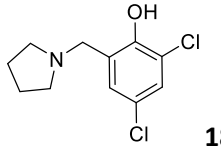

18H : Cream Solid (56%). ^{1}H NMR (400 MHz, 298 K, $CDCl_3$, δ_H, ppm); 9.83 (1H, s, OH), 7.24 (1H, d, J = 2.4 Hz, Ar*H*), 6.86 (1H, d, J = 2.4 Hz, Ar*H*), 3.81 (2H, s, CH_2), 2.66 (4H, m, NCH_2), 1.87 (4H, m, CH_2); ^{13}C{^{1}H} NMR (100 MHz, 298 K, $CDCl_3$, δ_C, ppm); 153.2 (*C*-O), 128.6 (Ar), 126.1 (Ar), 124.5 (Ar), 123.1 (Ar), 121.5 (Ar), 58.5 (N*C*H$_2$), 53.6 (N*C*H$_2$), 23.81 (*C*H$_2$). FT-IR (cm^{-1}) 3080.2 (C-H, aromatic), 2806.8 (C-H, alkane), 1455.9 (C=C, aromatic), 1259.5 (C-N), 795.51 (C-Cl, stretch). m/z [$C_{11}H_{13}Cl_2NO$ + H]$^+$ Calculated: 246.0453 g mol^{-1}, Experimental 246.0465 g mol^{-1}.

6.4.5. General Procedure for the synthesis of 19H

2-(bromomethyl)-4-nitrophenol (3.0 g, 13 mmol) was added to a stirred solution of pyrrolidine (1 mL, 13 mmol) and triethylamine (1.5 mL, 13 mmol) in THF (30 mL) and heated to reflux for 3 hours. Upon cooling the yellow precipitate was filtered off and washed with THF (2 × 20 mL). *In-vacuo* removal of solvent from the filtrate yielded a brown oil which was recrystallized twice from methanol. (63%, 8.1 mmol).[20]

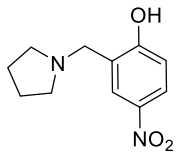

19H - Orange solid (8.1 mmol, 63%). ^{1}H NMR (400 MHz, 298 K, $CDCl_3$, δ_H, ppm); 9.29 (1H, s, OH), 8.08 (1H, dd, J = 2.8 Hz, J = 9.0 Hz, Ar*H*), 7.93 (1H, d, J = 2.8 Hz, Ar*H*), 6.80 – 6.83 (1H, d, J = 9.0 Hz, Ar*H*), 3.91 (2H, s, NCH_2), 2.70 (4H, m, NCH_2), 1.88 – 1.91 (4H, m, CH_2), ^{13}C{^{1}H} NMR (100 MHz, 298 K, C_6D_6, δ_C, ppm); 165.2 (*C*-O), 139.6 (Ar), 125.2 (Ar), 124.0 (Ar), 122.0 (Ar), 116.3 (Ar), 58.2 (NCH_2), 53.3 (NCH_2), 23.6 (CH_2). FT-IR (cm^{-1}) 2995 (C-H, Ar), 1593.3 (N-O), 1423 (C=C, Ar), 1357.1 (C-N), 1263.6 (N-O) 1087.1 (C-O). m/z $[C_{11}H_{14}N_2O_3 + H]^+$ Calculated: 223.1083 g mol^{-1}, Experimental 223.1077 g mol^{-1}.

6.5. Complex Synthesis and characterisation

6.5.1. Synthesis of M(L)X complexes (M = Ga, In)

Ligand (**1**H_2 or **2**H_2) (2.6 mmol) dissolved in THF (10 mL) was added dropwise to a stirred suspension of potassium hydride (5.2 mmol) in THF (10 mL) and stirred for 16 hours. The solution was then cooled to -78 °C and a solution of $GaCl_3$/$InCl_3$ (2.6 mmol) in anhydrous THF (10 mL) was added dropwise and after complete addition, the solution was left to stir for 2 hours more. After this time, the solvent was removed and the white powder which was solubilised in chloroform and filtered through celite. The supernatant was collected and removal of solvent yielding the crude product which was then purified. Washing with hexane yielded a white solid which was recrystallised in a toluene/hexane mixture

6.5.2. Synthesis of Al(L)Cl complexes

To a stirred solution of Ligand (**1**H_2 or **2**H_2) (2.6 mmol) in toluene (10 mL) at -78 °C, diethylaluminium chloride 1.0M in hexanes (1.742 mL, 1.73 mmol) was added dropwise. The solution was then warmed up to 25 °C and stirred for 1 hour. *In vacuo* removal of the solvent, washing with hexanes and recrystallization in a hexane/toluene mixture yielded a white crystalline solid.

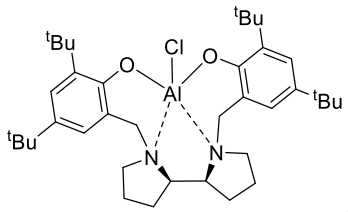

Al(**2**)Cl: White solid (0.6 g, 0.94 mmol, 55%). ^{1}H-NMR (400 MHz, 298 K, $CDCl_3$, δ_H, ppm); 7.23 (s, 2H, Ar), 6.73 (s, 2H; Ar), 4.45 (m, 2H, C*H*H), 3.32 (m, 6H; NC*H*), 2.84 (m, 2H, CH*H*) 2.17 (m, 2H, CH_2N), 1.98 (m, 2H, CH_2N), 1.86 (m, 2H, C*H*H), 1.42 (s, 18H, C$(CH_3)_3$)) 1.24 (s, 18H, C$(CH_3)_3$)); ^{13}C{^{1}H} NMR (100 MHz, $CDCl_3$, δ_C, ppm); 156.2 (*C*-O), 138.4 (Ar), 138.1 (Ar), 124.4 (*C*-H, Ar), 123.2 (*C*-H, Ar), 120.4 (Ar), 67.8 (N*C*H), 62.3 (N*C*H_2), 54.5 (N*C*H_2), 35.3 (*C*$(CH_3)_3$), 34.3 (*C*$(CH_3)_3$), 32.1 (C(*C*$H_3)_3$), 30.1 (C(*C*$H_3)_3$, 27.0 (*C*H_2), 21.8 (*C*H_2). Elemental Analysis (CHN), (Calculated; $C_{38}H_{58}AlClN_2O_2$) C: 71.61%, H: 9.17%, N: 4.39% (Experimental) C: 69.17 %, H: 9.12%, N: 4.31%.

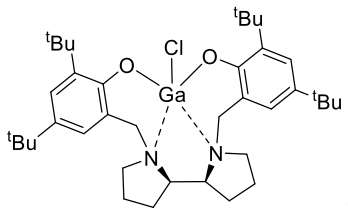

Ga(**2**)Cl: White solid (0.93g, 1.37 mmol, 53%). ^{1}H-NMR (400MHz, 298 K, $CDCl_3$, δ_H, ppm); 7.28 (s, 2H, Ar), 6.77 (s, 2H, Ar), 4.66 (d, 2H, J = 12.2 Hz, NC*H*HC), 3.75 (d, 2H, J = 2.5 Hz, NC*H*), 3.36 (d, 2H, J = 12.2 Hz, NCH*H*C) 2.92 (4H, m, CH_2N), 2.27 (m, 2H, C*H*H), 2.03 (m, 4H, CH_2), 1.90 (m, 2H, CH*H*), 1.48 (s, 18H, ^{t}Bu) 1.28 (s, 18H, ^{t}Bu); ^{13}C{^{1}H} (100 MHz, 298 K, $CDCl_3$, δ_C, ppm); 158.5 (*C*-O), 139.2 (Ar), 137.9 (Ar), 124.7 (*C*-H, Ar), 123.8 (*C*-H, Ar), 119.9 (Ar), 68.3 (N*C*H), 67.2 (N*C*H), 62.6 (N*C*H_2), 54.2 (N*C*H_2), 35.5 (*C*$(CH_3)_3$), 34.4 (*C*$(CH_3)_3$), 32.2 (C(*C*$H_3)_3$), 30.2 (C(*C*$H_3)_3$, 26.9 (*C*H_2), 26.0 (*C*H_2), 21.5 (*C*H_2). Elemental Analysis (CHN), (Calculated; $C_{38}H_{58}GaClN_2O_2$) C: 67.11%, H: 8.60%, N: 4.12% (Experimental) C: 66.57%, H: 8.12%, N: 4.21%.

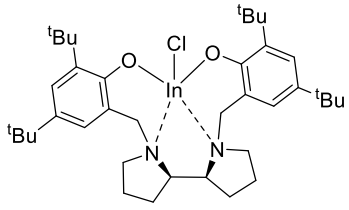

In(**2**)Cl: (1.61 g, 2.22 mmol, 85%). ^{1}H-NMR (400 MHz, $CDCl_3$, δ_H, ppm); 7.30 (s, 2H; ArH), 6.76 (s, 2H; ArH), 4.73 (d, 12.7 Hz, 2H, NC*H*HC), 3.41 (d, 2H, 2.5 Hz; NC*H*), 3.34 (d, 2H, 12.7 Hz; NCH*H*C) 3.10 (m, 2H; C*H*$_2$N), 3.00 (m, 2H; C*H*$_2$N), 2.31 (m, 2H; C*H*H), 2.03 (m, 4H; C*H*$_2$), 1.90 (m, 2H; CH*H*), 1.50 (s, 18H; C(CH_3)$_3$)) 1.28 (s, 18H; C(CH_3)$_3$)); ^{13}C-NMR (100 MHz, $CDCl_3$, δ_C, ppm); 159.5 (*C*-O), 138.5 (Ar), 136.2 (Ar), 123.9 (*C*-H, Ar), 123.8 (*C*-H, Ar), 118.8 (Ar), 66.1 (N*C*H), 61.6 (N*C*H$_2$), 52.4 (N*C*H$_2$), 34.2 (*C*(CH_3)$_3$), 32.9 (*C*(CH_3)$_3$), 30.8 (C(*C*H_3)$_3$), 28.7 (C(*C*H_3)$_3$, 25.3 (*C*H$_2$), 20.1 (*C*H$_2$). Elemental Analysis (CHN), (Calculated $C_{38}H_{58}InClN_2O_2$) C: 62.94%, H: 8.06%, N: 3.86% (Experimental) C: 63.01 %, H: 8.08%, N: 3.86%.

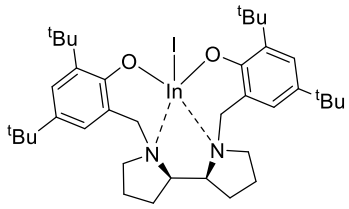

In(**2**)I: (345 mg, 0.42 mmol, 42%).^{1}H-NMR (400 MHz, $CDCl_3$, 253 K, δ_H, ppm); 7.29 (s, 2H; ArH), 6.76 (s, 2H; ArH), 4.76 (d, 12.7 Hz, 2H; NC*H*HC), 3.53 (d, 2.5 Hz 2H; NC*H*), 3.34 (d, 12.7 Hz, 2H; NCH*H*C) 3.10 (m, 2H; C*H*$_2$N), 2.97 (m, 2H; C*H*$_2$N), 2.31 (m, 2H; C*H*H), 1.99 (m, 4H; C*H*$_2$), 1.90 (m, 2H; CH*H*), 1.50 (s, 18H, (C(*C*H_3)$_3$), 1.28 (s, 18H, (C(*C*H_3)$_3$). ^{13}C-NMR (100 MHz, $CDCl_3$, 298 K, δ_C, ppm); 139.49 (Ar), 125.2 (Ar), 67.5 (N*C*H), 54.16 (N*C*H$_2$), 52.4 (N*C*H$_2$), 35.3 (*C*(CH_3)$_3$), 34.3 (*C*(CH_3)$_3$), 32.1 (C(*C*H_3)$_3$), 30.4 (C(*C*H_3)$_3$, 27.0 (*C*H$_2$), 20.9 (*C*H$_2$). Elemental Analysis (CHN), (Calculated $C_{38}H_{58}InIN_2O_2$) C: 55.89%, H: 7.16%, N: 3.43% (Experimental) C: 56.05 %, H: 7.19%, N: 3.42%.

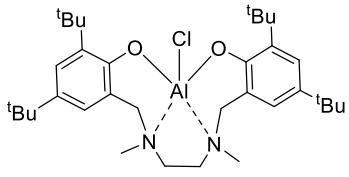

Al(**10**)Cl:(680 mg, 1.16 mmol, 61%). ^{1}H-NMR (400MHz, $CDCl_3$, δ_H, ppm): (*Major Series*) 7.30 (s, 2H, Ar), 6.81 (s, 2H, Ar), 4.52-4.49 (d, 12.4 Hz, 2H, CH*H*N), 3.20 (d, 12.4 Hz, 2H, C*H*HN), 2.98 (m, 4H, NC*H*$_2$), 2.44 (s, 6H, NC*H*$_3$), 1.47 (s, 18H, ^{t}Bu), 1.29 (s, 18H, ^{t}Bu), Due to significant overlap in tBu, Ar region full assignment of minor series is not possible. But it is clear from the NMR below. ^{13}C-NMR (100 MHz, $CDCl_3$, δ_C, ppm): 155.7 (*C*-O), 138.6 (Ar), 138.4 (Ar), 124.5 (Ar), 123.3 (Ar), 119.7 (Ar), 63.0 (*C*H$_2$N), 55.2 (*C*H$_2$N), 45.6 (N*C*H$_3$), 35.5 (*C*(CH_3)$_3$), 34.2 (*C*(CH_3)$_3$), 32.0 (C(*C*H_3)$_3$), 30.1 (C(*C*H_3)$_3$). Elemental Analysis (CHN):

(Calculated $C_{34}H_{54}AlClN_2O_2$) C: 69.77%, H: 9.30%, N: 4.79% (Experimental) C: 67.57%, H: 9.50%, N: 4.75%.

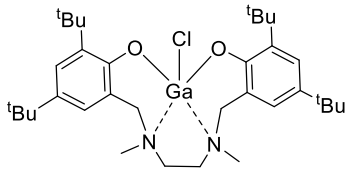

Ga(**10**)Cl: (565 mg, 0.9 mmol, 49%). ^{1}H-NMR (400 MHz, $CDCl_3$, δ_H, ppm): 7.31 (s, 2H, Ar), 6.80 (s, 2H, Ar), 4.71-4.68 (d, 12.1 Hz, 2H, C*H*HN), 3.25-3.22 (d, 12.1 Hz, 2H, CH*H*N), 3.16 (m, 2H, CH_2N), 2.95 (m, 2H, CH_2N), 2.42 (s, 6 H, CH_3), 1.51 (s, 18H, ^{t}Bu), 1.28 (s, 18H, ^{t}Bu); ^{13}C-NMR (100 MHz, $CDCl_3$, δ_C, ppm): 158.0 (*C*-O), 139.3 (Ar), 138.6 (Ar), 124.8 (Ar), 124.1 (Ar), 199.8 (Ar), 63.4 (*C*H_2N), 55.1 (*C*H_2N), 45.0 (N*C*H_3), 35.5 (*C*(CH$_3$)$_3$), 34.2 (*C*(CH$_3$)$_3$), 32.0 (C(*C*H$_3$)$_3$), 30.2 (C(*C*H$_3$)$_3$). Elemental Analysis (CHN): (Calculated $C_{34}H_{54}GaClN_2O_2$) C: 65.03%, H: 8.67%, N: 4.46% (Experimental) C: 64.92%, H: 8.80%, N: 4.57%.

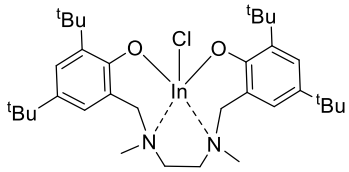

In(**10**)Cl: (790 mg, 1.18 mmol, 43%). ^{1}H-NMR (400 MHz, $CDCl_3$, δ_H, ppm): 7.31 (d, 2.5 Hz, 2H, Ar), 6.78 (d, 2.5 Hz, 2H, Ar), 4.81 (d, 11.8 Hz, 2H, CH*H*N), 3.20 (d, 11.83 Hz, 4H, C*H*HN), 2.93 (m, 2H, NCH*H*C), 2.40 (s, 6H, NCH_3), 1.53 (s, 18H, ^{t}Bu), 1.28 (s, 18H, ^{t}Bu); ^{13}C-NMR (100 MHz, $CDCl_3$, δ_C, ppm): 160.5 (*C*-O), 139.8 (Ar), 138.3 (Ar), 129.3 (Ar), 128.4 (Ar), 64.3 (*C*H_2N), 55.4 (*C*H_2N), 43.8 (N*C*H_3), 35.2 (*C*(CH$_3$)$_3$), 33.9 (*C*(CH$_3$)$_3$), 31.7 (C(*C*H$_3$)$_3$), 29.9 (C(*C*H$_3$)$_3$). Elemental Analysis (CHN), (Calculated $C_{34}H_{54}InClN_2O_2$) C: 60.67 %, H: 8.09%, N: 4.16%, (Experimental) C: 60.71 %, H: 8.14%, N: 4.16%.

6.5.3. Synthesis of $\{In_2(2)_2OEt(OH)\}$ and $\{In(7)OH\}_2$

NaOEt (2.4 mmol) in toluene (10 mL) was added dropwise to a stirred solution of In(**1**)Cl (0.44 mmol) in toluene (20 mL), the solution was then stirred for 16 hours. Filtration of the supernatant and *in vacuo* removal of the solvent yielded an orange precipitate which was recrystallised in hexane (2 mL).

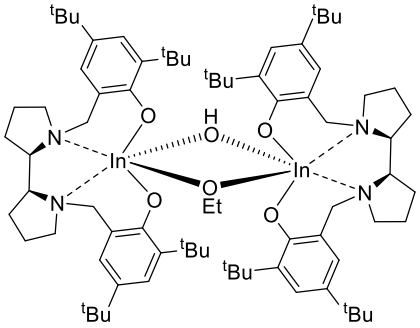

$\{In_2(\mathbf{2})_2OEt(OH)\}$: White powder (155 mg, 0.21 mmol, 8%). Assignation of ^{1}H-NMR peaks was not possible due to fluxionality in spectra with poor resolution in resonances. Low temperature ^{1}H NMR experiments in toluene-d_8 were not successful in resolving the resonances. Elemental (CHN) Analysis (Calculated $C_{78}H_{122}In_2N_4O_6$); C: 64.99 %, H: 8.53 %, N: 3.89 %, (Experimental); C: 62.23 %, H: 8.19 %, N: 3.71 %.

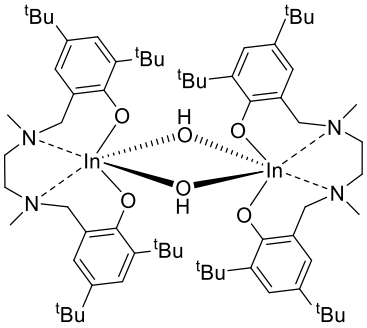

$\{In(\mathbf{7})OH\}_2$: White Powder (67 mg, 0.05 mmol, 15%). ^{1}H-NMR (400 MHz, 298 K, C_6D_6, δ_H, ppm): 7.76 (1H, d, J = 2.4 Hz, Ar), 7.59 (1H, d, J = 2.8 Hz, Ar), 7.57 (1H, d, J = 2.4 Hz, Ar), 7.48 (1H, d, J = 2.8 Hz, Ar), 7.04 (1H, d, J = 2.5 Hz, Ar), 6.74 (1H, d, J = 2.5 Hz, Ar), 6.69 (1H, d, J = 2.7 Hz, Ar), 6.61 (1H, d, J = 2.7 Hz, Ar), 5.35 – 5.37 (1H, d, J = 13.0 Hz, CH*H*), 5.29 – 5.32 (1H, d, J = 12.6 Hz, CH*H*), 5.00 – 5.04 (1H, d, J = 13.0 Hz, CH*H*), 3.22 (3H, s, CH_3), 3.04 – 3.10 (2H, td, J = 5.7 Hz, J = 12.6 Hz, CH), 3.07 (2H, dd, J = 5.7 Hz, J = 12.6 Hz, CH) 2.99 – 3.02 (1H, d, J = 12.6 Hz, CH*H*), 2.90 – 2.93 (1H, d, J = 12.6 Hz, CH*H*), 2.76 – 2.83 (2H, td, J = 3.1 Hz, J = 12.9 Hz, CH), 2.74 (3H, s, CH_3), 2.69 – 2.73 (2H, d, J = 12.6 Hz, CH*H*), 2.26 – 2.33 (2H, td, J = 3.1 Hz, J = 12.9 Hz, CH*H*), 1.96 (6H, s, CH_3), 1.92 (9H, s, CH_3), 1.69 (9H, s, CH_3), 1.43 (18H, s, CH_3), 1.30 (18H, s, CH_3). $^{13}C\{^1H\}$-NMR (100 MHz, , 298 K, $CDCl_3$, δ_C, ppm); 161.1 (*C*-O), 155.1 (*C*-O), 141.5 (Ar), 141.1 (Ar), 139.7 (Ar), 139.5 (Ar), 128.8 (Ar), 128.6 (Ar), 125.1 (Ar), 124.6 (Ar), 122.1 (Ar), 121.0 (Ar), 46.1 (NCH_2), 45.7 (NCH_2), 37.1 (N*C*H_2), 36.9

(N*C*H$_2$), 36.8 (N*C*H$_2$), 36.5 (N*C*H$_2$), 31.4 (*C*(CH$_3$)$_3$), 31.4 (*C*(*C*H$_3$)$_3$), 31.0 (C(*C*H$_3$)$_3$), 29.2 (C(*C*H$_3$)$_3$), 29.0 (C(*C*H$_3$)$_3$) 11.8 (N*C*H$_3$); 10.5 (N*C*H$_3$) Elemental (CHN) analysis (Calculated $C_{68}H_{110}In_2N_4O_6$); C: 62.38 %, H: 8.47 %, N: 4.28 %, (Experimental); C: 61.55 %, H: 8.21 %, N: 4.24 %.

6.5.4. Synthesis of indium salalen complexes

In air, InCl$_3$ (0.76mmol) was added to a solution of **12**H$_2$ (0.76 mmol) and triethylamine (0.74 mL, 1.52 mmol) in ethanol (60 mL) and the solution was heated to reflux. After 4 hours an white precipitate was present in the orange solution. The supernatant was collected and the solvent was removed *in vacuo*, yielding the crude product. The precipitate was solubilised in a hexane:toluene:DCM mixture (25:30:5) and the product was collected as crystals after 2 weeks at -20 °C, (650 mg, 0.59 mmol, 24% yield)

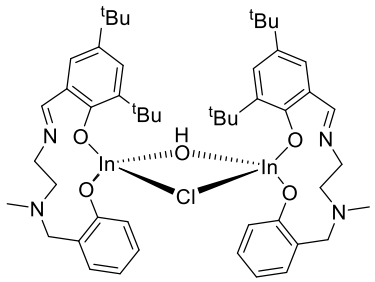

{In$_2$(**12**)$_2$OHCl}: Orange solid (650 mg, 0.59 mmol, 24% yield). ^{1}H-NMR (400 MHz, 298 K, CDCl$_3$, δ_H, ppm); 7.93 (2H, s, C*H*N), 7.17 – 7.22 (2H, td, J = 8.6 Hz, J = 2.0 Hz, Ar), 7.14 (2H, d, J = 2.4 Hz ,Ar), 6.96 – 6.98 (2H, dd, J= 7.9 Hz, J = 2.0 Hz, Ar), 6.79 (2H, d, J = 2.4 Hz, Ar), 6.71 – 6.73 (2H, d, J = 8.6 Hz, Ar), 6.50 – 6.54 (2H, t, J = 7.9 Hz, Ar) 4.35 (2H, d, J = 11.5 Hz, NC*H*), 3.68 (2H, d, J = 11.5 Hz, NC*H*), 3.21 – 3.57 (4H, m, NC*H$_2$*), 2.13 – 2.57 (4H, m, NC*H$_2$*), 3.02 (1H, s, OH), 2.81 (6H, s, CH$_3$), 1.24 (18H, s, ^{t}Bu), 1.12 (18H, s, ^{t}Bu). ^{13}C{^{1}H}-NMR (100 MHz, 298 K, CDCl$_3$, δ_C, ppm); 175.1 (*C*-O), 170.1 (*C*-O), 168.0 (H*C*N), 134.3 (Ar), 134.0 (Ar), 127.9 (Ar), 127.7 (Ar), 124.4 (Ar), 124.1 (Ar), 124.0 (Ar), 122.3 (Ar), 122.1 (Ar), 120.1 (Ar), 62.4 (N*C*H$_2$), 58.5 (NCH$_2$), 51.4 (NCH$_2$), 43.6 (N*C*H$_3$) 31.7 (C(*C*H$_3$)$_3$), 31.0 (C(*C*H$_3$)$_3$), 15.9 (*C*(CH$_3$)$_3$), 13.0 (*C*(CH$_3$)$_3$).); Elemental (CHN) Analysis (Calculated $C_{50}H_{70}ClIn_2N_4O_5$); C: 56.01 %, H: 6.58 %, N: 5.23 %, (Experimental); C: 57.8 %, H: 6.89 %, N: 5.26 %.

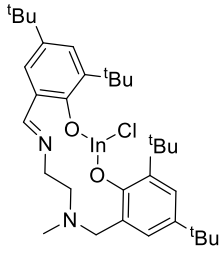

In(**13**)Cl: Orange solid (352 mg, 0.54 mmol, 32%) ^{1}H-NMR (400 MHz, 298 K, $CDCl_3$, δ_H, ppm); 8.38 (1H, s, C*H*N), 7.51 (1H, s, Ar), 7.31 (1H, s, Ar), 6.87 (1H, s, Ar), 6.84 (1H, s, Ar), 4.53 (1H, d, 11.8 Hz, C*H*HN), 3.83 (2H, t, 5.47 Hz, NCH_2), 3.32 (1H, d, 11.8 Hz, CH*H*N), 3.03 (2H, t, 5.47 Hz, NCH_2), 2.48 (3H, s, NCH_3), 1.49 (18H, s, (CH_3)$_3$), 1.28 (18H, s, (CH_3)$_3$). ^{13}C{H}-NMR (100 MHz, 298 K, $CDCl_3$, δ_C, ppm); 175.1 (*C*-O), 172.1 (*C*-O), 168.0 (H*C*N), 138.2 (Ar), 132.2 (Ar), 129.1 (Ar), 128.8 (Ar), 128.7 (Ar), 125.3 (Ar), 124.8 (Ar), 62.4 (*C*H_2N), 58.3 (NCH_2), 51.4 (N*C*H_2), 43.6 (NCH_3) 31.6 (C(*C*H_3)$_3$), 31.1 (C(*C*H_3)$_3$), 29.7 (C(*C*H_3)$_3$), 29.3 (C(*C*H_3)$_3$). 16.1 (*C*(*C*H_3)$_3$), 13.3 (C(*C*H_3)$_3$); Elemental (CHN) Analysis (Calculated $C_{33}H_{50}ClInN_2O_2$); C: 60.33 %, H: 7.67 %, N: 4.26 %, (Experimental); C: 61.57 %, H: 7.91 %, N: 4.13 %.

6.5.5. Synthesis of {Ln(L)O^{i}Pr}$_2$ and {Ln$_2$(L)$_2$O^{i}PrOH}

In a typical experiment: **2**H_2 (576 mg, 1.0 mmol) was dissolved in toluene (5 mL) was added to a stirred solution of Nd(O^{i}Pr)$_3$ (1.0 mmol) in toluene (10 mL). The solution was then heated to 60 °C and left to stir for 3 hours. After this time the solvent was removed and the solid was dissolved in the minimum quantity of dry hexane/toluene and left to recrystallise at -20 °C. The crystalline material was washed with cold hexane (3 x 1 mL) and dried under a vacuum. Where possible ^{1}H NMR and ^{13}C{^{1}H} NMR and ^{1}H DOSY spectra were collected for analysis. Otherwise each single crystal XRD and CHN microanalysis was used for characterisation.

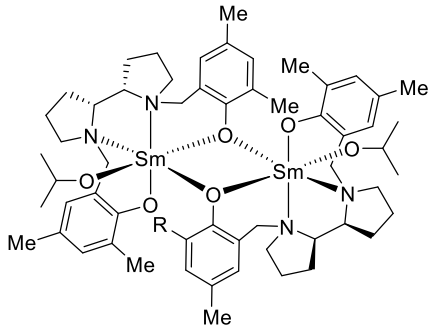

{Sm(**1**)O^{i}Pr}$_2$: White solid (310 mg, 51% yield). ^{1}H NMR (500 MHz, $CDCl_3$, δ_H, ppm); 7.92 (2H, Ar*H*), 7.43 (2H, Ar*H*), 6.90 (2H, Ar*H*), 6.25 (2H, d, J = 12.5 Hz, C*H*H), 6.18 (2H, OC*H*(CH$_3$)$_2$), *6*.01 (6H, CH_3), 5.21 (2H, C*H*H), 4.8 (2H, Ar*H*), 2.83 (2H, d, J = 12.5 Hz, CH*H*), 2.50 (6H, CH_3), 2.05 - 2.32 (12H, OCH(CH_3)$_2$), 2.00 (6H, CH_3), 1.88 (2H, CH*H*),

0.72 (4H, CH_2), 0.2 (6H, CH_3), -0.04 (2H, C*H*), -0.33 (2H, C*H*), -0.33 (2H, C*H*), -0.69 (4H, CH_2), -1.02 (4H, CH_2), -1.53 (2H, C*H*), -2.45 (2H, C*H*), -2.70 (2H, C*H*), -4.07 (2H, C*H*), -4.56 (2H, C*H*). 2D DOSY (500 MHz, $CDCl_3$ D_{sol}= 1.77x10^{-9} m^2s^{-1}, 298 K,) 5.89 x10^{-10} m^2s^{-1}. Elemental (CHN) Analysis; (Calculated: $C_{58}H_{82}N_4O_6Sm_2$) C: 56.54%, H: 6.71%, N: 4.55%, (Experimental) C: 56.70%, H: 6.81%, N: 4.46%.

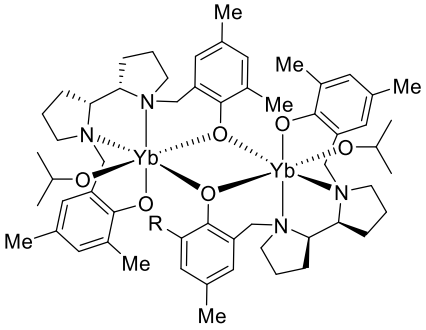

{Yb(**1**)O^{i}Pr}$_2$: White solid (298 mg, 47% yield). Elemental (CHN) Analysis; (Calculated: $C_{58}H_{82}N_4O_6Yb_2$) C: 54.53%, H: 6.47%, N: 4.39%, (Experimental) C: 54.16%, H: 6.59%, N: 4.34%.

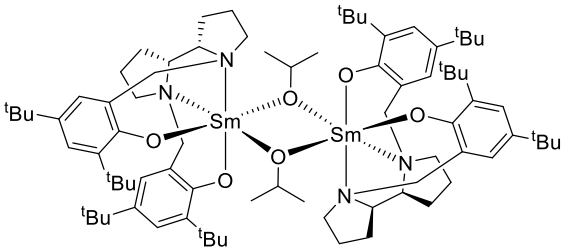

{Sm(**2**)O^{i}Pr}$_2$: White solid (55 mg, 7% yield). (Elemental (CHN) Analysis; (Calculated: $C_{82}H_{130}N_4O_6Sm_2$) C: 62.79%, H: 8.35%, N: 3.57%, (Experimental) C: 63.41%, H: 8.79%, N: 3.61%.

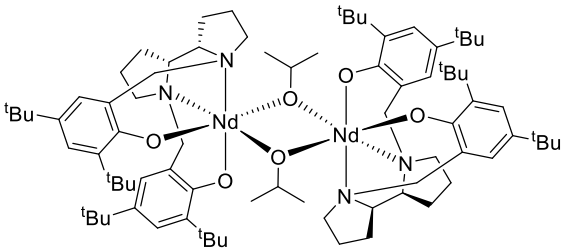

{Nd(**2**)O^{i}Pr}$_2$: Blue solid (680 mg, 86% yield). Elemental (CHN) Analysis; (Calculated: $C_{82}H_{130}N_4O_6Nd_2$) C 63.2 %, H: 8.42%, N: 3.60%, (Experimental) C: 62.74%, H: 8.16%, N: 3.62%.

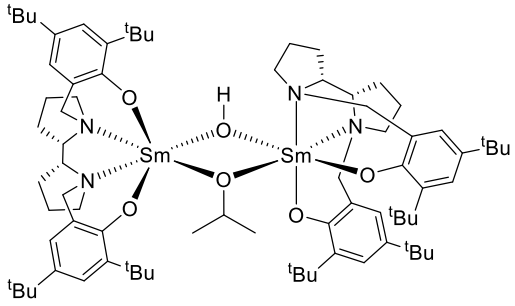

{Sm_2(**2**)$_2$(O^iPr)(OH)}: White solid (530 mg, 69% yield) (Elemental (CHN) Analysis; (Calculated: $C_{79}H_{124}N_4O_6Sm_2$) C: 62.16%, H: 8.19%, N: 3.67%, (Experimental) C: 61.66%, H: 8.15%, N: 3.68%.

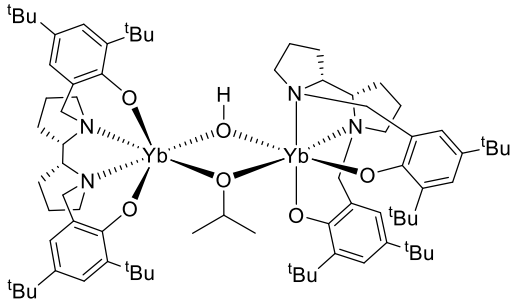

{Yb_2(**2**)$_2$(O^iPr)(OH)}: White solid (180 mg, 23% yield). Elemental (CHN) Analysis; (Calculated: $C_{79}H_{124}N_4O_6Yb_2$) C: 60.36%, H: 7.95%, N: 3.56%, (Experimental) C: 59.72%, H: 7.64%, N: 3.57%.

6.5.6. Synthesis of {Sm(2)OH}$_2$ complexes

De-ionised water (23 µL, 1.3 mmol) was added to a solution of {Sm_2(**2**)$_2$(O^iPr)(OH)} (0.13 mmol) in anhydrous toluene (3 mL). After an hour of stirring the solvent was removed *in vacuo* and the resultant solid as recrystallised in hot anhydrous hexane (2 mL). Over the course of 1 week at -20 °C crystalline product was yielded and washed with cold hexane (3 × 0.5 mL).

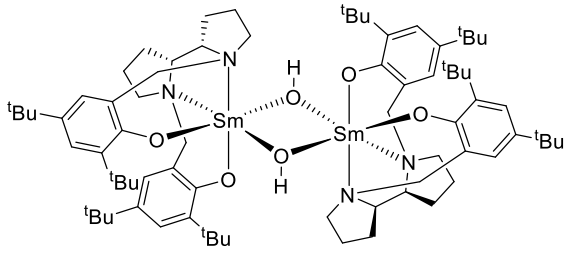

{Sm(**2**)OH}$_2$}: White solid (90 mg, 46%) ^{1}H NMR (500 MHz, $CDCl_3$, δ_H, ppm); 22.36 (1H, SmO*H*), 8.28 (2H, Ar*H*), 8.05 (2H, Ar*H*), 6.63 (2H, CH*H*), 3.14 (4H, NCH_2), 2.87 (2H, C*H*H), 1.93 (18H, (C(CH_3)$_3$)), 0.54 (18H, (C(CH_3)$_3$)), -0.85 (2H, CH_2), -2.04 (2H, CH_2), -3.02 (2H, CH_2), -4.48 (2H, CH_2), -7.22 (2H, CH_2); ^{13}C{^{1}H} NMR (100 MHz, $CDCl_3$, δ_C, ppm); 172.4 (*C*-O), 137.1 (Ar), 135.7 (Ar), 128.4 (Ar), 127.8 (Ar), 126.0 (Ar), 66.6

(NCH), 59.6 (NCH$_2$), 52.8 (NCH$_2$), 36.0 (*C*(CH$_3$)$_3$), 35.2 (*C*(CH$_3$)$_3$), 32.6 (C(*C*H$_3$)$_3$), 29.6 (C(*C*H$_3$)$_3$), 22.8 (*C*H)$_2$, 18.7 (*C*H)$_2$, 16.8 (*C*H)$_2$, 14.3 (*C*H)$_2$. 2D DOSY (500 MHz, 298 K, $CDCl_3$) , D_{sol} = 2.09 × 10^{-9} m^2 s^{-1}, D = 4.69 × 10^{-10} m^2 s^{-1}). Elemental (CHN) Analysis, (Calculated: $C_{76}H_{118}N_4O_6Sm_2$) C: 61.49 %, H: 8.01 %, N 3.77 %, (Experimental) C: 60.96 %, H 7.77 %, N 3.74 %.

6.5.7. Hydrolytic degradation of {Sm(1)O^{i}Pr}$_2$

Hydrolysis reactions were carried out by exposing a J-Youngs tube solution of {Ln(**1/2**)O^{i}Pr}$_2$ in $CDCl_3$ to a flow of compressed air through the solution via a needle for 30 minutes. The vessel was sealed and monitored via ^{1}H NMR spectroscopy periodically. Once degradation of the sample was complete ^{13}C{^{1}H} NMR and DOSY spectra were collected. *In vacuo r*emoval of the solvent followed by washing in cold hexane (3 × 0.5 mL) yielded the degraded product.

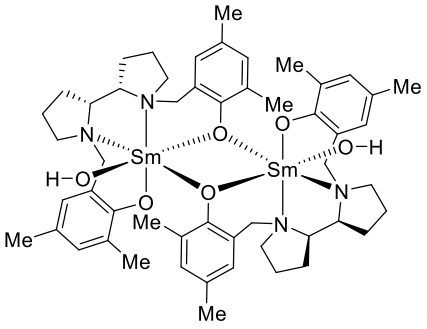

{Sm(**2**)OH}$_2$: White solid (50 mg, 56%) ^{1}H NMR (500 MHz, 298 K, $CDCl_3$, δ_H, ppm); 8.72 (2H, Ar), 7.11 (2H, Ar), 7.05 (2H, Ar), 5.92 (4H, NC*H*$_2$), 4.86 (2H, Ar), 3.36 (2H, NC*H*$_2$), 2.95 (4H, C*H*$_2$), 2.74 (4H, C*H*$_2$), 2.47 (4H, C*H*$_2$), 2.34 (6H, C*H*$_3$), 2.30 (4H, C*H*$_2$), 1.90 (6H, C*H*$_3$), 1.48 (4H, C*H*$_2$), 1.27 (4H, C*H*$_2$), 1.23 (6H, C*H*$_3$), 0.42 (6H, C*H*$_3$), -1.34 (4H, C*H*$_2$), -2.36 (4H, C*H*$_2$); ^{13}C{^{1}H} NMR (100 MHz, 298 K, $CDCl_3$, δ_C, ppm); 164.3 (*C*-O), 134.1 (Ar), 134.0 (Ar), 128.4 (Ar), 127.8 (Ar), 126.5 (Ar), 66.4 (N*C*H), 57.5 (NCH$_2$), 52.9 (NCH$_2$), 38.6 (*C*H$_3$), 35.2 (*C*H$_3$), 35.0 *C*H$_3$), 32.01 (*C*H$_3$), 18.8 (*C*H)$_2$, 14.3 (*C*H)$_2$. 2D DOSY (500 MHz, 298 K, $CDCl_3$) D_{sol} = 1.83 × 10^{-9} m^2 s^{-1}, D = 5.93 × 10^{-10} m^2 s^{-1}.

6.5.8. Synthesis of Al(L)$_2$Me complexes

A solution of $AlMe_3$ (2M) in hexane (0.5 mL, 1 mmol) was added dropwise to an ice-cold solution of **14**H (2 mmol) in toluene (10 mL). Upon addition the solution was warmed to 20 °C and left to stir. After 30 minutes the solvent was removed *in vacuo* and the crude product was washed with hexane (3 x 2 mL). The precipitate was dissolved in a hot hexane:toluene mixture. Crystalline products were isolated at -20 °C after 7 days (292 mg, 0.65 mmol, 65%).

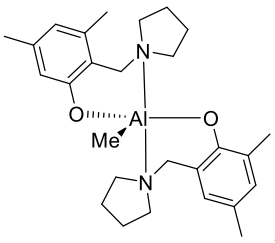

Al(**16**)$_2$Me: White solid (292 mg, 0.65 mmol, 65%). Fluxional at 298 K, Low temperature NMR did not provide complete structural clarity. ^{1}H NMR (400 MHz, 298 K, C_6D_6, δ_H, ppm, 298 K); 7.02 (2H, d, J = 2.0 Hz, Ar*H*), 6.52 (2H, d, J = 2.1 Hz, Ar*H*), 3.89 (2H, m, NCH_2), 3.48 (2H, m, NCH_2), 2.94 (8H, m, NCH_2), 2.35 (6H, s, CH_3), 2.29 (6H, s, CH_3), 1.41 (8H, m, CH_2) -0.51 (6H, s, CH_3). ^{13}C{^{1}H} NMR (100 MHz, 298 K, C_6D_6, δ_C, ppm); 156.9 (*C*-O), 131.3 (Ar), 127.9 (Ar), 127.0 (Ar), 124.9 (Ar), 122.6 (Ar), 77.2 (N*C*H$_2$), 58.5 (N*C*H$_2$), 22.8 (*C*H$_2$), 20.7 (*C*H$_3$), 18.2 (*C*H$_2$) -12.1 (*C*H$_3$). Elemental (CHN) Analysis; (Calculated $C_{27}H_{39}N_2O_2Al_1$) C: 71.97%, H: 8.72%, N: 6.22%, (Experimental) C: 71.56%, H: 8.68%, N: 6.14%.

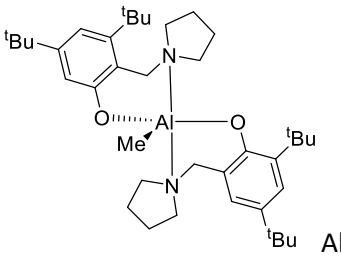

Al(**17**)$_2$Me: White solid (0.26 mmol, 26%). Fluxional at 298 K, Low temperature NMR did not provide complete structural clarity. ^{1}H NMR (400 MHz, 298 K, C_6D_6, δ_H, ppm, 298 K); 7.58 (2H, d, J = 2.7 Hz, Ar*H*), 6.78 (1H, d, J = 2.7 Hz, Ar*H*), 4.91 (2H, m, C*H*H), 3.02 (8H, m, CH_2), 1.71 (18H, s, (C(CH_3)$_3$)), 1.42 (18H, s, (C(CH_3)$_3$)), -0.58 (3H, s, CH$_3$). ^{13}C{^{1}H} NMR (100 MHz, 298 K, C_6D_6, δ_C, ppm); 157.2 (*C*-O), 138.4 (Ar), 137.4 (Ar), 128.6 (Ar), 124.9 (Ar), 123.6 (Ar), 60.0 (N*C*H$_2$), 53.5 (N*C*H$_2$), 35.4 (*C*(CH$_3$)$_3$), 34.2 (*C*(CH$_3$)$_3$), 32.1 (C(*C*H$_3$)$_3$) 30.6 (C(*C*H$_3$)$_3$), 23.1 (*C*H$_2$), 14.3 (*C*H$_2$) -10.71 (*C*H$_3$). Elemental analysis was consistently low on carbon.

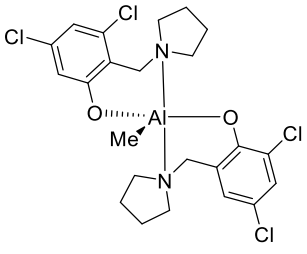

Al(**18**)$_2$Me: Yellow solid (0.64 mmol, 64%). Fluxional at 298 K, high temperature NMR provided enhanced structural clarity. ^{1}H NMR (400 MHz, C_6D_6, 298 K, δ_H, ppm, 353 K); 7.38 (2H, d, J = 2.3 Hz, Ar), 6.52 (2H, d, J = 2.3 Hz, Ar), 3.55 (2H, m, NCH_2), 3.15 (4H, m, NCH_2), 2.79 (4H, m, NCH_2), 1.32 (8H, m, CH_2), -0.69 (3H, s, CH_3), ^{13}C{^{1}H} NMR (100 MHz, C_6D_6, 298 K, δ_C, ppm): 154.7 (*C*-O), 129.0 (Ar), 125.8 (Ar), 125.5 (Ar), 124.5 (Ar), 121.0

(Ar), 57.1 (N*C*H$_2$), 53.1 (N*C*H$_2$), 22.4 (*C*H$_2$), 21.3 (*C*H$_2$), -12.3 (*C*H$_3$). Elemental (CHN) Analysis; (Calculated $C_{23}H_{27}Cl_4N_2O_2Al_1$) C: 51.88%, H: 5.11%, N: 5.26%, (Experimental) C: 51.65%, H: 5.06%, N: 5.03%.

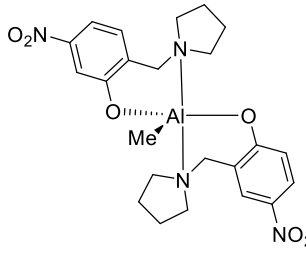

Al(**19**)$_2$Me: Orange solid (0.38 mmol, 38%). ^{1}H NMR (400 MHz, 298 K, C_6D_6, δ_H, ppm, 298 K); 8.12 – 8.15 (2H, dd, J = 3.4 Hz, J = 8.4 Hz, Ar), 7.76 (2H, d, J = 3.4 Hz, Ar), 6.41 – 6.44 (2H, d, J = 8.4 Hz, Ar), 3.12 – 3.22 (4H, m, NC*H*$_2$), 2.43 (8H, m, NC*H*$_2$), 1.31 (8H, m, C*H*$_2$), -0.76 (3H, s, C*H*$_3$). ^{13}C{^{1}H} NMR (100 MHz, 298 K, C_6D_6, δ_C, ppm); 166.3 (*C*-O), 139.3 (Ar), 129.3 (Ar), 126.0 (Ar), 123.5 (Ar), 119.3 (Ar), 58.1 (N*C*H$_2$), 53.7 (N*C*H$_2$), 23.3 (*C*H$_2$), -12.52 (Al-CH$_3$). Elemental (CHN) Analysis; (Calculated $C_{23}H_{29}N_4O_6Al_1$) C: 57.02%, H: 6.03%, N: 11.56%, (Experimental) C: 56.49%, H: 5.92%, N: 10.78%.

6.5.9. Synthesis of B(14)H$_2$ complexes

Pyrrolidine (5 mL, 59.8 mmol) was added to a stirred suspension of benzaldehyde (8.4 mL, 59.8 mmol) in ethanol (50 mL). The red solution was left to stir for 1 hour. $NaBH_4$ (5.7 g, 150 mmol) was added in small portions. The mixture was quenched with water (20 mL), filtered and the solvent was removed *in vacuo*. The resultant solid was extracted from CH_2Cl_2 (30 mL) with 1M HCl (3 × 30 mL), Brine (3 × 30 mL) and H_2O (3 × 30 mL), before being dried with $MgSO_4$. *In vacuo* removal of solvent and recrystallisation in hot hexane yielded the crystalline product upon cooling to room temperature after 5 hours, (8.45 mmol, 98%).

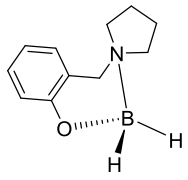

B(**14**)H$_2$: White solid (8.45 mmol, 98%). ^{1}H NMR (400 MHz, 298 K, C_6D_6, δ_H, ppm); 7.23 (1H, d, J = 7.6 Hz, Ar*H*), 7.06 (1H, d, J = 7.5 Hz, Ar*H*), 6.75 – 6.79 (1H, dd, J = 7.5 Hz, J = 7.6 Hz, Ar*H*), 6.64 – 6.67 (1H, d, J = 7.5 Hz, Ar*H*), 4.28 (1H, s, B*H*), 3.32 (2H, s, NC*H*$_2$), 2.94 (2H, m, NC*H*$_2$), 1.89 (2H, m, C*H*$_2$), 1.43 (2H, m, C*H*$_2$), 1.08 (2H, m, C*H*$_2$), ^{13}C{^{1}H} NMR (100 MHz, 298 K, C_6D_6, δ_C, ppm); 156.1 (*C*-O), 129.4 (Ar), 127.3 (Ar), 125.5 (Ar), 119.6 (Ar), 117.8 (Ar), 62.1 (N*C*H$_2$), 56.4 (N*C*H$_2$), 22.7 (*C*H$_2$). ^{11}B NMR (100 MHz, 298 K, C_6D_6, δ_B, ppm) 0.72 – 2.15 (t, J = 282 Hz, *B*(**X**)H$_2$). Elemental (CHN) Analysis; (Calculated $C_{11}H_{16}BNO$) C: 69.88%, H: 8.53%, N: 7.41%, (Experimental) C: 71.02%, H: 6.13%, N: 7.45%.

6.5.10. Synthesis of Al(L)Me_2 complexes

A solution of 2 M $AlMe_3$ in hexane (1 mL, 2 mmol) was added dropwise to an ice-cold solution of toluene (8 mL). To this solution **14**H (2 mmol) in toluene (2 mL) was added drop wise and the was warmed to 20 °C and left to stir. After 30 minutes the solvent was removed *in vacuo* and the crude product was washed with hexane (3 x 2 mL). The precipitate was redissolved in a hexane/toluene mixture. Crystalline products were isolated at -20 °C after 1 week (359 mg, 1.38 mmol, 59%).

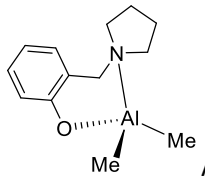

Al(**14**)Me_2: White solid. The major series (mono-ligated) appeared in a 2:1 ratio with the minor series (bis-ligated). ^{1}H NMR (400 MHz, C_6D_6, δ_H, ppm); (*major series*) 7.25 – 7.29 (1H, td, J = 8.3 Hz, J = 6.8 Hz, J = 2.3 Hz, Ar), 6.92 – 6.95 (1H, dd, J = 7.9 Hz, J = 2.3 Hz, Ar), 6.76-6.78 (1H, dd, J = 6.8 Hz, J = 1.2 Hz, Ar), 6.70 – 6.72 (1H, td, J = 8.3 Hz, 7.9 Hz, J = 1.2 Hz Ar) 3.19 (2H, s, NCH_2), 2.54 (2H, m, NCH_2), 1.83 (2H, s, NCH_2), 1.06-1.16 (4H, m, CH_2), -0.47 (6H, s, CH_3). (*minor series*) 7.20-7.24 (2H, td, J = 8.3 Hz, J = 6.8 Hz, J = 1.3 Hz, Ar), 7.17 – 7.19 (2H, dd, J = 7.5 Hz, J = 1.3 Hz, Ar), 6.81-6.82 (2H, dd, J = 6.8 Hz, J = 1.2 Hz, Ar) 6.67-6.70 (2H, td, J = 8.3 Hz, 7.5 Hz, J = 1.2 Hz Ar) 3.61 (4H, m. NCH_2), 2.78 (8H, m, NCH_2), 1.44 (8H, m, CH_2), -0.54 (3H, s, CH_3). $^{13}C\{^1H\}$ NMR (100 MHz, 298 K, C_6D_6, δ_C, ppm); (*only major series*) 160.8 (*C*-O), 130.8 (Ar), 129.3 (Ar), 120.3 (Ar), 119.6(Ar), 116.8 (Ar), 59.2 (NCH_2), 53.7 (NCH_2), 23.2 (CH_2), 22.4 (CH_2), -10.9 (CH_3). Due to the presence of two series the elemental analysis was compromised.

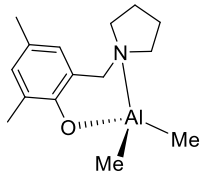

Al(**15**)Me_2: Yellow solid (359 mg, 1.38 mmol, 59%). ^{1}H NMR (400 MHz, 298 K, C_6D_6, δ_H, ppm); 6.99 (1H, s, Ar), 6.43 (1H, s, Ar), 3.23 (2H, s, CH_2), 2.56 (2H, m, NCH_2), 2.46 (3H, s, CH_3), 2.26 (3H, s, CH_3), 1.89 (2H, m, NCH_2) 1.12 – 1.18 (4H, m, CH_2), -0.45 (6H, s, CH_3), $^{13}C\{^1H\}$ NMR (100 MHz, 298 K, C_6D_6, δ_C, ppm); 156.7 (*C*-O), 132.5 (Ar), 129.3 (Ar), 125.7 (Ar), 125.1 (Ar), 120.6 (Ar), 59.4 (NCH_2), 53.9 (NCH_2), 22.4 (CH_2), 20.7 (CH_3), 16.8 (CH_3), -10.9 (CH_3), Elemental (CHN) Analysis; (Calculated $C_{15}H_{24}N_1O_1Al_1$) C: 68.94%, H: 9.26%, N: 5.36%,

(Experimental) C: 67.75%, H: 9.19%, N: 6.04%. A small discrepancy in the EA which may be due to solvent residues which were difficult to remove without degrading the compound.

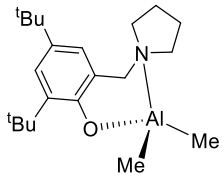

Al(**16**)Me_2: White solid (1.06 mmol, 53%) ^{1}H NMR (400 MHz, 298 K, C_6D_6, δ_H, ppm); 7.58 (1H, d, J = 2.6 Hz, Ar*H*), 6.76 (1H, d, J = 2.6 Hz, Ar*H*), 3.23 (2H, s, CH_2), 2.53 - 2.57 (2H, m, CH_2),), 1.81 – 1.87 (2H, m, CH_2), 1.72 (9H, s, (C(CH_3)$_3$)), 1.42 (9H, s, (C(CH_3)$_3$)), 1.11 – 1.19 (4H, m, CH_2), -0.45 (6H, s, CH_3). ^{13}C{^{1}H} NMR (100 MHz, 298 K, C_6D_6, δ_C, ppm); 156.7 (*C*-O), 138.2 (Ar), 138.1 (Ar), 124.3 (Ar), 123.8 (Ar), 121.5 (Ar), 59.8 (N*C*H_2), 53.6 (N*C*H_2), 35.2 (*C*(CH$_3$)$_3$), 33.9 (*C*(CH$_3$)$_3$), 31.8 (C(*C*H$_3$)$_3$) 29.7 (C(*C*H$_3$)$_3$), 22.0 (*C*H_2), -10.71 (*C*H_3). Elemental (CHN) Analysis; (Calculated $C_{21}H_{36}N_1O_1Al_1$) C: 73.00%, H: 10.50%, N: 4.05%, (Experimental) C: 73.64%, H: 10.85%, N: 4.14%.

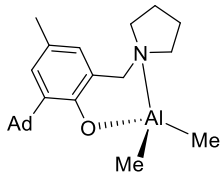

Al(**17**)Me_2: White solid (1.44 mmol, 72%). ^{1}H NMR (400 MHz, 298 K, C_6D_6, δ_H, ppm); 7.20 (1H, d, J = 2.1 Hz, Ar*H*), 6.46 (1H, d, J = 2.1 Hz, Ar*H*), 3.20 (2H, s, NCH_2), 2.56 (2H, m, NCH_2), 2.48 (6H, d, J = 2.7 Hz, CH_2), 2.35 (3H, s, CH_3), 2.15 – 2.17 (3H, m, C*H*), 1.83-1.94 (6H, m, CH_2), 1.80 (2H, m, CH_2), 1.11 – 1.20 (4H, m, CH_2) -0.43 (6H, s, CH_3), ^{13}C{^{1}H} NMR (100 MHz, 298 K, C_6D_6, δ_C, ppm); 157.4 (*C*-O), 139.3 (Ar), 128.7 (Ar), 127.9 (Ar), 125.1 (Ar), 122.5 (Ar), 59.6 (N*C*H_2), 54.0 (N*C*H_2), 41.1 (*C*H_2), 37.9 (*C*H_2), 37.5 (*C*H_2) 29.9 (CH) 22.4 (*C*H_2) 22.3 (CH_2) 21.2 (CH_3) -11.0 (*C*H_3), Elemental (CHN) Analysis; (Calculated $C_{24}H_{36}N_1O_1Al_1$) C: 75.55%, H: 9.51%, N: 3.67%, (Experimental) C: 73.57%, H: 9.45%, N: 3.71%.

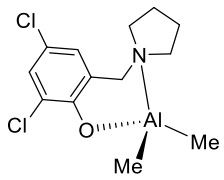

Al(**18**)Me_2 : White solid (1.38 mmol, 59%). ^{1}H NMR (400 MHz, 298 K, C_6D_6, δ_H, ppm); 7.38 (1H, d, J = 2.8 Hz, Ar*H*), 6.47 (1H, d, J = 2.8 Hz, Ar*H*), 2.89 (2H, s, CH_2), 2.38 (2H, m, NCH_2), 1.61 (2H, m, NCH_2) 1.11 (2H, m, CH_2), 1.01 (2H, m, CH_2), -0.57 (6H, s, CH_3) ^{13}C{^{1}H} NMR (100 MHz, 298 K, C_6D_6, δ_C, ppm); 155.3 (*C*-O), 130.5 (Ar), 127.7 (Ar), 125.5 (Ar), 123.8 (Ar), 120.9 (Ar), 58.4 (N*C*H_2), 54.0 (N*C*H_2), 22.4 (*C*H_2) -10.41 (*C*H_3). Elemental (CHN) Analysis; (Calculated $C_{13}H_{18}Cl_2N_1O_1Al_1$) C: 51.67%, H: 6.00%, N: 4.64%, (Experimental) C: 50.85%, H: 5.89%, N: 5.25%.

6.5.11. Synthesis of $Al_2(L)Me_5$ complexes

A solution of 2 M $AlMe_3$ in hexane (1 mL, 2 mmol) was added dropwise to a ice-cold solution of toluene (8 mL). To this solution **15**H (1 mmol) in toluene (2 mL) was added drop wise and the was warmed to 20 °C and left to stir. After 30 minutes the solvent was removed *in vacuo* and the crude product was washed with hexane (3 x 2 mL). The precipitate was redissolved in a hexane:toluene mixture. Crystalline products were isolated at -20 °C after 1 week (292 mg, 0.65 mmol, 59%).

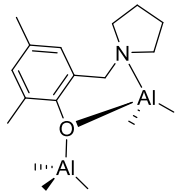

Al_2(**15**)Me_5: White powder (55 mg, 0.17 mmol, 17%). ^{1}H NMR (400 MHz, 298 K, C_6D_6, δ_H, ppm); 6.76 (1H, s, Ar*H*), 6.31 (1H, s, Ar*H*), 4.22 (2H, d, 12.7 Hz, C*H*H), 2.85 (1H, m, C*H*H), 2.38 (3H, s, CH_3), 2.25 (1H, d, 12.7 Hz, CH*H*), 2.11 (1H, m, CH*H*), 2.05 (3H, s, CH_3) 1.90 (1H, m, CH*H*), 1.48 (1H, m, CH*H*), 0.96 – 1.16 (4H, m, CH_2), -0.17 (3H, s, CH_3) -0.24 (9H, s, CH_3), -1.04 (3H, s, CH_3). ^{13}C{^{1}H} NMR (100 MHz, 298 K, C_6D_6, δ_C, ppm); 156.7 (*C*-O), 138.2 (Ar), 138.1 (Ar), 124.3 (Ar), 123.8 (Ar), 121.5 (Ar), 59.8 (N*C*H_2), 53.6 (N*C*H_2), 35.2 (*C*$(CH_3)_3$), 33.9 (*C*$(CH_3)_3$), 31.8 (C(*C*$H_3)_3$) 29.7 (C(*C*$H_3)_3$), 22.0 (*C*H_2), -10.71 (*C*H_3). Elemental (CHN) Analysis; (Calculated $C_{18}H_{33}Al_2NO$) C: 73.00%, H: 10.50%, N: 4.05%, (Experimental) C: 73.64%, H: 10.85%, N: 4.14%.

6.6. References

1 S. Mi. H. Hampton, Carissa, *Tetrahedron.*, 2016, **72**, 6064.

2 Khusnutdinov. Shchadneva; Khisamova, *Russ. J. Org. Chem.*, 2015, 51, 1545–1550.

3 C. N. Basu, Debashis; Allard, Marco M.; Xavier, Fernando R.; Heeg, Mary Jane; Schlegel, H. Bernhard; Verani, *Dalton Trans.*, 2015, **44**, 3454–3466.

4 T. Wolf, T. Steinbach and F. R. Wurm, *Macromolecules*, 2015, **48**, 3853–3863.

5 R. Evans, G. D. Poggetto, M. Nilsson and G. A. Morris, *Anal. Chem.*, 2018, **90**, 3987–3994.

6 R. Evans, Z. Deng, A. K. Rogerson, A. S. McLachlan, J. J. Richards, M. Nilsson and G. A. Morris, *Angew. Chemie - Int. Ed.*, 2013, **52**, 3199–3202.

7 N. Kazemi, T. A. Duever and A. Penlidis, *Macromol. React. Eng.*, 2011, **5**, 385–403.

8 H. Patino-Leal, P. M. Reilly and K. F. O'Driscoll, *J. Polym. Sci. Polym. Lett. Ed.*, 1980, **18**, 219–227.

9 E. Hauch, X. Zhou, T. A. Duever and A. Penlidis, *Macromol. Symp.*, 2008, **271**, 48–63.

10 V. Jaacks, *Macromol. Chem. Phys.*, 1972, **161**, 161–172.

11 P. C. Painter and M. M. Coleman, *Essentials of Polymer Science and Engineering*, DEStech Publications, Incorporated, 2008.

12 F. T. Wall, *J. Am. Chem. Soc.*, 1941, **63**, 1862–1866.

13 M. D. Jones, S. L. Hancock, P. McKeown, P. M. Schafer, A. Buchard, L. H. Thomas, M. F. Mahon and J. P. Lowe, *Chem. Commun.*, 2014, **50**, 15967–15970.

14 M. D. Jones, L. Brady, P. McKeown, A. Buchard, P. M. Schäfer, L. H. Thomas, M. F. Mahon, T. J. Woodman and J. P. Lowe, *Chem. Sci.*, 2015, **6**, 5034–5039.

15 K. Press, I. Goldberg and M. Kol, *Angew. Chemie - Int. Ed.*, 2015, **54**, 14858–14861.

16 E. L. Whitelaw, M. G. Davidson and M. D. Jones, *Chem. Commun.*, 2011, **47**, 10004–10006.

17 E. L. Whitelaw, M. D. Jones and M. F. Mahon, *Inorg. Chem.*, 2010, **49**, 7176–7181.

18 S. Mahato, S. Haldar and C. K. Jana, *Chem. Commun.*, 2014, **50**, 332–334.

19 R. K. J. Bott, D. L. Hughes, M. Schormann, M. Bochmann and S. J. Lancaster, *J. Organomet. Chem.*, 2003, **665**, 135–149.

20 B. Burlin, Gordon B. Nguyen, Dung M. Kotecka and K. H. Rieckmann, *Aust. J. Chem.*, 1993, **46**, 21–29.

Chapter 7

Appendix

7. Appendix

In(**2**)Cl

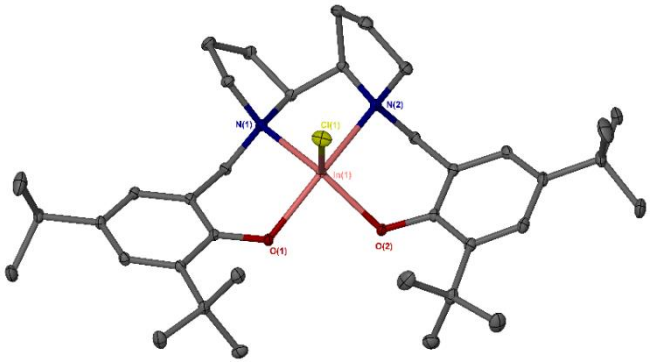

Empirical formula	C38 H58 Cl In N2 O2	
Formula weight	725.13	
Temperature	150(2) K	
Wavelength	1.54184 Å	
Crystal system	Monoclinic	
Space group	$P2_1/c$	
Unit cell dimensions	*a* = 12.3467(3) Å	α = 90°
	b = 15.8230(4) Å	β = 94.865(3)°
	c = 19.2186(5) Å	γ = 90°
Volume	3741.05(16) $Å^3$	
Z	4	
Density (calculated)	1.287 Mg/m^3	
Absorption coefficient	5.950 mm^{-1}	
F(000)	1528	
Crystal size	0.05 x 0.05 x 0.05 mm^3	
Theta range for data collection	3.62 to 73.09°.	
Index ranges	-15<=h<=15, -19<=k<=19, -20<=l<=23	
Reflections collected	51666	
Independent reflections	7472 [R(int) = 0.0280]	
Completeness to theta = 73.09°	99.8 %	
Absorption correction	Semi-empirical from equivalents	
Max. and min. transmission	1.000 and 0.83475	
Refinement method	Full-matrix least-squares on F^2	
Data / restraints / parameters	7472 / 0 / 409	
Goodness-of-fit on F^2	1.029	
Final R indices [I>2sigma(I)]	R1 = 0.0202, wR2 = 0.0499	
R indices (all data)	R1 = 0.0214, wR2 = 0.0506	
Largest diff. peak and hole	0.281 and -0.605 $e.Å^{-3}$	

In(**2**)I

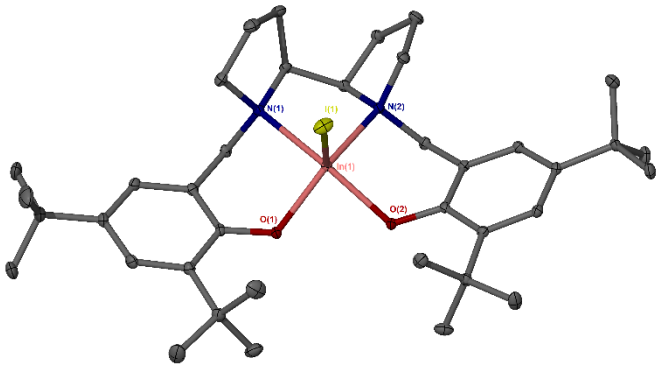

Empirical formula	C38 H58 I In N2 O2	
Formula weight	816.58	
Temperature	150(2) K	
Wavelength	1.54184 Å	
Crystal system	Monoclinic	
Space group	$P2_1/c$	
Unit cell dimensions	a = 12.01000(10) Å	α = 90°
	b = 16.7440(2) Å	β = 92.9080(10)°
	c = 18.8821(2) Å	γ = 90°
Volume	3792.21(7) $Å^3$	
Z	4	
Density (calculated)	1.430 Mg/m^3	
Absorption coefficient	11.614 mm^{-1}	
F(000)	1672	
Crystal size	0.05 x 0.05 x 0.03 mm^3	
Theta range for data collection	3.53 to 70.08°.	
Index ranges	-14<=h<=14, -16<=k<=20, -23<=l<=21	
Reflections collected	29570	
Independent reflections	7205 [R(int) = 0.0297]	
Completeness to theta = 70.08°	100.0 %	
Max. and min. transmission	0.7600 and 0.5944	
Refinement method	Full-matrix least-squares on F^2	
Data / restraints / parameters	7205 / 0 / 409	
Goodness-of-fit on F^2	1.018	
Final R indices [I>2sigma(I)]	R1 = 0.0230, wR2 = 0.0574	
R indices (all data)	R1 = 0.0251, wR2 = 0.0586	
Largest diff. peak and hole	1.319 and -0.482 e.$Å^{-3}$	

Al(**2**)Cl

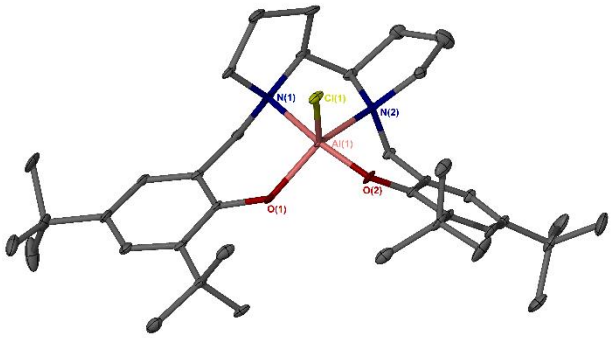

Empirical formula	C38 H56 Al Cl N2 O2	
Formula weight	635.28	
Temperature	150(2) K	
Wavelength	1.54184 Å	
Crystal system	Monoclinic	
Space group	*I*2/a	
Unit cell dimensions	*a* = 22.54430(10) Å	α = 90°
	b = 12.93050(10) Å	β = 93.53°
	c = 25.52250(10) Å	γ = 90°
Volume	7425.95(7) Å^3	
Z	8	
Density (calculated)	1.136 Mg/m^3	
Absorption coefficient	1.386 mm^{-1}	
F(000)	2752	
Crystal size	0.30 x 0.20 x 0.10 mm^3	
Theta range for data collection	3.47 to 68.24°.	
Index ranges	-27<=h<=27, -15<=k<=14, -30<=l<=30	
Reflections collected	62374	
Independent reflections	6820 [R(int) = 0.0257]	
Completeness to theta = 68.24°	100.0 %	
Max. and min. transmission	0.8738 and 0.6812	
Refinement method	Full-matrix least-squares on F^2	
Data / restraints / parameters	6820 / 0 / 420	
Goodness-of-fit on F^2	1.028	
Final R indices [I>2sigma(I)]	R1 = 0.0418, wR2 = 0.1165	
R indices (all data)	R1 = 0.0427, wR2 = 0.1175	
Largest diff. peak and hole	0.946 and -0.477 e.Å^{-3}	

Ga(**2**)Cl

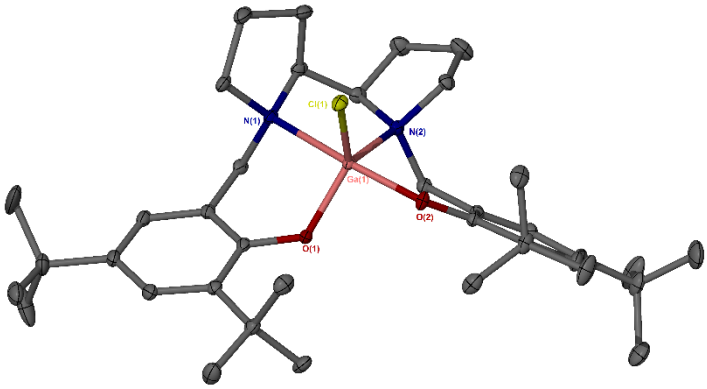

Empirical formula	C38 H58 Cl Ga N2 O2	
Formula weight	680.03	
Temperature	150(2) K	
Wavelength	1.54184 Å	
Crystal system	Monoclinic	
Space group	*I*2/*a*	
Unit cell dimensions	*a* = 22.41840(10) Å	α = 90°
	b = 12.91110(10) Å	β = 93.3540(10)°
	c = 25.80380(10) Å	γ = 90°
Volume	7456.02(7) Å1	
Z	8	
Density (calculated)	1.212 Mg/m^3	
Absorption coefficient	1.914 mm^{-1}	
F(000)	2912	
Crystal size	0.20 x 0.20 x 0.15 mm^3	
Theta range for data collection	3.43 to 73.36°.	
Index ranges	-23<=h<=27, -15<=k<=15, -31<=l<=32	
Reflections collected	82162	
Independent reflections	7485 [R(int) = 0.0222]	
Completeness to theta = 73.36°	99.8 %	
Max. and min. transmission	0.7622 and 0.7008	
Refinement method	Full-matrix least-squares on F^2	
Data / restraints / parameters	7485 / 0 / 410	
Goodness-of-fit on F^2	1.021	
Final R indices [I>2sigma(I)]	R1 = 0.0290, wR2 = 0.0779	
R indices (all data)	R1 = 0.0297, wR2 = 0.0785	
Largest diff. peak and hole	0.693 and -0.458 e.$Å^{-3}$	

$In_2(\mathbf{2})_2(OH)OEt$

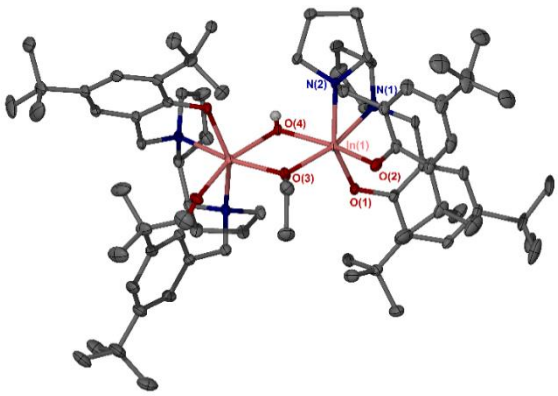

Empirical formula	C93 H157 Cl0 In2 N4 O6	
Formula weight	1656.87	
Temperature	150(2) K	
Wavelength	1.54184 Å	
Crystal system	Monoclinic	
Space group	*I*2/a	
Unit cell dimensions	*a* = 17.9334(3) Å	α = 90°
	b = 16.6462(2) Å	β = 99.1720(10)°
	c = 32.2729(3) Å	γ = 90°
Volume	9511.0(2) $Å^3$	
Z	4	
Density (calculated)	1.157 Mg/m^3	
Absorption coefficient	4.247 mm^{-1}	
F(000)	3556	
Crystal size	0.05 x 0.05 x 0.02 mm^3	
Theta range for data collection	2.77 to 66.60°.	
Index ranges	-21<=h<=19, -19<=k<=19, -38<=l<=38	
Reflections collected	68760	
Independent reflections	8390 [R(int) = 0.0485]	
Completeness to theta = 66.60°	99.9 %	
Max. and min. transmission	0.9199 and 0.8157	
Refinement method	Full-matrix least-squares on F^2	
Data / restraints / parameters	8390 / 46 / 530	
Goodness-of-fit on F^2	1.041	
Final R indices [I>2sigma(I)]	R1 = 0.0383, wR2 = 0.1072	
R indices (all data)	R1 = 0.0435, wR2 = 0.1118	
Largest diff. peak and hole	1.054 and -0.396 e.$Å^{-3}$	

{In(**2**)OH}$_2$

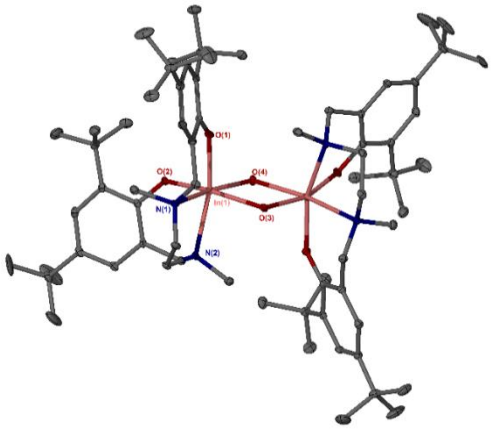

Empirical formula	C86 H128 In2 N4 O6	
Formula weight	1543.56	
Temperature	150(2) K	
Wavelength	0.71073 Å	
Crystal system	Monoclinic	
Space group	*C*2/c	
Unit cell dimensions	*a* = 32.9983(10) Å	α = 90°
	b = 10.1446(2) Å	β = 112.352(4)°
	c = 26.8020(8) Å	γ = 90°
Volume	8298.0(4) Å^3	
Z	4	
Density (calculated)	1.236 Mg/m^3	
Absorption coefficient	0.607 mm^{-1}	
F(000)	3272	
Crystal size	0.15 x 0.15 x 0.10 mm^3	
Theta range for data collection	3.22 to 26.02°.	
Index ranges	-40<=h<=39, -12<=k<=12, -33<=l<=33	
Reflections collected	57164	
Independent reflections	8149 [R(int) = 0.0695]	
Completeness to theta = 26.02°	99.5 %	
Max. and min. transmission	0.9417 and 0.9144	
Refinement method	Full-matrix least-squares on F^2	
Data / restraints / parameters	8149 / 0 / 459	
Goodness-of-fit on F^2	1.057	
Final R indices [I>2sigma(I)]	R1 = 0.0416, wR2 = 0.0711	
R indices (all data)	R1 = 0.0611, wR2 = 0.0766	
Largest diff. peak and hole	0.492 and -0.475 e.Å^{-3}	

In(**10**)Cl

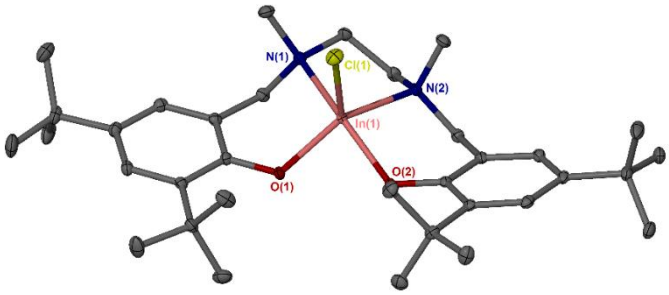

Empirical formula	C48 H70 Cl In N2 O2	
Formula weight	857.33	
Temperature	150(2) K	
Wavelength	1.54184 Å	
Crystal system	Orthorhombic	
Space group	*P*bca	
Unit cell dimensions	*a* = 21.6467(9) Å	α = 90°
	b = 13.1050(7) Å	β = 90°
	c = 32.3338(9) Å	γ = 90°
Volume	9172.5(7) Å^3	
Z	8	
Density (calculated)	1.242 Mg/m^3	
Absorption coefficient	4.933 mm^{-1}	
F(000)	3632	
Crystal size	0.30 x 0.20 x 0.01 mm^3	
Theta range for data collection	2.73 to 74.50°.	
Index ranges	-16<=h<=27, -16<=k<=16, -40<=l<=40	
Reflections collected	63191	
Independent reflections	9393 [R(int) = 0.0408]	
Completeness to theta = 74.50°	100.0 %	
Max. and min. transmission	0.9523 and 0.3192	
Refinement method	Full-matrix least-squares on F^2	
Data / restraints / parameters	9393 / 0 / 503	
Goodness-of-fit on F^2	1.045	
Final R indices [I>2sigma(I)]	R1 = 0.0312, wR2 = 0.0818	
R indices (all data)	R1 = 0.0347, wR2 = 0.0839	
Largest diff. peak and hole	1.395 and -0.493 e.Å^{-3}	

Al(**10**)Cl

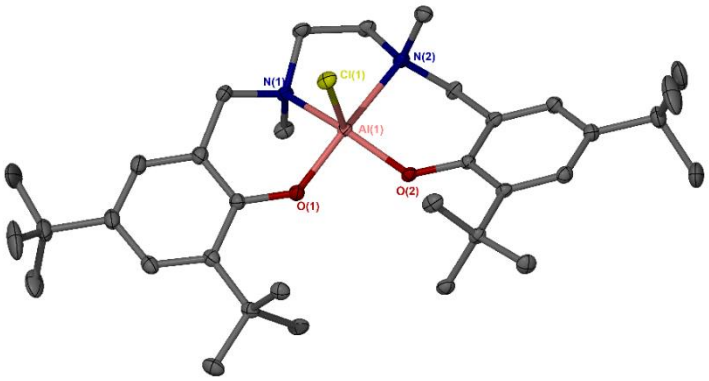

Empirical formula	C38.50 H64.50 Al Cl N2 O2	
Formula weight	649.85	
Temperature	150(2) K	
Wavelength	1.54184 Å	
Crystal system	Monoclinic	
Space group	*C*2/c	
Unit cell dimensions	*a* = 33.7559(5) Å	□ = 90°
	b = 13.9577(2) Å	β = 102.820(2)°
	c = 17.7422(3) Å	γ = 90°
Volume	8150.9(2) Å^3	
Z	8	
Density (calculated)	1.059 Mg/m^3	
Absorption coefficient	1.268 mm^{-1}	
F(000)	2844	
Crystal size	0.150 x 0.100 x 0.050 mm^3	
Theta range for data collection	3.439 to 73.379°.	
Index ranges	-41<=h<=41, -17<=k<=17, -21<=l<=20	
Reflections collected	82822	
Independent reflections	8175 [R(int) = 0.0413]	
Completeness to theta = 67.684°	100.0 %	
Refinement method	Full-matrix least-squares on F^2	
Data / restraints / parameters	8175 / 75 / 487	
Goodness-of-fit on F^2	1.083	
Final R indices [I>2sigma(I)]	R1 = 0.0746, wR2 = 0.2122	
R indices (all data)	R1 = 0.0768, wR2 = 0.2142	
Extinction coefficient	n/a	
Largest diff. peak and hole	1.402 and -0.496 e.Å^{-3}	

Ga(**10**)Cl

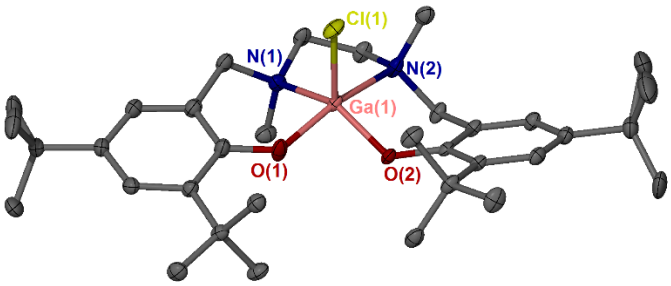

Empirical formula	$C_{40}H_{68}ClGaN_2O_2$
Formula weight	714.13
Temperature/K	150.01(10)
Crystal system	monoclinic
Space group	*C*2/c
a/Å	32.9563(6)
b/Å	14.0324(2)
c/Å	17.9476(2)
α/°	90
β/°	101.3759(15)
γ/°	90
Volume/Å^3	8136.9(2)
Z	8
ρ_{calc}g/cm^3	1.166
μ/mm^{-1}	1.772
F(000)	3088.0
Crystal size/mm^3	0.2 × 0.15 × 0.1
Radiation	CuKα (λ = 1.54184)
2Θ range for data collection/°	5.47 to 146.874
Index ranges	-40 ≤ h ≤ 40, -17 ≤ k ≤ 17, -22 ≤ l ≤ 16
Reflections collected	46467
Independent reflections	8157 [R_{int} = 0.0267, R_{sigma} = 0.0155]
Data/restraints/parameters	8157/81/435
Goodness-of-fit on F^2	1.020
Final R indexes [I>=2σ (I)]	R_1 = 0.0426, wR_2 = 0.1126
Final R indexes [all data]	R_1 = 0.0458, wR_2 = 0.1154
Largest diff. peak/hole / e Å^{-3}	0.85/-0.45

In_2(**12**)$_2$(OH)Cl

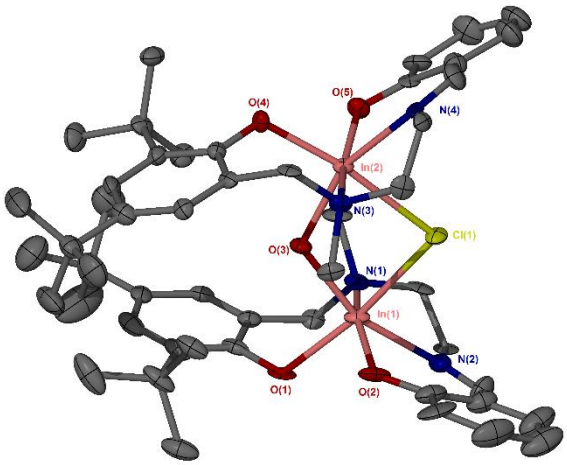

Empirical formula	C68 H92 Cl In2 N4 O6	
Formula weight	1326.55	
Temperature	150(2) K	
Wavelength	1.54184 Å	
Crystal system	Triclinic	
Space group	*P*-1	
Unit cell dimensions	*a* = 14.1699(8) Å	α = 94.998(5)°
	b = 15.5623(13) Å	β = 98.210(4)°
	c = 16.6554(6) Å	γ = 109.593(6)°
Volume	3388.6(4) Å^3	
Z	2	
Density (calculated)	1.300 Mg/m^3	
Absorption coefficient	6.193 mm^{-1}	
F(000)	1382	
Crystal size	0.05 x 0.02 x 0.02 mm^3	
Theta range for data collection	2.71 to 73.36°.	
Index ranges	-17<=h<=17, -19<=k<=19, -20<=l<=20	
Reflections collected	18999	
Independent reflections	18999 [R(int) = 0.0000]	
Completeness to theta = 73.36°	98.2 %	
Max. and min. transmission	0.8862 and 0.7471	
Refinement method	Full-matrix least-squares on F^2	
Data / restraints / parameters	18999 / 90 / 723	
Goodness-of-fit on F^2	1.086	
Final R indices [I>2sigma(I)]	R1 = 0.1128, wR2 = 0.3240	
R indices (all data)	R1 = 0.1528, wR2 = 0.3479	
Largest diff. peak and hole	3.693 and -2.067 e.Å^{-3}	

{Nd(**2**)O^{i}Pr}$_2$

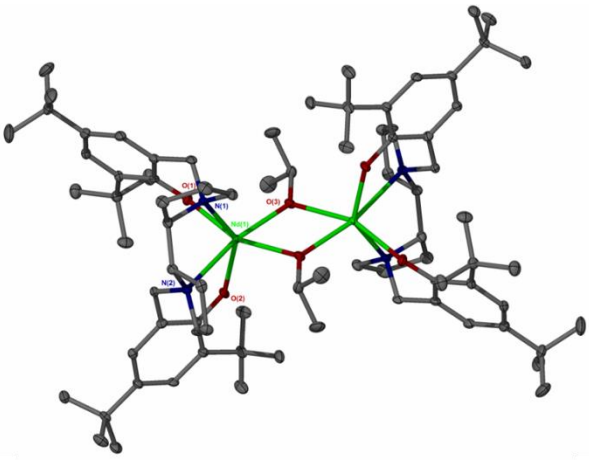

Empirical formula	C55 H81 N2 Nd O3	
Formula weight	962.46	
Temperature	150(2) K	
Wavelength	1.54184 Å	
Crystal system	Monoclinic	
Space group	$P2_1/c$	
Unit cell dimensions	a = 19.3846(5) Å	α = 90°
	b = 24.2686(6) Å	β = 96.970(2)°
	c = 10.9610(3) Å	γ = 90°
Volume	5118.4(2) Å^3	
Z	4	
Density (calculated)	1.249 Mg/m^3	
Absorption coefficient	8.054 mm^{-1}	
F(000)	2036	
Crystal size	0.05 x 0.03 x 0.03 mm^3	
Theta range for data collection	2.93 to 70.07°.	
Index ranges	-23<=h<=23, -29<=k<=29, -8<=l<=13	
Reflections collected	10771	
Independent reflections	10771 [R(int) = 0.0000]	
Completeness to theta = 70.07°	99.4 %	
Max. and min. transmission	0.8240 and 0.6889	
Refinement method	Full-matrix least-squares on F^2	
Data / restraints / parameters	10771 / 84 / 607	
Goodness-of-fit on F^2	1.057	
Final R indices [I>2sigma(I)]	R1 = 0.0470, wR2 = 0.1142	
R indices (all data)	R1 = 0.0663, wR2 = 0.1214	
Largest diff. peak and hole	1.277 and -1.329 e.Å^{-3}	

{Sm(**2**)O^{i}Pr}$_2$

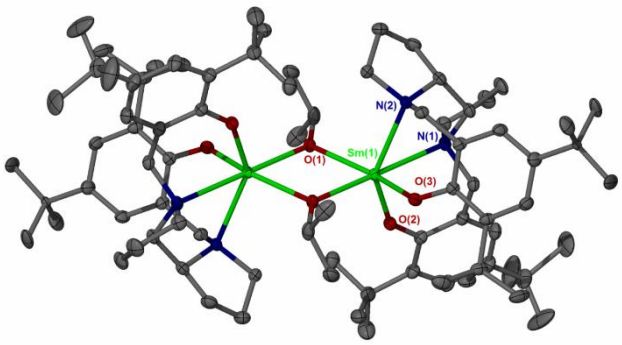

Empirical formula	C47 H79 N2 O3 Sm	
Formula weight	870.47	
Temperature	150.01(10) K	
Wavelength	1.54184 Å	
Crystal system	Monoclinic	
Space group	$P2_1/c$	
Unit cell dimensions	a = 14.9466(2) Å	α = 90°
	b = 15.2718(2) Å	β = 92.9960(10)°
	c = 20.4709(2) Å	γ = 90°
Volume	4666.33(10) Å^3	
Z	4	
Density (calculated)	1.239 Mg/m^3	
Absorption coefficient	9.732 mm^{-1}	
F(000)	1844	
Crystal size	0.150 x 0.110 x 0.110 mm^3	
Theta range for data collection	2.961 to 73.401°.	
Index ranges	-18<=h<=18, -18<=k<=18, -22<=l<=25	
Reflections collected	72176	
Independent reflections	9343 [R(int) = 0.0601]	
Completeness to theta = 67.684°	100.0 %	
Absorption correction	Semi-empirical from equivalents	
Max. and min. transmission	1.00000 and 0.61578	
Refinement method	Full-matrix least-squares on F^2	
Data / restraints / parameters	9343 / 48 / 622	
Goodness-of-fit on F^2	1.072	
Final R indices [I>2sigma(I)]	R1 = 0.0380, wR2 = 0.0982	
R indices (all data)	R1 = 0.0421, wR2 = 0.1011	
Extinction coefficient	n/a	
Largest diff. peak and hole	1.574 and -1.072 e.Å^{-3}	

{Sm(**1**)O^{i}Pr}$_2$

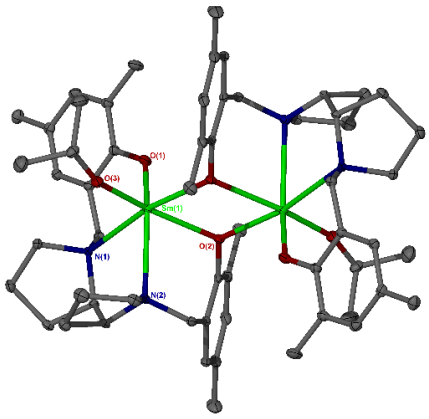

Empirical formula	C65 H90 N4 O6 Sm2	
Formula weight	1324.10	
Temperature	150(10) K	
Wavelength	0.71073 Å	
Crystal system	Monoclinic	
Space group	C2/c	
Unit cell dimensions	*a* = 24.6223(9) Å	α = 90°
	b = 11.6978(3) Å	β = 119.614(5)°
	c = 24.2817(9) Å	γ = 90°
Volume	6080.2(4) Å^3	
Z	4	
Density (calculated)	1.446 Mg/m^3	
Absorption coefficient	1.966 mm^{-1}	
F(000)	2720	
Crystal size	0.300 x 0.250 x 0.200 mm^3	
Theta range for data collection	3.310 to 30.326°.	
Index ranges	-34<=h<=32, -16<=k<=15, -33<=l<=33	
Reflections collected	50350	
Independent reflections	8408 [R(int) = 0.0278]	
Completeness to theta = 25.242°	99.8 %	
Absorption correction	Semi-empirical from equivalents	
Max. and min. transmission	1.00000 and 0.90428	
Data / restraints / parameters	8408 / 42 / 374	
Goodness-of-fit on F^2	1.127	
Final R indices [I>2sigma(I)]	R1 = 0.0262, wR2 = 0.0529	
R indices (all data)	R1 = 0.0319, wR2 = 0.0551	
Largest diff. peak and hole	1.087 and -0.578 e.Å^{-3}	

{Yb(**1**)O^{i}Pr}

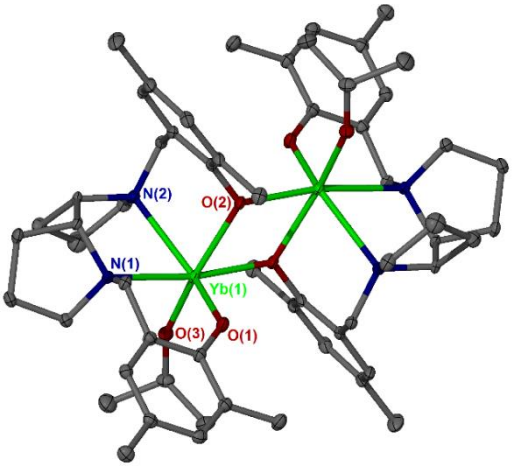

Empirical formula	C65 H90 N4 O6 Yb2	
Formula weight	1369.49	
Temperature	150(2) K	
Wavelength	1.54184 Å	
Crystal system	Monoclinic	
Space group	*C*2/*c*	
Unit cell dimensions	*a* = 24.3739(4) Å	α = 90°
	b = 11.55720(10) Å	β = 120.374(2)°
	c = 24.3550(4) Å	γ = 90°
Volume	5918.98(15) Å^3	
Z	4	
Density (calculated)	1.537 Mg/m^3	
Absorption coefficient	6.110 mm^{-1}	
F(000)	2784	
Crystal size	0.30 x 0.25 x 0.20 mm^3	
Theta range for data collection	4.18 to 73.09°.	
Index ranges	-30<=h<=30, -14<=k<=14, -26<=l<=30	
Reflections collected	10307	
Independent reflections	10320 [R(int) = 0.0000]	
Completeness to theta = 73.09°	99.3 %	
Max. and min. transmission	0.3745 and 0.2615	
Refinement method	Full-matrix least-squares on F^2	
Data / restraints / parameters	10320 / 66 / 368	
Goodness-of-fit on F^2	1.129	
Final R indices [I>2sigma(I)]	R1 = 0.0357, wR2 = 0.1133	
R indices (all data)	R1 = 0.0391, wR2 = 0.1160	
Largest diff. peak and hole	1.478 and -0.951 e.Å^{-3}	

{Sm_2(**2**)$_2$O^{i}PrOH}

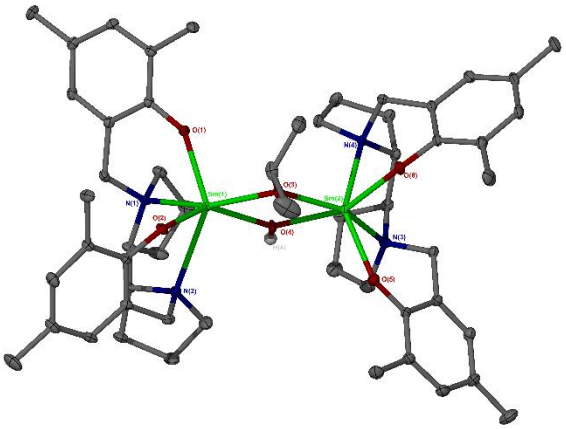

Empirical formula	C185 H286 N8 O12 Sm4	
Formula weight	3415.60	
Temperature	149.9(3) K	
Wavelength	0.71073 Å	
Crystal system	Triclinic	
Space group	*P*-1	
Unit cell dimensions	*a* = 11.3821(4) Å	α = 66.212(3)°
	b = 20.7041(7) Å	β = 77.270(3)°
	c = 21.4578(8) Å	γ = 87.858(3)°
Volume	4505.8(3) Å^3	
Z	1	
Density (calculated)	1.259 Mg/m^3	
Absorption coefficient	1.342 mm^{-1}	
F(000)	1796	
Crystal size	0.200 x 0.150 x 0.050 mm^3	
Theta range for data collection	3.421 to 30.294°.	
Index ranges	-16<=h<=16, -27<=k<=29, -30<=l<=27	
Reflections collected	45044	
Independent reflections	23204 [R(int) = 0.0255]	
Completeness to theta = 25.242°	99.7 %	
Absorption correction	Semi-empirical from equivalents	
Max. and min. transmission	1.00000 and 0.90187	
Refinement method	Full-matrix least-squares on F^2	
Data / restraints / parameters	23204 / 63 / 1042	
Goodness-of-fit on F^2	1.024	
Final R indices [I>2sigma(I)]	R1 = 0.0323, wR2 = 0.0636	
R indices (all data)	R1 = 0.0510, wR2 = 0.0711	

{Yb_2(**2**)$_2$O^{i}PrOH}

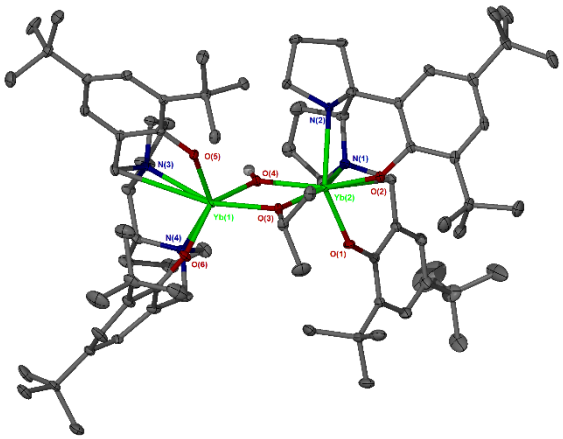

Empirical formula	C185 H286 N8 O12 Yb4	
Formula weight	3506.36	
Temperature	150.01(10) K	
Wavelength	1.54184 Å	
Crystal system	Triclinic	
Space group	*P*-1	
Unit cell dimensions	*a* = 11.4225(10) Å	α = 65.578(7)°
	b = 20.2868(12) Å	β = 77.839(7)°
	c = 21.5670(17) Å	γ = 88.124(6)°
Volume	4440.1(6) Å^3	
Z	1	
Density (calculated)	1.311 Mg/m^3	
Absorption coefficient	4.186 mm^{-1}	
F(000)	1828	
Crystal size	0.025 x 0.025 x 0.025 mm^3	
Theta range for data collection	2.541 to 70.137°.	
Index ranges	-13<=h<=11, -24<=k<=24, -26<=l<=20	
Reflections collected	35041	
Independent reflections	16785 [R(int) = 0.0270]	
Completeness to theta = 67.684°	99.9 %	
Absorption correction	Semi-empirical from equivalents	
Max. and min. transmission	1.00000 and 0.89428	
Data / restraints / parameters	16785 / 135 / 1146	
Goodness-of-fit on F^2	1.029	
Final R indices [I>2sigma(I)]	R1 = 0.0268, wR2 = 0.0622	
R indices (all data)	R1 = 0.0349, wR2 = 0.0658	
Extinction coefficient	n/a	
Largest diff. peak and hole	0.852 and -0.952 e.Å^{-3}	

{Sm(**2**)OH}$_2$

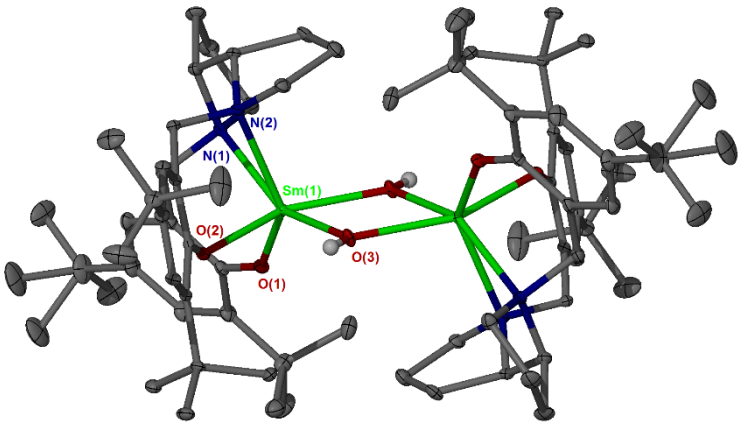

Empirical formula	C97 H142 N4 O6 Sm2	
Formula weight	1760.84	
Temperature	150.00(10) K	
Wavelength	1.54184 Å	
Crystal system	Monoclinic	
Space group	$P2_1/c$	
Unit cell dimensions	a = 18.1468(2) Å	α = 90°
	b = 21.0931(2) Å	β = 105.332(10)°
	c = 12.25180(10) Å	γ = 90°
Volume	4522.74(8) Å^3	
Z	2	
Density (calculated)	1.293 Mg/m^3	
Absorption coefficient	10.053 mm^{-1}	
F(000)	1848	
Crystal size	0.200 x 0.200 x 0.100 mm^3	
Theta range for data collection	3.281 to 73.119°.	
Index ranges	-22<=h<=22, -20<=k<=25, -14<=l<=15	
Reflections collected	35230	
Independent reflections	8982 [R(int) = 0.0452]	
Completeness to theta = 67.684°	100.0 %	
Max. and min. transmission	1.00000 and 0.51989	
Refinement method	Full-matrix least-squares on F^2	
Data / restraints / parameters	8982 / 13 / 590	
Goodness-of-fit on F^2	1.037	
Final R indices [I>2sigma(I)]	R1 = 0.0314, wR2 = 0.0776	
R indices (all data)	R1 = 0.0370, wR2 = 0.0810	
Extinction coefficient	n/a	
Largest diff. peak and hole	1.557 and -1.049 e.Å^{-3}	

B(**14**)H_2

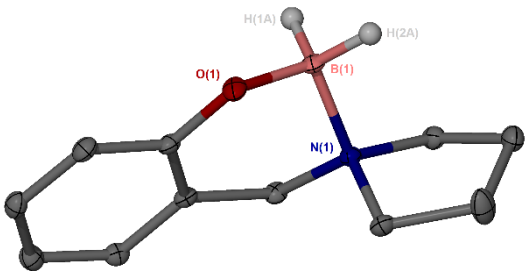

Empirical formula	C22 H32 B2 N2 O2	
Formula weight	378.11	
Temperature	150(2) K	
Wavelength	1.54184 Å	
Crystal system	Orthorhombic	
Space group	*P*bca	
Unit cell dimensions	*a* = 18.0556(6) Å	α = 90°
	b = 6.0420(2) Å	β = 89.957(4)°
	c = 18.6169(10) Å	γ = 90°
Volume	2030.95(14) $Å^3$	
Z	4	
Density (calculated)	1.237 Mg/m^3	
Absorption coefficient	0.598 mm^{-1}	
F(000)	816	
Crystal size	0.300 x 0.050 x 0.020 mm^3	
Theta range for data collection	4.751 to 72.648°.	
Index ranges	-13<=h<=22, -7<=k<=7, -22<=l<=21	
Reflections collected	11432	
Independent reflections	2009 [R(int) = 0.0666]	
Completeness to theta = 67.684°	99.9 %	
Refinement method	Full-matrix least-squares on F^2	
Data / restraints / parameters	2009 / 0 / 135	
Goodness-of-fit on F^2	1.028	
Final R indices [I>2sigma(I)]	R1 = 0.0453, wR2 = 0.1124	
R indices (all data)	R1 = 0.0600, wR2 = 0.1230	
Extinction coefficient	n/a	
Largest diff. peak and hole	0.237 and -0.249 e.$Å^{-3}$	

Al(**15**)$_2$Me

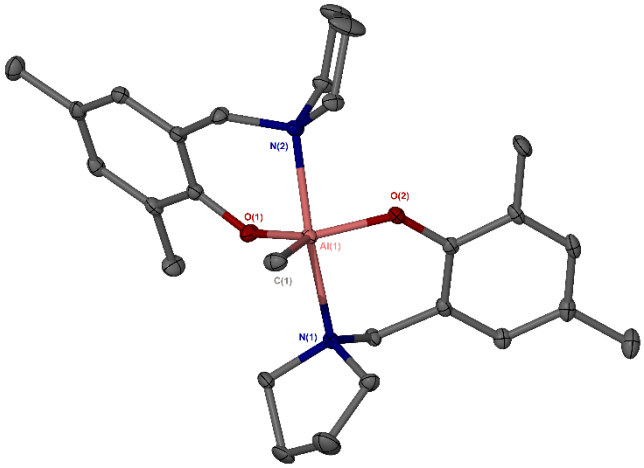

Empirical formula	C27 H39 Al N2 O2	
Formula weight	450.58	
Temperature	150(2) K	
Wavelength	1.54184 Å	
Crystal system	Monoclinic	
Space group	*P*21/n	
Unit cell dimensions	*a* = 10.8909(14) Å	α = 90°
	b = 18.512(3) Å	β = 112.158(15)°
	c = 13.3281(15) Å	γ = 90°
Volume	2488.7(6) Å^3	
Z	4	
Density (calculated)	1.203 Mg/m^3	
Absorption coefficient	0.904 mm^{-1}	
F(000)	976	
Crystal size	0.100 x 0.050 x 0.050 mm^3	
Theta range for data collection	4.305 to 70.075°.	
Index ranges	-13<=h<=13, -22<=k<=22, -10<=l<=16	
Reflections collected	17480	
Independent reflections	4729 [R(int) = 0.0642]	
Completeness to theta = 67.684°	100.0 %	
Refinement method	Full-matrix least-squares on F^2	
Data / restraints / parameters	4729 / 0 / 295	
Goodness-of-fit on F^2	1.170	
Final R indices [I>2sigma(I)]	R1 = 0.0660, wR2 = 0.1610	
R indices (all data)	R1 = 0.0878, wR2 = 0.1711	
Extinction coefficient	n/a	
Largest diff. peak and hole	0.941 and -0.407 e.Å^{-3}	

Al(**16**)$_2$Me

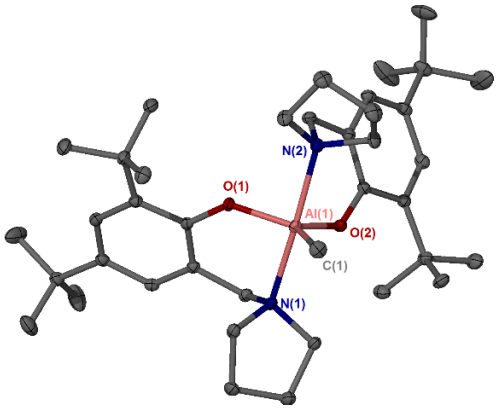

Empirical formula	C84.50 H137 Al2 N4 O4	
Formula weight	1326.93	
Temperature	150.01(10) K	
Wavelength	1.54184 Å	
Crystal system	Triclinic	
Space group	*P*-1	
Unit cell dimensions	*a* = 10.8961(7) Å	α = 100.543(4)°
	b = 13.2106(6) Å	β = 98.543(5)°
	c = 14.4915(7) Å	γ = 99.173(4)°
Volume	1990.29(19) Å^3	
Z	1	
Density (calculated)	1.107 Mg/m^3	
Absorption coefficient	0.705 mm^{-1}	
F(000)	730	
Crystal size	0.180 x 0.150 x 0.020 mm^3	
Theta range for data collection	3.155 to 72.587°.	
Index ranges	-13<=h<=13, -16<=k<=11, -10<=l<=17	
Reflections collected	12925	
Independent reflections	7689 [R(int) = 0.0366]	
Completeness to theta = 67.684°	99.8 %	
Max. and min. transmission	1.00000 and 0.87998	
Refinement method	Full-matrix least-squares on F^2	
Data / restraints / parameters	7689 / 138 / 568	
Goodness-of-fit on F^2	1.020	
Final R indices [I>2sigma(I)]	R1 = 0.0540, wR2 = 0.1270	
R indices (all data)	R1 = 0.0750, wR2 = 0.1405	
Extinction coefficient	n/a	
Largest diff. peak and hole	0.389 and -0.295 e.Å^{-3}	

Al(**18**)$_2$Me

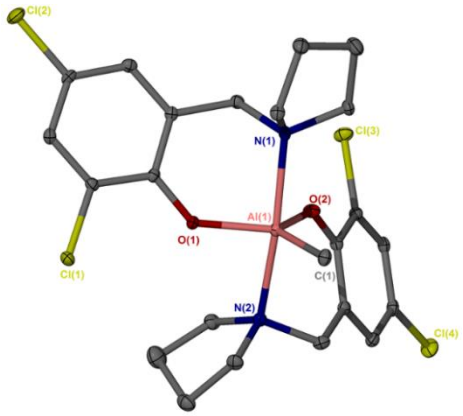

Empirical formula	C23 H27 Al Cl4 N2 O2	
Formula weight	532.24	
Temperature	150(2) K	
Wavelength	0.71073 Å	
Crystal system	Monoclinic	
Space group	*C*-2/c	
Unit cell dimensions	*a* = 21.0889(13) Å	α = 90°
	b = 10.8026(5) Å	β = 114.293(7)°
	c = 22.9874(13) Å	γ = 90°
Volume	4773.2(5) Å^3	
Z	8	
Density (calculated)	1.481 Mg/m^3	
Absorption coefficient	0.558 mm^{-1}	
F(000)	2208	
Crystal size	0.200 x 0.100 x 0.100 mm^3	
Theta range for data collection	3.416 to 25.346°.	
Index ranges	-25<=h<=25, -13<=k<=13, -27<=l<=27	
Reflections collected	14294	
Independent reflections	4283 [R(int) = 0.0331]	
Completeness to theta = 25.242°	98.1 %	
Absorption correction	Semi-empirical from equivalents	
Max. and min. transmission	1.00000 and 0.96606	
Refinement method	Full-matrix least-squares on F^2	
Data / restraints / parameters	4283 / 0 / 290	
Goodness-of-fit on F^2	1.029	
Final R indices [I>2sigma(I)]	R1 = 0.0366, wR2 = 0.0805	
R indices (all data)	R1 = 0.0488, wR2 = 0.0865	
Largest diff. peak and hole	0.830 and -0.315 e.Å^{-3}	

Al(**19**)$_2$Me

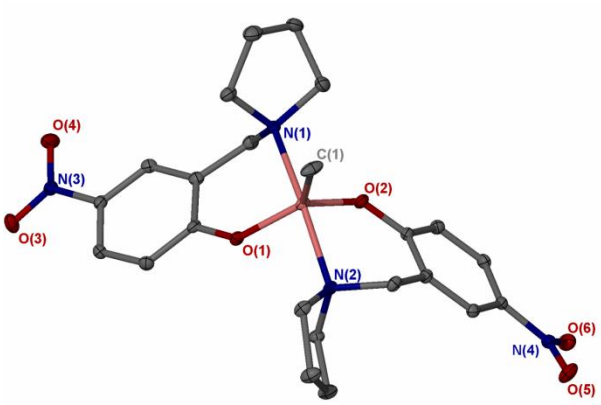

Empirical formula	$C_{23}H_{29}AlN_4O_6$
Formula weight	484.48
Temperature/K	150.00(10)
Crystal system	monoclinic
Space group	$P2_1/n$
a/Å	12.8573(4)
b/Å	10.4558(3)
c/Å	18.0303(6)
α/°	90
β/°	107.072(4)
γ/°	90
Volume/Å^3	2317.06(14)
Z	4
ρ_{calc}g/cm^3	1.389
μ/mm^{-1}	1.178
F(000)	1024.0
Crystal size/mm^3	0.396 × 0.271 × 0.078
Radiation	CuKα (λ = 1.54184)
2Θ range for data collection/°	7.508 to 145.96
Index ranges	-15 ≤ h ≤ 15, -12 ≤ k ≤ 12, -22 ≤ l ≤ 21
Reflections collected	5357
Independent reflections	5357 [R_{int} = 0.0417, R_{sigma} = 0.0146]
Data/restraints/parameters	5357/0/309
Goodness-of-fit on F^2	1.063
Final R indexes [I>=2σ (I)]	R_1 = 0.0449, wR_2 = 0.1296
Final R indexes [all data]	R_1 = 0.0493, wR_2 = 0.1336
Largest diff. peak/hole / e Å^{-3}	0.81/-0.30

Al(**14**)Me_2

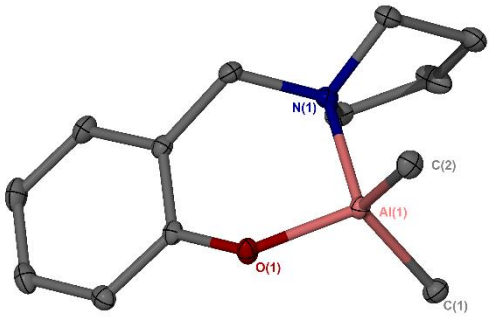

Empirical formula	C13 H20 Al N O	
Formula weight	233.28	
Temperature	150(2) K	
Wavelength	1.54184 Å	
Crystal system	Monoclinic	
Space group	$P2_1/c$	
Unit cell dimensions	a = 9.6264(2) Å	α = 90°
	b = 7.2241(3) Å	β = 101.363(2)°
	c = 18.9098(4) Å	γ = 90°
Volume	1289.25(7) $Å^3$	
Z	4	
Density (calculated)	1.202 Mg/m^3	
Absorption coefficient	1.203 mm^{-1}	
F(000)	504	
Crystal size	0.300 x 0.200 x 0.100 mm^3	
Theta range for data collection	4.685 to 70.067°.	
Index ranges	-11<=h<=11, -8<=k<=8, -22<=l<=23	
Reflections collected	18092	
Independent reflections	2444 [R(int) = 0.0238]	
Completeness to theta = 67.684°	100.0 %	
Absorption correction	Semi-empirical from equivalents	
Max. and min. transmission	1.00000 and 0.70554	
Refinement method	Full-matrix least-squares on F^2	
Data / restraints / parameters	2444 / 0 / 147	
Goodness-of-fit on F^2	1.055	
Final R indices [I>2sigma(I)]	R1 = 0.0318, wR2 = 0.0865	
R indices (all data)	R1 = 0.0324, wR2 = 0.0870	
Extinction coefficient	n/a	
Largest diff. peak and hole	0.241 and -0.227 $e.Å^{-3}$	

Al(**15**)Me_2

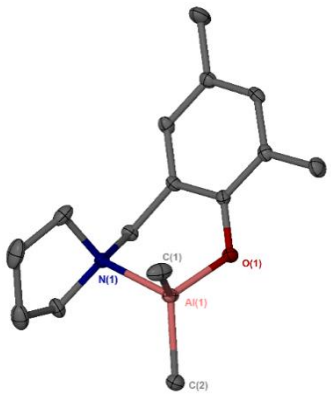

Empirical formula	C15 H24 Al1 N1 O1	
Formula weight	261.33	
Temperature	150(2) K	
Wavelength	0.71073 Å	
Crystal system	Monoclinic	
Space group	*P*-2_1/n	
Unit cell dimensions	*a* = 14.2044(14) Å	α = 90°
	b = 10.7402(5) Å	β = 107.424(9)°
	c = 20.9581(19) Å	γ = 90°
Volume	3050.6(5) $Å^3$	
Z	8	
Density (calculated)	1.138 Mg/m^3	
Absorption coefficient	0.123 mm^{-1}	
F(000)	1136	
Crystal size	0.300 x 0.300 x 0.300 mm^3	
Theta range for data collection	3.441 to 25.026°.	
Index ranges	-16<=h<=16, -12<=k<=12, -24<=l<=24	
Reflections collected	31476	
Independent reflections	5374 [R(int) = 0.0672]	
Completeness to theta = 25.026°	99.8 %	
Absorption correction	Semi-empirical from equivalents	
Max. and min. transmission	1.00000 and 0.94709	
Refinement method	Full-matrix least-squares on F^2	
Data / restraints / parameters	5374 / 0 / 333	
Goodness-of-fit on F^2	1.027	
Final R indices [I>2sigma(I)]	R1 = 0.0553, wR2 = 0.1174	
R indices (all data)	R1 = 0.0874, wR2 = 0.1324	
Largest diff. peak and hole	0.272 and -0.222 $e.Å^{-3}$	

Al(**16**)Me_2

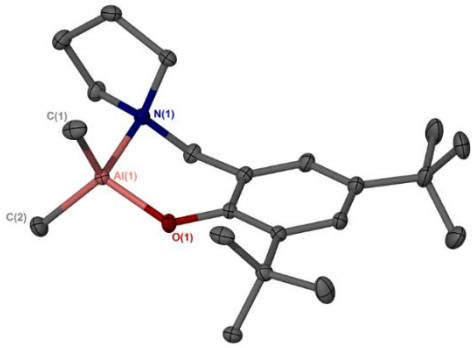

Empirical formula	C21 H36 Al N O	
Formula weight	345.49	
Temperature	150(2) K	
Wavelength	1.54184 Å	
Crystal system	Orthorhombic	
Space group	*I*-ba2	
Unit cell dimensions	*a* = 24.5360(3) Å	α = 90°
	b = 15.4808(3) Å	β = 90°
	c = 11.8029(2) Å	γ = 90°
Volume	4483.18(13) $Å^3$	
Z	8	
Density (calculated)	1.024 Mg/m^3	
Absorption coefficient	0.822 mm^{-1}	
F(000)	1520	
Crystal size	0.200 x 0.100 x 0.100 mm^3	
Theta range for data collection	3.376 to 70.063°.	
Index ranges	-29<=h<=29, -18<=k<=18, -13<=l<=14	
Reflections collected	29451	
Independent reflections	4024 [R(int) = 0.0328]	
Completeness to theta = 67.684°	100.0 %	
Absorption correction	Semi-empirical from equivalents	
Max. and min. transmission	1.00000 and 0.88066	
Refinement method	Full-matrix least-squares on F^2	
Data / restraints / parameters	4024 / 4 / 256	
Goodness-of-fit on F^2	1.143	
Final R indices [I>2sigma(I)]	R1 = 0.0376, wR2 = 0.1063	
R indices (all data)	R1 = 0.0387, wR2 = 0.1072	
Absolute structure parameter	0.017(13)	
Largest diff. peak and hole	0.251 and -0.188 e.$Å^{-3}$	

Al(**17**)Me_2

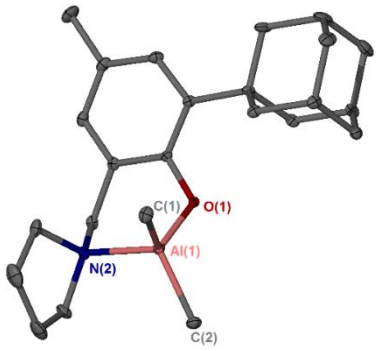

Empirical formula	C24 H36 Al N O	
Formula weight	381.52	
Temperature	150(2) K	
Wavelength	0.71073 Å	
Crystal system	Orthorhombic	
Space group	*P*21	
Unit cell dimensions	*a* = 8.0510(4) Å	α = 90°
	b = 15.4091(8) Å	β = 90°
	c = 17.1720(7) Å	γ = 90°
Volume	2130.34(18) $Å^3$	
Z	4	
Density (calculated)	1.190 Mg/m^3	
Absorption coefficient	0.109 mm^{-1}	
F(000)	832	
Crystal size	0.300 x 0.150 x 0.050 mm^3	
Theta range for data collection	3.469 to 30.153°.	
Index ranges	-11<=h<=10, -21<=k<=17, -22<=l<=23	
Reflections collected	16041	
Independent reflections	5566 [R(int) = 0.0348]	
Completeness to theta = 25.242°	99.2 %	
Max. and min. transmission	1.00000 and 0.92138	
Refinement method	Full-matrix least-squares on F^2	
Data / restraints / parameters	5566 / 0 / 247	
Goodness-of-fit on F^2	1.042	
Final R indices [I>2sigma(I)]	R1 = 0.0477, wR2 = 0.0984	
R indices (all data)	R1 = 0.0604, wR2 = 0.1047	
Absolute structure parameter	-0.14(8)	
Extinction coefficient	n/a	
Largest diff. peak and hole	0.267 and -0.242 e.$Å^{-3}$	

Al(**18**)Me_2

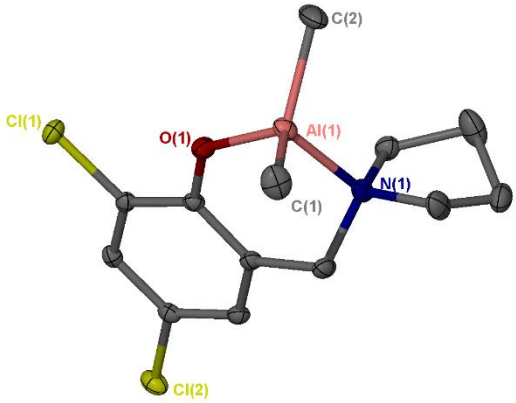

Empirical formula	C26 H36 Al2 Cl4 N2 O2	
Formula weight	604.33	
Temperature	150(2) K	
Wavelength	1.54184 Å	
Crystal system	Monoclinic	
Space group	$P2_1/c$	
Unit cell dimensions	a = 7.69360(10) Å	α = 90°
	b = 29.7729(5) Å	β = 93.9040(10)°
	c = 13.10210(10) Å	γ = 90°
Volume	2994.21(7) $Å^3$	
Z	4	
Density (calculated)	1.341 Mg/m^3	
Absorption coefficient	4.370 mm^{-1}	
F(000)	1264	
Crystal size	0.100 x 0.100 x 0.050 mm^3	
Theta range for data collection	2.968 to 73.410°.	
Index ranges	-9<=h<=9, -36<=k<=34, -16<=l<=16	
Reflections collected	47644	
Independent reflections	6004 [R(int) = 0.0323]	
Completeness to theta = 67.684°	100.0 %	
Refinement method	Full-matrix least-squares on F^2	
Data / restraints / parameters	6004 / 0 / 349	
Goodness-of-fit on F^2	1.099	
Final R indices [I>2sigma(I)]	R1 = 0.0352, wR2 = 0.0959	
R indices (all data)	R1 = 0.0367, wR2 = 0.0970	
Extinction coefficient	n/a	
Largest diff. peak and hole	0.330 and -0.267 $e.Å^{-3}$	

Al_2(**15**)Me_5

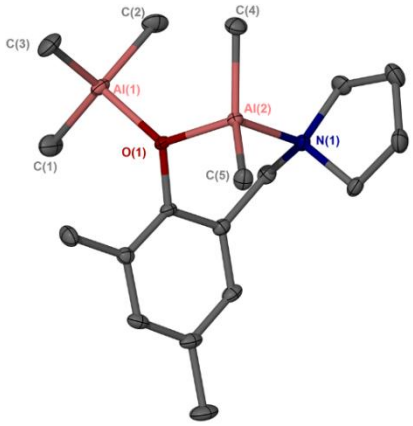

Empirical formula	C18 H33 Al2 N O	
Formula weight	333.41	
Temperature	150(2) K	
Wavelength	0.71073 Å	
Crystal system	Monoclinic	
Space group	*I*2/a	
Unit cell dimensions	*a* = 15.701(5) Å	α = 90°
	b = 11.773(3) Å	β = 100.47(3)°
	c = 22.982(5) Å	γ = 90°
Volume	4177(2) $Å^3$	
Z	8	
Density (calculated)	1.060 Mg/m^3	
Absorption coefficient	0.141 mm^{-1}	
F(000)	1456	
Crystal size	0.200 x 0.200 x 0.150 mm^3	
Theta range for data collection	3.411 to 27.484°.	
Index ranges	-20<=h<=20, -15<=k<=15, -29<=l<=29	
Reflections collected	33298	
Independent reflections	4780 [R(int) = 0.0376]	
Completeness to theta = 25.242°	99.8 %	
Refinement method	Full-matrix least-squares on F^2	
Data / restraints / parameters	4780 / 0 / 206	
Goodness-of-fit on F^2	1.032	
Final R indices [I>2sigma(I)]	R1 = 0.0409, wR2 = 0.1061	
R indices (all data)	R1 = 0.0537, wR2 = 0.1125	
Extinction coefficient	n/a	
Largest diff. peak and hole	0.295 and -0.174 e.$Å^{-3}$	